# TESIS DOCTORAL

**2023**

# Application of compact flow channel geometries to pressurised solar receivers: A numerical and experimental analysis

**David Jonathan D'Souza**

**PROGRAMA DE DOCTORADO EN TECNOLOGÍAS INDUSTRIALES**

**DIRECTORA: MARÍA JOSÉ MONTES PITA**
**CODIRECTOR: JOSÉ GONZÁLEZ AGUILAR**
**CODIRECTOR: MANUEL ROMERO ÁLVAREZ**

# Abstract

Concentrated solar thermal energy systems have an immense potential to renewably and sustainably address the growing global energy demand. The application scope of these technologies is broad and ranges from power generation to industrial process heating which in itself is wide ranging. The ability of concentrated solar thermal technologies to produce heat, via a working fluid, at high temperatures is what allows for this broad range of application. Operating temperatures in excess of 1000 °C can well be attained through concentrated solar thermal.

A critical component of any concentrated solar thermal system is its receiver which is the subsystem that absorbs the concentrated solar radiation incident on it and transfers it to a heat transfer fluid that passes through it. The efficiency and effectiveness with which the solar receiver is able to transfer the incident radiation to the heat transfer fluid largely decides the overall performance of any concentrated solar thermal system.

In this thesis, a novel type of solar receiver, is proposed and explored with the objective of developing receivers with performances rivalling or bettering those of the state of the art. The proposed receivers are based on compact heat exchanger concepts in so far that the flow channels of the receivers imitate those typically used in compact heat exchangers. The motivation behind this are the well understood and demonstrated performance enhancements achieved in compact heat exchangers, especially when the working fluid is a gas or a supercritical fluid. This improved performance owes itself to the compactness of the flow channels which boosts the heat transfer to the fluid though at the expense of an increased pressure drop. Smaller sized receivers, which is an inherent feature and advantage of compact structures, results in savings in material costs.

There are several compact flow channel geometries, commonly used in compact heat exchangers, which may be employed in solar receivers. In order to evaluate the performance of each of these flow channel geometries, a numerical model of solar receivers using a pressurised fluid has been developed. The numerical model has been programmed in such a way as to easily facilitate the inclusion of different flow channel geometries and vary their respective geometrical configurations.

Applying the developed numerical model to a central solar pressurised air receiver power plant coupled to a supercritical carbon dioxide Brayton cycle, a steady state parametric and optimisation analysis was performed on six different receiver flow channel geometries. The six geometries selected were the plain rectangular, plain triangular, wavy, offset strip, perforate and louvred fin flow channels. Four geometrical parameters, common to all flow channel geometries, were identified and varied in the parametric study. These are the channel height, channel breadth, channel wall thickness and number of vertical channels. Performance indicators for receiver evaluation were studied and it was determined that exergy efficiency, which accounts for both heat transfer to the fluid and pressure drop in it besides the incident solar radiation, is a useful tool for optimisation and comparison.

The parametric study revealed that perforated fin receivers, followed by plain rectangular and wavy fin receivers, exhibited the highest exergy efficiencies with taller and narrower channels with thicker walls and fewer vertical channels improving this efficiency. The methodology used in this analysis, besides the receiver operating conditions and system modelling assumptions, greatly affects the results and relative performances of the receiver configurations. A validation of the model and some of its underlying assumptions was conducted by comparing it to a previous study and a more complex three-dimensional computational fluid dynamics model.

To substantiate the findings of the numerical model, an experimental campaign on receivers of differing flow channel geometric configurations was proposed. The high flux solar simulator of the IMDEA Energy institute, namely KIRAN-42, was employed as the radiation heat source for the experiments. A calorimetric testbed was designed, assembled and commissioned for the purpose of experimentation on pressurised gas receivers. Procedures for the operation and control of the pressurised receiver testbed were established after a series of preliminary test runs.

Four variants of the plain rectangular fin receiver were designed and fabricated using additive manufacturing. The geometrical variations in the receivers were increased height, increased breadth, and reduced channel wall thickness respectively. The receivers were manufactured in stainless steel and Inconel 718 though only the stainless-steel receivers were experimented on. An experiment plan was drawn out specifying the experimental characterisation to be performed on each receiver. This was performed varying the mass flow rate of air, receiver inlet pressure and incident radiation peak flux.

The experimental campaign confirmed important findings and predictions of the pressurised receiver numerical model. These include the maximum thermal efficiency and pressure loss occurring at the smallest channel size and also the positive effect of taller and narrower channels. The maximum thermal efficiency observed was 94.7% at an inlet pressure of 12 bar, a mass flow rate of 2 g $s^{-1}$ and a peak incident flux of 400 kW $m^{-2}$ with the corresponding pressure drop measured at below 1% of the inlet pressure. This performance, in terms of thermal efficiency and relative pressure drops, is on par and even surpasses the state-of-the-art receivers of its type. Such high thermal efficiencies (above 90%) and low relative pressure drops (below 1%) were observed for other operating conditions and receiver geometries as well.

The numerical model of the receiver was modified to better represent experimental realities such as the flow channel surface roughness, non-uniform incident radiation, uneven receiver surface absorptance and receiver inlet/outlet section pressure losses. While the pressurised receiver numerical model generally corresponded well with the experiments, within the bounds of experimental error, a sensitivity analysis was performed to evaluate the influence of operational parameters that had significant associated uncertainties. These included the mass flow rate, incident radiation flux, inlet pressure, air composition and receiver surface absorptance. The performance indicators evaluated in this sensitivity analysis were the receiver outlet temperature, pressure drop, thermal and energy efficiencies.

In conclusion, the use of compact flow channels in pressurised gas receivers has been numerically and experimentally demonstrated to produce high performance receivers. When optimised for geometry, these receivers can effectively transfer incident solar radiation to the heat transfer fluid at thermal efficiency and pressure drop combinations that rival and excel the state of the art in pressurised gas receivers.

# Resumen

Los sistemas de energía solar térmica concentrada tienen un inmenso potencial para hacer frente de forma renovable y sostenible a la creciente demanda mundial de energía. El ámbito de aplicación de estas tecnologías es amplio y abarca desde la generación de energía eléctrica hasta la producción de calor para multitud de procesos industriales. Estas tecnologías tienen la capacidad de producir calor en un amplio rango de temperaturas, a través de un fluido de trabajo, lo que permite su adaptación a una amplia gama de aplicaciones. Las tecnologías de concentración solar permiten alcanzar perfectamente temperaturas de funcionamiento superiores a 1.000 °C.

Un componente crítico de cualquier sistema solar térmico de concentración es el receptor, que es el subsistema que absorbe la radiación solar concentrada que incide sobre él, procedente del elemento concentrador, y la transfiere a un fluido caloportador que lo atraviesa. El rendimiento y la efectividad con los que el receptor solar es capaz de transferir la radiación incidente al fluido caloportador influye notablemente sobre el rendimiento global de cualquier sistema solar térmico de concentración.

En esta tesis, se propone y analiza un nuevo tipo de receptor solar con el objetivo de desarrollar receptores con rendimientos similares o mejores a los referidos en el estado del arte. El receptor propuesto se basa en el concepto de intercambiador de calor compacto, ya que los canales de circulación del fluido a su través, imitan a los utilizados habitualmente en este tipo de intercambiadores de calor. El motivo de esta similitud es el mejor funcionamiento y rendimiento que se consigue en los intercambiadores de calor compactos, especialmente cuando el fluido de trabajo es un gas o una fase supercrítica. Esta mejora del rendimiento se debe a la compacidad de los canales de flujo, que aumenta la transferencia de calor al fluido, aunque a expensas de una mayor caída de presión. El menor tamaño de los receptores, que es una característica inherente y una ventaja de las estructuras compactas, redunda en un ahorro de costes de material.

Existen varias geometrías compactas de canal de flujo, utilizadas habitualmente en los intercambiadores de calor compactos, que pueden emplearse en los receptores solares. Para evaluar el rendimiento de cada una de estas geometrías compactas, se ha desarrollado un modelo numérico de receptores solares que utilizan un fluido presurizado. El modelo numérico programado es muy versátil, permitiendo la inclusión de diferentes geometrías de canales de flujo y diferentes valores de sus parámetros geométricos.

A continuación, se ha aplicado el modelo numérico desarrollado a una central termosolar de torre central, que emplea aire presurizado en el receptor y está acoplada a un ciclo Brayton de dióxido de carbono supercrítico. Se ha realizado un análisis paramétrico y de optimización en estado estacionario de seis geometrías compactas diferentes. Las seis geometrías seleccionadas fueron de tipo: aleta plana rectangular, aleta plana triangular, aleta curvada, aleta desplazada, aleta perforada y aleta dentada. En el estudio paramétrico se identificaron y variaron cuatro parámetros geométricos comunes a todas las geometrías. Se trata de la altura del canal, la anchura del canal, el grosor de la pared del canal y el número de canales verticales. Se analizaron diferentes indicadores de rendimiento para la evaluación del receptor y se determinó que el rendimiento exergético, que tiene en cuenta tanto la transferencia de calor al fluido como la caída de presión en el mismo, además de la radiación solar incidente, es una herramienta útil para la optimización y la comparación.

El estudio paramétrico puso de manifiesto que los receptores de aletas perforadas, seguidos de los receptores de aletas rectangulares lisas y curvadas, presentaban los rendimientos exergéticos más elevados, ya que dicho rendimiento se ve favorecido por el empleo de canales más altos y estrechos, junto con paredes más gruesas

y menos canales verticales. La metodología utilizada en este análisis, además de las condiciones de funcionamiento del receptor y las hipótesis de modelización del sistema, afecta en gran medida a los resultados y al rendimiento relativo de las configuraciones del receptor. Se realizó una validación del modelo y de algunos de sus supuestos subyacentes comparándolo con un estudio anterior y con un modelo tridimensional más complejo de dinámica de fluidos computacional.

Para corroborar los resultados del modelo numérico, se diseñó y realizó una campaña experimental con receptores de distintas configuraciones geométricas de los canales de flujo. El simulador solar de alto flujo del instituto IMDEA Energía, KIRAN-42, se empleó como fuente de calor por radiación para los experimentos. Se diseñó, montó y puso en marcha un banco de pruebas calorimétrico para la experimentación con receptores de gas a presión. Tras una serie de pruebas preliminares, se establecieron los procedimientos de funcionamiento y control del banco de pruebas de receptores presurizados.

Se diseñaron cuatro variantes del receptor de aleta plana rectangular y se fabricaron mediante fabricación aditiva. Las variaciones geométricas de los receptores consistieron en un aumento de la altura, un aumento de la anchura y una reducción del grosor de la pared del canal, respectivamente. Los receptores se fabricaron en acero inoxidable y en Inconel 718, aunque sólo se experimentó con los de acero inoxidable. Se elaboró un plan de ensayos en el que se especificaba la caracterización experimental que debía realizarse en cada receptor. Para ello, se consideraron como variables el caudal másico de aire, la presión de entrada al receptor y el flujo pico de radiación incidente.

La campaña experimental sirvió para confirmar las principales conclusiones y predicciones del modelo numérico del receptor presurizado. Entre ellos se incluyen el máximo rendimiento térmico y la pérdida de presión que se producen con el tamaño de canal más pequeño, así como el efecto positivo de los canales más altos y estrechos. El rendimiento térmico máximo observado fue del 94,7% a una presión de entrada de 12 bar, un caudal másico de 2 g $s^{-1}$ y un flujo incidente máximo de 400 kW $m^{-2}$, con la correspondiente pérdida de carga medida por debajo del 1% de la presión de entrada. Este rendimiento, en términos de eficiencia térmica y caídas de presión relativas, está a la par e incluso supera a los receptores más avanzados de su tipo. Estas altas eficiencias térmicas (por encima del 90%) y bajas caídas de presión relativas (por debajo del 1%) se observaron también para otras condiciones de funcionamiento y geometrías del receptor.

El modelo numérico del receptor se modificó para representar mejor determinadas características, como la rugosidad de la superficie del canal, la radiación incidente no uniforme, la absorbancia desigual de la superficie del receptor y las pérdidas de presión de la sección de entrada/salida del receptor. Aunque el modelo numérico del receptor presurizado se correspondía en general bien con los experimentos, dentro de los límites del error experimental, se realizó un análisis de sensibilidad para evaluar la influencia de los parámetros operativos que tenían incertidumbres asociadas significativas. Entre ellos se incluían el caudal másico, el flujo de radiación incidente, la presión de entrada, la composición del aire presurizado y la absortancia de la superficie del receptor. Los indicadores de rendimiento evaluados en este análisis de sensibilidad fueron la temperatura de salida del receptor, la caída de presión y las eficiencias térmica y energética.

Como conclusión, en esta Tesis se ha demostrado, numérica y experimentalmente, el uso de receptores en canales compactos para gases presurizados como un diseño de alto rendimiento. Cuando se optimiza su geometría, estos receptores pueden transferir eficazmente la radiación solar concentrada al fluido caloportador,

con un rendimiento térmico y caída de presión que rivalizan y superan las prestaciones de los receptores de gas presurizado presentes en la bibliografía técnica.

# Acknowledgements

First and foremost, I would like to thank my thesis supervisor Maria Jose without whose guidance and support this thesis would not have been possible. It was only after her involvement with my research that I finally felt a sense of direction and purpose to my work. Despite the seemingly never-ending and increasingly impossible impediments, your limitless patience, humility and understanding as a supervisor always encouraged me to push forward. I am truly fortunate to have had such a dedicated and caring supervisor.

From IMDEA Energy, I must thank my supervisors Jose Gonzalez and Manuel Romero, who gave me the opportunity to learn and grow in a dynamic unit that has such an incredible array of experimental research facilities from the solar heliostat field and tower to the high flux solar simulators and the myriad of test rigs in between. Under their astute leadership, I felt empowered to explore and learn more about the capabilities of solar energy. Jose is an extraordinary repository of information across a vast breadth of subjects, and a true scientist who would happily spend any amount of time and resources to get to the root of the question posed. His ability to scientifically reason and logically uncover the crux of each unresolved problem that arose is something I strive to emulate. Manuel, who always has time for an interesting anecdote, is nothing short of a treasure chest of knowledge on solar thermal research; his invaluable insight goes well beyond project reports and he never fails to forget the people behind the work.

I count myself lucky to have had the chance to work alongside the incredible group of colleagues in the High Temperature Processes Unit at IMDEA Energy. From Rui Chen, Mario Sanchez, Alejandro Martinez, Celia Roldan, Borja Antona, Ayoub Benkhlafa, Francesco Rovense and Ivan Bravo (affectionately dubbed “the pre-COVID group”) to Ricardo Conceiçao, Arkaitz Gonzalez, Ruben Garcia, Beatriz Herrero, Andres Martin-Fuertes, Enrique Rodriguez, Kaijun Jiang (the legend), Germilly Barreto, Charles-Alexis Asselineau, Anibal Rodriguez and Lourdes Rosa - I would not have made it through without you lot and I’m really glad to have met you all. I wish you all the best that life has to offer.

My family are the only reason I am here and to them I owe everything. My mom, whose selfless compassion and empathy are matched only by her perseverance and untiring industry - you have always inspired me to be better. My Dad, who has perfected the art of working smarter and taking the time to assess a problem before getting to fixing it - whatever I know in problem solving I have learnt from you. My sister Erika, who like with so many things in our lives, has gone and done it first. Though it’s true that I ended up proof-reading far more of your thesis’ early drafts that you have mine, I am grateful that you put up with my meandering phone calls complaining about this, that or the other. Your strength of character and courage to chart the uncharted have been a guiding light to me for longer than I can remember. Nana, Aunt Louisa and Uncle Padma: though I haven’t come back to Pune since arriving in Spain and starting this doctorate, you are with me always and the values I learnt from my time with you remain with me constantly. I love you all dearly and I hope that I have made you proud.

This thesis work has been developed within the framework of the ACES2030-CM project, funded by the Regional Research and Development in Technology Programme 2018 (ref. P2018/EMT-4319).

## Table of Contents

## List of figures

## List of tables

## Nomenclature

Acronyms:

| | |
|---|---|
| ASME | American Society of Mechanical Engineers |
| CR | Central Receiver |
| HTF | Heat Transfer Fluid |
| CHE | Compact Heat Exchanger |
| CST | Concentrated Solar Thermal |
| CSP | Concentrated Solar Power |
| CFD | Computational Fluid Dynamics |
| EA | Electrically Assisted |
| EDM | Electrical Discharge Machining |
| HCE | Heat Collector Element |
| HTF | Heat Transfer Fluid |
| HTM | Heat Transfer Medium |
| HE | Heat Exchanger |
| IRENA | International Renewable Energy Agency |
| LCOE | Levelized Cost of Electricity |
| LF | Louvred Fin |
| LFR | Linear Fresnel Reflector |
| LMTD | Log Mean Temperature Difference |
| NIST | National Institute of Standards and Technology |
| NREL | National Renewable Energy Laboratory |
| OSF | Offset Strip Fin |
| PCHE | Printed Circuit Heat Exchanger |
| PD | Paraboloid Dish |
| PF | Perforated Fin |
| PGR | Pressurised Gas Receiver |
| PFHE | Plate Fin Heat Exchanger |
| PHE | Plate Heat Exchanger |
| PRF | Plain Rectangular Fin |
| PTC | Parabolic Trough Collector |
| PTF | Plain Triangular Fin |
| RNM | Resistance Network Model |
| RPC | Reticulated Porous Ceramic |
| $sCO_2$ | Supercritical Carbon Dioxide |
| SCR | Solar Central Receiver |
| SHE | Spiral Heat Exchanger |
| SLM | Selective Laser Melting |
| STPP | Solar Thermal Power Plant |
| TRM | Thermal Resistance Model |

WF Wavy Fin

## Latin letters

| | |
|---|---|
| A | Area ($m^2$) |
| B | Breadth (m) |
| $c_p$ | Specific heat at constant pressure (J $kg^{-1}$ $K^{-1}$) |
| D | Diameter (m) |
| F | View factor (-) |
| $f_D$ | Darcy pressure friction loss factor (-) |
| $f_F$ | Fanning pressure friction loss factor (-) |
| h | Specific enthalpy (J $kg^{-1}$) |
| H | Height (m) |
| $h_{conv}$ | Convection heat transfer coefficient (W $m^{-2}$ $K^{-1}$) |
| j | Colburn factor (-) |
| k | Thermal conductivity (W $m^{-1}$ $K^{-1}$) |
| L | Length (m) |
| M | Mass (kg) |
| $\dot{m}$ | Mass flow rate (kg $s^{-1}$) |
| N | Number of channels/elements (-) |
| Nu | Nusselt number (-) |
| ΔP | Pressure Drop (Pa) |
| p | Pitch (m) |
| P | Pressure (Pa) |
| Pr | Prandtl number (-) |
| $\dot{Q}$ | Thermal power (W) |
| r | Radius (m) |
| R | Thermal Resistance (K $W^{-1}$), Ideal gas constant (J $kg^{-1}$ $K^{-1}$) |
| Re | Reynolds number (-) |
| t | Channel wall thickness (m) |
| T | Temperature (K) |
| U | Overall heat transfer coefficient (W $m^{-2}$ $K^{-1}$) |
| v | Velocity (m $s^{-1}$) |
| V | Volume ($m^3$) |

## Greek Letters

| | |
|---|---|
| η | Efficiency (-) |
| ρ | Density (kg $m^{-3}$) |
| $\mu$ | Dynamic viscosity (Pa s) |
| Δ | Differential |
| δ | Half angle of the cone subtended by the sun's disc (rad) |

Subscripts

| | |
|---|---|
| 0 | Base case |
| abs | Absorbed |
| amb | Ambient |
| ap | Aperture |
| avg | Average |
| b | Base wall |
| c | Channel |
| cond | Conduction |
| conv | Convection |
| e | Element, electrical |
| h | Hydraulic, horizontal |
| in | Inlet |
| opt | Optical |
| out | Outlet |
| p | Pressure, plate |
| rad | Radiation |
| rec | Receiver |
| ref | Reflection |
| th | Thermal |
| v | Vertical |
| w | Wall |

*To my loved ones, near and far away, this work is dedicated to you.*

# Chapter 1. Introduction

## 1.1. Concentrated Solar Thermal Systems

There are simultaneously a growing global consumption of energy as well as a demand for renewable energy sources to play a greater role in meeting the world's energy requirements [1]–[4]. However, despite this, fossil fuels continue to dominate the energy mix and may continue to do so unless urgent action is taken. A significant factor contributing to the lack of penetration of renewable energy is that not all sectors are able to utilise most renewable energy sources directly [3], [5], [6]. In the current techno-economic scenario, the dominant renewable technologies (wind and solar photovoltaics) are unable to compete and usurp conventional systems across all sectors of the energy load spectrum.

A good example of this is in the industrial and transportation sectors (which jointly comprise over 80% of global energy demand) in which renewable energy sources are very poorly represented [2], [3] as can be observed in Figure 1. Even in the electricity sector, in which renewables have made far greater inroads, the most commercialised and common renewables (i.e. solar photovoltaics and wind) have the issue of dispatchability in the electricity that they produce [7].

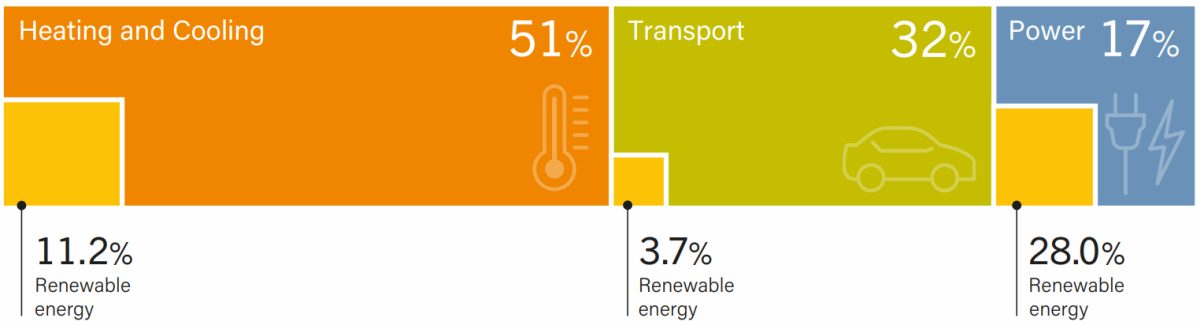


Figure 1. Sector-wise distribution of total final energy consumption with the corresponding renewable energy proportion (2019) [3]

Concentrated Solar Thermal (CST) can address several of these issues. It can be more readily used for industrial process heating, thermal desalination and potentially even process cooling [8]. Thermochemical applications of CST are also of growing interest with far reaching potential from mineral processing [9] to fuel production [10]. A synopsis of the applications of CST, outside of electricity generation, will be covered in section 1.1.3.

Power generation using conventional thermodynamic cycles has been the primary sector of interest in the application of CST for several decades [8], [11]–[13] and it is in the electricity generation sector that CST technologies have seen the most commercial application [14]. When CST is used specifically for power generation, the technology is more commonly referred to as Concentrated Solar Power (CSP). There are currently 114 CSP plants in operation, with a cumulative capacity of 6.31 GW, with 10 plants under construction [15].

CST couples well with thermal energy storage (TES) systems, which are relatively well developed, affordable and commercialised means of energy storage [16]–[19], to permit dispatchable energy loads [20]–[23]. Current thermal energy storage technologies can be classified as either sensible heat [24], latent heat [25] and thermochemical heat storage systems [26]. Of these sensible heat storage systems are the most deployed, especially using molten salts as a working fluid [16], [18]. Modern TES systems can store energy for several hours and have good scalability. This combination with TES affords CST systems near 24 hour operation capability.

### 1.1.1. Features & types of CST

As the name suggests, CST systems involve the concentration of solar radiation for the sole purpose of delivering energy at higher temperatures than would be possible with non-concentrating systems such as flat plate collectors [8]. Higher process temperatures are required for several industrial processes and CST is the only solar energy technology that is currently able to provide heat at these elevated temperatures as is shown in Figure 2.

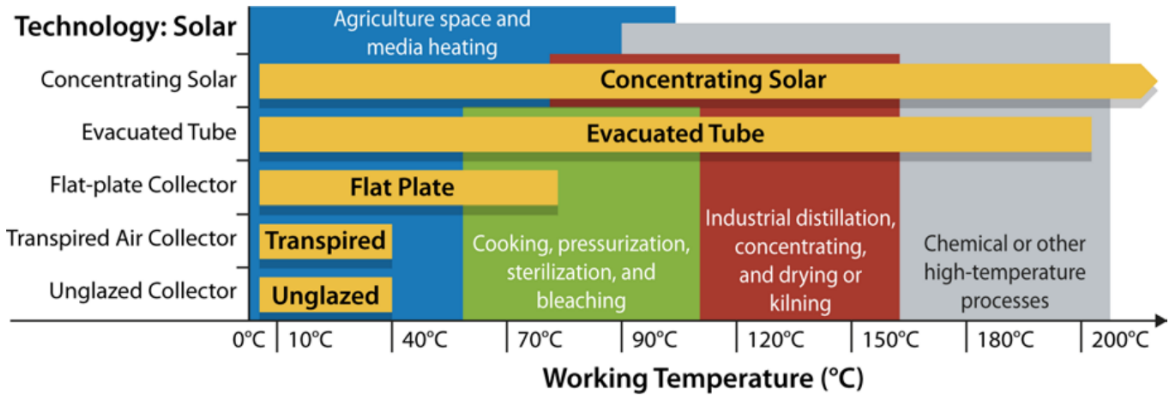


Figure 2. Operating temperature ranges of solar thermal technologies superimposed on select thermal industrial processes [27].

In general, all CST systems are comprised of a concentrator and a receiver. The concentrator is the optical system that directs solar radiation onto the receiver whose function it is to convert the concentrated incident radiation into useful thermal energy. The concentrators, also commonly termed as collectors, are primarily highly reflective mirrors of various geometries depending on the CST type that may be continuous reflectors or discretised. There are two varieties of CST systems, classified on the basis of the method of concentration, as line focussed and point focussed systems. Line focussing systems concentrate the incident solar radiation onto a line along which the receiver lies whereas point focussing systems concentrate the light to a point at which the receiver is located.

Point focussing systems require much smaller receiver areas as the light is concentrated onto a point i.e. a smaller area and hence these systems are capable of achieving much higher temperatures than line focussing systems. In other words, line focussing systems can concentrated the incident solar radiation flux between 30-80 times whereas point focussing systems can do so up to concentration factors of 1000 [28]. Being two dimensional concentrators, line focussing systems only require single axis tracking mirrors whereas point focussing systems require two axis tracking mirrors as the concentrator is three dimensional [29].

Parabolic trough (PT) and linear Fresnel reflectors (LFR) are the principal variants of line focussing systems while central receiver systems (CR) and paraboloid dish (PD) are the two main subtypes of point focussing systems. These four main types of CST systems are diagrammatically represented in Figure 3.

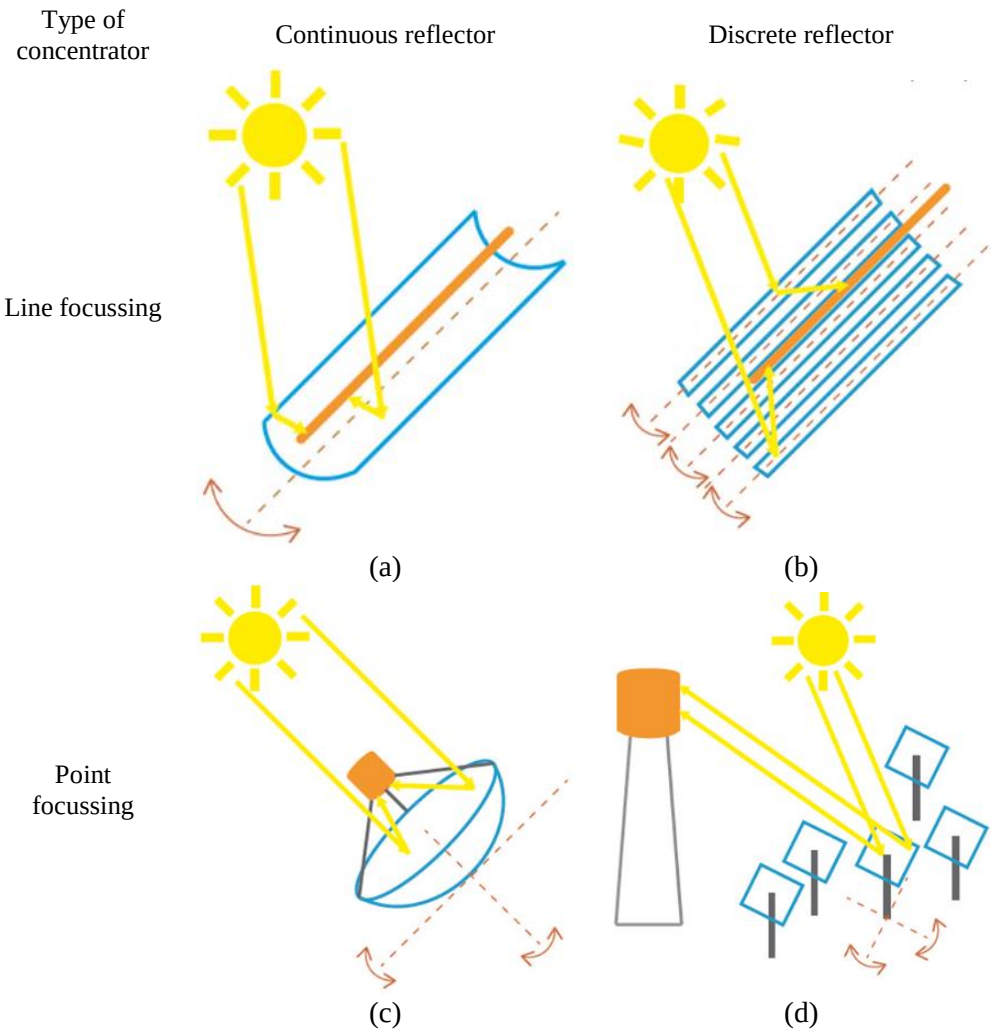


Figure 3. CST types: (a) PT, (b) LFR, (c) PD and (d) CR. Dashed lines and arrows indicate axes and directions of rotation respectively. Blue lines mark the concentrators/collectors and the receivers are coloured orange [30].

Parabolic trough (PT) technologies use a continuous parabolic reflector to linearly concentrate the incident solar radiation. The receiver remains fixed while the entire concentrating reflector rotates about a single axis tracking the sun along the day. Commercially available PTs achieve concentration ratios within the 50 to 80 range [28]. They are the most widely deployed CSP technology variant with almost 4.7 GW of PT systems operational accounting for 74.35% of all CSP plants in operation [15].

Linear Fresnel reflector (LFR) systems also use a fixed receiver but the reflectors are multiple mirrors, either plane (flat) or slightly parabolic, located parallel to the ground with each mirror rotating about its own axis to focus the incident solar radiation linearly on the receiver. Such LFR systems can achieve concentration ratios in the 30 to 70 range [31]. There is currently 255.7 MW of LFR capacity in operation comprising just over 4% of the total CSP capacity [15].

Paraboloid dish (PD) technologies create a paraboloidal reflector by either using a continuous reflector or separate sections. In these systems, the receiver is fixed on the paraboloidal focal point itself and hence both reflector and receiver rotate when aligning, along two axes as there is three-dimensional concentration, to the direct normal radiation. The receiver must be sized in such a way as to minimise the shadow it casts on the reflectors which may achieve concentration ratios above 2000 [31]. There are no active CSP plants that use PDs [15].

Central receiver (CR) systems employ several heliostats, which are reflectors on the ground, to reflect incident sunlight on a point on a tower. Each heliostat moves independently (along two degrees of freedom) as the day progresses in order to align itself and focus its reflected ray on the elevated target point on the tower. The collective action of the heliostat field is to concentrate the sunlight, by concentration ratios from 200 to several thousand, on the aperture of the receiver [14], [32], [33]. CR plants have a little over 1.3 GW capacity in operation which comprise a little over 20% of the active CSP capacity [15].

The breakdown of each respective CSP technology in the overall operational capacity mix is shown in Figure 4.

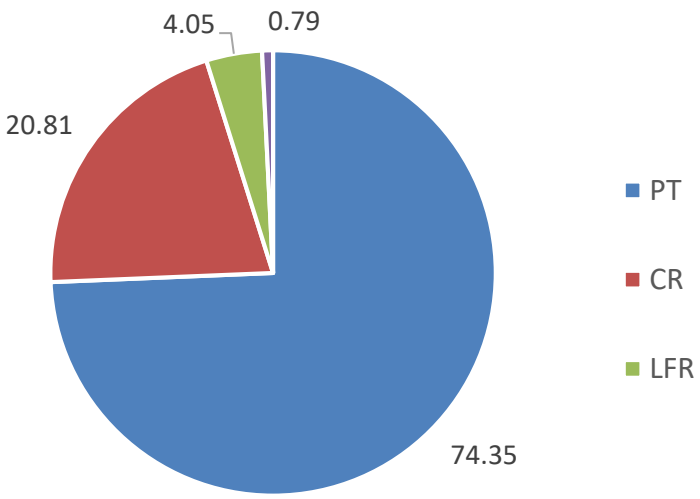


Figure 4. Share (percentage) of various CSP technologies in the operational CSP capacity mix [15].

### 1.1.2. Heat transfer fluids

The selection of the heat transfer medium (HTM), or the working medium that circulates in the solar receiver, is one of the most critical design choices as the properties of the HTM largely influence the overall performance and operating envelope of the system. This in turn impacts the applicability of the CST system employing the HTM to different process applications. The process temperature requirements is a critical design point of CST systems and is discussed in more detail in the following section about the applications of CST (section 1.1.3).

To maximise the thermal efficiency i.e. solar to useful heat conversion, the non-solid HTM or heat transfer fluid (HTF) must have a low viscosity with high thermal conductivity and volumetric heat capacity [34]. This combination of thermo-physical properties also prevents overheating of the receiver material and the induction of thermal stresses in the solid walls of the receiver itself as the HTF is capable of more effective heat evacuation. Apart from heat transfer enhancement, pressure drop in the receiver and solar loop is also an important criterion which is primarily determined by the properties of the HTF. The pressure drop is a crucial performance parameter to minimise as it is directly related to the parasitic pumping/recirculation work that is required to be performed in order to circulate the HTF in the circuit [35].

In addition to these performance related aspects, the HTF must be cost effective, environmentally non-hazardous, non-corrosive, physically and chemically stable over the range of operating temperatures and pressures and easy to handle and store.

Thermal oil is the most commonly used HTF with its use reported in over 60% of operational CSP plants [15] and such mineral or synthetic oils being tested as working fluids as early as the 1970's [31] in demonstration project plants. Among the primary reasons behind the historically widespread use of thermal oils are their good thermal stability, relatively low price, low vapour pressure and long life. Thermal oils may have an operational lifetime of over 30 years when operated within their upper temperature limits and a suitable oil ullage system is in place to treat the HTF and maintain its purity as these thermal oils naturally decompose and are more chemically unstable at higher temperatures [29], [31], [36]. The relatively high rates of degradation may serve to dampen the heat capacity of the HTF besides leading to the evolution of gases which must be removed so as to not reduce the heat transfer coefficient due to higher gas to liquid proportions in the thermal oil. Hydrogen gas evolution is particularly troublesome as it may penetrate through the absorber tube walls and enter the vacuum insulation, if one is used as is generally the case with PT receivers, and increase the heat losses to the ambient [37]. Another significant limitation of thermal oils is that their temperature limit is below 400 °C which severely limits its applicability to higher temperature process applications. Additionally, leakages of thermal oil are a fire hazard due to their relatively low fire points and also an environmental contamination risk due to these oils' elevated toxicities.

Given these substantial drawbacks of thermal oils, molten salts are more frequently being employed especially in applications that require higher operating temperatures which typically deploy solar tower/central receiver systems [29]. Molten salts currently in use in CST plants are composed of a mixture of potassium nitrate and sodium nitrate in the ratio of 2:3 and, importantly, are stable up to 600 °C besides being relatively inexpensive (1 € $kg^{-1}$) [13]. Owing to their good thermal and chemical stability, molten salts are also widely deployed as thermal storage media. This provides an additional advantage when using molten salts since it obviates the use of an intermediary heat exchanger between the solar field circuit and TES circuit. This in turn greatly reduces system cost and complexity.

On the downside, molten salts have a high freezing point and can start solidifying at temperatures of around 240 °C which leads to salt crystallisation and the formation of plugs that creates blockages in the circuit [31]. To prevent this, heating elements, called heat traces, are required across the pipelines and components to ensure the molten salt is sufficiently heated at all times. Heat tracing is a major parasitic energy loss in molten salt systems and their implementation incurs a significant material and financial cost [35]. Additionally, corrosion and erosion caused by molten salts, especially closer to the receiver when the molten salt becomes more chemically unstable at higher temperature, is a concern that needs to be monitored and entails the use of corrosion resistant alloys [38], [39].

Gases offer unique advantages when compared to thermal oil or molten salts [35], [40]. They are chemically and physically stable over a wide range of temperatures and pressures and hence do not require any heat tracing or oil ullage. This stability also simplifies the startup and shutdown procedures of the plant. The candidate gases, which will be discussed in more depth shortly, are environmentally benign, non-toxic and inexpensive. Corrosion and erosion risks to the piping and system components are also minimum, especially if appropriate filters are used, as the gases are mostly inert. The higher operational temperatures of gases (> 1000 °C) allows for more efficient thermal storage as the temperature difference of the fluid entering and leaving the solar field, and hence the thermal gradient in the TES, is greater permitting smaller TES sizes.

However, gases have far lower heat transfer coefficients as they have lower densities as compared to other fluids [31]. Owing to its poor thermophysical properties, the heat transfer to the fluid is worse in the case of gases which can lead to serious overheating concerns in the receiver [35]. This consideration is what truly limits

the design operating temperature of gas receivers more than the gas' temperature stability itself and it also necessitates the use of high temperature materials in the receiver. Lower densities, and thus higher specific volumes, also imply larger pressure drops in the circuit which call for greater pumping power in order to circulate the gas in the solar loop.

Pressurisation of the gases offsets these disadvantages, to an extent, by ensuring that there is adequate mass flow in all flow channels of the receiver thus avoiding flow instabilities and excessive local heating characteristic of volumetric/atmospheric receivers [41],[42],[43]. Besides, if the gas is pressurised, the pressure drop is reduced for an equivalent mass flow rate and cross section area as density is approximately proportional to pressure, thus the velocity is much lower at high pressure [44]. The circulation power requirement to pump the gas is inversely proportional to the square of the gas pressure [45]. Additionally, the HTF is not limited to air, which is the case with atmospheric gas receivers and other gases with more favourable heat transfer characteristics may be used [46].

The gases generally considered for use in pressurised gas receivers include, but are not limited to, helium (He), carbon dioxide ($CO_2$) and air [34]. Helium has a higher thermal conductivity and specific heat and hence a better thermal efficiency when operating at the same temperatures [47] although it has a lower density. The main drawback with the use of helium is its cost and propensity to leak given its atoms' small size. $CO_2$ is a good alternative as it has a higher density than compared to other gases at the same pressure and temperature levels. However, in the case of water infiltration, $CO_2$ reacts to form carbonic acid which is corrosive in nature especially to carbon steels. A system using $CO_2$ as its HTF must employ some drying agent to reduce this effect [31].

Air, while having worse thermophysical properties, has the strong advantage of system simplicity, conventionality and low cost. The requirement of HTF drying is not as critical in the case of air as is the case with $CO_2$ but it is still recommended as water in the circuit always poses a corrosion and oxidation risk. The presence of oxygen ($O_2$) in air also poses oxidation concerns in systems that employ air as the HTF. An inexpensive solution to minimise oxidation without significantly compromising on HTF performance vis-à-vis air, is to use nitrogen ($N_2$) as the working fluid which has similar properties as air [31].

Exergetic and energetic analyses into the use of various pressurised gases (air, nitrogen, $CO_2$, helium, neon and argon) for CST was performed through a parametric study varying the mass flow rate and inlet temperature [48], [49]. Helium was identified as having the best exergy efficiency, which accounts for both heat transfer to fluid as well as pressure drop, up to inlet temperatures of 650 K after which $CO_2$ has the better efficiency. Air and nitrogen have similar exergy efficiencies which are better than those of neon and argon. A plot of the exergy efficiencies of the different gases as a function of the inlet temperature is shown in Figure 5.

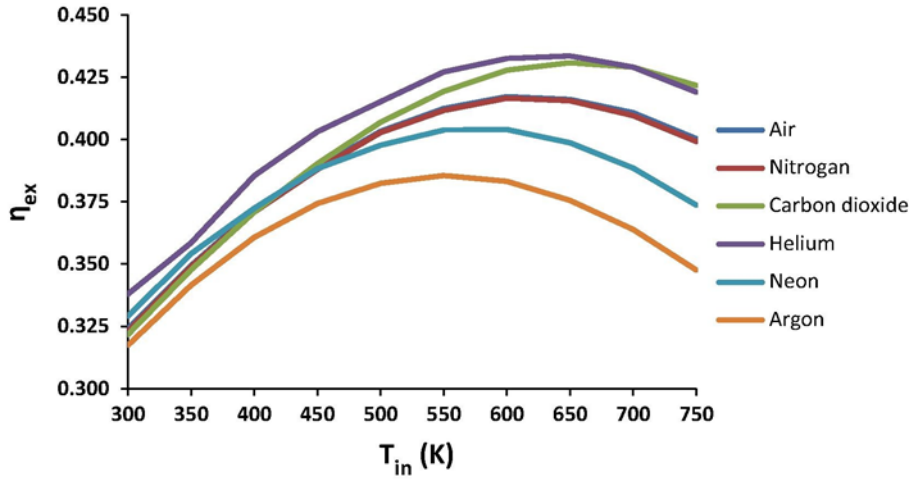


Figure 5. Exergy efficiency ($\eta_{ex}$) of gases as a function of inlet temperature ($T_{in}$) at optimum mass flow rates that maximise exergy efficiency for each gas at each inlet temperature level [48].

In the thermal analysis, neon is observed to have the higher thermal efficiency at low temperatures, while helium is the most appropriate solution in the region from 350 K to 500 K. In higher temperature levels, carbon dioxide is the gas with the greater thermal efficiency. Air and nitrogen again show similar behaviour and perform better than neon and argon though worse than helium and $CO_2$.

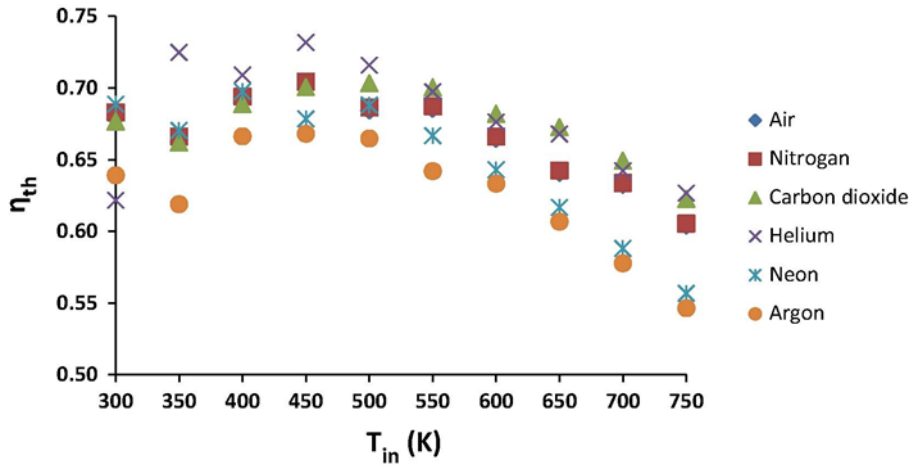


Figure 6. Thermal efficiency ($\eta_{th}$) of gases as a function of inlet temperature ($T_{in}$) at mass flow rates corresponding to optimum exergy efficiency for each gas at each inlet temperature level [48].

### 1.1.3. Applications of CST

Concentrated solar thermal technologies can be applied to the production of power, where the technology is then more commonly referred to as Concentrated Solar Power (CSP), or the production of heat for downstream industrial processes. CSP plants typically use steam Rankine thermodynamic cycles though gas Brayton cycles are promising candidates for future CSP plants [50]. A typical steam Rankine cycle plant driven by concentrated solar energy is presented in Figure 7. The operating temperature of such a plant is largely dependent on the types of CSP system used and the HTF selected. Parabolic trough systems using thermal oils can generate steam at around 370 °C. On the other hand, if molten salts are used as the HTF or direct steam generation is used in solar

tower systems, higher steam temperatures, up to 540 °C, can be achieved. This higher steam temperature boosts the thermal efficiency of the plant as the steam turbine operates more efficiently [23].

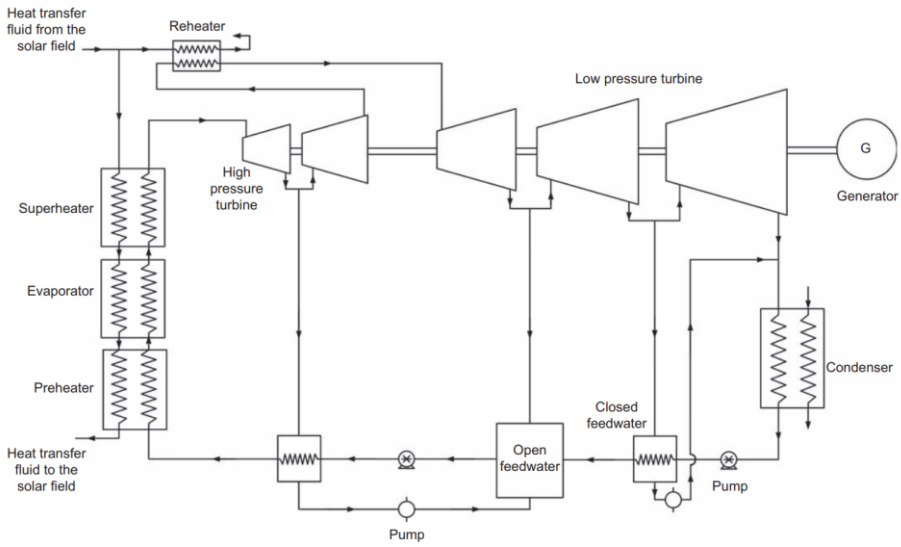


Figure 7. Steam Rankine cycle plant coupled to solar field [51].

Gas Brayton cycles have higher thermal efficiencies than steam Rankine cycles at higher turbine inlet temperatures as can be seen in Figure 8. This is especially true in the case of supercritical $CO_2$ ($sCO_2$) Brayton cycles which also have the advantage of smaller turbine weight and volume which results in the overall system having a lower thermal mass besides a less complex power block as compared to steam Rankine cycle plants due to the higher density of the fluid and simpler cycle design [52].

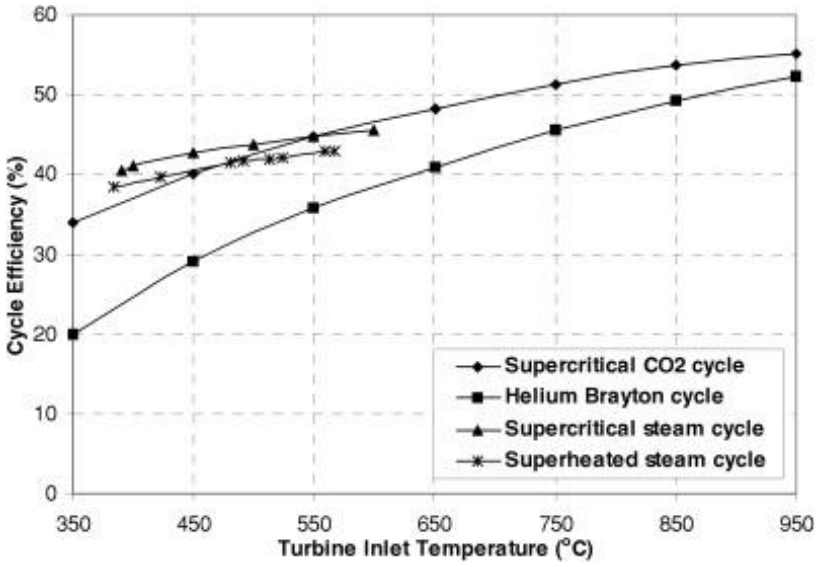


Figure 8. Comparative efficiencies of various power cycles [53].

It is for these reasons that $sCO_2$ Brayton cycle power plants are considered the next generation of CSP plants and considerable research endeavour is being invested in furthering its development [35]. The simplest Brayton cycle layout is shown in Figure 9 and it can employ any suitable gas as its working fluid including $sCO_2$, helium and air.

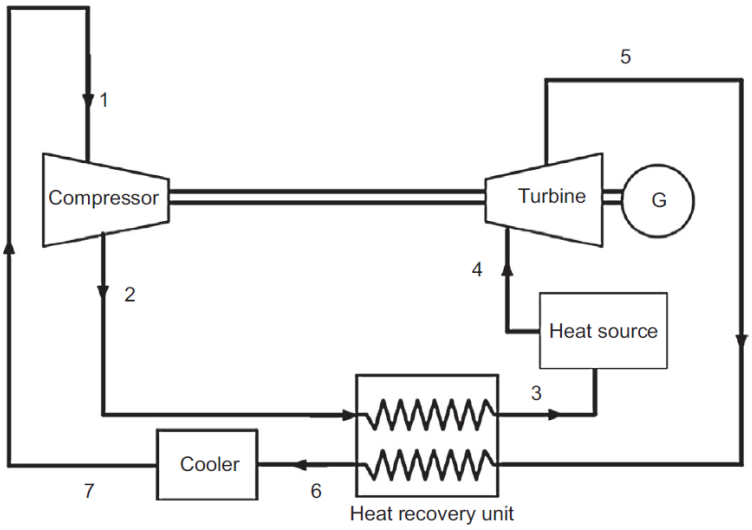


Figure 9. Simple regenerative closed Brayton cycle [54].

It should be noted though that the simple regenerative Brayton cycle is not the most thermally efficient one and there are several variations that result in higher efficiencies especially using $sCO_2$ as the working fluid [54], [55] though a detailed review into these alternative cycles is beyond the scope of this work.

The use of CST for industrial process heat is a field of growing commercial and research interest as CST system variants are capable of sustainably meeting a wide range of temperature demands from energy intensive industrial processes without releasing damaging pollutants unlike conventional fossil fuel heat sources [56]. A non-exhaustive list [57] of some of the key industrial processes which CST could be coupled to as a heat source, along with their temperature requirements, can be found in Figure 10.

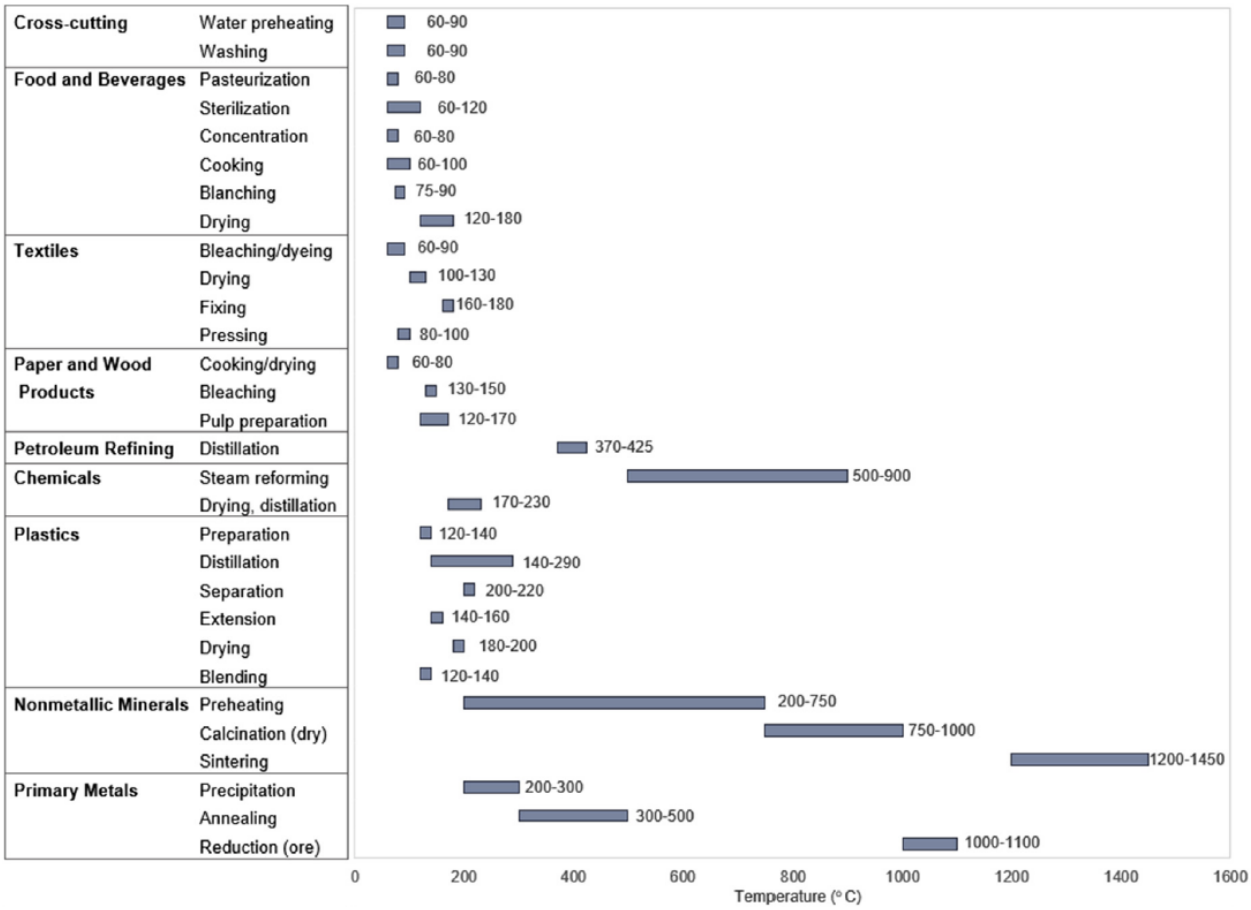


Figure 10. Industrial processes with temperature ranges [57].

There are several more potential thermal and thermochemical processes such as desalination or calcination whose thermal load may be met by CST [31] but a detailed review into this field of application of CST is beyond the scope of this work.

## 1.2. Compact heat exchangers

The definition of a compact heat exchanger (CHE) is relatively arbitrary but may be broadly defined as a heat exchanger having a surface area density above 700 $m^2/m^3$ or a hydraulic diameter of below 6 mm if at least one fluid is a gas [58]–[60]. The reduction in channel size, i.e. compactness of CHEs leads to the following outcomes:

1) A reduction in the space/required for the same effective heat transfer area. This can cause significant savings in material costs [61]
2) Smaller fluid passages lead to a higher heat transfer coefficient as it varies as a negative power of the hydraulic diameter of the passage [62]
3) Increased pressure drop [58]

CHEs are particularly relevant when using gases [60] as they have lower densities when compared to liquids and hence require higher pumping demand to overcome the higher friction power as a proportion of the heat transferred to the fluid. When the friction power is high, typically a solution to the heat exchanger design would be to increase the number of parallel flow channels to reduce the flow velocity. The flow velocity is a crucial design parameter as it decides both the heat transfer rate per unit surface area, which varies as something less than the first power the flow velocity, and the friction power which varies as something between the square and cube of the same.

Increasing the number of parallel flow channels to decrease the flow velocity, and hence the friction power, will thus also reduce the heat transfer rate per unit of surface area but this reduction will be far lower than that of the friction power. To compensate for this loss of heat transfer, the surface area must be increased by increasing the length of the flow channels which will also correspond to an increase in the friction power but this increase will be roughly proportional to the heat transfer rate increase.

Gases, with their friction power restrictions, require low mass velocities (mass flow rate per unit cross sectional flow area) and this combined with the generally poor thermal conductivity of gases results in low heat transfer rates per unit surface area. Therefore, greater surface areas are necessary in the heat exchanger when gases are employed. CHEs achieve this objective by increasing the surface area density while boosting the heat transfer coefficient through compact channels [62].

### 1.2.1. Features & types of CHE

There are several variants of CHEs but the most the most widespread and commercial ones may be broadly classified as: Plate Heat Exchanger (PHE), Plate-Fin Heat Exchanger (PFHE), Printed circuit heat exchanger (PCHE), and Spiral heat exchanger (SHE)

Plate Heat Exchangers (PHEs) are comprised of parallel plates corrugated in such a way that the corrugations between adjacent plates cross one another to form narrow winding flow channels. The plates themselves are held by a rigid frame with gaskets providing the sealing between streams. An example of a gasketed PHE can be seen in Figure 11.

PHEs have high heat transfer coefficients because of their small hydraulic diameter and good heat transfer caused by the corrugations which serve to increase the turbulence and advection of the fluid from the channel centre to the near wall. The corrugations also destroy the boundary layer and inhibit new layer formation and reattachment [58]. The gaskets tend to limit the temperature to which the PHE can operate. Additionally the PHEs have higher pressure drops due to their narrow channels which can also be blocked by flow contaminants [63].

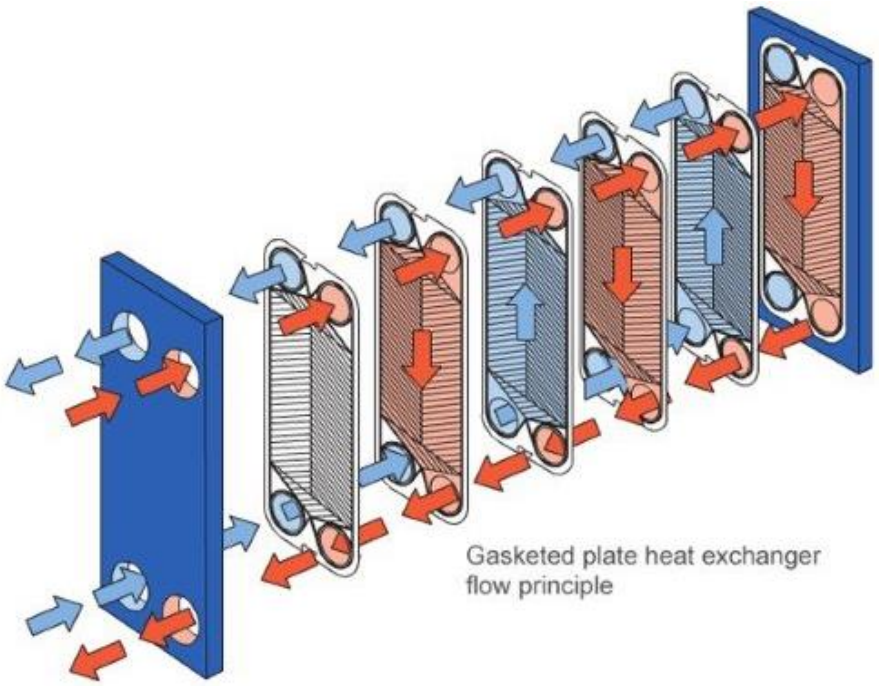


Figure 11. Flow principle of PHEs [64].

Plate-Fin Heat Exchangers (PFHEs) consist of alternate finned patterns which are separated vertically by flat sheets and along the sides by side bars to form channels as can be seen in Figure 12 below.

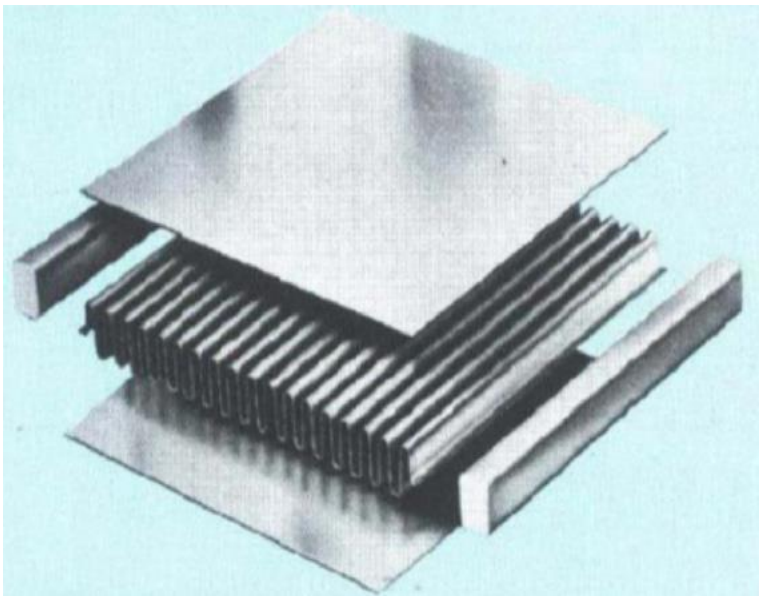

Figure 12. PFHE (exploded view) [58].

Brazing is used to attach the parting sheets, fins and side edges. The fluid channels are the spaces between the fins and each fluid flows on across the parting sheet. There is a wide scope for optimisation in design with parameters such as the number of the plates, the size of the plate and fin, the height of the fin and the type of fin being easily adjustable [65]. The ease in rearranging fin layouts allows the PFHE to operate in cross-flow, counter-flow, cross-counterflow or co-current flow.

The fins perform the dual function of enhancing the heat transfer by increasing the wetted surface area while reducing the hydraulic diameter and thermal resistance and also provide structural support and allow the CHE to withstand higher pressures. There are several types of fins including perforated, serrated and herringbone besides plain fin. Each fin has different features (in terms or relative heat transfer enhancement and pressure drops) and hence applications [58].

PFHEs are prone to fouling owing to their small channels and, moreover, they cannot be cleaned mechanically. Hence fluid streams with fouling potential must use a filtration system. In addition to this, PFHEs are more expensive as more detail is required in their manufacture.

Printed Circuit Heat Exchangers (PCHEs) are formed by diffusion bonding plates which have been previously photo-chemically etched. The diffusion bonding process results in extremely robust and metallic heat exchangers that can withstand extremely high internal pressures. The lifetime and corrosion resistance is also greatly improved due to the diffusion bonding process. This is because of the nature of diffusion bonding in which a period of thermal soaking allows for grain growth which smoothens joint interfaces and provides them with strength comparable to that of the base material [66], [67].

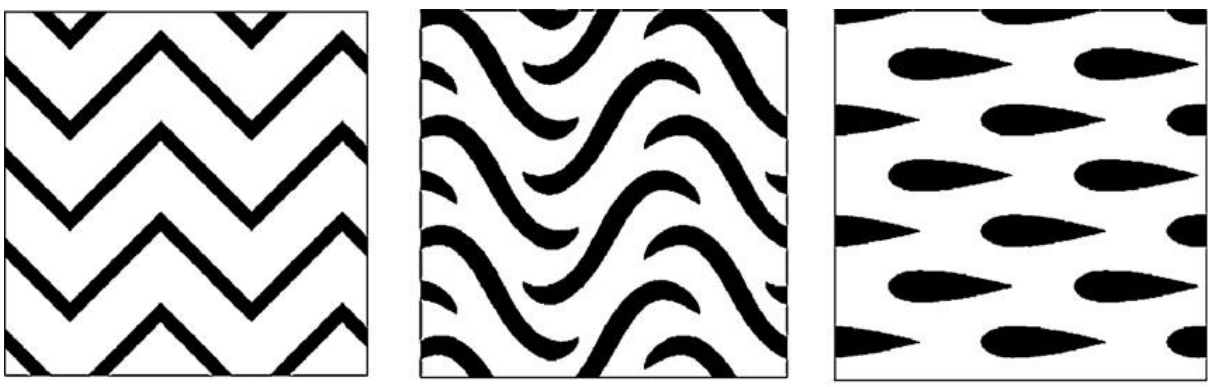

Figure 13. Types of PCHEs with various flow channel geometries [66].

PCHEs may be configured to operate in parallel, counter or cross flow or any combination of these. As with all CHE, the small channel size improves the heat transfer process. The unique advantage of PCHEs are their high operating pressure tolerance and inherent safety owing to the fact that there are no gaskets or brazed materials. Leakage is also hence a negligible factor as the PCHE is practically one solid without discontinuities.

High pressure drops are the main drawback of PCHEs especially at low-medium pressures where it is more of a constraint.

Spiral Heat Exchangers (SHE) or circular (helical) heat exchangers are formed by rolling out two metal sheets to form concentric spirals of rectangular cross-section as can be seen in Figure 14.

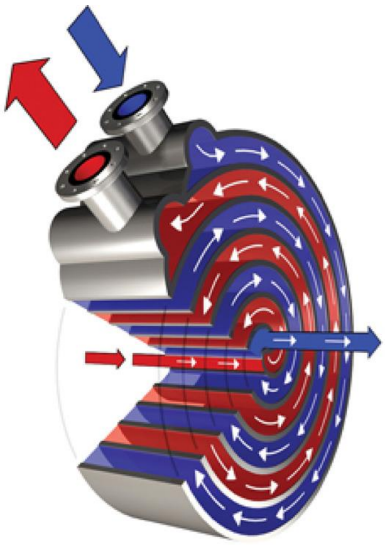

Figure 14. Spiral Heat Exchanger [58].

Depending on how the edges are sealed (welded or with gaskets) there may be double spiral counter flow, one in spiral the other cross flow (across the spiral) or a combination of one being counter and cross flow [68]. The curvature of the fluid passage causes a centrifugal force which, in turn, causes eddy currents and vortices that greatly improve the heat transfer [69].

### 1.2.2. CHEs for solar receiver applications

There have been several studies investigating the use of CHEs as the intermediary HE between the solar field and the power block [67],[70],[71]. but fewer studies into directly using CHE geometries and concepts for solar receivers, as summarised in the next paragraphs.

The operational limits of the main types of CHEs are presented in [58], although it should be noted that these limits are not absolute and largely depend on the materials used and manufacturing processes. It is intended to be indicative of the relative capacities of each type of CHE.

Table 1. Operational limits of CHEs. PHE represents Plate Heat Exchanger; PFHE stands for Plate Fin Heat Exchanger; PCHE denotes Printed Circuit Heat Exchanger; and SHE denotes Spiral Heat Exchanger [58].

| **CHE Type** | **Maximum temperature (°C)** | **Maximum pressure (bar)** |
|---|---|---|
| Gasketed PHE | 200-250 | 35 |
| Brazed PHE | 225 | 45 |
| PFHE | 800 | 120 |
| Diffusion bonded PFHE | 800 | 620 |
| PCHE | 900 | 500-1000 |
| SHE | 540 | 25 |

Given the high temperature requirements of all solar receivers (> 900 °C), Plate Heat Exchangers (PHEs) are not feasible and the CHEs must use materials that can withstand such temperatures such as ceramics, nickel and titanium alloys. Diffusion bonded Plate Fin Heat Exchangers (PFHEs) and Printed Circuit Heat Exchangers (PCHEs) were considered the most suitable candidates for application as solar receivers, due to their high efficiency as well as mechanical strength. Nevertheless, for typical pressurised gas receiver (PGR) working pressures, even in the case of direct coupling with a supercritical power cycle (approximately 200 bar), it is sufficient to use a diffusion bonded PFHE type, so the research has focused on this type, yielding to several prototypes described in next section.

Finally, it is interesting to note that there are additive methods to manufacture these compact structures including Electrically Assisted (EA) forming [72] and Selective Laser Melting (SLM) [73] that provide a greater degree of flexibility in the design of the CHE microchannels There are also novel techniques, specifically Electrical Discharge Machining (EDM), employed to increase the aspect ratio (channel height to width) in PFHEs [74],[75].

## 1.3. Solar Central Receivers using pressurised gases

Pressurised gas receivers may be classified, on the basis of the mechanism of the solar radiation absorption and heat transfer to the HTF, as directly, indirectly or hybrid irradiated receivers [47]. As the name suggests, directly irradiated receivers have their flow channels irradiated or alternatively, the solid surface in contact with the HTF as well as the HTF itself are directly illuminated. On the other hand, indirect receivers have a solid physical separation between the irradiated surface and the flow channels of the HTF.

This analysis will focus on indirectly irradiated receivers as directly irradiated receivers are limited in their operating pressure by the fragility of the quartz glass window [47], [76]. For CSP plants being proposed with novel $sCO_2$ Brayton power cycles, $sCO_2$ and the HTF should have similar operating pressures to ease the design of the intermediate heat exchanger [55]. The high pressure and low pressure extremes of the $sCO_2$ cycle are around 250 bar and 75 bar respectively [54], [55], [77], [78] which are beyond the capacity of quartz windows [76]. Hence in order to achieve HTF pressures close to those used in the $sCO_2$ cycle, an indirect receiver must be used.

A brief description of selected pressurised gas receivers (which have been experimentally tested) followed by a table with more technical details and relevant calculated parameters will be presented and summarised.

### 1.3.1. SOLGATE tubular Receiver

A modular tubular receiver designed in a cavity shape (in order to trap more incident solar radiation) was the concept proposed by the SOLGATE (Solar hybrid Gas and Electric Turbine) project [79]. As the project name indicates, it intended to integrate CST into a gas turbine cycle. The tubular receiver, which is focussed on here, was used as the low temperature heat source module to preheat the air before further heating subsequent modules. The goal of the receiver (Figure 15) was, hence, to heat the air after the compressor from 350 °C to 550 °C.

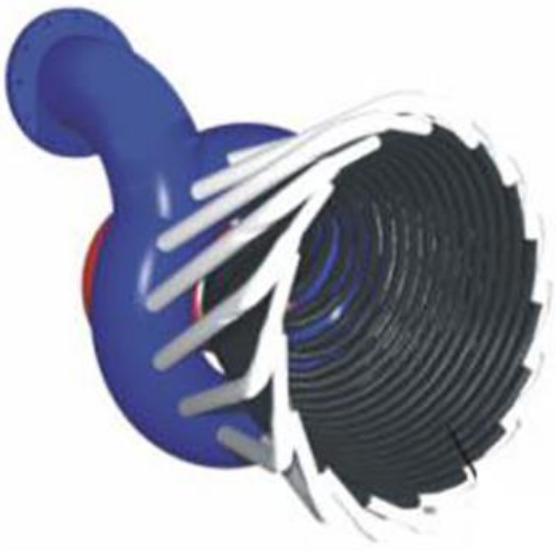

Figure 15: SOLGATE Receiver [79].

The SOLGATE receiver had one main inlet (and outlet) which split into 16 parallel tubes. Each tube had a diameter of 28 mm and a length of 2.3 m.

### 1.3.2 SOLHYCO tubular Receiver

Building on the success of the tubular cavity receiver concept of SOLGATE, the SOLHYCO (Solar-Hybrid Power and Cogeneration Plants) project aimed to design a pressurised air receiver that would singularly heat the air to a high temperature before entry into a combustion chamber. The objectives of the SOLGATE receiver (Figure 16) were to achieve a high thermal efficiency, a pressure drop below 100 mbar and air outlet temperatures up to 800 °C without heating the tubes over 900 °C [80], [81].

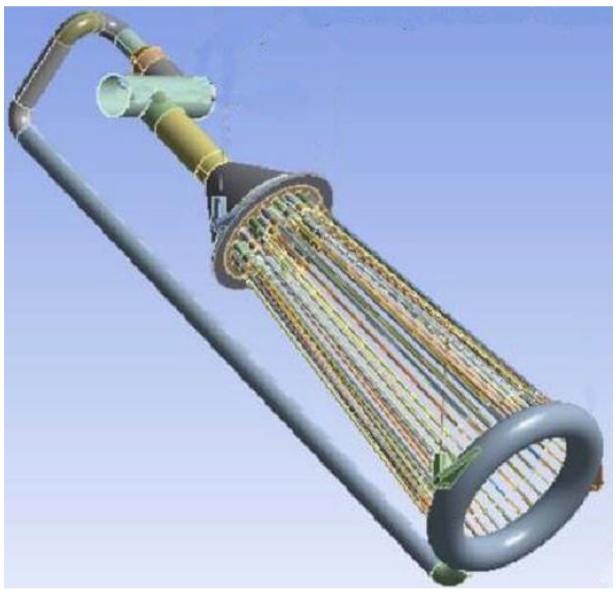

Figure 16: SOLHYCO Receiver [81].

The receiver had 40 straight 2.5 m tubes (each with an outer diameter of 26.7 mm and thickness of 2.11 mm) inside the cavity with 0.9 m aperture diameter.

Wire coil inserts (Figure 17) were used in every tube to eliminate the thermal boundary layer and promote fluid mixing and hence enhancing the heat transfer.

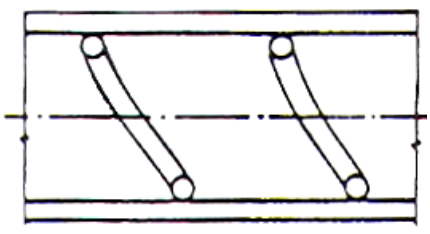

Figure 17. Wire coils used inside tubes of SOLHYCO Receiver [80].

The wire coils had a wire diameter for 2 mm and a pitch of 55.4 mm. An analytical model showed the addition of the wire coils reduced the required overall receiver tube length by 54.8 m or 35.4%

### 1.3.3. SOLUGAS tubular Receiver

Improving and scaling up the SOLHYCO receiver concept, the SOLUGAS tubular receiver consisted of 10 panels, each with 17 tubes of 5m length, and aimed to heat pressurised air from around 300 °C to 800 °C at

thermal efficiencies of 80% [82]. The tubes individually had an inner diameter of 19.6 mm and a thickness of 1.4 mm.

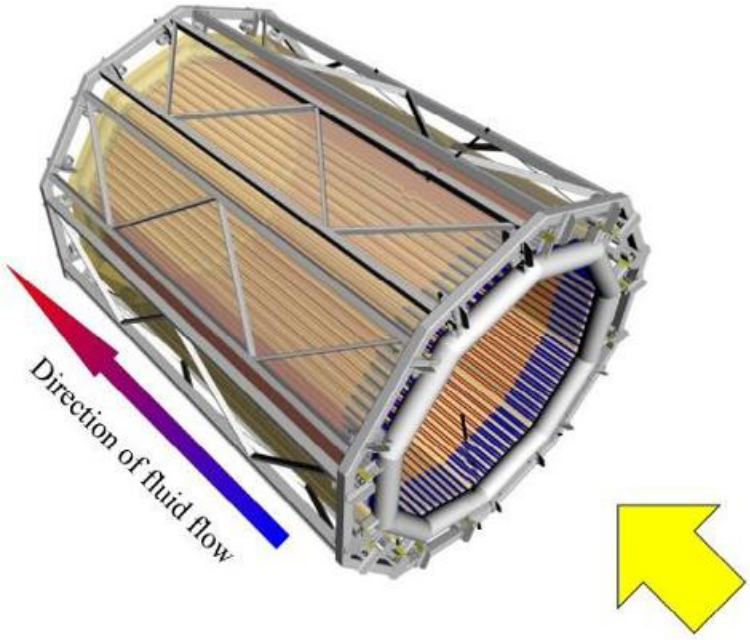


Figure 18. SOLUGAS Receiver [82].

### 1.3.4. Flat Panel Tubular Receiver

As a base case for a novel tubular receiver panel arrangement [83], three flat plate panels of 13 parallel pipes welded to inlet/outlet header manifolds are tested with pressurised air (Figure 19). Although the receiver was designed to use $sCO_2$, the preliminary experiments (which are presented here) were performed with pressurised air. Each tube had an outer diameter of 12.7 mm and a wall thickness of 1.651 mm

### 1.3.5. Bladed Receiver

The bladed receiver has, in front of three flat tubular panels, three inclined (50°) panels (blades) that each have 9 tubes. The individual tubes are identical to the ones used in the Flat Panel Receiver. The bladed panels serve to better absorb the incident solar radiation and reduce thermal losses. It was found that this bladed arrangement increased the thermal efficiency by at least 6% over the Flat Panel Receiver [35], [83], [84]

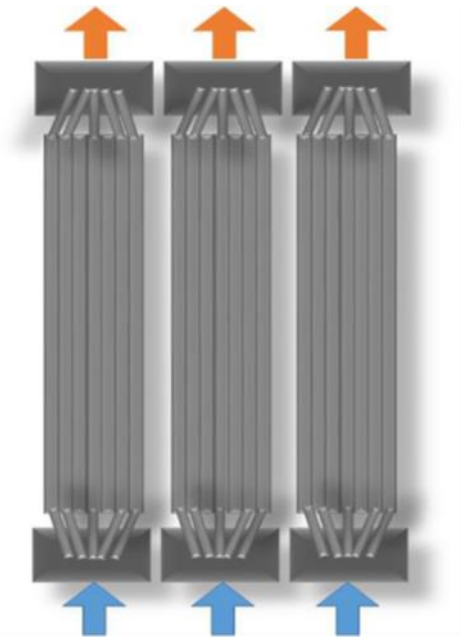

Figure 19. Flat Plate Tubular Receiver [83].

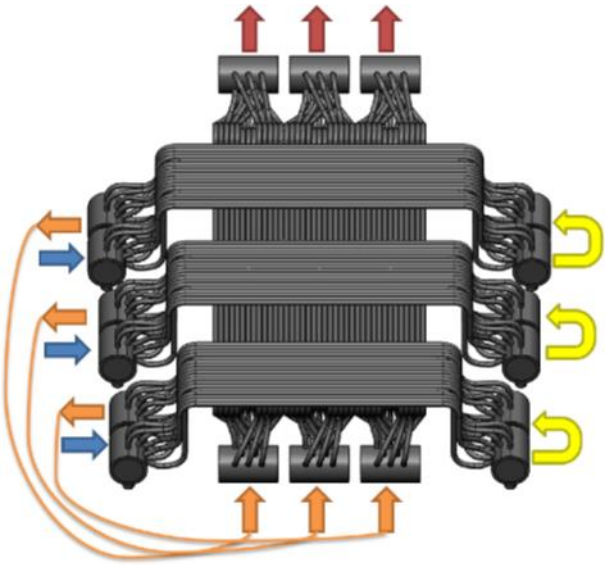

Figure 20. Bladed Tubular Receiver [83], [84].

### 1.3.6. Embedded circumferential Receiver

In this receiver the incident solar radiation enters a square cavity around which pressurised air flows [85]. The aperture of the receiver (Figure 21(a)) was 96 mm x 96 mm and its cavity length was 194 mm.

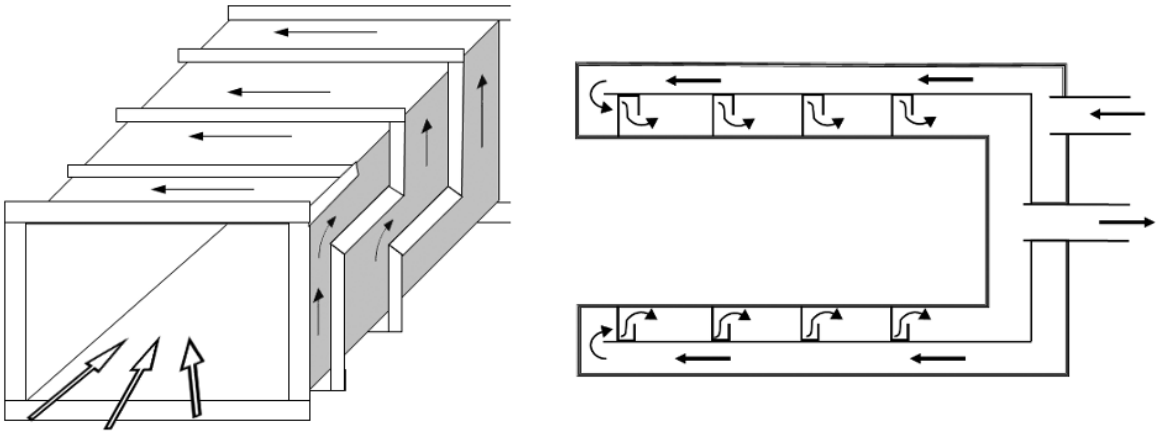

(a) (b)

Figure 21. Embedded Receivers [85]: (a) circumferential, (b) axial

### 1.3.7. Embedded axial Receiver

This receiver is similar to the previously described one, except that the flow is no longer around the circumference but along its length. Baffles are used to enhance heat transfer [85]. The cavity of this receiver (Figure 21(b)) was smaller than the circumferential type at a 70 mm x 70 mm aperture.

### 1.3.8. Microchannel Receiver

The microchannel receiver was designed based on Compact Heat Exchanger (CHE) concepts and geometries reviewed by the same research group previously [58]. The receiver was divided into 12 parallel

channels with each channel being 1 mm wide and 3 mm high. Rectangular ribs were attached on top of each channel. These ribs had the same width as the channel and a height and pitch of 2 mm and 1 mm respectively. The first rib was placed just at the entrance of the air passage as can be seen in Figure 22 [73].

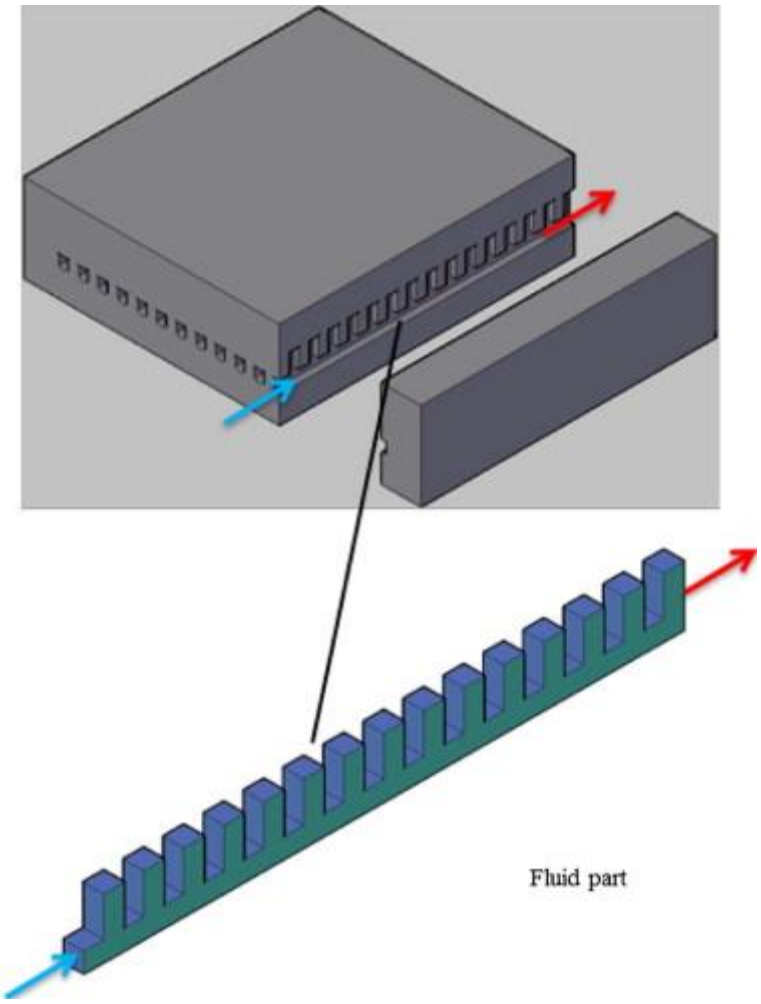


Figure 22. Microchannel Receiver [73].

The receiver was manufactured using Selective Laser Melting (SLM). The upper (top) surface of 30 mm x 30 mm was the irradiated plane.

### 1.3.9. Cavity Receiver with Reticulated Porous Ceramic (RPC) Lining (low power)

As can be seen in Figure 23, the concept of such receivers is to use a porous foam (usually SiC ceramics) on the inner lining of the receiver cavity to improve the heat transfer between the heated cavity walls and the HTF [86]. In this 3kW receiver [87], a cylindrical cavity of 30 mm in diameter (inner), 75 mm in length and 5 mm thick walls made of sintered α-silicon carbide (SSiC) had a 15 mm thick RPC made of 10 ppi SiC foam.

The receiver was designed with the intention of its use for driving a combined Brayton-Rankine cycle. The nominal temperatures and pressures at the gas turbine inlet are in the range of 1000–1600 K and 5–30 bars and this set the design operating point for the receiver.

### 1.3.10. RPC Cavity Receiver (high power)

A scaled up (50 kW) version of the previous RPC Cavity receiver was developed and experimented on [88] with similar objectives i.e. to achieve outlet air temperatures in the range of 700-1400 °C at pressures between 3-35 bar for use with gas turbines.

As with the smaller receiver, the cavity itself was constructed of SSiC and the RPC of SiC. The cavity's inner diameter was 250 mm with a length of 500 mm and a wall thickness of 7 mm. The ceramic foam on the annulus had three configurations; 10 ppi, 20 ppi and 10 ppi with air flow baffles.

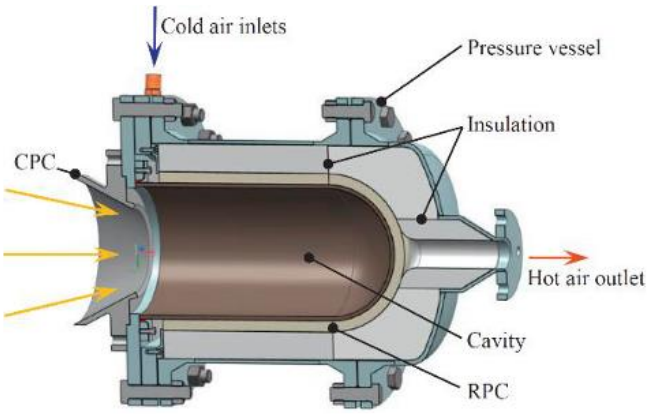


Figure 23. Cavity Receiver with RPC Lining [47].

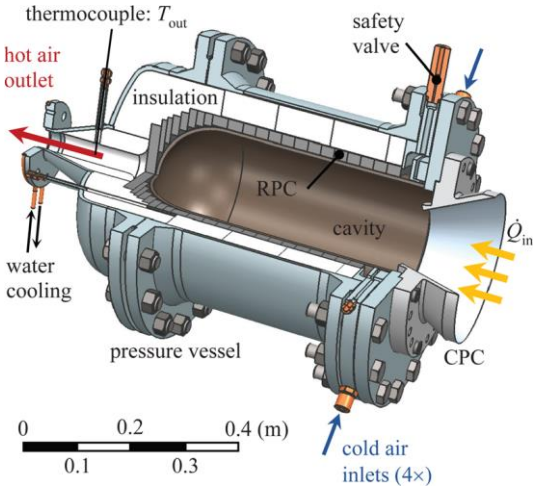


Figure 24. RPC Cavity Receiver (high power).

### 1.3.11. Impinging cavity receiver (preliminary)

The impinging cavity receiver is a novel concept [89]–[92] that uses high velocity jets of air, directed at the cavity walls, to enhance the convection heat transfer coefficient and hence the heat transfer. The principle of the same can be seen in Figure 25. The concept was developed and tested at the KTH Royal Institute of Technology, Sweden.

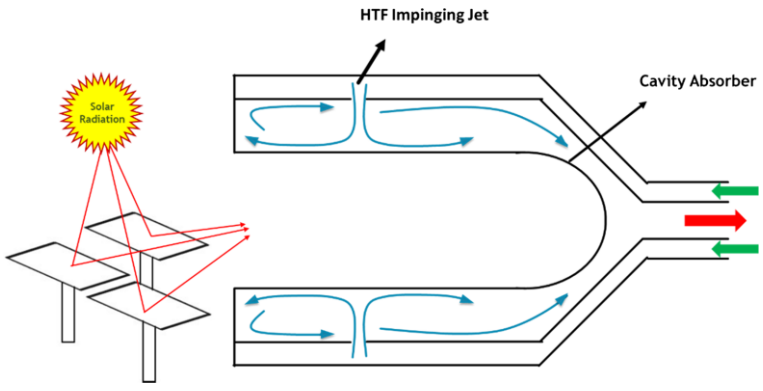


Figure 25. Impinging cavity receiver working [47].

The preliminary experiments used a cavity receiver of 280 mm in diameter and 250 mm in length with 12 nozzles (of 10 mm in diameter). The annulus was chosen as 40 mm to reduce the potential thermal gradients and influence of flow distribution.

The stated objective of the receiver was to achieve a pressure drop below 3%, a thermal efficiency of at least 75%, absorber temperature gradients below 200 °C to avoid thermal stress and an air outlet temperature of above 800 °C in order for its intended use with a gas turbine [93].

The experiments showed poor performance in terms of thermal efficiency (43%-53%) and very low outlet temperatures (160-253 °C) although the pressure drop was low 1-2.5 mbar. This poor thermal performance, and deviation from analytical expectations, was attributed to poor insulation and oxidation of the inner cavity surface [93].

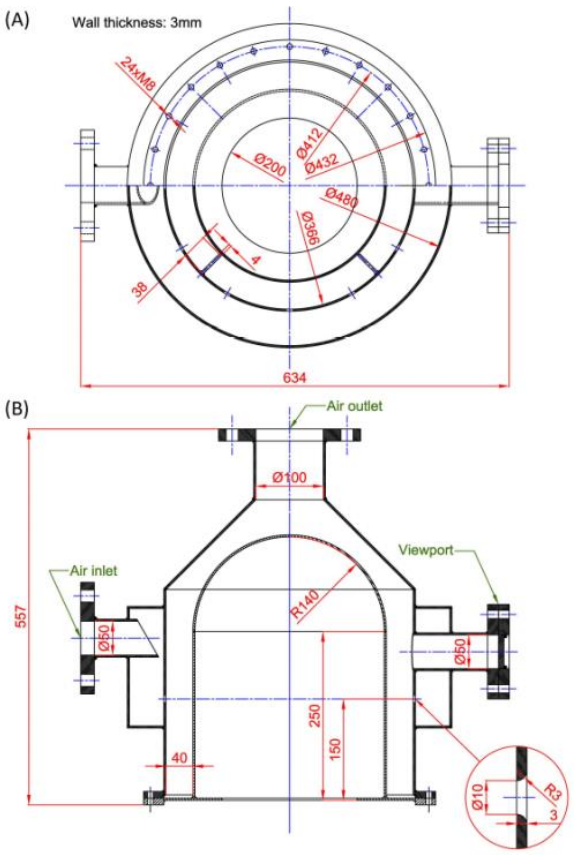


Figure 26. Design of the preliminary impinging cavity receiver [93].

## 1.3.12. Impinging cavity receiver (improved)

The same Impinging cavity receiver (Figure 26), in terms of the design and system configuration, was used in the second round of experimentation [94] with the addition of 80 mm thick ceramic wool insulation around the receiver and a Pyromark® 2500 flat black paint on the absorber surface to improve its absorptivity. Another change was the addition of a heat exchanger to preheat the air before entering the receiver. These changes resulted in an improved efficiency (74%) and an air outlet temperature of up to 810 °C although with a preheated inlet air temperature of 674 °C.

## 1.3.13. Summary of pressurised gas receivers

A table with more detailed technical specifications and calculated parameters of the receivers mentioned above can be found in the appendix. To summarise, indirectly irradiated pressurised gas receivers can be classified, on the basis of their geometry, as tubular, cavity (annular) or microchannel receivers. While these receivers can operate at higher pressures, they suffer the penalty of the extra thermal resistance of the absorbing/incident surface through which the HTF is heated. Hence the primary objective of these receiver types is to better the heat transfer

to the HTF which is further hampered by the inherently poor thermophysical properties of gases in general. Pressure losses are a major degrading factor, however, as they increase the pumping power required on the one hand but are almost inevitable especially when attempting to enhance the heat transfer to the HTF. A careful optimisation must therefore be carried out when assessing the performance and in the design phase of pressurised gas receivers.

Tubular receivers, which are the most studied, demonstrated and understood type, are able to achieve high air outlet temperatures and are also able to be deployed in different configurations so as to make use of the cavity effect or other solar trapping arrangements and can hence achieve higher optical efficiencies [83]. While tubular receivers boast low pressure drops of below 2% of their inlet pressure, the thermal efficiency of such receivers does not exceed 80%.

Other proposed pressurised receivers have sought to improve on the performance of the conventional tubular receiver but inevitably face the same competing considerations of thermal efficiency maximisation and pressure drop minimisation. While some receivers, notably the flat panel, bladed and embedded receivers, are able to achieve high efficiencies, they do so at the cost of excessive pressure drops well above 10% of the inlet pressure. On the other hand, other receiver concepts, such as the RPC and impinging cavity receivers, have lower pressure drops below 1% of their inlet pressure levels. However, the corresponding thermal efficiencies attained by these receivers is also lower, often below 60%.

Further numerical analyses and experimental work needs to be carried out on microchannel receivers as well as the many innovative concepts within the subset of cavity receivers including impinging jets, embedded channels and RPC lined cavities. New concepts to better the heat transfer to the working fluid as well as reducing the pressure drop are also called for in the development of the next generation of pressurised gas receivers.

## 1.4. Performance indicators

The performance of a solar receiver may be evaluated by different performance indicators. These include, but are not limited to, exergy efficiency, thermal efficiency, optical efficiency and pressure drop [40]. Exergy and entropy analyses provide interesting tools in the performance assessment of receivers and may generate useful objective functions for optimisation. Such an objective function must simultaneously account for the useful fluid heat gain and the undesirable heat losses and pressure losses. In conventional heat exchanger theory, functions minimising the entropy rise are widely used [95],[96]. Entropy is generated in the fluid due to the heat gain and also the pressure drop. The general equation quantifying the entropy addition is given by equation (1):

$$\Delta S_{HTF} = \frac{\dot{q}_{conv,HTF}^2}{\pi\, k_{avg}\, T_{avg}^2\, Nu_{avg}} + \frac{32\, \dot{m}^3\, f_D}{\pi^2\, \rho_{avg}^2\, T_{avg}\, D_h^5}\ . \tag{1}$$

In equation (1), the first term on the right hand side is the contribution made by heat transfer, while the second term is the contribution due to fluid friction; $\dot{q}_{conv_{HTF}}$ is the convection heat transfer per unit length; $\dot{m}$ is the mass flow rate per channel, $f_D$ is the Darcy friction factor; $T_{avg}$ is the average fluid temperature; $\rho_{avg}$ is the average fluid density; $k_{avg}$ is the average fluid conductivity; $Nu_{avg}$ is the average Nusselt number; and $D_h$ is the hydraulic diameter. A drawback of using equation (1) in isolation is that it does not account for the solar energy supplied to the receiver but merely the entropy generated by the fluid. Alternatively, exergy gain in the fluid may also be used [97] with the expression for compressible fluids being equation (2)

$$\Delta Ex_{HTF} = \dot{m}\ \left[\Delta h\left(1 - \frac{T_{amb}}{T_{LMTD}}\right) + n\, R\, T_{amb} \ln\left(\frac{P_{out}}{P_{in}}\right)\right]\ , \tag{2}$$

where $T_{amb}$ is the ambient temperature; $T_{LMTD}$ is the log mean temperature difference between the outlet and inlet; $n$ is the number of moles; $R$ is the ideal gas constant; and $P$ is the average fluid pressure. Both equation (1) and (2) have the heat gain term on the left and the pressure drop/fluid friction term on the right. To factor in the receiver heat losses, the exergy associated to the incident solar radiation is calculated by the Parrot equation (3) [98]:

$$\Delta Ex_{solar} = \dot{Q}_{solar}\ \left[1 - \frac{4\, T_{amb}}{3\, T_{sun}}(1 - \cos\delta)^{1/4} + \frac{T_{amb}}{3\, T_{sun}}\right]\ , \tag{3}$$

where $\dot{Q}_{solar}$ is the total incident solar radiation on the receiver, also appearing in equation (3); $T_{sun}$ is the equivalent temperature of the sun as a blackbody (~5800 K); and δ is the half–angle of the cone subtended by the sun's disc (δ ~ 4.7 mrad, on a clear day). Combining equations (2) and (3), a parameter henceforth referred to as the exergy efficiency is obtained as expressed in equation (4);

$$\eta_{exergy} = \frac{\Delta Ex_{HTF}}{\Delta Ex_{solar}}\ . \tag{4}$$

The exergy efficiency, defined in equation (4), factors in all three effects pertinent to the performance of a solar receiver. It can hence act as an objective function to each receiver type, evaluating it for each permutation of the operating parameters, within their ranges, to determine which is the optimum set for each configuration and overall. As mentioned before, there are also other performance indicators that are evaluated and presented including energy efficiency [99], defined in equation (5), optical efficiency [87], defined in equation (6) and the widely used thermal efficiency given in equation (7).

$$\eta_{energy} = \frac{\dot{Q}_{HTF}}{\dot{Q}_{solar}} \,, \tag{5}$$

$$\eta_{opt} = \frac{\dot{Q}_{abs}}{\dot{Q}_{solar}} \,, \tag{6}$$

$$\eta_{thermal} = \frac{\dot{Q}_{conv,HTF}}{\dot{Q}_{abs}} \,, \tag{7}$$

where $\dot{Q}_{HTF}$ is the useful heat transferred to the HTF and $\dot{Q}_{abs}$ is the absorbed solar radiation.

## 1.5. Objectives and scope

The main focus of this thesis is the application of compact flow channels of various geometries to pressurised gas receivers to improve their performance. Utilising flow channel geometries and concepts that are well established in compact heat exchangers and applying them in solar receivers, it is endeavoured to achieve the performance improvements realised, due to increased compactness and novel geometries, in compact heat exchangers and replicate them in solar receivers using pressurised gases. The objective of this work is hence to develop high performance novel solar receivers using compact flow channel geometries.

The evaluation of the performance of these solar receivers with various compact flow channel geometries is conducted using numerical modelling and experimental analyses of selected receiver geometries. The numerical model is intended to be versatile and able to test the performance of receivers with several flow channel geometries and variations to each channel geometry type. Following this numerical analysis, a pressurised receiver testbed must be designed, installed and commissioned in order to perform the following step of the development process, i.e. experimental testing. Pressurised receivers must also be designed, employing the numerical model as required, and fabricated to this end.

The subsequent experimental campaign must be designed to physically demonstrate and experimentally validate the findings of the numerical modelling analysis. In this work, the scope is limited to the application of compact flow channels to solar receivers for central receiver solar towers but it should be noted that the concepts herein may well be applied to other concentrating solar thermal technologies and variants thereof.

In summary, the objectives of this thesis are:

1) Develop a simplified and versatile pressurised receiver numerical model capable of implementing multiple compact flow channel geometries and configurations
2) Apply the developed receiver model to a CSP system in order to identify the optimum compact flow channel geometrical configuration for the application
3) Design, install and commission a pressurised receiver testbed using the KIRAN 42 high flux solar simulator at IMDEA Energy
4) Design and fabricate pressurised receivers to be used for the experimental analysis
5) Prepare procedures for the operation of the testbed, experiment procedure and design of experiments
6) Perform experimental characterisation of receivers and analyse experiment results
7) Experimentally validate receiver numerical model by comparing its predictions with experiment results and findings
8) Perform a sensitivity analysis to evaluate and quantify the effects of different control parameters on the receiver performance

## 1.6. Structure of thesis

In chapter 1, an introduction to the different types of concentrated solar thermal technologies is provided with sections on the use of different heat transfer fluids, especially pressurised gases, and applications of concentrated solar technologies. An overview on compact heat exchanger technologies, with their subtypes and unique features, is presented with a focus on the suitability of their application to solar receivers. A state of the art review of indirectly irradiated pressurised gas solar receivers is then laid out as this is the category into which compact channel geometry receivers can most easily fit. Performance indicators that may be used in solar receiver analysis and optimisation studies are also briefly presented.

Chapter 2 is dedicated to the numerical modelling of pressurised gas receivers using compact flow channels. The numerical model is developed and explained in terms of its working principles and governing equations. As the objective of the model is to incorporate multiple flow channel geometries, each with its own peculiarities, the numerical model must be developed to allow for versatility in its use. The second part of the chapter is the application of the receiver model to a supercritical carbon dioxide Brayton cycle plant coupled to a central receiver solar tower system. Different flow channel geometries are introduced and applied to the receiver model with a parametric study optimising to find the best combination of geometric parameters for each flow channel geometry. The resulting optimum geometrical configurations for each flow channel type are then compared and discussed. A validation of the model is carried out by directly comparing it to a previous study as well as a more thorough validation by comparing the receiver model to a three dimensional computational fluid dynamics simulation that could validate some of the key simplifying assumptions made by the model. Finally the conclusions of the work and future work with the numerical model of the receiver are discussed.

Following the numerical analysis, Chapter 3 delves into the preparation, development and design of the experimental campaign. Beginning with the description of the KIRAN 42 high flux solar simulator and the capacities of its associated test facilities. The development of the experimental setup and calorimetric testbed for the planned experimental work is then detailed along with information about the particular instrumentation used and the related error analysis of the measurement equipment. The design of the receivers to be used in the experimental campaign is also explained subsequently. Preliminary test runs are conducted and the results and learnings of the same are presented as a means to eventually arrive at the experimental procedures to be followed, and modifications to the testbed to be undertaken, when performing the final experiments. Finally, the experiment design and overall experimental campaign is described.

Chapter 4 dives into the experiments with the receivers using the receiver testbed that was previously developed. Each of the receivers is first individually analysed with peculiarities related to their experimentation and their behaviour in general explained. A comparison is then made between the receivers tested to contrast their performances at different operating conditions. Errors, being an inescapable reality of experimental work, are evaluated for their effect on the performance of the receivers through a sensitivity analysis in which the operational parameters that are deemed to be most relevant to the receiver performance are analysed.

Finally, the conclusions to the thesis are presented and the work done is summarised. Future research outlooks and endeavours that naturally offshoot from this work are discussed as well as challenges that were faced in the development of this research, both numerical and experimental.

# Chapter 2. Numerical model of the pressurised receiver

## 2.1. Introduction

Multiple internal flow channel geometries, inspired by compact heat exchanger concepts, may be used in solar receivers to improve their performance [44]. In order to analyse and compare each of these solar receivers with various flow channel geometries, a thermo-fluidic numerical model has been developed. The conceptualisation and development of the mathematical receiver model, selection of different channel geometries based of compact heat exchanger designs and application of the model to a concentrated solar power plant in order to compare and contrast the various geometries and the influence of key common design parameters defining each one are all detailed in this chapter.

A guiding principle behind the development of the numerical model was to inculcate versatility and simplicity in order to easily adapt the model to different flow geometries, working fluids, incident radiation conditions, receiver solid material and operating conditions of the working fluid. Beyond facilitating the inclusion of multiple internal channel geometries for analysis, this intrinsic flexibility of the model also permits a wide range of parametric studies and application of the receiver model to several concentrated solar thermal plant concepts.

In this chapter, a comparative analysis of the performance of pressurised gas receivers with various internal flow channel geometries, laid out in section 2.2.2, is performed with each individual receiver subtype further analysed in a parametric study varying four parameters (section 2.4.2) common to all receiver geometry subtypes. A brief introduction to some thermo-mechanical aspects related to external receiver design is given in section 2.2.1.

The thermal model of the microchannel pressurised gas receiver, presented in section 2.3, is applied after setting a suitable operational framework and boundary conditions for the receiver. These operating conditions are reported in section 2.4, when describing the global Solar Thermal Power Plant (STPP) based on the microchannel pressurised gas receiver. After establishing these boundary conditions, the sizing and operating conditions of the receiver subsystem are set out in section 2.4.1. The geometrical characterisation of the different Plated Fin Heat Exchanger (PFHE) compact structures, as well as the scope of the parametric study, are presented in section 2.4.2. The numerical model used to analyse and compare the various CHE geometric structures is detailed in section 2.3.1.

Section 1.5 is devoted to the results including an analysis of the performance and behaviour of the different receiver types (section 2.5.1) and a comparative analysis (section 2.5.2). Exergy efficiency, defined in the previous chapter (section 1.4), is identified as a suitable figure of merit as it considers the exergy increase associated to the fluid heat gain, and the exergy decrease caused by the pressure drop and the heat loss. The results present the optimal geometric parameters for each compact structure and the comparison between optima.

A validation of the developed numerical model is carried out in section 2.6 by comparing it with previous studies (section 2.6.1) as well as by analysing the simulation results of a three-dimensional model performed on a commercial Computational Fluid Dynamics (CFD) software (section 2.6.2). At last, section 2.7 summarises the main conclusions, as well as future research lines. The appendix also provides the complementary information related to the heat transfer and pressure drop correlations used in the numerical model besides additional results.

## 2.2. Design of the solar receiver and flow channels

### 2.2.1. Thermo-mechanical considerations

Solar receivers must be designed to maximise the energy conversion from the incident solar radiation to the heat transfer fluid (HTF). This implies minimising the thermal resistance to this heat transfer process besides the heat losses to the ambient. These goals though are often inhibited by thermo-mechanical, engineering and, ultimately, economic constraints. Thermo-mechanical restrictions refer to those physical limits of the individual components, which together form the grander receiver system, themselves owing to their material properties and operating conditions. Engineering challenges broadly refer to those limitations of current engineering capacities which include, but are not limited to, manufacturing, assembly, monitoring and control capabilities. Ultimately, economic feasibility is the omnipresent and all-encompassing criterion limiting any design as, irrespective of whether a design may be technically conceivable, if it is not commercially viable to build, operate and maintain the system/component, it will not have any real world application which is the intended objective.

While the broad engineering and economic constraints are evident and will not be elaborated further, the thermo-mechanical considerations will be explained in more detail. For a pressurised solar receiver with a flat wall separating the incident radiation from the pressurised fluid, as in Figure 27, there are the following considerations:

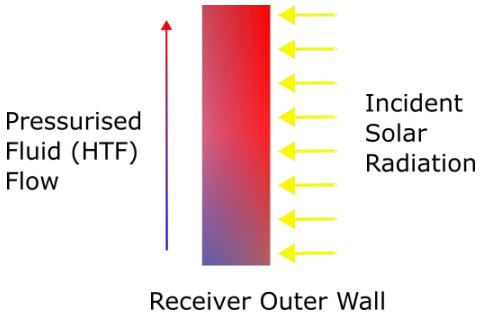


Figure 27. Simplified illustration of the physical phenomena occurring around the receiver outer wall that is exposed to solar radiation on one side and the HTF on the other. The thermal gradient is meant to depict the general trend across the wall's depth and along the HTF flow direction with blue to red indicating colder and hotter regions respectively.

There exists a natural temperature gradient from the external irradiated surface to the internal surface in contact with the HTF. This gradient depends on the thermal resistance of the receiver which in turn is a factor of the thermal conductivity of the solid material of the receiver, the convective heat transfer coefficient to the HTF, the thermal capacity of the HTF, etc. A high thermal gradient increases the thermal strain on the solid material and eventually causes thermal deformations, reducing the operational life of the receiver.

The reduction of this thermal gradient is hence vital and may be achieved by, among other things, reducing the thickness of the receiver wall. But there is a minimum wall thickness required as it must be sufficiently strong to withstand forces exerted by the pressurised HTF passing through the receiver. This is because the pressure inside the flow channel, pressing against the internal surface of the receiver wall in Figure 27, also exerts a force and induces stresses in the receiver wall. The receiver wall must be sufficiently thick as to withstand these stresses induced by internal pressure, further complicated by the fact that solid material strength worsens at the elevated temperatures typical of solar receivers.

Such thermo-mechanical considerations are vitally important to the operational longevity and safe operation of the receiver. They provide operational limits to the design and sizing of the receiver and its internal structures. Conventionally, the design by rule approach is used for the sizing of components with pertinent international and national standards such as [100]–[102] utilised as direct references and guides. More recently though another design approach has grown in popularity namely the design by analysis approach. As the name suggests, a design by analysis uses analytical tools, chiefly finite element analyses and simulations, to more precisely identify the stresses in the components as opposed to design by rule which, more simply, follows sets of equations which, after entering the required design parameters, provides the safe operating limits of the component.

The design by rule approach, following the ASME Section VIII Division I [102] has been utilised in this work in section 2.4.2 to determine the parameter limits when conducting a parametric study varying the geometry of the proposed receiver, as will be detailed in the subsequent sections.

### 2.2.2. Internal flow channel geometries

The selected Compact Heat Exchanger (CHE) channel geometries, for the internal flow paths of each absorber, analysed and compared in this work are the following [68]: Plain Rectangular Fin (PRF), Plain Triangular Fin (PTF), Wavy Fin (WF), Offset Strip Fin (OSF), Perforated Fin (PF) with rectangular cross-section, and triangular shaped Louvred Fin (LF). These geometries are presented in Figure 28.

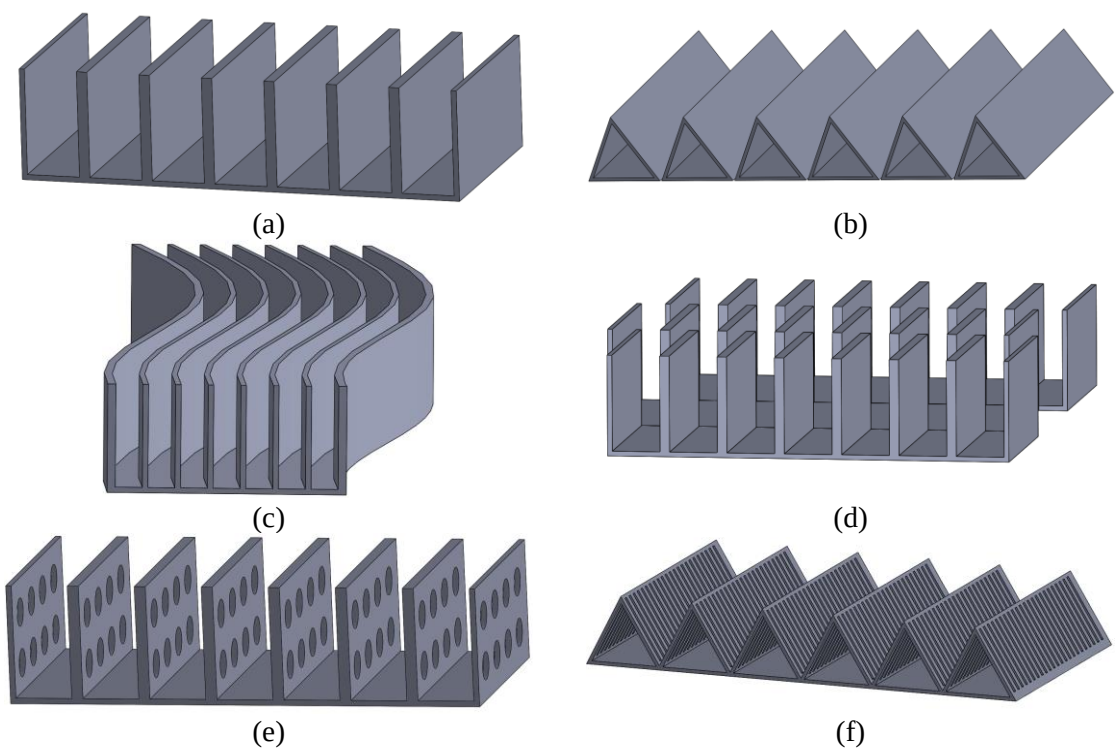


Figure 28. CHE channel geometries analysed in the pressurised air receiver model. (a) Plain Rectangular Fin (PRF); (b) Plain Triangular Fin (PTF); (c) Wavy Fin (WF); (d) Offset strip Fin (OSF); (e) Perforated (Rectangular) Fin (PF); and (f) Louvred (Triangular) Fin (LF).

It should be noted here that there are other potential flow channel geometries but these are the most commonplace geometries used in compact heat exchangers [68] and were hence selected for this study. The

channel geometries presented in Figure 28 can be characterised by common parameters. Identifying these parameters and studying the effects of their variations will allow for an optimisation analysis that reveals the best parameter set for each channel geometry type. Besides, the analysis also facilitates a comparison among the different receivers, each with different channel geometries. This will be discussed in more detail in the design of the parametric study in section 2.4.2.

## 2.3. Thermo-fluid dynamic model

In order to analyse the various proposed compact structures for the pressurised receiver, a bi-dimensional model has been developed, exploiting its implicit simplicity and versatility, permitting different geometries to be easily incorporated and evaluated. The overall structure of the receiver model is portrayed in Figure 29.

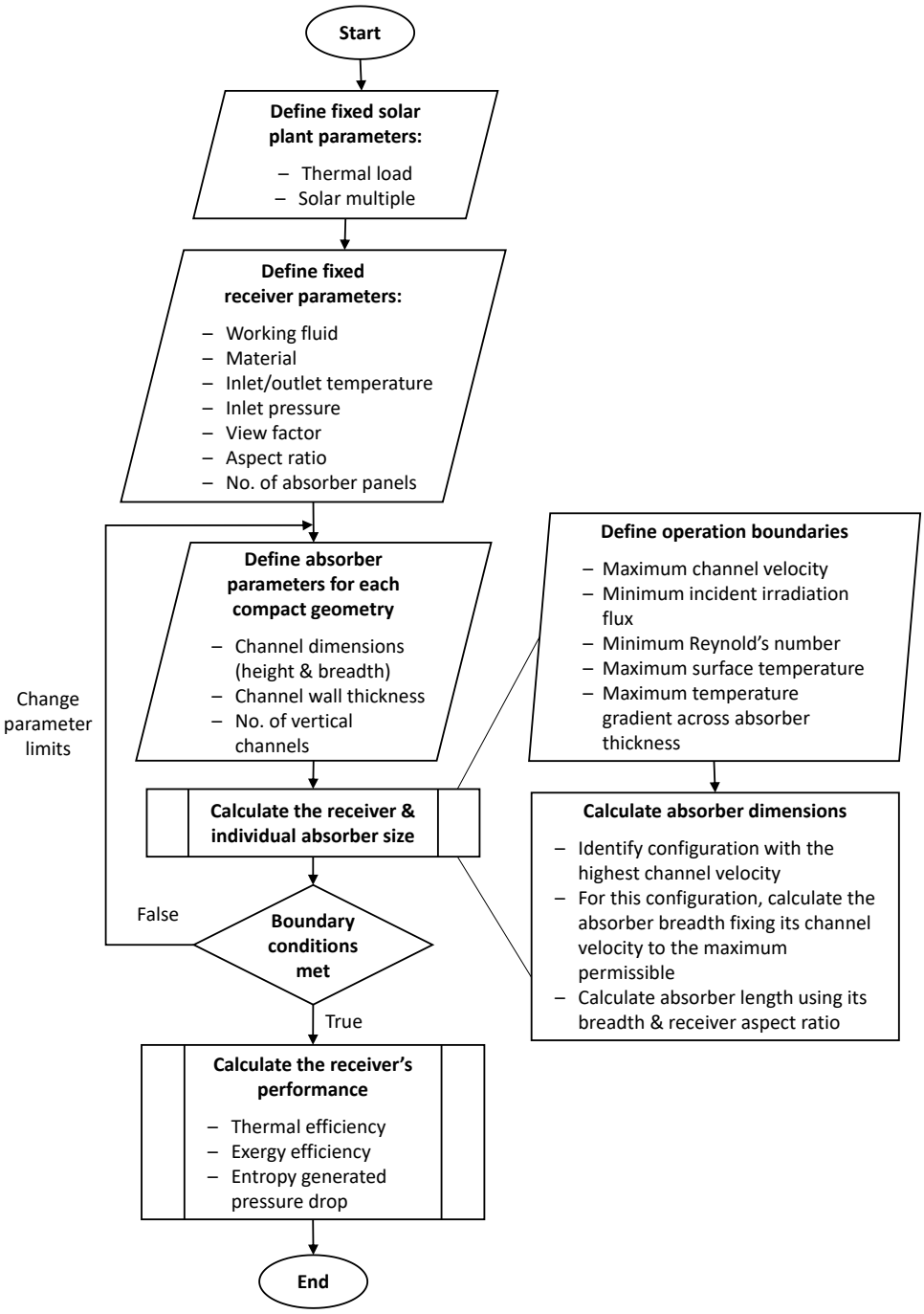


Figure 29. Overall process flow of the pressurised air receiver model.

After determining the global operating conditions of the receiver, the analysis of the individual absorber is performed. It is important to note that all absorbers of the receiver are considered to operate under the same conditions and hence only one absorber need be analysed to comprehend the performance of the overall receiver.

### 2.3.1. Heat transfer model

The model works by dividing the absorber into multiple elements along its length i.e. the flow direction, each referred to as a Heat Collector Element (HCE), and enforcing an energy balance on the individual elements along the flow direction. A thermal resistance model, discussed in more detail in the following section, is applied within each HCE to determine the thermal gradient along the absorber depth. The simultaneous use of the two heat transfer models, one along the flow direction and the other along the absorber depth, can be visualised in Figure 30.

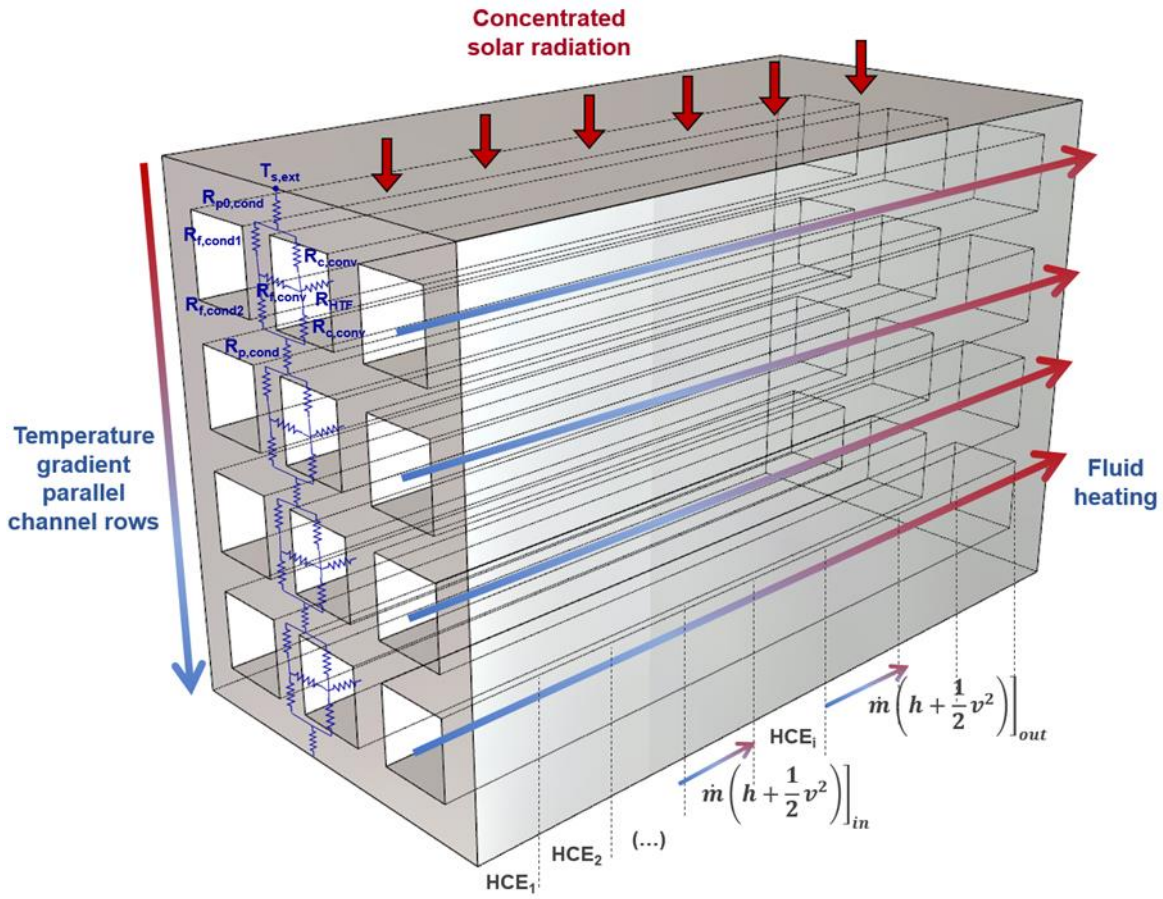


Figure 30. Bidimensional numerical model: diagrammatic representation of working principle [103].

For each HCE, the radial heat flux is initially assumed to be uniform and normal to the incident plane surface, and it is evaluated at the average temperature between the inlet and outlet of the HCE. It is assumed that there is no heat transfer across the breadth of the receiver i.e. the temperature across the receiver breadth is uniform. These are conventional assumptions for bi-dimensional solar receiver models [104],[105].

For each HCE, the incident concentrated solar radiation ($\dot{Q}_{solar}$) impinges and is absorbed by the absorber panel ($\dot{Q}_{abs}$). Most of this absorbed radiation is transmitted by conduction through the panel walls and the compact structure ($\dot{Q}_{cond,wall}$) to be finally transmitted by convection to the working fluid ($\dot{Q}_{conv,HTF}$). Since the outer wall of the panel is usually at a higher temperature than the ambient, there is a convection and radiation heat loss ($\dot{Q}_{loss,conv}$ and $\dot{Q}_{loss,rad}$, respectively). The total heat loss also includes the contribution due to reflected radiation ($\dot{Q}_{loss,ref}$), which is not absorbed by the panel. These heat transfer phenomena are summarised in equations (8)-(11):

$$\dot{Q}_{solar} = \dot{Q}_{abs} + \dot{Q}_{loss,ref} \ , \tag{8}$$

$$\dot{Q}_{abs} = \dot{Q}_{cond,wall} + \dot{Q}_{loss,conv} + \dot{Q}_{loss,rad} \ , \tag{9}$$

$$\dot{Q}_{cond,wall} = \dot{Q}_{conv,HTF} \ , \tag{10}$$

$$\dot{Q}_{loss} = \dot{Q}_{loss,conv} + \dot{Q}_{loss,rad} + \dot{Q}_{loss,ref} \ . \tag{11}$$

This system of four equations is completed by a first law energy balance applied to the working fluid, as it passes through each HCE as expressed in equation (12);

$$\dot{Q}_{conv,HTF} = \dot{m} \left[ (h_{out} - h_{in}) + \frac{1}{2} \left( v_{out}^2 - v_{in}^2 \right) \right] , \tag{12}$$

where $\dot{m}$ is the mass flow rate, $h$ is the enthalpy and $v$ is the fluid velocity. In this equation, potential energy is neglected. The required HTF thermal properties at the HCE outlet are calculated once the HCE inlet thermal properties and the boundary conditions are known. Of course, the inlet conditions of an element are simply the outlet conditions of the preceding element with the exception of the very first element whose inlet conditions are predefined.

The outlet pressure is determined by calculating the pressure drop across the element and subtracting that from the inlet pressure. With these two properties known, the remaining required fluid properties can be determined. This process is sequentially implemented from the first HCE (at the absorber inlet) to the final HCE (at the absorber outlet). The conduction heat transfer between adjoining HCEs is not considered and there are no heat transfer boundary conditions imposed at the inlet and outlet nor at the back surface of the receiver.

If the HTF outlet temperature is within the tolerance range of the setpoint, the performance indicators of the absorber (thermal and exergy efficiency, pressure drop, etc.) are evaluated before proceeding to the next absorber configuration. These process steps are schematically outlined in Figure 31. Determination of the heat transfer coefficient and friction factor is required in each HCE and is done by implementing empirical and semi-empirical correlations. These correlations are unique to each CHE geometry and are tabulated in the annexes A.2 and A.3.

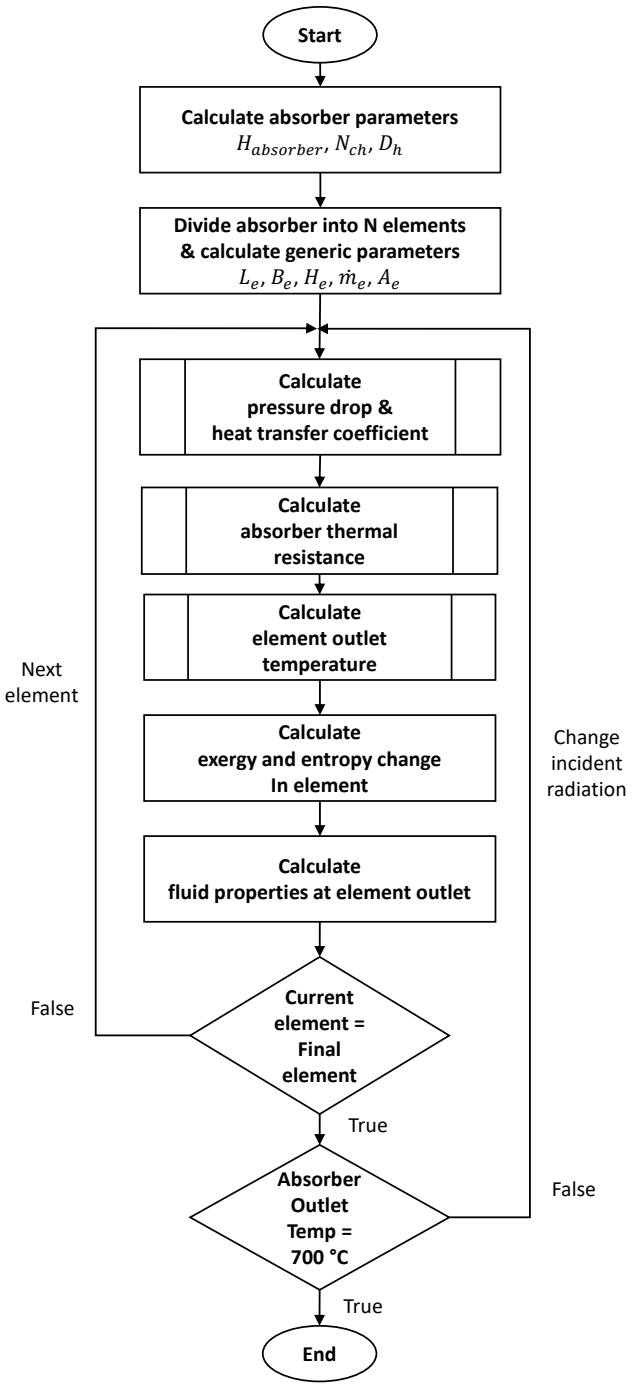


Figure 31. Absorber evaluation subprocess.

### 2.3.2. Thermal resistance model

As indicated previously, to quantify the external surface heat losses it is first required to determine the absorber's surface temperature. This temperature distribution through the absorber depth (from the irradiated front surface to the back of the absorber) is determined using a Thermal Resistance Model (TRM) accounting for the fluid flow characteristics and the thermal properties of the receiver material [106],[107],[108]. Figure 32 depicts the thermal model for the simplest geometry, plain rectangular fin, but is also indicative of the other geometries.

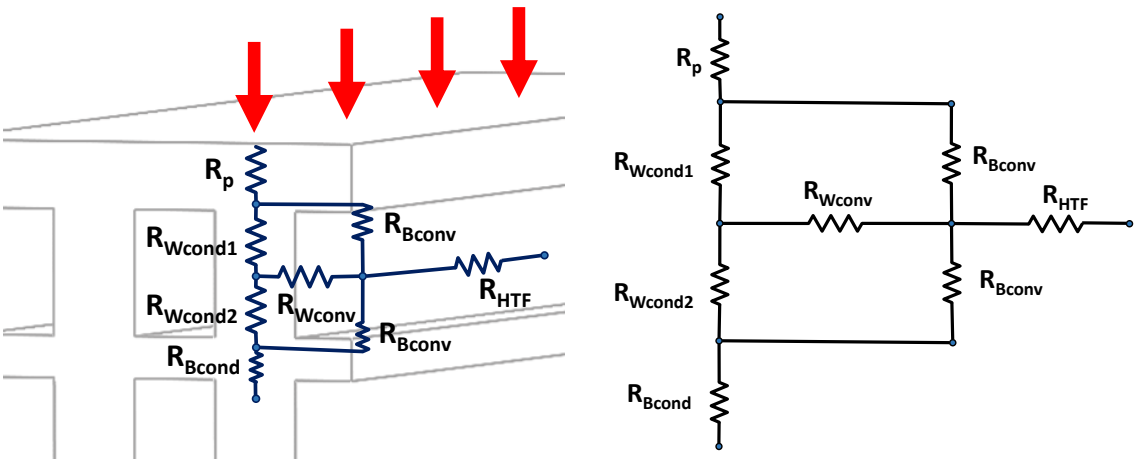


Figure 32. Thermal resistance model in HCE of absorber with plain rectangular fin geometry. Red arrows indicate the irradiated plane and direction of heat transfer.

Referring to Figure 32, the thermal resistances from the irradiated surface to the end of the first flow channel row (and the beginning of the second) are the conductive plate resistance ($R_p$), convective channel wall resistance ($R_{w,conv}$), conductive resistance of the base wall ($R_{b,cond}$), convective resistance of the base wall ($R_{b,conv}$), conductive resistance of the channel wall which is divided into two halves ($R_{w,cond}$) and finally the thermal resistance due to the HTF heat gain ($R_{HTF}$). The pattern is repeated from one channel row to the next and hence the TRM may be built factoring in the number of vertical channels/rows ($N_{cv}$).

The equation set to determine the thermal resistance for each HCE through a flow channel is further detailed in equations (13-19). The influence of the main geometrical parameters that define the absorber, presented in Figure 35, on the thermal resistance is evident with their prominence in the following set of equations. The conductive thermal resistance of the top plate wall ($R_p$) is defined in equation (13);

$$R_p = \frac{t_p}{k_{absorber}\left(\frac{B_c}{2}\right) L_e}\ , \tag{13}$$

where $t_p$ is the top plate thickness, $k_{absorber}$ is the thermal conductivity of the absorber and $L_e$ is the length of the HCE. The convective thermal resistance of the channel walls ($R_{w,conv}$) is given in equation (14),

$$R_{w,conv} = \frac{1}{h_{conv}\, H_c\, L_e}\ , \tag{14}$$

where $h_{conv}$ is the heat transfer coefficient. The convective and conductive thermal resistance of the base wall ($R_{b,conv}$ and $R_{b,cond}$) are respectively calculated by equations (15) and (16),

$$R_{b,conv} = \frac{1}{h_{conv}\left(\frac{B_c}{2}\right)L_e}\ , \tag{15}$$

$$R_{b,cond} = \frac{t}{k_{absorber}\left(\frac{B_c + t}{2}\right)L_e}\ . \tag{16}$$

Equation (17) computes the conductive thermal resistance of the channel half wall ($R_{w,cond}$),

$$R_{w,cond} = \frac{H_c}{2\,k_{absorber}\left(\frac{t}{2}\right)L_e}\ . \tag{17}$$

The thermal resistance due to the fluid heat gain ($R_{HTF}$) is defined in equation (18),

$$R_{HTF} = \frac{1}{\rho\, c_p\, v\, A_c}\ , \tag{18}$$

where $\rho$ is the density, $c_p$ is the specific heat and $v$ is the fluid velocity. Referring to Figure 32, the total thermal resistance of vertically aligned half-channels in a HCE (which can seamlessly extend to describe the thermal resistance of the whole HCE) is expressed in equation (19):

$$\begin{aligned} R_{absorber} = R_p + N_{cv}\ \Big[ & R_{b,cond} \\ & + \Big\{ R_{b,conv} \\ & \parallel \Big( R_{w,cond} + \Big( \big( R_{w,cond} + R_{b,conv} \big) \parallel R_{w,conv} \Big) \Big) + R_{HTF} \Big\} \Big]\ . \end{aligned} \tag{19}$$

where the parallel symbol (‖) between two terms $x$ and $y$ ($x \parallel y$) notates one-half of the harmonic mean of $x$ and $y$. As mentioned previously, this thermal resistance model has been developed specifically for the plain rectangular fin geometry, but it is indicative of all the compact structures analysed, if the correlations for convection heat transfer coefficient and friction factor are specified for each of them. These correlations are summarised in the appendix in Table 32 and Table 33 respectively.

## 2.4. Application of the model to a central solar receiver plant

The performance analysis of a solar receiver primarily requires an adequate framework, which is fixed by the overall STPP performance at design point. The operating conditions of the receiver are firstly imposed by the useful thermal power required by the thermal cycle. Although this pressurised receiver can be coupled to several power cycles, a supercritical carbon dioxide ($sCO_2$) power cycle has been considered following a layout similar to that depicted in Figure 33.

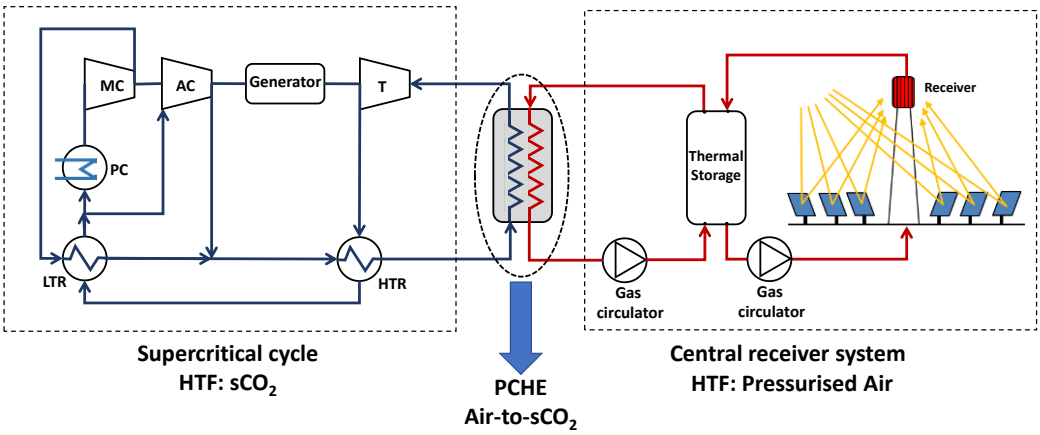


Figure 33. Scheme of a STPP based on a pressurised air central receiver coupled to a supercritical $CO_2$ power cycle.

As shown in Figure 33, the supercritical layout selected is the conventional recompression thermodynamic cycle though it should be noted that the cycle chosen serves only as a framework to set the boundary steady state operating conditions of the receiver. The cycle power output has been set at 10 $MW_e$ with a solar multiple of 1.5. An electrical power of 10 $MW_e$ is considered representative for an initial prototype that will later be scaled to a commercial level. The isentropic efficiencies of both the turbine and the compressors have been set at 92% and 88%, respectively; a dry cooling by means of a precooler is assumed; and the $sCO_2$ pressure and temperature at the turbine inlet are 200 bar and 688 ºC, respectively. At these conditions, the nominal thermal efficiency is 49.57%, thus the thermal power required in the primary heat exchanger is 20.17 $MW_{th}$ [67]. Assuming a thermal efficiency in the source heat exchanger equal to 98%, and considering the solar multiple previously mentioned, the total thermal power in the central solar receiver is 30.26 $MW_{th}$. The heat transfer fluid in the proposed receiver is pressurised air. The air temperatures at the inlet and outlet of the solar receiver are also determined by the power cycle conditions. Specifically, if the source heat exchanger is assumed to be balanced and the temperature difference between the two fluid streams is constant and fixed at 12 ºC, then the inlet and outlet air temperatures are 557.6 ºC and 700 ºC, respectively. The air pressure at the receiver inlet is taken as 25 bar. Since the pressure difference between $sCO_2$ and pressurised air streams is high, a Printed Circuit Heat Exchanger (PCHE), which is capable of operating under such conditions, is recommended for use as the Heat Exchanger (HE), coupling the solar field to the power cycle with previous studies having undertaken such design studies [67].

For the receiver simulation model, the thermodynamic properties of the pressurised air have been sourced from the NIST database [109], for temperature steps below 1.5 ºC and pressure steps of roughly 1 mbar.

Furthermore, assumed environmental conditions are the ambient temperature at 25 ºC, the sky temperature at 15 ºC and the wind speed equal to 1 m $s^{-1}$.

### 2.4.1. Overall receiver and plant system

Before making a performance analysis of the various compact structures, it is first necessary to define an overall receiver structure. As shown in Figure 34, an external cylindrical receiver configuration has been defined having 20 rectangular panels in a parallel configuration, uniformly irradiated, through which pressurised air flows in a single pass. These absorber panels (henceforth referred to as absorbers) are assembled so as to form 2 vertical rows of 10 cylindrically arranged absorbers. CHE structures are implemented in each absorber. Cold air enters from a common inlet manifold, located between the two rows, before splitting into the individual absorbers. This configuration is similar to the one adopted for the $sCO_2$ receiver proposed by NREL [110].

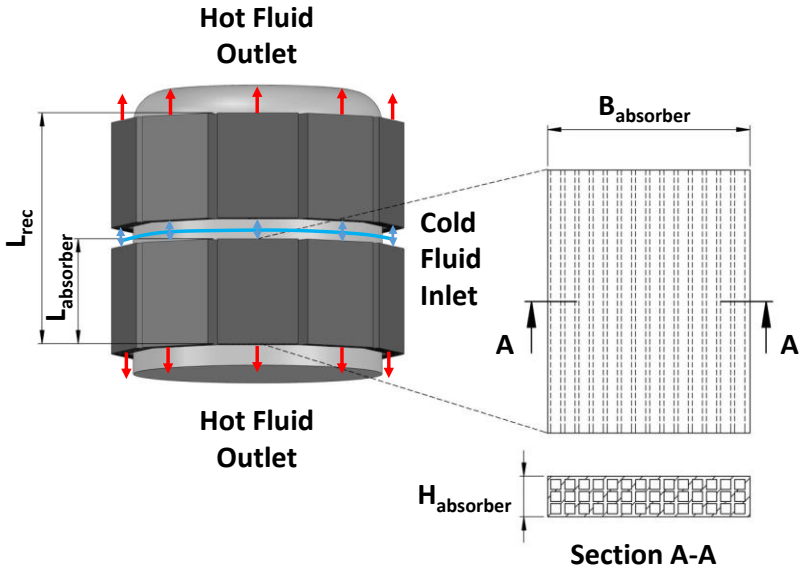


Figure 34. Receiver configuration, i.e. external cylindrical like receiver comprised of 20 parallel rectangular absorber panels arranged cylindrically in 2 vertical rows.

Inconel 617 has been selected as the receiver material because of its machinability and high temperature corrosion resistance [111],[112]. Deferring to the state of the art [12],[33], the receiver aspect ratio (receiver length to diameter ratio) is fixed at 0.7 with the maximum and minimum mean incident fluxes set at 800 kW $m^{-2}$ and 400 kW $m^{-2}$. These along with additional operation boundary conditions, summarised in Table 2, are used to size the absorbers and, in turn, the overall receiver in an iterative process which is detailed in Section 2.4.

Table 2. Operational boundaries conditions of pressurised air receiver.

| Parameter | Unit | Operating Limits | |
|---|---|---|---|
| | | Minimum | Maximum |
| Mean incident flux | kW $m^{-2}$ | 400 | 800 |
| Channel velocity | m $s^{-1}$ | - | 50 |
| Outer surface temperature | ºC | - | 800 |
| Absorber temperature gradient (outer to back surfaces) | ºC | - | 200 |
| Reynolds number | - | $10^4$ | - |

The temperature gradient from the absorber's external irradiated surface to the back is expected to be high given the low thermal conductivity of Inconel 617 [111] and the generally poor heat transfer characteristics of air; hence the addition of an upper limit to this temperature gradient as well as mean incident flux which are both presented in Table 1. As a consequence of air's low density, the absorber cross section area, directly related to the absorber breadth and hence receiver diameter, required for a given absorber mass flow rate and channel velocity is relatively high. Keeping this in mind, the number of absorbers in parallel (which determines the mass flow rate in each absorber) and the bounds of mean incident flux have been set to maintain a reasonable receiver aspect ratio. Given that the absorbers tend to broader and shorter dimensions, stacking the absorbers one above the other mitigates, to an extent, the low receiver aspect ratio issue by effectively doubling the receiver length. These considerations ultimately give shape to the conceived receiver configuration shown in Figure 34

For the working temperatures considered in this study (above 700 ºC), a cavity type receiver is most recommended to reduce radiation heat losses [12]. Nevertheless, there is a recent research line that seeks to decrease the radiation losses by the reduction of the view factors, using microscopic or macroscopic geometries that would act as solar traps [39],[113]. At the microscopic scale, the external receiver proposed has adopted the configuration developed by NREL for their pressurised microchannel receiver [110], as mentioned in the state of the art review. This design employs cylindrical quartz tubes attached perpendicularly to its external surface, in such a way as to reduce the view factor and the convective losses.

For the external receiver proposed in this work, cylindrical quartz tubes with an aspect ratio (height-to-diameter ratio) of 0.5 are considered. The view factor of this cavity is calculated using a conventional formula for parallel circular disks with centres along the same normal [114],

$$F_{rec-ap} = \frac{1}{2}\left[X - \sqrt{X^2 - 4\left(\frac{R_2}{R_1}\right)^2}\right], \tag{20}$$

where $X = 1 + \frac{1+{R_2}^2}{{R_1}^2}$, $R_1 = \frac{r_1}{L}$, $R_2 = \frac{r_2}{L}$; $r_1$/$r_2$ and L are the quartz cylinder radius and length, respectively. Assuming $R_1 = R_2 = 1$, $X = 3$ and the view factor is $F_{rec-ap} = 0.382$, which is the value introduced in the program. It is important to point out that this estimation of the view factor can be varied if different configurations are adopted as solar traps, the emissivity value may also be changed if different materials are considered. One of the advantages of the simulation model developed is its versatility to adapt to many designs. A summary of the proposed receiver model and its working conditions are presented in Table 3.

Table 3. Summary of the main thermal and geometric parameters of the pressurised air receiver.

| **Parameter** | **Unit** | **Value** |
|---|---|---|
| Material | - | Inconel 617 |
| Inlet temperature | °C | 557.6 |
| Outlet temperature | °C | 700.0 |
| Inlet pressure | bar | 25 |
| Mass flow rate | kg $s^{-1}$ | 191.49 |
| Receiver area | $m^2$ | 63.44 |
| Receiver length | m | 3.79 |
| Receiver diameter | m | 5.41 |

## 2.4.2. Parameters related to channel geometries

Four parameters, common to all channel geometries, have been identified as the most crucial and these are the channel height ($H_c$), channel breadth ($B_c$), channel wall thickness ($t$) and the number of vertical channels or rows ($N_{cv}$). Note that the thicknesses of the walls separating horizontally and vertically adjacent channels are taken as identical ($t$).

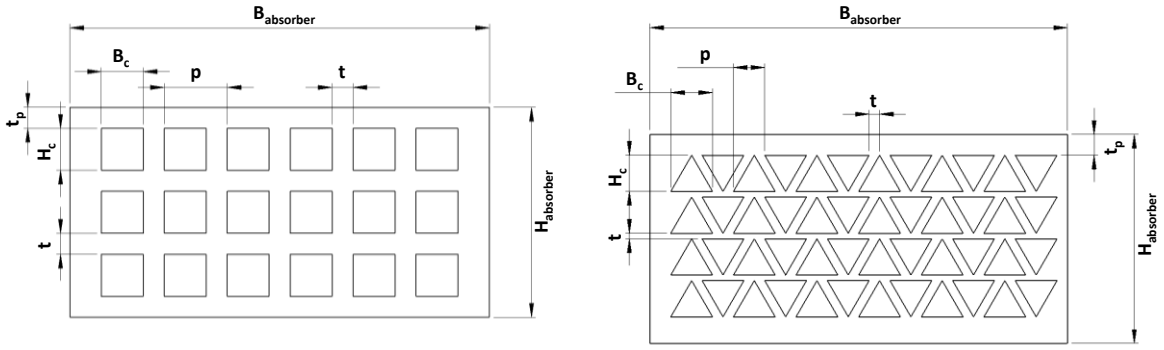


Figure 35. Channel geometrical parameters for rectangular fin (left) and triangular fin (right) receivers.

All the channel geometries are either rectangular or triangular shaped channels when viewed from the flow inlet/outlet. Figure 35 depicts the geometric parameters defining these structures including the previously defined constant absorber breadth ($B_{absorber}$) besides derived parameters such as the channel pitch ($p$) and absorber height ($H_{absorber}$), both of which are calculated after defining the four variable parameters.

The parametric study varying the four parameters uses the datapoints presented in Table 4 and all combinations of the variables are fed into the simulation model. It should be noted that for the LF geometry, $H_c$ and $B_c$ were initiated at 7 mm as excessive pressure drops were observed at lower values.

Table 4. Parametric study performed for optimisation analysis.

| **Parameter** | **Unit** | **Studied Parameter Values** | | | | |
|---|---|---|---|---|---|---|
| $H_c$ | mm | 6.00[&] | 8.25 | 10.50 | 12.75 | 15.00 |
| $N_{cv}$ | - | 3 | 5 | 7 | 8 | 10 |
| $B_c$ | mm | 6.00[&] | 8.25 | 10.50 | 12.75 | 15.00 |
| $t$ | mm | 1.00 | 1.50 | 2.00 | 2.50 | 3.00 |

[&]For the LF geometry, $H_c$ and $B_c$ are initiated at 7 mm to avoid excessive pressure drop.

## 2.5. Results and Discussion

### 2.5.1. Parametric study

This section presents the results of the parametric study over the range of the four parameters shown in Table 4. channel height ($H_c$), channel breadth ($B_c$), number of vertical channels ($N_{cv}$), and channel thickness ($t$). It is important to note that only the most relevant and representative figures are selected, given the large scope and quantum of graphical information.

The general expected behaviour and performance of the receiver is first elaborated. Increasing the hydraulic diameter, by increasing the channel height and/or the channel breadth, will reduce the fluid flow velocity in the channels. This will adversely affect the convection coefficient and worsen the heat transfer to the fluid. Consequently, more input heat will be required to achieve the same outlet temperature. The thermal resistance of the absorber will also rise causing higher absorber outer surface temperatures and hence increased thermal losses. On the other hand, the decreased fluid velocity reduces the overall pressure drop in the receiver.

Besides changes to the hydraulic diameter, the fluid velocity is also affected by the number of channels. For a fixed mass flow rate in the receiver, the increase in the number of channels results in decreasing velocity, as the same flow is divided into more channels. The number of horizontal channels is calculated accounting for the fixed absorber breadth and the variable channel breadth and channel wall thickness. An increase in the number of vertical channels hence causes the increase in the thermal resistance by reducing the convective heat transfer coefficient besides by increasing the number of thermal resistances in series in the absorber network. The pressure drop is also expected to decrease with greater channels as it is indirectly related to channel velocity.

Regarding the absorber's equivalent thermal resistance, the channel wall thickness is an important parameter in determining the conductive thermal resistance with thicker walls reducing this resistance and hence allowing for better heat transfer through the solid volume. Thicker walls also reduce the number of horizontal channels and hence, as explained previously, the increase in fluid velocity associated with fewer channels results in higher convection coefficient and lower convective thermal resistance. However, a negative consequence of this effect is that the resulting pressure drop is larger owing to the higher velocities.

As observed in Figure 36, the highest exergy efficiency (58.80%) occurs at the largest channel thickness ($t$ = 3 mm) and smallest number of vertical channels ($N_{cv}$ = 3) within the analysed range. The bettering of the heat transfer, with increased channel thickness and reduced vertical channels, clearly outweighs the increased pressure drop, as marked by the rising exergy efficiency. As it will be seen in Figure 10, the rising channel thickness also favoured the energy efficiency.

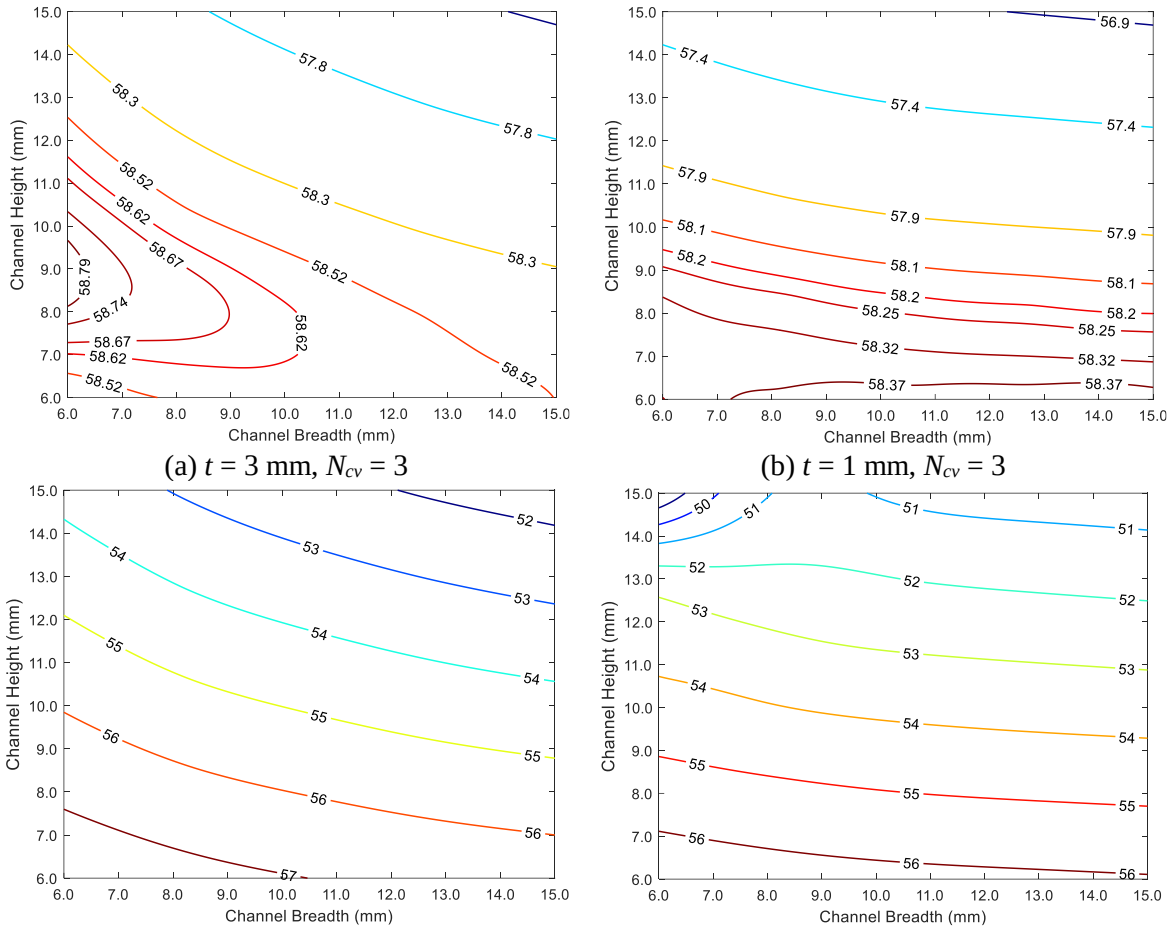


Figure 36. Exergy efficiency (in %) as function of the channel breadth and height for different channel thickness and number of vertical channels for the plain rectangular fin geometry. (a) $t$ = 3 mm, $N_{cv}$ = 3; (b) $t$ = 1 mm, $N_{cv}$ = 3; (c) $t$ = 3 mm, $N_{cv}$ = 10; and (d) $t$ = 1 mm, $N_{cv}$ = 10.

In both Figure 36(a) and Figure 36(b), it is observed that rectangular channels are optimal though with different aspect ratios in each case. This difference in aspect ratios can be attributed to the competing effects of conduction through the solid channel wall and convection to be the preferred mode of heat transfer offering the least thermal resistance. Conduction is favourable when the channel walls are thicker, which leads to the preference for channels with a lower breadth and hence more horizontal channels and channel walls as seen in Figure 36(a). To keep the pressure drop in check, the hydraulic diameter must be sufficiently large which entails a larger channel height to compensate for the optimal channel breadth being at its minimum.

The inverse of this phenomenon is seen in Figure 36(b) when the channel thickness is low and convection offers the less thermally resistive path compared to conduction. Wider channels reduce the number of horizontal channels and channel walls; shorter channels further reduce the solid volume and the related conductive thermal resistance.

When the number of vertical channels is high, as is the case in Figure 36(c) and Figure 36(d), the channel velocities are so low that the pressure drop factor in the efficiency is inconsequential. This is further evidenced by the fact that the corresponding energy efficiency contours i.e. Figure 37(c) and Figure 37(d), are identical in trend. The maximum exergy efficiency hence occurs at the smallest channel sizes with the largest channel thickness which together provide the least thermal resistance and best heat transfer to the fluid.

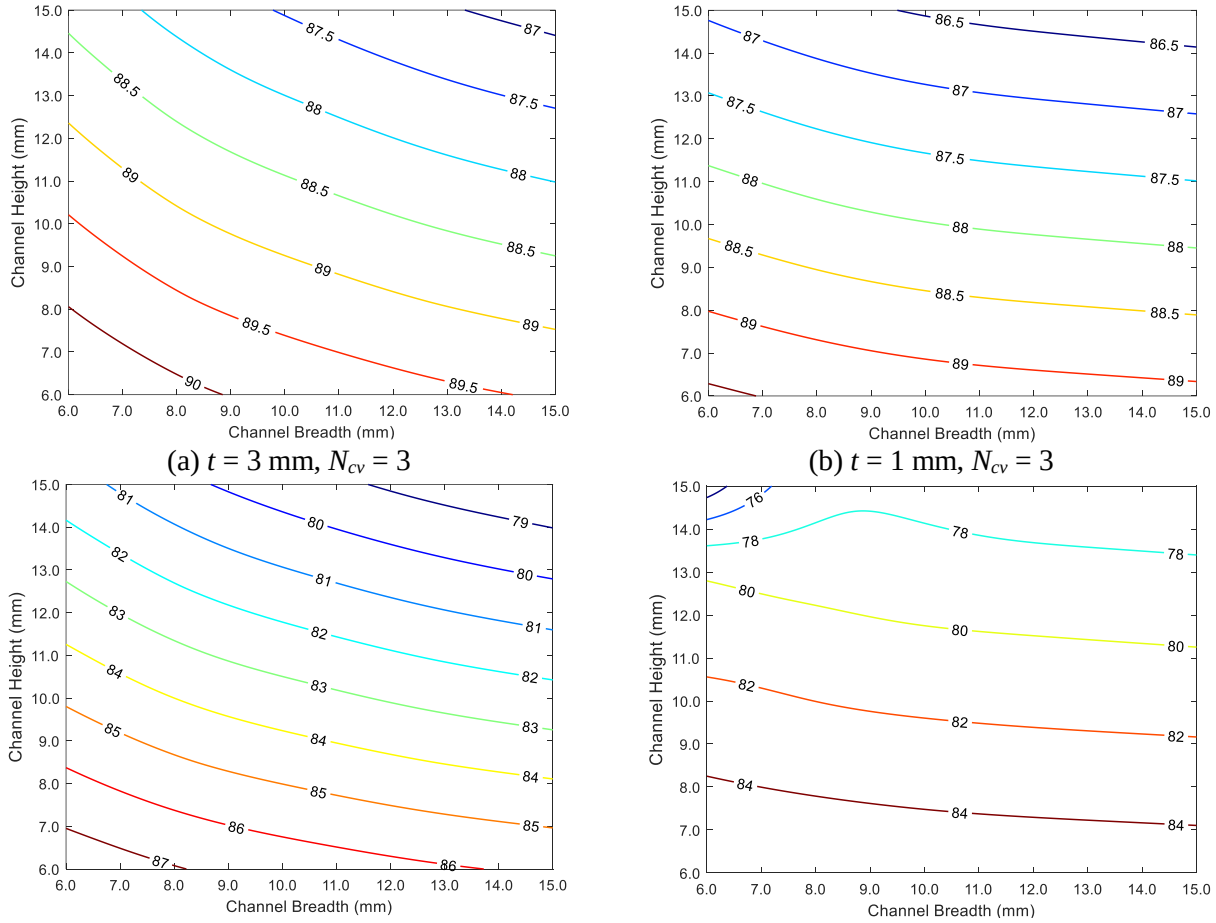


Figure 37. Energy efficiency (in %) as function of the channel breadth and height for different channel thickness and number of vertical channels in the plain rectangular fin geometry. (a) $t$ = 3 mm, $N_{cv}$ = 3; (b) $t$ = 1 mm, $N_{cv}$ = 3; (c) $t$ = 3 mm, $N_{cv}$ = 10; and (d) $t$ = 1 mm, $N_{cv}$ = 10.

In parallel, Figure 37 shows the energy efficiency variation for the same parametric study applied to the plain rectangular fin geometry. From this, it is evident that the behaviour of the energy efficiency is relatively simple as it only considers the heat transfer phenomena and not the related pressure drop. Smaller and fewer channels with thicker walls all work to increase the energy efficiency. These trends hold true for all receiver configurations. On the other hand, the exergy efficiency behaviour in other receiver configurations is more complex as the HTF flow characteristics are significantly different. The exergy and energy efficiency contour plots for the other geometries are presented in the appendix.

Sankey and Grassmann diagrams, shown in Figure 11, help visualise the energetic and exergetic phenomena occurring in the receiver respectively. These diagrams have been generated for the optimum geometrical configuration of the plain rectangular fin receiver, i.e. the parameter set resulting in the maximum exergy efficiency.

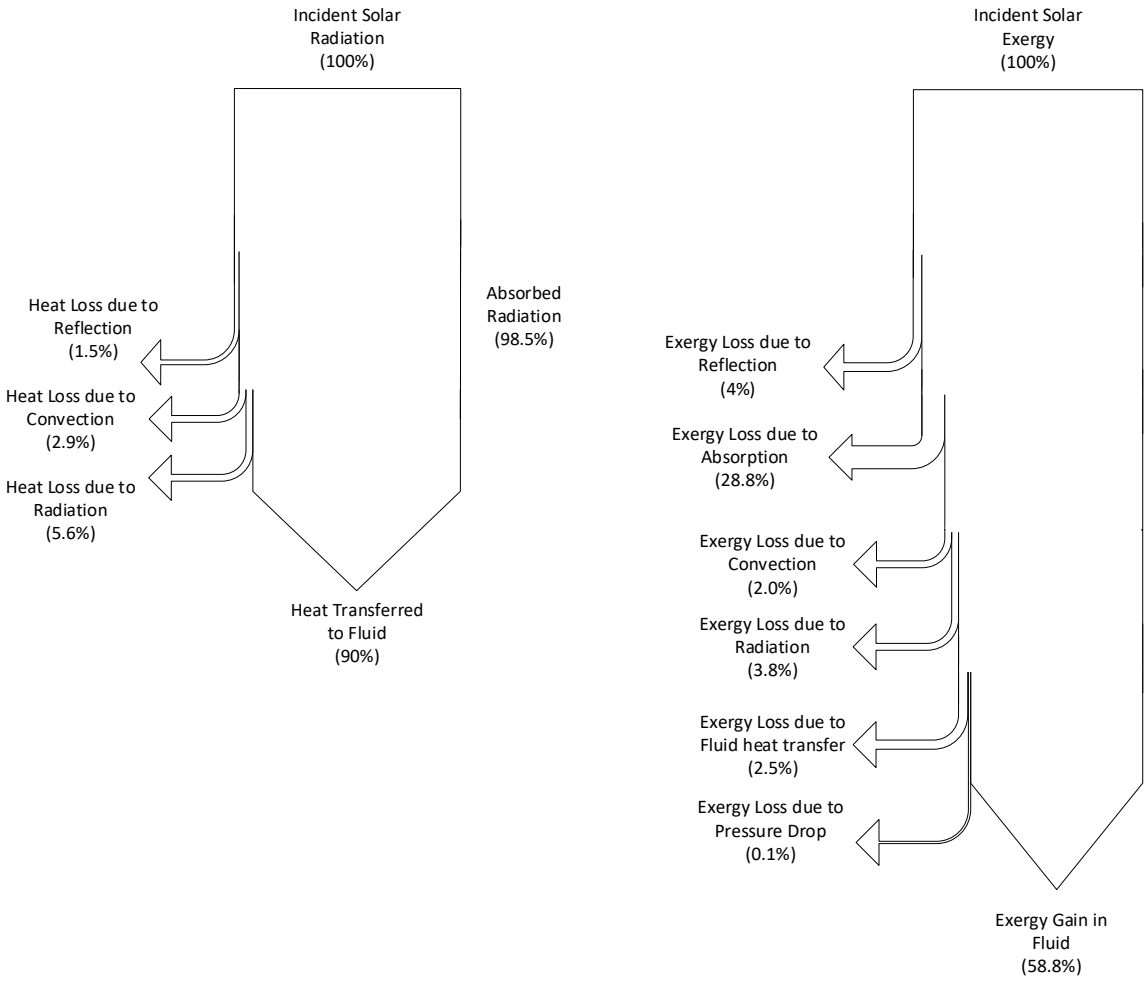


(a) Sankey (energy flow) diagram (b) Grassmann (exergy flow) diagram

Figure 38. Sankey and Grassmann diagram depicting the energy and exergy flow in the plain rectangular fin geometry receiver with the optimum (maximum exergy efficiency) configuration set: $H_c$ = 8.25 mm, $t$ = 3 mm, $N_{cv}$ = 3, $B_c$ = 6 mm.

Referring to Figure 11(a), the three energy loss mechanisms, namely reflection, convection and radiation, subtract from incident solar radiation on the receiver as has been described in section 2.4. The final heat transferred to the fluid, after deducting the energy losses, represents the same energy efficiency as described by equation (18). There are more physical phenomena that cause exergy loss in the system, quantified as per standard exergy analyses [115],[116], as can be seen in Figure 11(b). It is observed that the highest exergy loss is associated with the absorption of the incident solar exergy by the receiver. While the exergy loss related to pressure drop, as a fraction of the solar exergy, is negligible it is nonetheless critical to the performance of the receiver as is clear from Figure 9 and the ensuing discussion. The net exergy gain in the fluid corresponds to the exergy efficiency as defined in equation (17).

## 2.5.2. Comparative and optimisation analysis

Using the exergy efficiency as the objective function to be maximised, the different receiver geometries have been optimised (within the operating range of the four varied parameters) for the configuration yielding the highest exergy efficiency. The energy efficiency and the pressure drop corresponding to these configurations have also been tabulated and it can be found in Table 4.

Table 5**.** Receiver configurations yielding maximum exergy efficiency.

| **Receiver compact geometry** | **(Maximum) exergy efficiency (%)** | **Energy efficiency (%)** | **Pressure drop (bar)** | **Absorber panel dimensions** | | | |
|---|---|---|---|---|---|---|---|
| | | | | $H_c$ (mm) | $N_{cv}$ (-) | $B_c$ (mm) | $t$ (mm) |
| PRF | 58.80 | 89.96 | 0.35 | 8.25 | 3 | 6.00 | 3.00 |
| PTF | 55.33 | 85.43 | 0.55 | 6.00 | 5 | 6.00 | 3.00 |
| WF | 58.37 | 89.01 | 0.24 | 6.00 | 5 | 6.00 | 3.00 |
| OSF | 56.09 | 86.62 | 0.57 | 12.75 | 3 | 6.00 | 3.00 |
| PF | 59.21 | 90.14 | 0.19 | 6.00 | 3 | 6.00 | 3.00 |
| LF | 53.03 | 81.82 | 0.53 | 7.00 | 3 | 7.00 | 1.00 |

As it can be observed from Table 5, the perforated rectangular fin has the highest exergy efficiency (59.21%), followed by the plain rectangular fin (58.8%) and the wavy fin (58.37%). The corresponding energy efficiency also follows a similar trend (90.14%, 89.96% and 89.01% respectively). Owing to the inherent differences in each geometry's heat transfer and pressure drop characteristics, the resulting optimal configuration for each geometry is different. Simply put, the exergy efficiency is highest when the heat transfer to the fluid is maximal i.e. the heat losses are minimal and the pressure drop over the flow length is minimal. These two factors run opposed to one another i.e. better fluid heat transfer necessitates greater pressure drop.

In this regard there are interesting trade-offs seen between the number of vertical channels and the channel dimensions, especially its height. This can be clearly visualised in the contour plots of the different geometries at their optimal configurations in Figure 39 which excludes the plain rectangular fin geometry to avoid repeating Figure 36**(**a). Comparing the plain triangular fin geometry's optimal configuration in Figure 39(b) with its performance using fewer vertical channels in Figure 39(a), it can be seen that the trends in both ultimately serve to reduce the pressure drop though in different ways. By either increasing the number of channels, as is the case with the wavy fin in addition to the plain triangular fin, or the hydraulic diameter, which is the case with the plain rectangular and offset strip fin, this purpose may be sufficiently served.

In the case of the perforated fin, the pressure drop is sufficiently low to allow for the configuration with, theoretically, the greatest pressure drop to coincide with the optimal exergy efficiency operation point. The louvred fin geometry has the interesting feature of combining higher convective heat transfer with greater pressure loss and this is what leads to its optimal configuration having the smallest channel thickness. However, this excessive pressure loss causes it to have the worst exergy efficiency.

It should be noted though that the relative differences between the various CHE optimal configurations (especially the aforementioned top three performers) are not large and may fall within the range of modelling uncertainty. In this regard, the correlations in the appendix already have uncertainties in the range of 3-10%. While the precise values of these performance indicators may be further refined and their errors ascertained, these results provide a good indication of the relative performances of the different receiver internal flow geometries. They

also highlight the immense scope of work in this area and the importance of a thorough and careful optimisation analysis paying heed to the selection of objective functions and figures of merit.

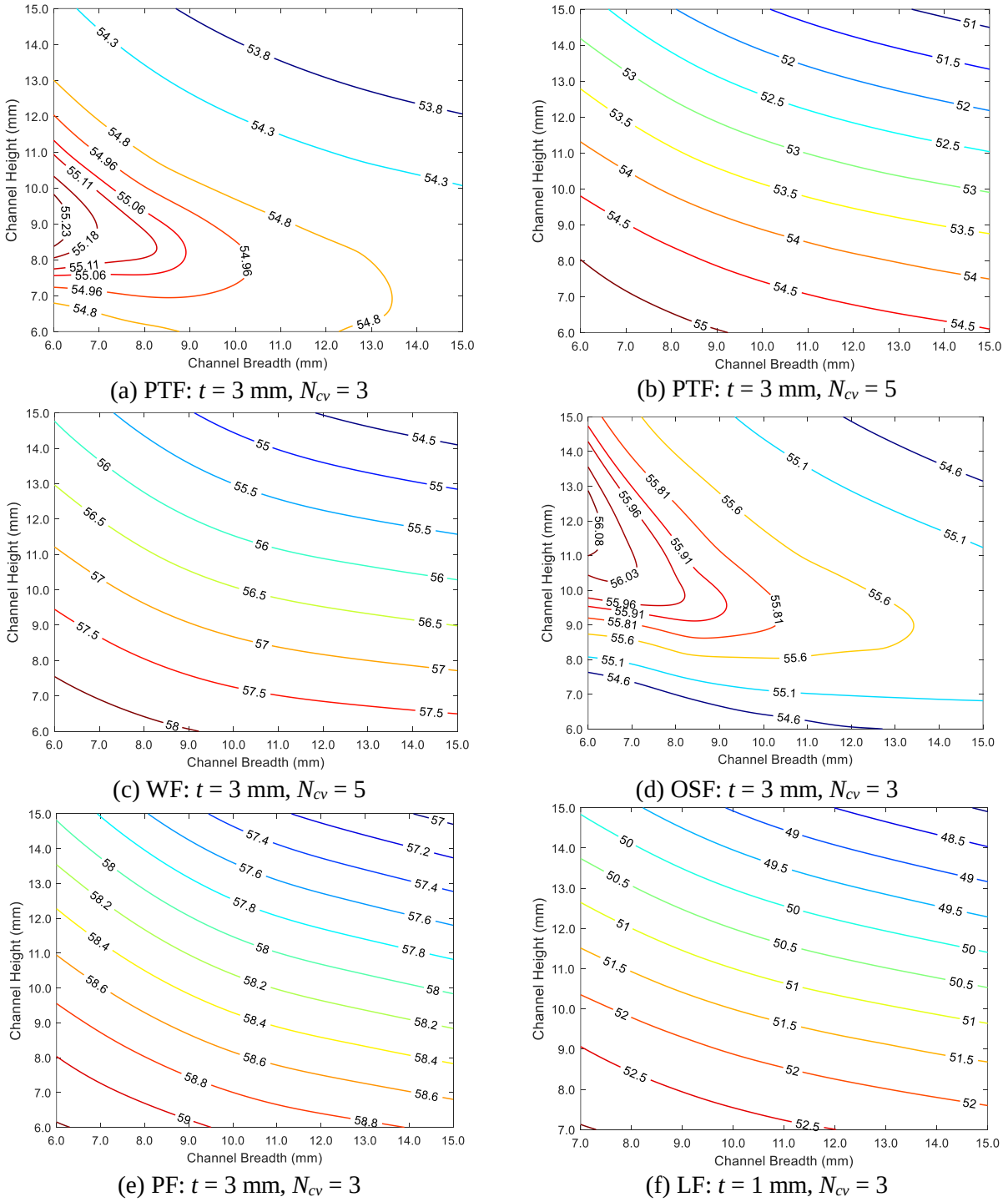


(a) PTF: $t$ = 3 mm, $N_{cv}$ = 3

(b) PTF: $t$ = 3 mm, $N_{cv}$ = 5

(c) WF: $t$ = 3 mm, $N_{cv}$ = 5

(d) OSF: $t$ = 3 mm, $N_{cv}$ = 3

(e) PF: $t$ = 3 mm, $N_{cv}$ = 3

(f) LF: $t$ = 1 mm, $N_{cv}$ = 3

Figure 39. Exergy efficiency as function of the channel breadth and height, for different absorber geometries. (a) PTF: $t$ = 3 mm, $N_{cv}$ = 3; (b) PTF: $t$ = 3 mm, $N_{cv}$ = 5; (c) WF: $t$ = 3 mm, $N_{cv}$ = 5; (d) OSF: $t$ = 3 mm, $N_{cv}$ = 3; (e) PF: $t$ = 3 mm, $N_{cv}$ = 3; (f) LF: $t$ = 1 mm, $N_{cv}$ = 3.

## 2.6. Validation of the model

### 2.6.1. Direct validation by comparison with previous study

The thermo-fluid dynamic model has been validated by comparison with data from a Resistance Network Model (RNM) and a Computational Fluid Dynamics (CFD) model implemented using the Icepak 4.2 software [108]. The RNM itself was validated using the CFD model and some limited experimentation. It should be noted that the given application of the model used for validation was for heat sinks and not specifically for solar receivers. However, since it uses a single heat flux on one surface and has a multilayer microchannel geometry, it is well suited for application to solar receiver modelling. The model employed for validation was used to simulate the behaviour of a plain rectangular fin receiver with three channels; one horizontal and three verticals. Copper was used as the solid material and a heat flux of 2 W is applied on the top surface. The model used channels of 0.2 mm × 0.8 mm with a channel thickness of 0.2 mm. The overall length, breadth and height were 30 mm, 0.6 mm and 3.2 mm, respectively. Water was used as fluid with flow rates of 2 ml $min^{-1}$, 6 ml $min^{-1}$ and 10 ml $min^{-1}$. However, results using a flow rate of 2 ml $min^{-1}$ were invalid for the validation given the heat transfer and pressure drop correlations used.

As observed in Figure 40, the temperature rise in the current model matches that predicted by the validation model and the CFD simulation. There is a significant deviation noted at the beginning and end of the receiver which can be attributed to inherent assumptions made in both models. The current model assumes a uniform heat flux distribution whereas the validation model iteratively solves for the heat flux and temperature distribution (finite difference method) keeping the integrated heat flux over the irradiated surface as constant. The receiver outlet temperature, which may be considered one of the most relevant parameters for receiver's performance evaluation, is well predicted by the model with deviations from the CFD tool and validation model less than 2%.

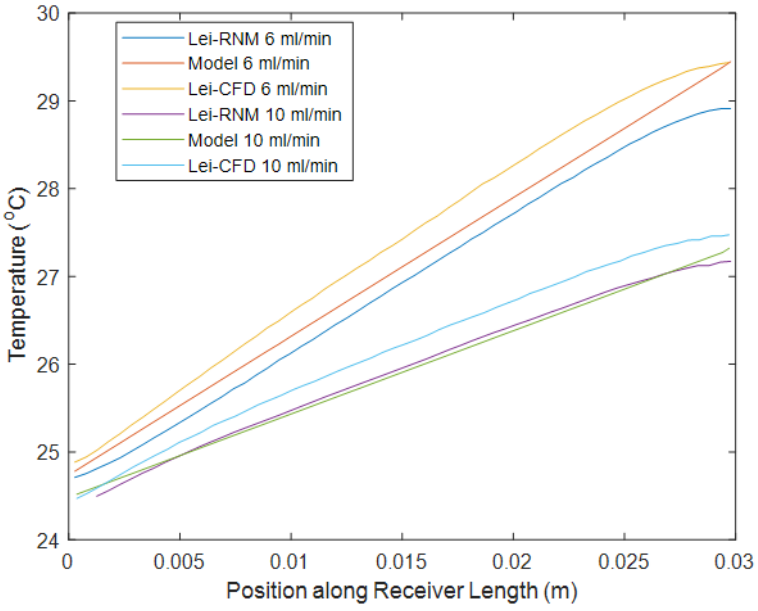


Figure 40. Temperature evolution comparison between model developed in this work and resistance network model and CFD simulations given by Lei [108].

## 2.6.2. Comparison with in-house developed CFD model

A three-dimensional model of a plain rectangular fin receiver was developed in the COMSOL Multiphysics software environment [117] to compare and contrast its findings with those of the bi-dimensional numerical model used in this study. It is also hoped to justify the simplifying assumptions used to reduce the model to a two dimensional one.

The 3D receiver model itself, displayed in Figure 41, was designed and sized so as to be suitable for experimental analysis which is the principal subject of the following chapters. The details pertaining to its design are elucidated in chapter 3 (section 4).

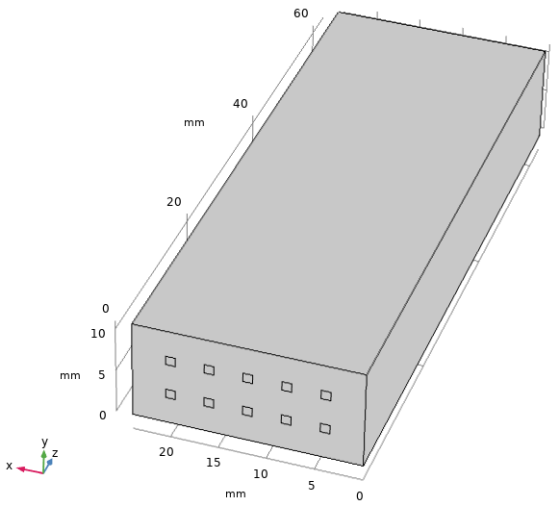


Figure 41. Three dimensional receiver model used in CFD analysis

The receiver design parameters used in the CFD study are summarised in Table 6.

Table 6. Design parameters of receiver used in CFD analysis

| Quantity | Symbol | Unit | Value |
|---|---|---|---|
| Channel breadth | $B_c$ | mm | 1 |
| Channel height | $H_c$ | mm | 1 |
| Top Plate (outermost wall) thickness | $t_{pt}$ | mm | 3 |
| Base Plate (outermost wall) thickness | $t_{pb}$ | mm | 3 |
| Side Plate (outermost wall) thickness | $t_{ps}$ | mm | 3.5 |
| Channel wall thickness | $t$ | mm | 3 |
| Number of horizontal channels | $N_{ch}$ | - | 5 |
| Number of vertical channels | $N_{cv}$ | - | 2 |

Based on the internal design parameters, the overall receiver sizing can be determined:

Receiver height $H_{receiver} = 2 \times t_p + N_{cv} \times H_c + (N_{cv} - 1) \times t = 11\ mm$

Receiver breadth $B_{receiver} = 2 \times t_p + N_{ch} \times B_c + (N_{ch} - 1) \times t = 24\ mm$

Receiver Incident Area $A_{receiver} = 13.68\ cm^2$

The material of the receiver was chosen as stainless steel AISI 316L. The operating conditions of the CFD simulation were set as are presented in Table 7. Pressurised air was used as the working fluid with 'weakly compressible flow' which considers the density variation in the fluid a function of its temperature at a constant reference pressure. This differs slightly from the numerical model which calculates the fluid properties as functions of both the pressure and temperature but nevertheless this fluid model was chosen for the CFD analysis as it is a simplified formulation, leading to increased computational speed. Moreover, as the pressure drop in the receiver is relatively small, this assumption reasonable. The k-ε turbulence model is used in this CFD study.

Table 7. Receiver operating conditions for CFD simulation study

| Quantity | Symbol | Unit | Value |
|---|---|---|---|
| Mass flow rate | $\dot{m}_{rec}$ | g s | 2 |
| Incident heat flux | $\dot{q}_{rec}$ | kW m$^{-2}$ | 200 |
| Fluid inlet temperature | $T_{inlet,HTF}$ | K | 300 |
| Outlet fluid pressure | $p_{outlet}$ | bar | 4 |

Only one face of the receiver is irradiated, as is highlighted in Figure 42, while the other faces are adiabatic. A constant heat flux of 200 kW m$^{-2}$ is applied on the 'irradiated' surface which also has radiation heat losses to the environment at 20 °C.

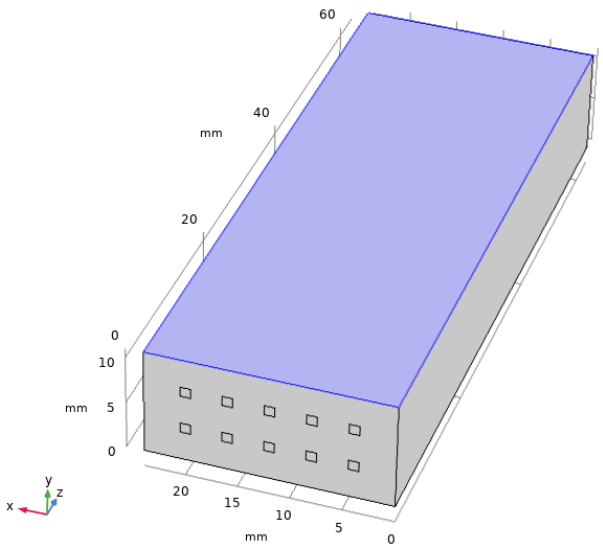


Figure 42. Irradiated surface of receiver in CFD simulation model. Non-highlighted surfaces are insulated.

One of the principal simplifications of the bi-dimensional thermo-fluid model is the assumption that the lateral temperature gradient, across the breadth of the receiver, is negligible. This permits the reduction of the model to a two dimensional one in which only the heat transfer in the flow direction and through the depth of the receiver are considered. As can be seen in Figure 43, the temperature distribution across the receiver breadth (measured along horizontal line between the two vertical channel rows) does not significantly vary (≤ 1%) at neither the inlet, middle nor outlet cross-sections.

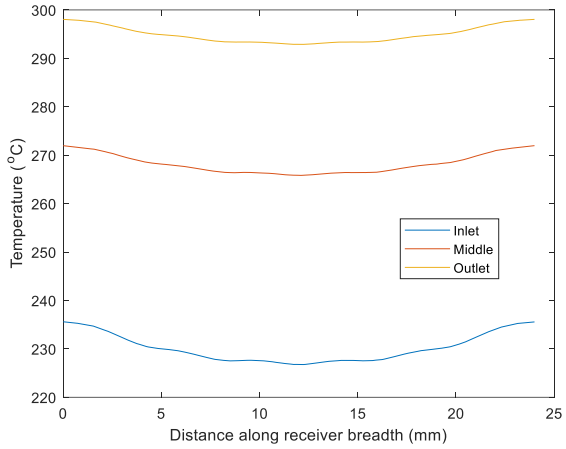


Figure 43. Temperature distribution (solid) across receiver breadth at different cross-sections along flow direction measured along central horizontal (between channel rows)

Beyond this finding, the behaviour of the distribution is expected as there is more cooling away from the insulated side walls and in the microchannel section. The overall temperature distribution in the receiver is shown in Figure 44 where the solid temperature rise along the flow direction is evident besides the expected gradient from the irradiated (top) surface to the bottom. The effect of the adiabatic walls boundary condition is evident in Figure 44(b) where the inlet and outlet regions have a tapering effect as was observed in the study conducted in [108].

It should be noted though that Figure 44(a) depicts the solid surface temperature distribution and not the bulk temperature of the solid which is why it differs slightly from Figure 44(b) though not significantly. Figure 44(b) plots the temperature along three measurement lines running in parallel along the receiver length at the same height (centre of the receiver between the two channel rows) and one in the horizontal centre and the other two lines either side of it.

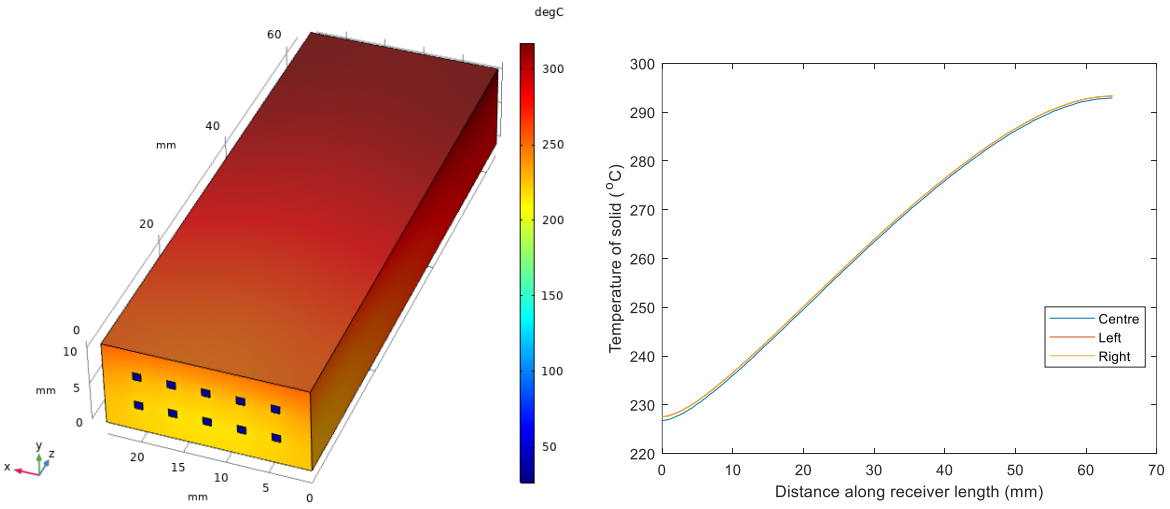


(a) (b)

Figure 44. Temperature distribution over receiver: (a) isometric projection; (b) Solid temperature profiles along three lines in vertical centre (between channel rows) and horizontally in centre and either side of central line running the length of the receiver

The temperature rise in the fluid from inlet to outlet is presented in Figure 45. The higher temperature levels seen in Figure 45(a) are because the fluid temperatures close to the solid wall are visible and not the bulk fluid temperature. The fluid temperature close to the channel wall is much higher than the fluid temperature at the centre of the channel which is measured in Figure 45(b).

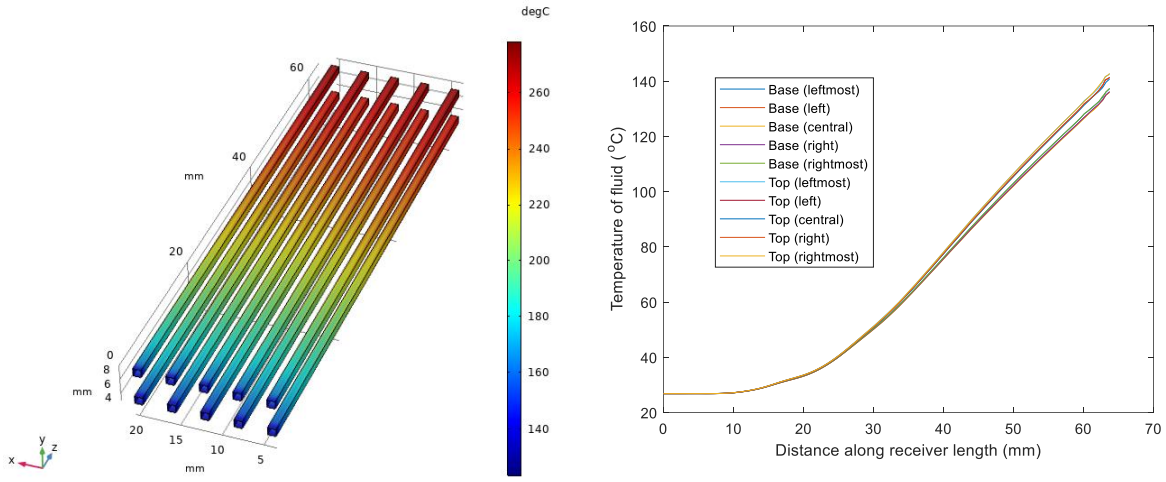


(a) (b)

Figure 45. Temperature evolution in fluid over receiver length/flow direction: (a) 3D view of all channels, (b) temperatures along lines running through centres of all channels

In Figure 45(b) it is observed that the fluid temperature at the centre of the channel doesn't initially heat up as it progresses down the flow channel before its rate of temperature rise increases and then becoming more linear. This behaviour can be attributed to the thermal inertia and diffusivity of the fluid which causes slower temperature change at the inlet and a steady rise of temperature till its outlet.

In order to make a comparison with the pressurised receiver numerical model, the bulk fluid temperature must be used as this is ultimately what is evaluated in the numerical model. A plot comparing these bulk fluid temperatures in the receiver numerical model and the CFD model is presented in Figure 46.

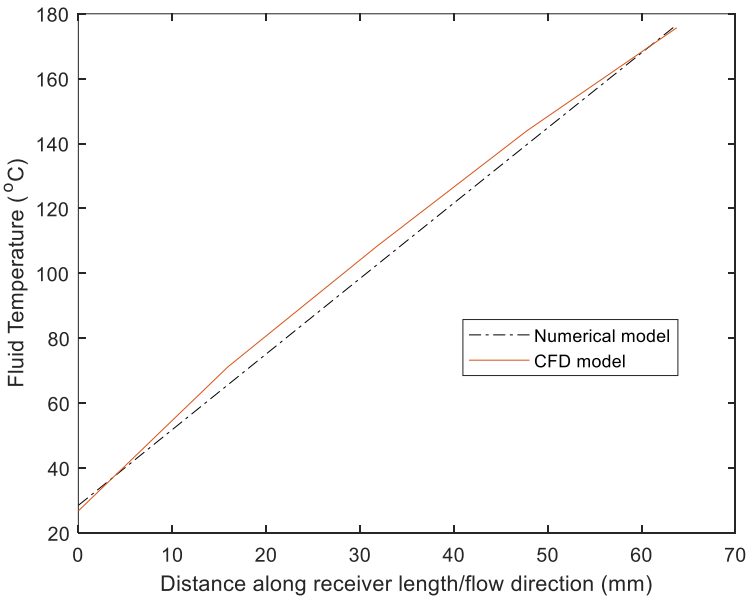


Figure 46. Bulk fluid temperature along receiver length in receiver numerical model and CFD model

The pressure drop in the fluid as it progresses along the flow channel is plotted in Figure 47. This variation in pressure along the receiver length is largely as predicted though the numerical model does show a slightly higher rate of pressure loss which is likely due to the specific friction factor correlations used in the two models.

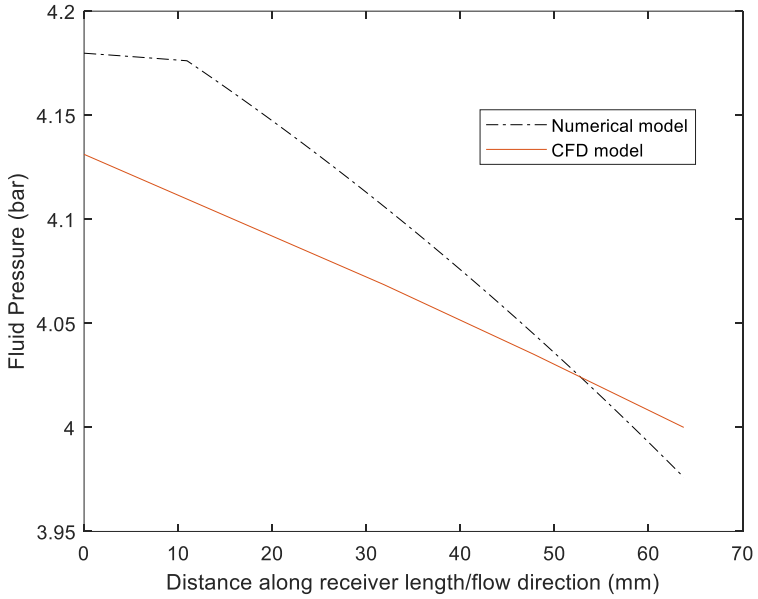


Figure 47. Fluid pressure as a function of flow channel length

The bidimensional thermo-fluid model developed in this study is a simplified version of the three-dimensional CFD model. Its principal objectives are to provide the most critical fluid conditions and receiver performance parameters, under specified inputs, such as fluid outlet temperature, pressure, receiver solid temperature, heat losses etc. It cannot directly be contrasted and compared to a three dimensional CFD model as it has not been designed to produce the level of in-depth analysis that a specialised CFD tool such as COMSOL is capable of performing. However, in terms of predicting the outlet temperature and pressure drop, which may be considered some of the most critical performance indicators, a good agreement within 2% is seen between the two models. Besides this, the CFD model provides some interesting insights into the working of a pressurised receiver using microchannels and additional work may be carried out in this area to evaluate the effect of microchannel geometries, operating and boundary conditions on the performance of the receiver.

## 2.7. Conclusions

Compact heat exchangers are a commercially demonstrated technology that improves the heat transfer and the volumetric efficiency of heat exchange devices. Such compact heat exchangers come in many geometrical forms, when it comes to the internal channels or flow paths, each with their unique properties. The application of these concepts to solar towers results in microchannel receivers that show the potential of operating at high temperatures while maintaining high reliability and thermal efficiency. This is especially true when the heat transfer fluid employed is a pressurised gas, as smaller channels are thermo-mechanically more capable of handling such fluids. In this context, this study has investigated the use of different receiver internal flow geometries, inspired by compact heat exchanger concepts, to analyse the performance of various microchannel receivers. It has been assumed that the heat transfer fluid through the receiver is pressurised air. In this analysis, the particular conditions at the receiver inlet/outlet are determined by coupling the receiver to a supercritical $CO_2$ recompression cycle, although other coupling possibilities would also be valid.

For this microchannel receiver, the compact geometries analysed were the plain rectangular fin, plain triangular fin, perforated fin, wavy fin, offset strip fin and the louvred fin. Besides comparing several compact geometries, internal parametric and optimisation studies were performed with each flow geometry to determine the optimum configuration. The parameters varied were the channel height, breadth, wall thickness (between channels) and the number of vertical channels (number of channels along the height dimension).

Exergy efficiency has been defined and identified as a suitable performance indicator and objective function to be maximised for the optimisation study. It is deemed suitable as it accounts for the heat losses besides the heat transferred to the fluid and the pressure drop across the receiver. Perforated fin followed by plain rectangular and wavy fin receivers were identified as the best performing receiver subtypes.

The thermal resistance of the receiver, in addition to the pressure drop, plays an important role in determining the optimal geometric configuration. For the best heat transfer to the fluid, which is an important part of the exergy efficiency, the smallest channels or lowest hydraulic diameters are preferred. If this causes excessive pressure drops, either deeper channels or a greater number of vertical channels is preferred to improve the exergy efficiency by mitigating the pressure drop. In virtually all cases narrower channels with thicker walls are favoured because of the better conduction through the solid receiver channel walls compared to the parallel heat flow path of convection via the pressurised air. The lower thermal resistance lowers the receiver's heat loss, as well as provides a more uniform temperature through the receiver.

The methodology used in the analysis, its inherent assumptions in addition to the operating and boundary conditions and limits, lends itself to the characteristics of gas phase receivers and the unique challenges posed in studying such receivers. The selection of operating and boundary conditions including, but not limited to, parameters such as the channel velocity, view factor and incident flux play an important part in the receiver's performance and optimal configuration. Investigating the physical limits and phenomena limiting the operation boundary of gas receivers, aside from developing methodologies for their analysis, appears as an interesting area of study.

A three dimensional Computational Fluid Dynamics (CFD) model was used to provide additional insights into the functioning of the receiver and largely validated a key assumption of the simplified model i.e. the uniform temperature across the breadth of the receiver which permitted the simplification and reduction of the problem to a bidimensional one. The outlet temperature and pressure drop, which are key performance parameters of the developed numerical model, correspond well with the findings of the more detailed simulation model

besides previous studies' results. Such a CFD analysis may be performed on the other flow geometries and operating parameters as well to validate their findings, provide meaningful insights into the receiver's performance and potentially improve the simplified model.

The present results indicate a promising scope to the use of compact heat exchanger concepts for solar receivers especially with regards the internal flow channel geometry. While the results themselves carry some uncertainties (an area of future investigation), this analysis clearly demonstrates the utility of using exergy efficiency as a performance indicator and it provides indications to the comparative performance of different receiver geometry types.

# Chapter 3. Experiment preparation and design

## 3.1. Introduction

Following the conclusion of the development of the pressurised receiver numerical model and ensuing results from its exploitation, an experimental validation of the same is proposed. In order to do this, a pressurised receiver testbed has to be designed, assembled and commissioned. The pressurised receivers themselves, being the centrepiece of the experimental analysis, must be designed and fabricated in such a way as to demonstrate experimentally the expected findings of the numerical analysis through their experimental characterisation.

The experiment campaign will employ a high flux solar simulator as its radiation heat source. In this chapter, high flux solar simulators (HFSS) in general and the KIRAN 42, which will be used in this experiment campaign, in particular will be thoroughly described in section 3.2.

Following this, the development of the pressurised receiver experimental testbed will be explained in section 3.3, including a description of the instrumentation and measurement equipment used. The designing of the pressurised receivers is also addressed in section 3.5.

After the assembly of the entire testbed and introduction of the pressurised receivers to it, preliminary experiment runs are performed in cold (without the HFSS) and hot conditions which are elaborated in section 3.6. It is from these preliminary experiment runs that critical shortcomings in the receiver testing were identified and addressed and final procedures for the operation of the testbed were formulated as presented in section 3.7. These progressive learnings through successive test runs are documented in this chapter as well as the final operational procedures arrived at.

Finally the chapter concludes with the design of experiments, described in section 3.8, in which the experimental characterisation of the receiver is planned varying selected operating parameters at distinct operating points. This experimental design is to be applied to each receiver tested

.

## 3.2. The high flux solar simulator KIRAN 42

### 3.2.1. Solar Simulators: An Overview

Laboratory scale testing, including experimental characterisations, using HFSS is an important stage in the development cycle before on-sun experimentation. This holds true in the case of new solar receiver and reactor models. Experimentation on novel concepts and prototypes of solar receivers in on-sun conditions is relatively more challenging than experimenting on the same in indoor HFSS test beds [118]. This is mainly due to the higher associated expenses of installation, operation and maintenance of Central Receiver System (CRS) test facilities. Indoor experimental facilities also generally allow for greater adaptability and operational flexibility, for example incident radiation fluxes can be readily and controllably varied or maintained at constant flux levels and experiment runs are not dictated by outdoor conditions [119] which results in shorter and less risk prone experimental campaigns.

A solar simulator is essentially a device that can approximate natural sunlight in terms of spectral distribution [120]. When used in concentrated solar energy systems, the HFSS must perform the dual task of being the radiation (light) source as well as the optical concentrator to obtain the required levels of irradiance on the target plane. This concentrator function is a homologue of that performed by the heliostat field or parabolic dish in a solar field in on-sun experiments. A HFSS hence consists of two components, the light source which is referred to as the lamp and the reflector which acts as the concentrator. Ellipsoidal reflectors are widely used as concentrators in HFSS [121], [122] as they have high optical efficiencies [123] when correctly aligned. The principle and operation of these reflectors will be discussed in more detail in the following section.

Several studies have been conducted into the use of various light sources in solar simulators and the appropriateness of each light source in terms of how well its spectrum matches the solar spectrum [124]. The most common light sources used in HFSS are xenon arc, metal halide, argon arc lamps and tungsten halide. The KIRAN 42 HFSS employs xenon short-arc lamps which use a high voltage electric arc to create light in an ionised high pressure xenon gas atmosphere [125], [126]. Xenon arc lamps have crucial advantages such as a spectral balance that does not significantly change with power variation [127] and excellent continuum in the ultra-violet through the visible band with a stable spectral qualities though they present strong emission lines in the near infrared 800–1000 nm region, as it is shown in Figure 48.

This causes a considerable shift in the energy balance of the emitted radiation towards the infrared with 49% of the total energy being emitted by the xenon lamp in this spectral range versus only 37% in the solar spectrum [121]. This necessitates artificial cooling from either air cooling or water cooling systems depending on the lamp's wattage. The reflectors too need cooling, normally by forced air cooling, to prevent thermal expansion and deformation due to overheating [128].

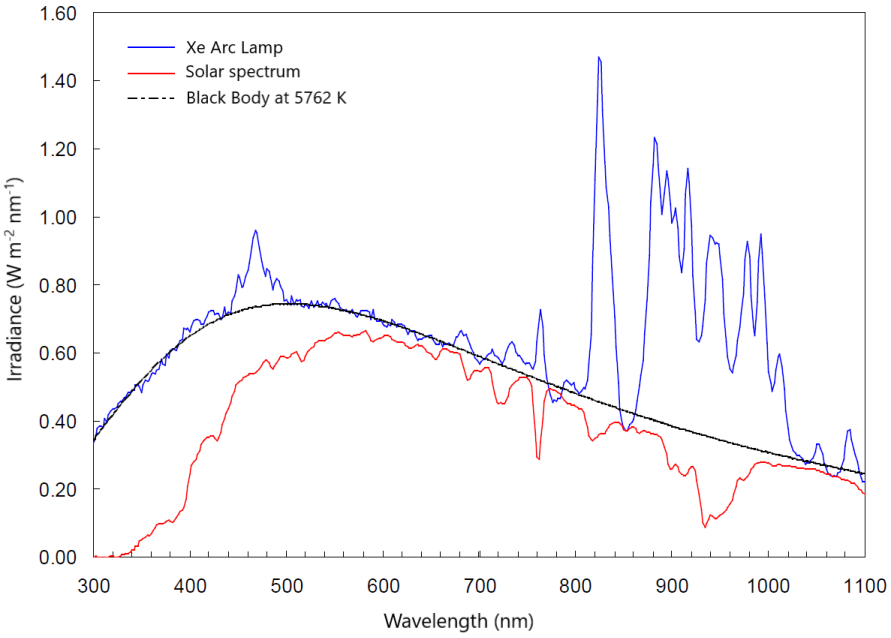


Figure 48. Xenon arc spectral emission versus standard solar spectrum [121]

While the xenon arc lamp's emission spectrum is more heavily weighted toward the infrared region as compared to the solar spectrum, this deviation may not be significant to the analysis of a receiver using a xenon arc lamp HFSS [129], [130]. Considering that a receiver's primary function is to maximise the amount of incident radiation absorbed (and later transferred to a fluid) and minimise the radiation loss by emission, a high absorptance (ideally 1) is desired in the wavelength range of 300-2500 nm approximately and a low emittance (ideally 0) beyond 2500 nm to prevent high temperature radiation losses. This is illustrated in Figure 49. Thus when evaluating the performance of a receiver using a solar simulator it is the average incident flux on its surface, across the spectral range of interest, that is of greater relevance than an accurate spectral fitting of the artificial light source. A more significant disadvantage to the use of xenon arc lamps owes to its high pressure (up to 40 bar) gas pressure which poses an explosive risk. Their radiation outputs are also sensitive to the power input which necessitates specialised power supplies [126], [127].

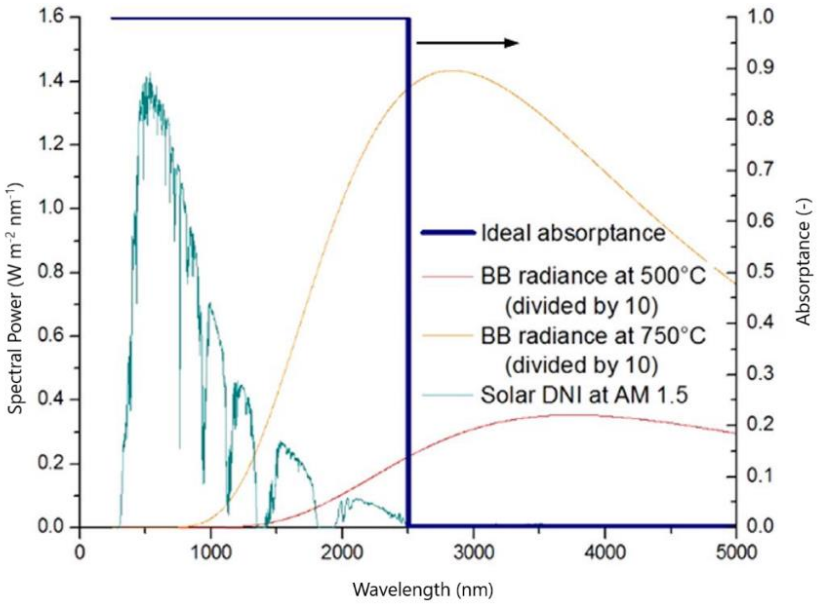


Figure 49. Ideal receiver absorptive behaviour with blackbody (BB) radiation at 500 °C and 700 °C, divided by a factor of 10 for illustrative clarity, and solar spectrum [121], [131].

### 3.2.2. Description and Characterisation of the KIRAN 42 HFSS

The KIRAN 42 HFSS is a multi-lamp high flux solar simulator located in the IMDEA Energy Institute, Madrid. It comprises of 7 Xenon short arc lamps which are arranged in a hexagonal array (see Figure 50) with each lamp having a nominal electrical input of 6 $kW_e$. Truncated ellipsoidal reflectors are positioned and used, in conjunction with the lamps, in such a way as to possess a common focal point. After its initial experimental characterisation [132], the KIRAN 42 has been subsequently used in other experimental efforts [133], [134] besides studies into its configuration [135] and potential lamp pointing strategies [136].

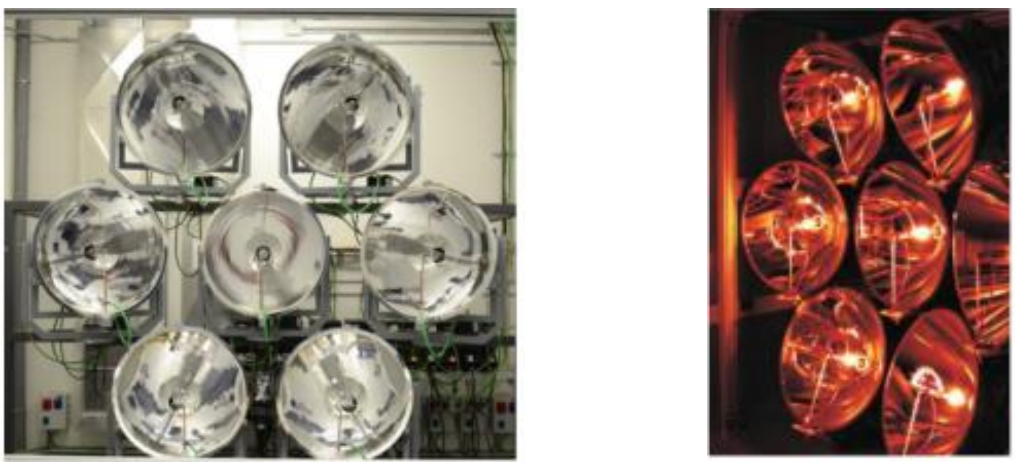

Figure 50. KIRAN 42 High Flux Solar Simulator. (Left) front view, (right) KIRAN 42 in operation (from observation window)

From previous characterisation and experimental works [132], [134], the cumulative incident power of the KIRAN 42 is 14 $kW_{th}$ on the focal plane with a peak flux of 3500 kW $m^{-2}$. It should be noted though that these values are based on experiments carried out in 2013 and several changes, including scheduled replacement of the

lamps, has been carried out the KIRAN 42 since then. Moreover these values are based on all lamps pointing at their common focus which is often not desired especially when attempting to achieve a homogeneous radiation flux profile.

Consider Figure 51 of the flux distribution profile of all 7 lamps of the KIRAN 42 pointed at the common focal point. It is clear that radiation flux (referred to as power density in Figure 51) decreases further away from the focal point radially in the focal plane.

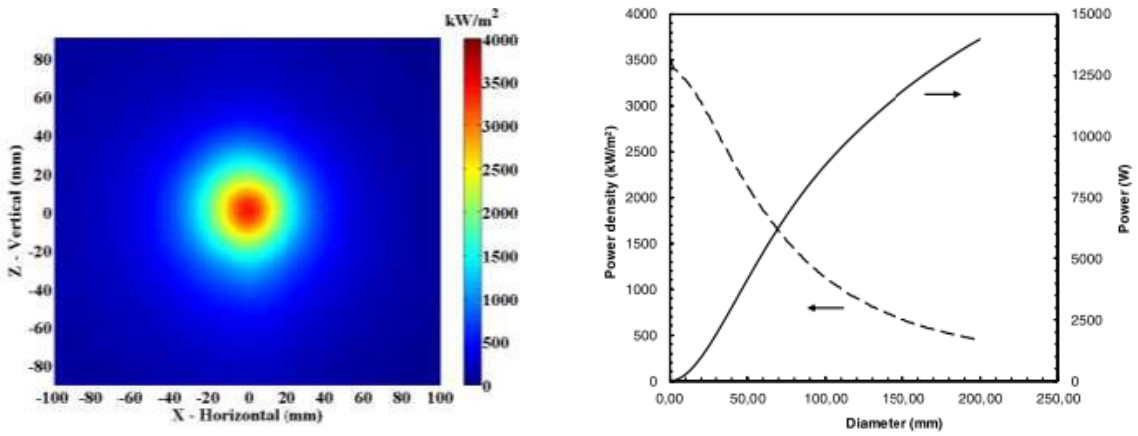


Figure 51. Radiation Flux profile at the focal plane (left) & Power/Power Density vs Diameter (right) [132].

The radiation flux distribution plays an important role in the performance and service life of a solar receiver. In the case of external receivers, if there is a large peak to average flux ratio i.e. the flux distribution profile is not homogeneous, there may be excessive thermal strains on the receiver external surface [137] which would reduce the receiver's operational life. The radiation flux profile is especially relevant in the case of volumetric receivers as inhomogeneity in the flux profile is considered to be potential cause for flow instabilities and thus worsened receiver performance [138]–[140]. Reducing the inhomogeneity in the flux profile is thus crucial and previous works have made use of radiation homogenisers to achieve this [134], [141], [142].

In this experimental work, a combination of target plane positioning and adjusted lamp pointing is used to achieve a homogenising effect on the radiation incident on the absorber face. As mentioned previously, the KIRAN 42 employs truncated ellipsoidal reflectors in all 7 lamps. Briefly, ellipsoidal reflectors work on the principle that if the light source (Xenon arc lamp in this case) is placed at one focus the light reflected off the ellipsoidal reflector will be concentrated at the second focus [121], [122]. This principle can be seen in Figure 52 where the light source (idealised as a point source) at the primary focal point F1 has its light reflected and concentrated at the secondary focal point F2.

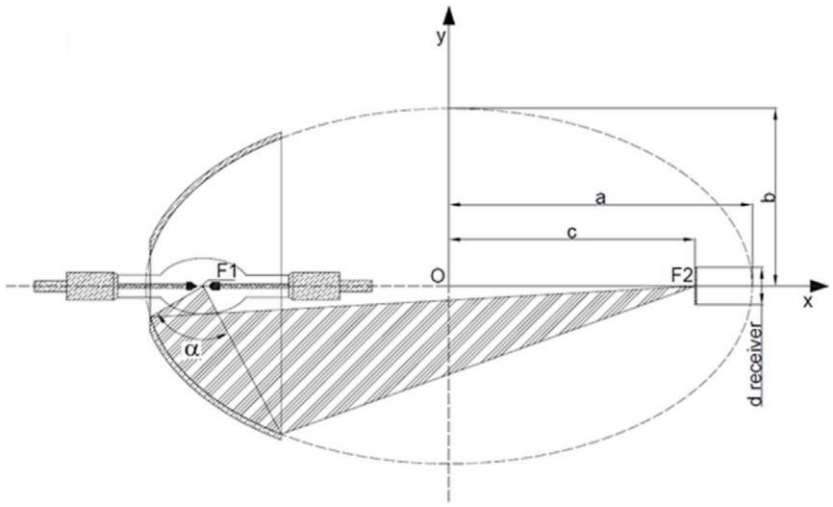


Figure 52. Schematic of a truncated ellipsoid with ideal reflection for a point light source. Here F1 and F2 are the foci with a distance 2c between them; a is the semi-major axis and b is the semi-minor axis [121].

Placing the target plane (i.e. the absorber's front surface) away from this secondary focal point, but along the optical axis of the reflector, achieves two effects. Firstly, the peak flux and total radiation power will reduce and secondly, the 'spot' (the roughly circular region of high radiation flux) will be more spread out. In other words, the radiation flux profile will become more homogenous at the cost of radiation power. This effect can be clearly seen in Figure 53 where one flux map is taken at the focal plane (Figure 53(a)) and the latter is taken 300 mm away from the focal plane (Figure 53(b)). The contour plots of Figure 53 have been made by truncating the radiation level at 100 kW $m^{-2}$. The axes limits in Figure 53(b) are larger than those of Figure 53(a), indicating that the radiation is more spread out. The peak flux at the focal plane is 347 kW $m^{-2}$ whereas the corresponding value 300 mm in front of this plane is only 310 kW $m^{-2}$. In terms of incident radiative power, at the focal plane, a square (with a side of 2 cm) centred at the point of peak flux, receives 127 W against the 118 W received when the target plane is out of focus.

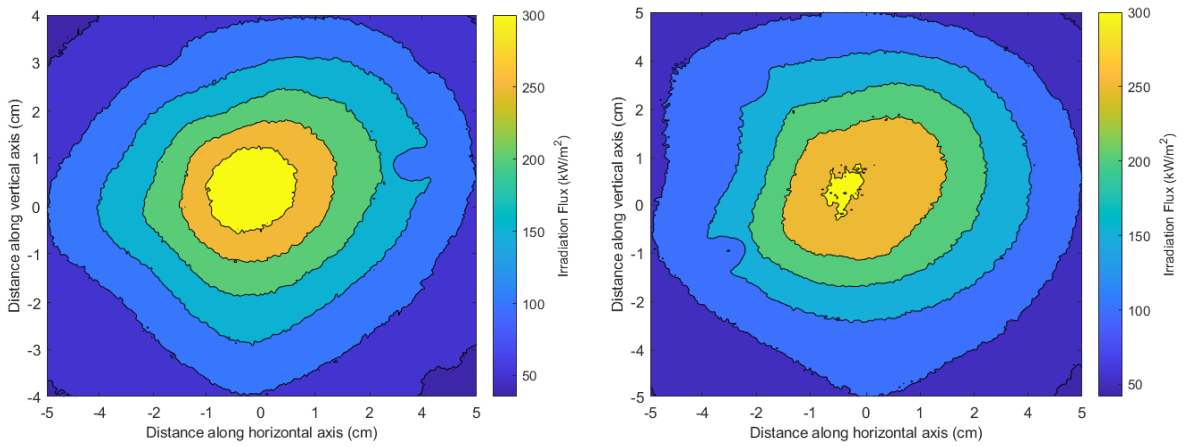


Figure 53. Radiation flux maps of central lamp of KIRAN42: (left) at focal plane; (right) 300 mm away from focal plane.

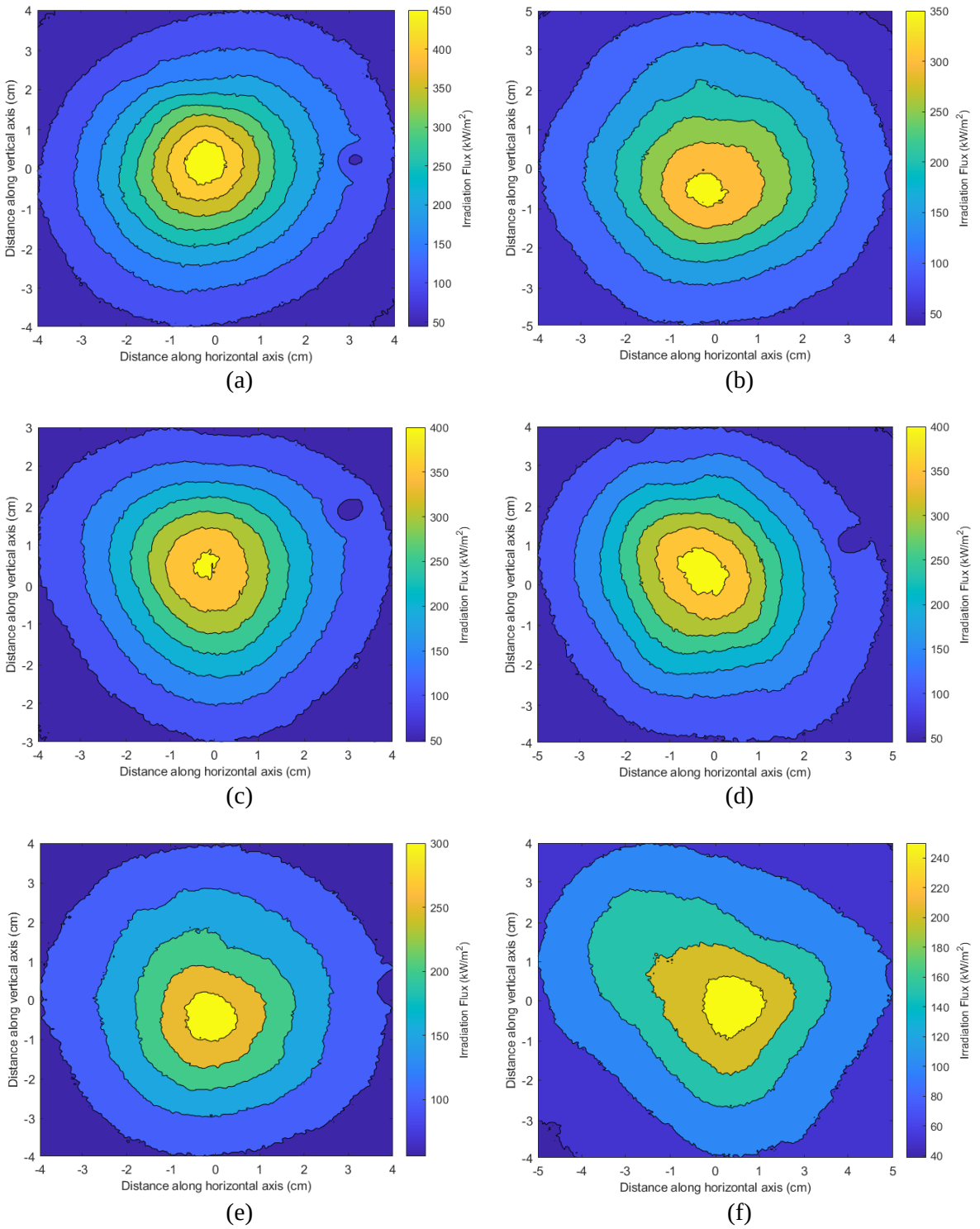


Figure 54. Radiation flux maps of the lamps of KIRAN 42 at the focal plane with the lamps pointing at the common focal point. (a) Lamp 1: Peak flux = 483 kW $m^{-2}$, Total power on plane = 2.14 kW; (b) Lamp 2. Peak flux = 367 kW $m^{-2}$, Total power on plane = 2.02 kW; (c) Lamp 3: Peak flux = 410 kW $m^{-2}$, Total power on plane = 2.00 kW; (d) Lamp 5: Peak flux = 432 kW $m^{-2}$, Total power on plane = 2.41 kW; (e) Lamp 6: Peak flux = 330 kW $m^{-2}$, Total power on plane = 1.87 kW; (f) Lamp 7: Peak flux = 277 kW $m^{-2}$, Total power on plane = 2.04 kW.

The other tactic employed to achieve better homogeneity of the flux profile is to point some of the lamps away from the common focal point. This has the dual effect of homogenising the incident radiation on the target plane by ensuring it will be out of focus as well as repositioning the spot of the lamp to be at the desired position on the target plane. The drawback of moving a lamp's spot away from the centre of the absorber, where it would otherwise be pointing, is excessive spillage as can be observed by the growing difference between the total incident power and the power on absorber.

To assess the current state of the KIRAN 42 HFSS, a characterisation of each of its 7 lamps is carried out on the focal plane with all the lamps pointing at the common focal point. There are multiple methods of characterisation but the one used in this analysis is the flux mapping or indirect method. The results of this characterisation are the radiation flux maps that are presented in Figure 54. The flux map of lamp 4, which is the central lamp, has already been presented in Figure 53(a) and is hence omitted from the subset of figures in Figure 54. The general objective of such characterisations is the determination of the lamp's incident peak flux, total beam power, incident radiation flux distribution besides the spatial uniformity, temporal stability and spectral distribution [122].

Over time the radiation power of the lamps diminishes and/or becomes unstable due to erosion at the electrodes [122] which is why it is recommended to restrict their operating life to 500 hours [143]. The KIRAN 42 HFSS uses OSRAM XBO 6000 W/DHP XL OFR lamps which, when newly installed, can provide a peak flux of over 500 kW $m^{-2}$. Observing the flux maps in Figure 54, it is clear that lamps 6 and 7 are performing poorly. This is either due to ageing of the lamps or some misalignment of the lamps with respect to the reflector.

As mentioned before, the availability and versatility of high flux solar simulators are what make them ideal candidates for lab scale experimental works requiring a concentrated solar spectrum light source. This study will employ the KIRAN 42 high flux solar simulator as its heat and light source. Combining the seven flux maps reveals the maximum limit of radiative power that the KIRAN 42 HFSS can provide and this is seen in Figure 55.

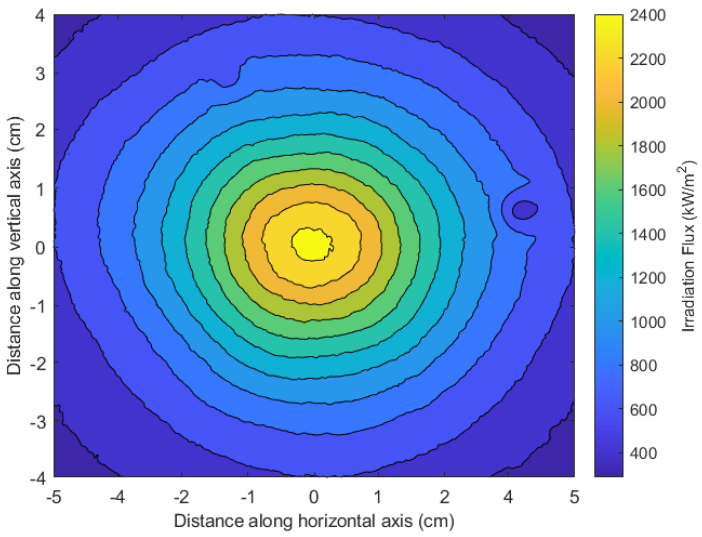


Figure 55. Radiation flux map of KIRAN 42 HFSS at focal plane with all lamps in operation pointing at the common focal point.

# 3.3. Pressurised Receiver Experimental Setup

## 3.3.1. Development of the calorimetric testbed

In order to experimentally analyse the pressurised absorbers proposed in this study, it is necessary to first develop and commission a calorimetric experimental facility. The primary purpose of this testbed is to quantify the heat transfer occurring in the absorber i.e. from the KIRAN 42 HFSS to the HTF while permitting control of some key operating parameters.

When designing and sizing the testbed, the factors limiting the operating envelope of the testbed must be borne in mind. One of the main operating limits of the testbed is the incident radiation which has been covered in detail in the previous section on the KIRAN 42 HFSS. Another critical limiting parameter is the mass flow rate of the HTF. An ambitious experimental campaign, which is called for in this study as will be discussed in the experiment plan in section 3.8, requires a large quantity of HTF. It was initial considered to use compressed air from a compressor but, as will be seen in section 3.6, this was untenable as the HTF composition could not be controlled and hence led to a large uncertainty and inconsistency in the results. Utilising other gases such as helium (He) or carbon dioxide ($CO_2$) at such a scale would be prohibitively expensive.

It was thus decided to use pressurised air with a fixed composition from high pressure cylinders. These gas cylinders, supplied by Nippon Gases, are of 50 L and contain pressurised dry air at 200 bar with a composition of 79% Nitrogen ($N_2$) and 21% Oxygen ($O_2$). As one cylinder is used per experiment (after which it has to be replaced and a new experiment started) and assuming an experiment duration of 100 minutes, the maximum potential mass flow rate of the testbed is ascertained to be 2 g $s^{-1}$ as calculated in equation (21). Regarding the assumed experiment duration, 20 minutes are required for radiation flux from the lamps to stabilise [133] followed by, potentially, 20 minutes for each operating point and 4 operating points varying the radiation flux for each point. When thermal equilibrium in the absorber is reached (discussed in more detail in section 3.7), the operator may move from one operation point to the next. It is impossible to predict how long the absorber might take to achieve this equilibrium and hence a generous time of 20 minutes has been allotted for it.

$$\dot{m}_{max} = \frac{\rho\, V_{cyl}}{Experiment\ time} \tag{21}$$

$$= \frac{232.02\frac{kg}{m^3} \times \frac{1000\ g}{1\ kg} \times 50\ L \times \frac{1\ m^3}{1000\ L}}{100\ min \times 60\frac{s}{min}} \approx 2\ g\ s^{-1}\ ,$$

where $\rho$ is the density of air at 200 bar and 20 °C, and $V_{cyl}$ is the internal volume of the cylinder (50 L)

The inlet pressure is a less critical design factor and is relatively more discretionary, though once its upper limit is decided the piping and instrumentation must be suitably rated to operate under the design pressures. It was decided to limit the testbed to a maximum of 25 bar. With these design parameters, a testbed was designed around a 'blackbox' pressurised absorber as can be seen in Figure 56.

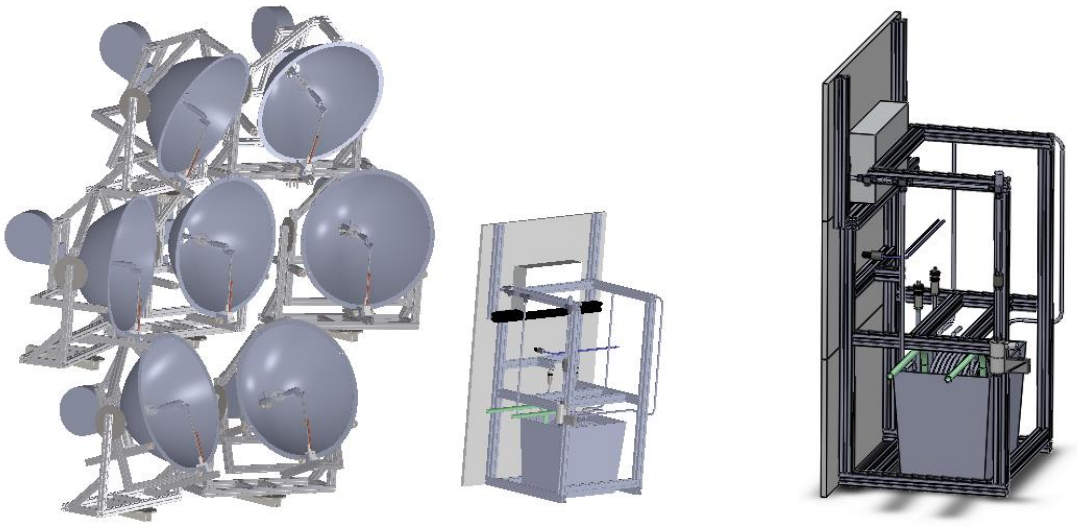

Figure 56. Experimental facility developed for gas phase receiver testing with KIRAN 42 HFSS in position (left) and at close up projected view (right).

The testbed was designed with the objective of flexibility in operating conditions and limits. Multiple receiver concepts may be tested individually or in some combination (series/parallel) given the multi-lamp high flux solar simulator and its intrinsically manipulable pointing strategies. This is especially relevant for experiments in which a higher than ambient inlet temperature is required. Electric heating of flowing air is difficult and expensive as compared with simply using an absorber as a 'preheater' to achieve the desired elevated inlet HTF temperature in the receiver of interest.

As mentioned previously, the testbed has been designed with the receiver as a 'blackbox' which provides for significant flexibility when designing the receiver. The receiver design is limited by the movable table size and load bearing capacity besides considerations of the incident radiation profile. The maximum permissible mass flow rate dictated by the testbed is also a critical design factor when sizing the receiver to be experimented on. The absorber's material (normally a metal alloy such as those from the Inconel or Haynes' series), surface coating, dimensions and internal flow geometry are some of the receiver properties that may be varied to study their influence on its performance.

The experimental testbed has been currently assembled, as shown in Figure 57, to use pressurised air from 5-25 bar at mass flow rates up to 2 g $s^{-1}$. Flexibility of the testbed permits several potential receiver analyses to be performed in the future, depending on the findings of previous studies, with little to no change in the setup. Manipulation of upstream and downstream valves, testbed position and lamp(s) pointing strategy provides a simple means of operation and control of the experiment and potential to perform several parametric analyses.

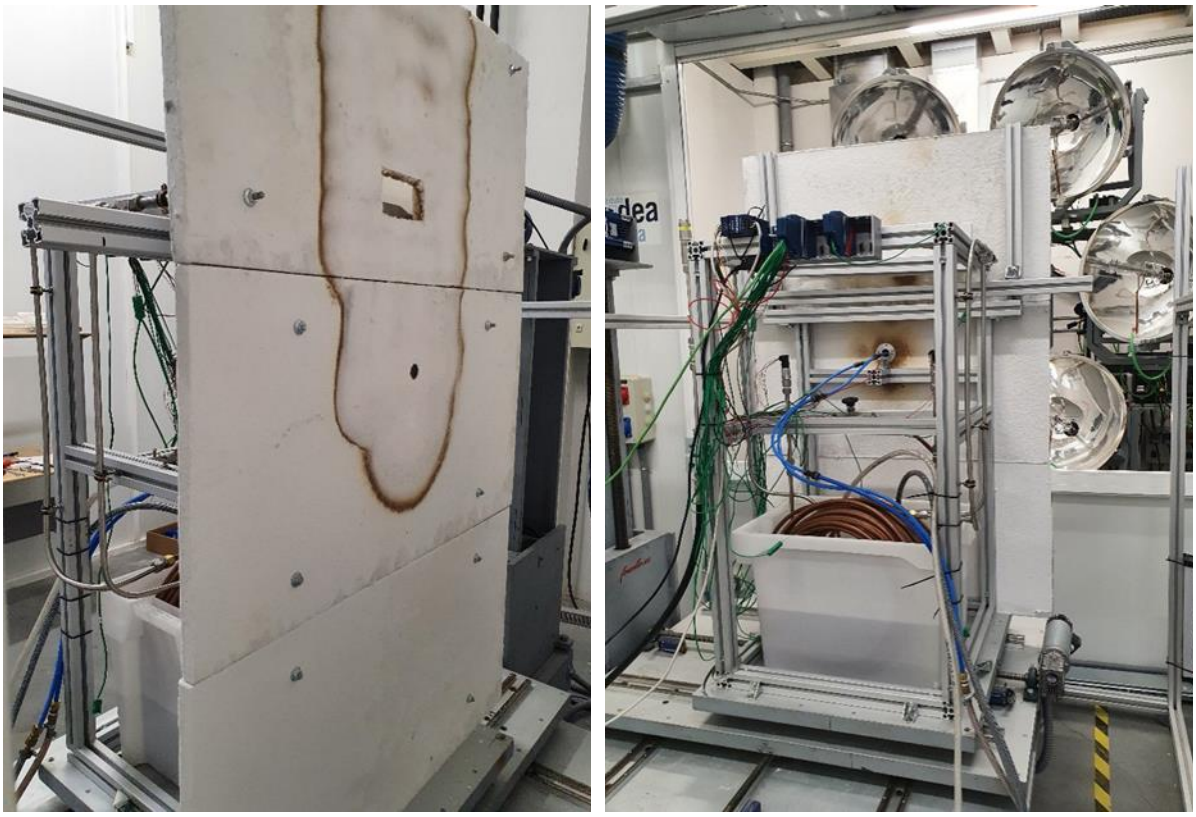

Figure 57. Pressurised receiver testbed as seen from front (left) and back (right).

### 3.3.2. Instrumentation

The piping and instrument diagram can be seen in Figure 58. Starting from the pressurised air cylinder that supplies air, initially at 200 bar though this pressure falls continuously as the cylinder's air is expended, the high pressure air passes through a pressure regulator that delivers a constant output pressure as required by the experiment. The air then flows through a mass flowmeter that measures the mass flowrate of the air stream. Subsequently, a check valve and pressure relief valve are installed to ensure the safety of the system and prevent any risk of backflow and overpressure respectively. Both of these scenarios are potential dangers in case of a major blockage downstream which could be detrimental to the mass flowmeter and even posing an explosive risk if hot pressurised air were to enter the cylinder.

Absolute pressure sensors are placed before and after the receiver as well as thermocouples to quantify the heat transfer in the HTF owing to the receiver. A series of thermocouples are also proposed at various locations on the surface of the receiver to assess the solid temperature and its variations across the length and breadth of the receiver. The heated air then passes through a length of coiled tubing submerged in a cold water tank before the air is eventually discharged to the environment at room temperature. A needle valve, before this exhaust, is placed so as to ensure adequate backpressure at the receiver outlet.

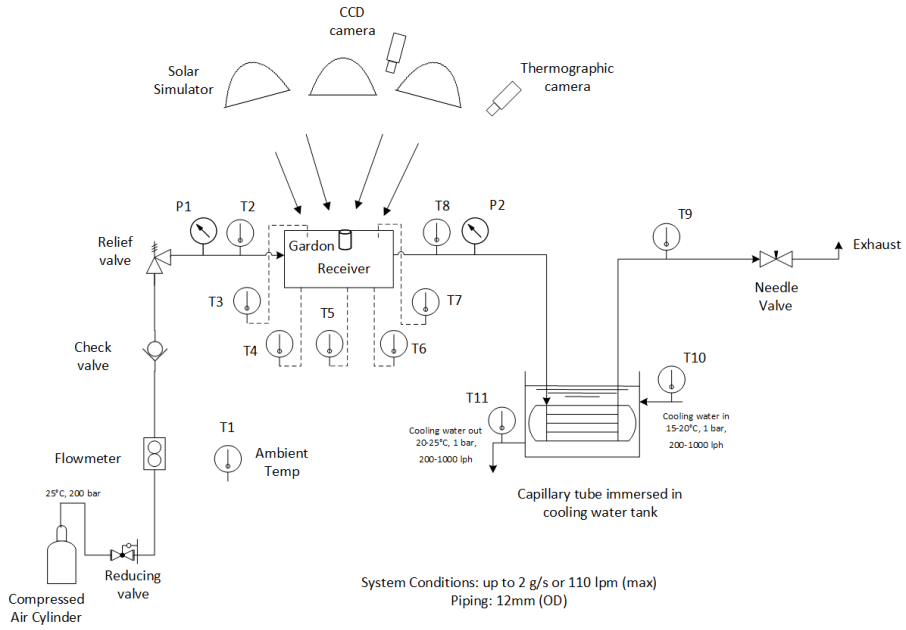


Figure 58. Piping and Instrumentation Diagram of testbed.

The water in the tank is continuously cooled by a chiller that maintains the water's temperature at set point (generally 20 °C). In addition to the calorimetric testbed, the system instrumentation also includes a closed-circuit diagram (CCD) camera and a thermographic or infra-red (IR) camera. Both these cameras are situated behind the lamps of the KIRAN 42 HFSS and are pointed towards the receiver testbed. The CCD camera, with a light intensity filter, is used to safely view the testbed from the front while the lamps are on and is essential in generating the radiation flux profiles/maps. The thermographic camera allows for a temperature profile of the receiver by measuring the emission signature from the same. A gardon radiation flux meter is utilised to quantify the radiation flux incident on the receiver.

All the data from the instrumentation (excluding cameras) is communicated through National Instrument data acquisition devices, including C series modules and chassis, to the LabVIEW computer software. In LabVIEW several programs, or virtual instruments (VIs) as illustrated in Figure 59, were created to facilitate the visualisation of the experiment in progress and save the experiment data at regular time intervals. This data can then be further processed, in post-processing software such as MATLAB, Python, Excel, etc. to reveal performance indicators including thermal and exergy efficiencies, heat gain, pressure drop, etc.

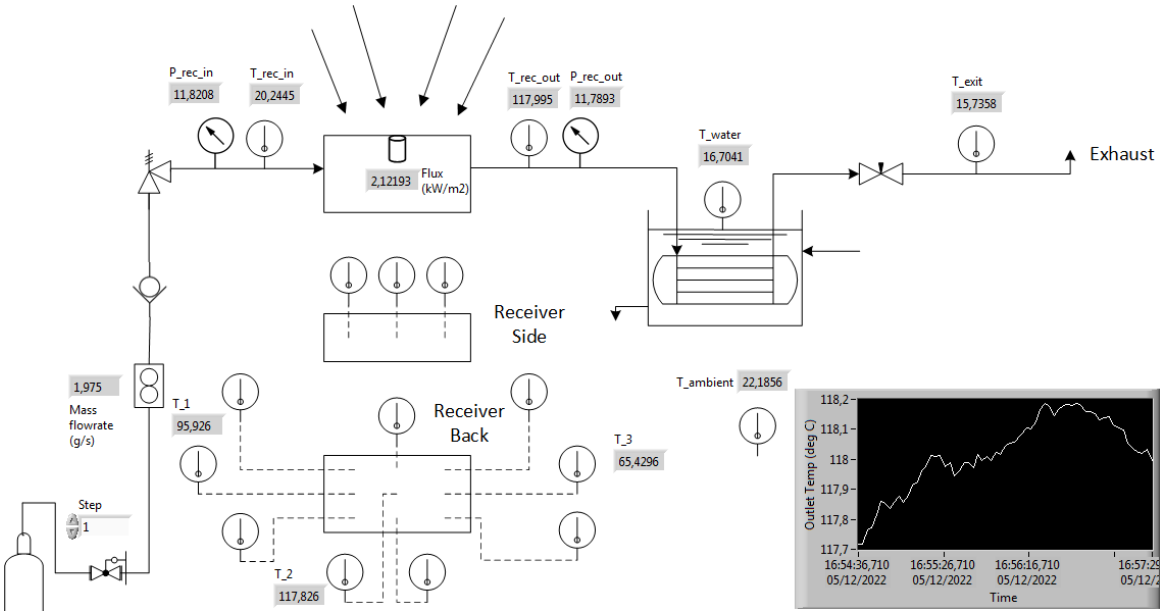


Figure 59. LabVIEW VI used for experiment data visualisation and logging.

In addition to the instrumentation on the testbed, a spectrophotometer is used to measure the absorptivity of the receiver/absorber before and after experiments have been conducted on it. As will be apparent in section 3.6.2, an oxide layer with significantly different optical (absorption) properties develops on the surface of the absorber when it is subjected to elevated temperatures. This effect needs to be accounted for and is done by using a spectrophotometer with an integrating sphere. The measurement of the absorptivity of the absorber is done at three different regions, namely the inlet, centre and outlet of the absorber external surface. A customised 3D printed absorber sample holder was prepared as the absorber was longer though narrower than the spectrophotometer's measurement window.

Pictures of the most important components and measurement instruments of the testbed are presented in the appendix. Table 8, in the following section, details the instrumentation employed including their individual measurement ranges, accuracies, manufacturers and models.

## 3.4. Uncertainty and error analysis

An uncertainty analysis was carried out to determine the uncertainty error in the measured parameters and its influence on the final results and performance indicators. Such an analysis is crucial, especially in experimental work, to quantify the inaccuracies and validity of experimentally determined outputs [144]. This analysis has been performed conforming to the International Organization for Standardization (ISO) guide [145] which employs the Taylor Series Method (TSM) to model experiment errors and their propagation.

It is first necessary to calculate the error in measured variables such as temperatures from temperature sensors, mass flowrates from flowmeters etc. In this study, measured variable errors were divided into experimental errors, instrumentation/calibration errors and random errors. The total error of a measured variable ($\Delta z$) was calculated as the root mean square of its experimental, instrumental and random error as;

$$\Delta z = \sqrt{\sigma_{exp}^2 + \sigma_{ins}^2 + \sigma_{random}^2}\ , \tag{22}$$

where $\Delta z$ is the total error of the measured variable, $\sigma_{exp}$ is the experimental error of the measured variable, $\sigma_{ins}$ is the instrumentation/calibration error of the measured variable, $\sigma_{random}$ is the random error of the measured variable. Experimental error is the error that arises due to the dispersion or variation of the measured variable during the experiment run. This is a typical and unavoidable feature of timewise experiments where variations or 'unsteadiness' of a parameter in time will occur regardless of whether or not the system is operating in 'steady-state' conditions. One standard deviation from the mean value over the analysed time interval was taken as the experimental error. Instrumentation/calibration error arises due to inaccuracies in the measuring device itself and is a physical limitation of the device which cannot be altered/minimised. The instrumentation errors of the various measuring devices can be found in Table 8. Random error is one which quantifies the disruptive effect of a largely uncontrollable environmental factor, such as ambient temperature, humidity etc on the measured variable. This error can only be approximately quantified after a number of experiment repetitions which in this campaign could only be conducted to a limited degree given time constraints.

The final output parameter, whose uncertainty is to be determined, is a function of some measured and derived variables. As it is a multivariate function, its error must account for the individual errors of each independent variable. To quantify this effect, the TSM law of error propagation [144], [145] is applied to give a probable error for a multivariate function $f$ with $n$ independent variables as;

$$\Delta f\left(z_{i,i=1,\dots,n}\right) = \sqrt{\sum_{i=1}^{n}\left(\frac{\partial f(z_i)}{\partial z_i}\Delta z_i\right)^2}\ , \tag{23}$$

The evaluation of the measured and final parameter errors was carried out for each experiment run using equations (25) and (26).

Table 8. Instrumentation used in testbed.

| **Instrument** | **Manufacturer** | **Model** | **Measured parameter** | **Unit** | **Operating / Measurement Range** | **Instrument Error** |
|---|---|---|---|---|---|---|
| Gardon flux gauge | Vatell Corporation | TG-1000 | Radiation flux | kW $m^{-2}$ | 0 – 1600 | 3% |
| Thermocouples | TC Ltd | Type K (class 1) | Temperature | °C | **Continuous**: 0 – 1100 **Short Term**: -180 – 1350 | $\begin{cases} \pm 1.5, & -40 < T < 375 \\ 0.4\%\ T, & 375 < T < 1000 \end{cases}$ |
| Mass flowmeter | Bronkhorst | F-111AC | Mass flow rate | g $s^{-1}$ | 0 – 2.15 | 0.5% |
| Pressure transducer | TC Ltd | 716-912 | Absolute pressure | bar | 0 – 16 | 0.5% |
| Spectrophotometer | Perkin Elmer | LAMBDA 1050+ | Radiation absorptivity | - | 175 - 3300 nm | 1% |

## 3.5. Development of the receiver samples

As mentioned in section 3.3.1, the pressurised receiver testbed was designed around a receiver 'blackbox' with the intention of providing flexibility in the design of the receiver or absorber. However there are still some limiting design parameters set by the testbed, especially the maximum mass flow rate. Using this as a starting point, designs of receiver samples for experimentation were conceived as will be explained subsequently.

Since the receivers to be tested are to be of a relatively small size and are designed for a one-off experiment campaign, additive manufacturing was identified as the preferred means of fabricating the microchannel receivers. Of course, as noted in Chapter 1, there are several alternative means of production of such compact geometry structures including but not limited to brazed or diffusion bonded finned plates formed by chemical etching or fin forming machines. However these techniques require components and equipment dedicated to a single receiver design concept which is inherently time consuming besides being prohibitively expensive for the production of a single sample. As noted by one of the conventional compact heat exchanger manufacturers contacted for this purpose, the initial capital cost when spread over a large volume of produced pieces will work out more cost effective. While this holds true for commercial scale production, for one-off fabrication projects of a complex and compact geometry structures, additive manufacturing oftentimes proves more favourable in both lead time and cost.

It was desired to study the effect of the receiver material on the performance of the receiver and hence it was proposed to manufacture receivers of stainless steel (316L) and Inconel 718 by the Selective Laser Melting (SLM) additive manufacturing method.

Receivers of different internal flow geometries are proposed to be built to investigate the effect of the variation of these geometrical parameters on the performance of the receiver. These experimental investigations aimed at providing an experimental validation of the numerical model developed in chapter 2 and its findings. To this end, the four geometrical design parameters identified and varied in the numerical model (channel height, wall thickness, number of vertical channels and channel breadth) will also be varied in the proposed experimental receiver designs.

As there are four geometrical parameters varied, there will be four receiver variations. To expedite the experiment campaign, the outer dimensions of the receivers are designed identical to one another. This will facilitate mounting and dismounting of samples and instrumentation (especially thermocouples) and will allow for the same thermal insulation block to be used for all samples.

From chapter 2, the perforated fin and plain rectangular fin receivers were found to have the best performances. Given the slight but inescapable inaccuracies of 3D printing holes and overhangs (sags and shape deformations) [146], it was decided to manufacture all the receiver samples using the plain rectangular fin compact flow geometry.

The designs for the receiver samples were carried out as follows:

For a maximum mass flow rate of $\dot{m}_{rec} = 2\ g\ s^{-1}$

Assuming a receiver with a thermal efficiency of 85%, its thermal power is:

$$\dot{Q}_{rec} = \frac{\dot{m}_{rec} \times (h_{rec_{out}} - h_{rec_{in}})}{0.85}$$

$$= 0.612\ kW$$

$h_{rec_{out}}$ = 557 kJ/kg at $p_{rec\_out}$ = 20 bar & $T_{rec\_out}$ = 275 °C &

$h_{rec_{in}}$ = 297 kJ/kg at $p_{rec\_in}$ = 20 bar & $T_{rec\_in}$ = 25 °C

Taking the temperature gain in the receiver to be 250°C.

From the numerical model, it was observed that smaller channels are required to achieve the required channel flow velocities (20-30 m $s^{-1}$) around which the most favourable operating conditions occurred. For a channel flow velocity ($v_c$) of 20 m $s^{-1}$ and at the average air density ρ (at 150 °C & 12 bar) of 9.8 kg $m^{-3}$, the total number of channels is:

$$N_c = \frac{\dot{m}_{rec}}{\dot{m}_{channel}} = \frac{\dot{m}_{rec}}{\rho\, v_c\, A_c} = \frac{0.002\,\frac{kg}{s}}{9.87\,\frac{kg}{m^3} \times 20\,\frac{m}{s} \times 0.001\,m \times 0.001\,m} = 10.13$$

where $\dot{m}_{channel}$ is the mass flow rate in an individual channel, $A_c$ is the wetted cross section area of a channel taken as a 1 mm x 1mm cross section. The following receiver parameters are fixed at: channel breadth $B_c = 1\ mm$, channel height $H_c = 1\ mm$.

The outer plate thicknesses have been set at a minimum of 3 mm though this is well above the requirements of the ASME standard [102] referred to when making the design the procedures of which has been briefly described in Chapter 2. The internal geometrical configuration of a base case receiver was set as shown in Table 9.

Table 9. Base case experimental receiver internal geometry.

| Quantity | Symbol | Unit | Value |
|---|---|---|---|
| Channel breadth | $B_c$ | mm | 1 |
| Channel height | $H_c$ | mm | 1 |
| Top Plate (outermost wall) thickness | $t_{pt}$ | mm | 3 |
| Base Plate (outermost wall) thickness | $t_{pb}$ | mm | 3 |
| Side Plate (outermost wall) thickness | $t_{ps}$ | mm | 3.5 |
| Channel wall thickness | $t$ | mm | 3 |
| Number of horizontal channels | $N_{ch}$ | - | 5 |
| Number of vertical channels | $N_{cv}$ | - | 2 |

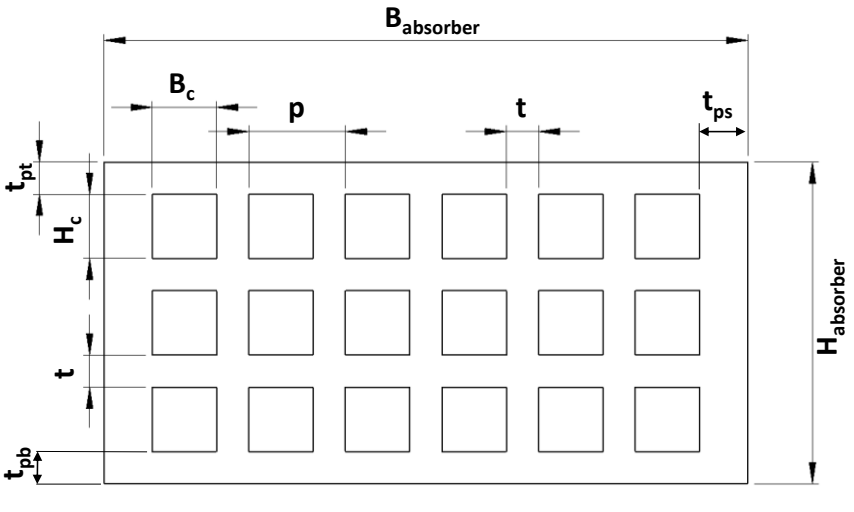


Figure 60. Geometrical parameters of proposed receiver (cross sectional view).

Referring to Figure 60, the receiver height and breadth can now be determined as:

Receiver height $H_{receiver} = t_{pt} + t_{pb} + N_{cv} \times H_c + (N_{cv} - 1) \times t = 11\ mm$

Receiver breadth $B_{receiver} = 2 \times t_{ps} + N_{ch} \times B_c + (N_{ch} - 1) \times t = 24\ mm$

Fixing the incident radiation flux at 400 kW m$^{-2}$, the required receiver length is:

$$L_{receiver} = \frac{\dot{Q}_{rec}}{q_{avg}\ B_{receiver}} = \frac{0.612\ kW}{400\ \frac{kW}{m^2} \cdot 0.024\ m} = 63.75\ mm$$

Receiver Area $A_{receiver} = 13.68\ cm^2$

A plain rectangular fin receiver can be built with the above specifications. Using this design as a base, four receiver sample designs are proposed.

Plain Rectangular Fin model (PR1):

As discussed previously, geometrical configuration of the PR1 base case is summarised in Table 10:

Table 10. PR1 receiver geometry.

| Quantity | Symbol | Unit | Value |
|---|---|---|---|
| Channel breadth | $B_c$ | mm | 1 |
| Channel height | $H_c$ | mm | 1 |
| Top Plate (outermost wall) thickness | $t_{pt}$ | mm | 3 |
| Base Plate (outermost wall) thickness | $t_{pb}$ | mm | 3 |
| Side Plate (outermost wall) thickness | $t_{ps}$ | mm | 3.5 |
| Channel wall thickness | $t$ | mm | 3 |
| Number of horizontal channels | $N_{ch}$ | - | 5 |
| Number of vertical channels | $N_{cv}$ | - | 2 |

Plain Rectangular Fin increased channel height model (PR2):

The geometrical configuration of the PR2 receiver is summarised in Table 11. Increasing the channel height, while maintaining the overall receiver dimensions the same as in PR1, requires a reduction in the base plate thickness. The top plate thickness is not changed as it plays a more critical role in the heat transfer to the fluid being the separating plate between the exposed irradiated plate and the first flow channel row. The bottom plate is only in contact with the insulation and hence its thickness is less important and is not expected to significantly affect the heat transfer to the fluid.

Table 11. PR2 receiver geometry.

| Quantity | Symbol | Unit | Value |
|---|---|---|---|
| Channel breadth | $B_c$ | mm | 1 |
| Channel height | $H_c$ | mm | 2 |
| Top Plate (outermost wall) thickness | $t_{pt}$ | mm | 3 |
| Base Plate (outermost wall) thickness | $t_{pb}$ | mm | 1 |
| Side Plate (outermost wall) thickness | $t_{ps}$ | mm | 3.5 |
| Channel wall thickness | $t$ | mm | 3 |
| Number of horizontal channels | $N_{ch}$ | - | 5 |
| Number of vertical channels | $N_{cv}$ | - | 2 |

Plain Rectangular Fin increased channel breadth model (PR3):

The geometrical configuration of the PR3 receiver is summarised in Table 12. In order to maintain the same overall receiver dimensions as the previous receivers while increasing the channel breadth, the side plate thickness must be reduced.

Table 12. PR3 receiver geometry.

| Quantity | Symbol | Unit | Value |
|---|---|---|---|
| Channel breadth | $B_c$ | mm | 2 |
| Channel height | $H_c$ | mm | 1 |
| Top Plate (outermost wall) thickness | $t_{pt}$ | mm | 3 |
| Base Plate (outermost wall) thickness | $t_{pb}$ | mm | 3 |
| Side Plate (outermost wall) thickness | $t_{ps}$ | mm | 1 |
| Channel wall thickness | $t$ | mm | 3 |
| Number of horizontal channels | $N_{ch}$ | - | 5 |
| Number of vertical channels | $N_{cv}$ | - | 2 |

Plain Rectangular Fin decreased channel wall thickness model (PR4):

The geometrical configuration of the PR4 receiver is summarised in Table 13. The same increased channel height configuration used in PR2 is replicated in PR4 though with smaller channel wall thicknesses. These changes are accommodated by decreasing the base plate thickness and increasing the side plate thickness so as to maintain the overall receiver dimensions.

Table 13. PR4 receiver geometry.

| Quantity | Symbol | Unit | Value |
|---|---|---|---|
| Channel breadth | $B_c$ | mm | 1 |
| Channel height | $H_c$ | mm | 2 |
| Top Plate (outermost wall) thickness | $t_{pt}$ | mm | 3 |
| Base Plate (outermost wall) thickness | $t_{pb}$ | mm | 2 |
| Side Plate (outermost wall) thickness | $t_{ps}$ | mm | 4 |
| Channel wall thickness | $t$ | mm | 2 |
| Number of horizontal channels | $N_{ch}$ | - | 6 |
| Number of vertical channels | $N_{cv}$ | - | 2 |

Summary of Experimental Absorbers Proposed:

With the receiver sample designs finalised, the four proposed models were simulated for the design case of a mass flow rate of 2 g $s^{-1}$ and an average radiation flux of 400 kW $m^{-2}$ and the results of this study, in terms of expected outlet temperature and pressure drop, are given in Table 14. It should be noted though that a range of mass flow rates and radiation fluxes are proposed in the experiment campaign for characterising each receiver which will be explained in more detail in section 3.8 about the design of experiments.

Table 14. Summary of receiver sample designs and expected performance.

| **Receiver (notation)** | **Geometric Parameters** | | | | **Predicted Results** | | **Instrument Error** | |
|---|---|---|---|---|---|---|---|---|
| | $H_c$ (mm) | $t$ (mm) | $N_{cv}$ (rows) | $B_c$ (mm) | Outlet Temp (°C) | Pressure drop (mbar) | Temp (°C) | Pressure (mbar) |
| Plain Rectangular (PR1) | 1 | 3 | 2 | 1 | 305.0 | 123.2 | 1.5 | 80 |
| Plain Rectangular (PR2) | 2 | 3 | 2 | 1 | 299.8 | 28.5 | 1.5 | 80 |
| Plain Rectangular (PR3) | 1 | 3 | 2 | 2 | 298.5 | 25.5 | 1.5 | 80 |
| Plain Rectangular (PR4) | 2 | 2 | 2 | 1 | 298.6 | 20.3 | 1.5 | 80 |

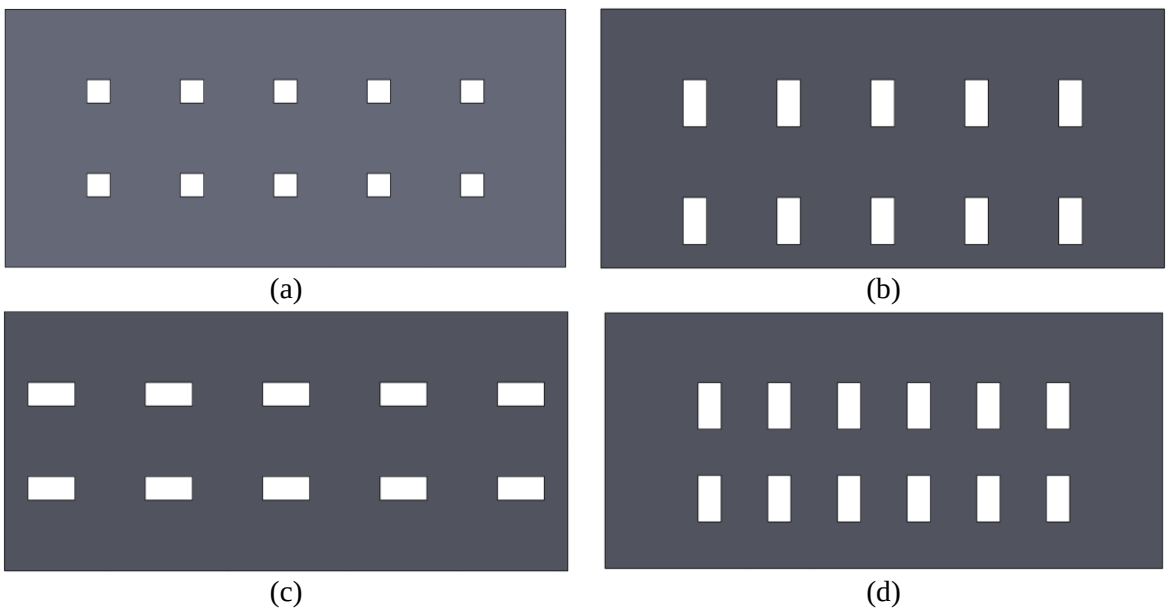


Figure 61. Cross-sectional view of proposed experimental receivers: (a) PR1, (b) PR2, (c) PR3, (d) PR4.

## 3.6. Preliminary experiment runs

The pressurised receiver testbed, after assembly, was commissioned over a series of tests of the instrumentation and the system operation. A log of these experiments can be found in Table 15 but will also be discussed in this section. Learnings from these initial trial runs were used to formulate the procedures of operation and use of the testbed which are detailed in the following section 3.7.

Before any receiver was installed, a pipe section was used in its place to test for leakages in the assembly and to test the functionality of the instrumentation and LabVIEW data acquisition system. These initial tests were carried out on the 29$^{th}$ of July and 1$^{st}$ of August, as can be noted in Table 15, and served to demonstrate the operability of the testbed and its instrumentation.

### 3.6.1. Cold tests (without use of KIRAN 42 HFSS)

When a cold (no lamp on) static pressure leakage test is performed by closing the exhaust valve and opening the cylinder and regulator valve, the line pressure (measured at the 'receiver' inlet) will rise continually before tapering off while the mass flow rate will continuously fall as the system is charged. The mass flow rate eventually stabilises at around 0.01 g s$^{-1}$ as can be observed in Figure 62 and Figure 63. In the same test run, further opening the regulator valve resulted in the equilibrium line pressure shifting from around 10 bar to almost 15 bar.

It was also observed that flow only occurred after a certain cracking pressure at the inlet of the pressure relief valve but this pressure could be changed by adjusting the valve spring. Another interesting finding was that when a charged (pressurised) system has its exhaust valve opened, the line pressure does not eventually stabilise. This can be clearly seen in Figure 64 when despite the exhaust valve being opened twice to try to achieve a relatively constant mass flow rate and system pressure, the absolute pressure of the line continuously rises. Hence in order to conduct experiments at high pressures it is recommended to start from a depressurised system (or lower system) to the design system operating pressure. These findings were definitively confirmed after the installation and testing of a pressurised receiver in dynamic flow conditions, shown in Figure 67, as will be later discussed.

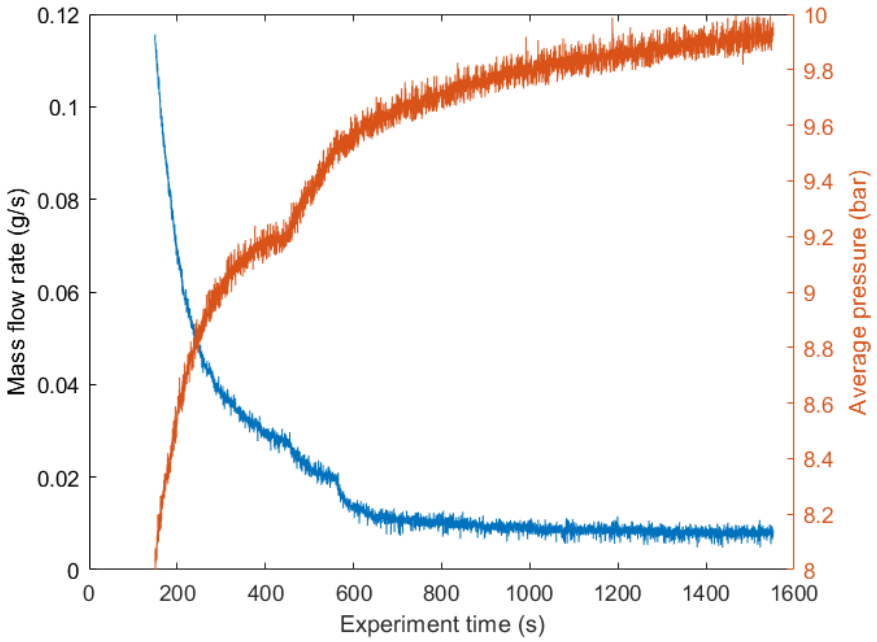


Figure 62. Static pressure test at 10 bar conducted on 01/08/2022.

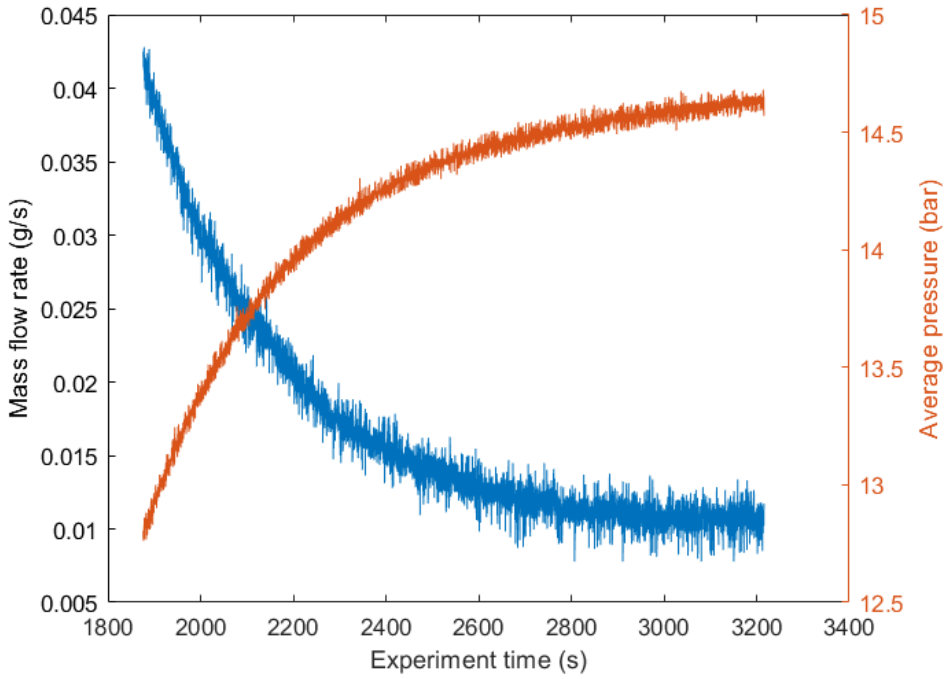


Figure 63. Static pressure test at 15 bar conducted on 01/08/2022.

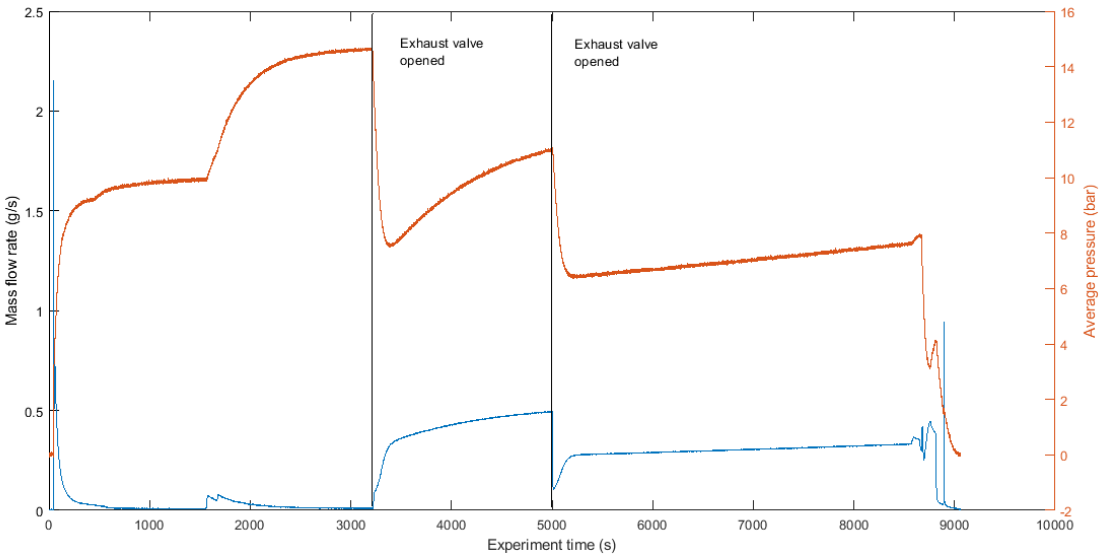


Figure 64. Mass flow rate and absolute system pressure across experiment run on 01/08/2022.

After the successful completion of the cold tests with a pipe section in place of a receiver, a stainless steel (SS) receiver of the PR1 geometry was installed in the testbed as can be seen in Figure 65. Cold leak tests were again conducted on the 3rd and 4th of August to ensure the tightness of the line.

Figure 65. PR1 geometry receiver installed in testbed as on 03/08/2022.

The static leak test, shown in Figure 66, proved the pressure tightness of the 3D printed receiver and that it could withstand elevated pressures.

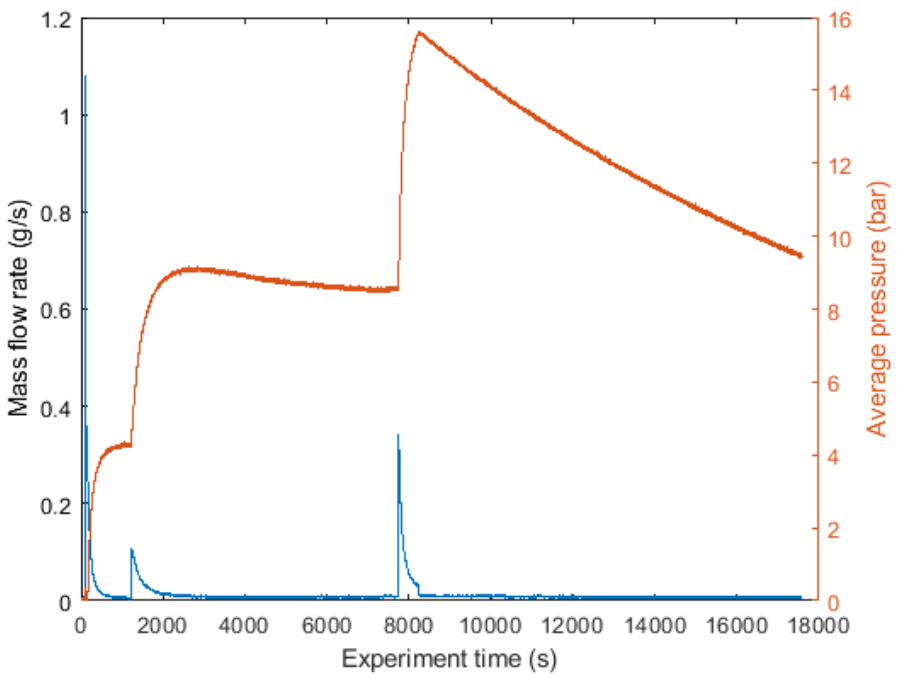


Figure 66. Cold static leak test conducted on stainless steel PR1 receiver on 03/08/2022.

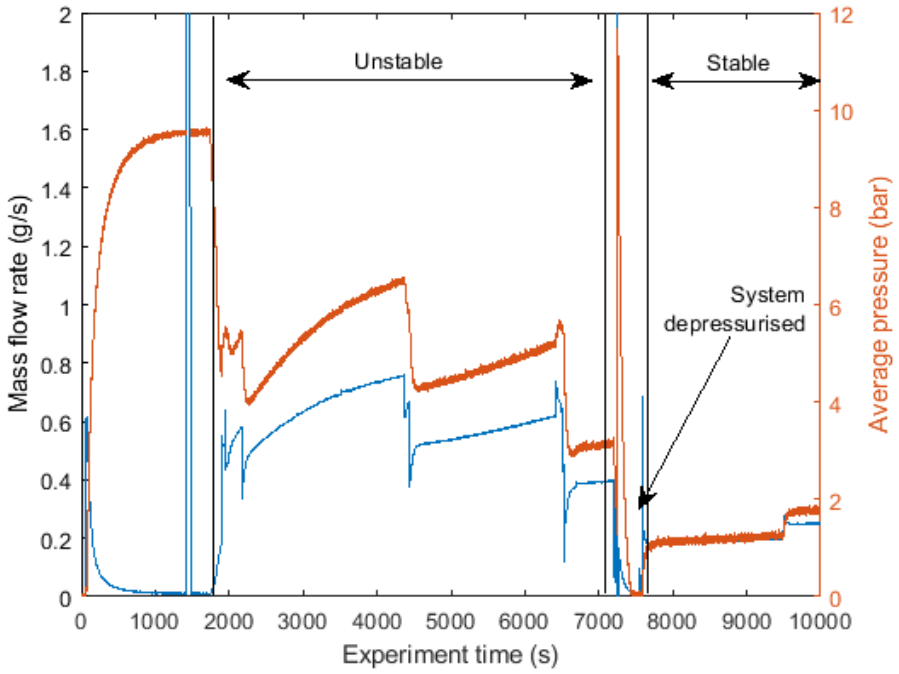


Figure 67. Cold static and dynamic tests conducted on stainless steel PR1 receiver on 04/08/2022

The receiver was then tested statically and dynamically on the 4th of August which is demonstrated in Figure 67. After the high pressure static tests, the exhaust valve was opened to try to achieve stability but, as was found previously, the mass flow rate and system pressure do not stabilise but only increase continuously. The line was then completely depressurised by closing the cylinder valve, leaving the exhaust valve open, and then re-pressurised by re-opening the cylinder valve. This resulted in stable operating conditions and definitively verified the previous findings of mass flow rate and system pressure stability reaching equilibrium and stability only when the system is moved from lower pressure to higher.

### 3.6.2. Hot tests (using the KIRAN 42 HFSS)

Following the successful conclusion of the cold tests, the preliminary hot tests (i.e. experiment runs that include the use of one or more lamps of the KIRAN 42 HFSS) could be conducted. A rudimentary insulation of protective alumina radiation shields was erected around the installed receiver as can be seen in Figure 68.

Figure 68. Alumina radiation shield around receiver as on 11/08/2022 (before experiment)

For the initial experiment run using the KIRAN 42 HFSS, to minimise any risk, the safest operating conditions were chosen. This meant operation at a high mass flow rate (for better heat evacuation from the receiver solid body) and low system pressure and radiation flux. It was decided to use a mass flow rate of 2 g $s^{-1}$, receiver inlet pressure of 4 bar and peak radiation flux of 200 kW $m^{-2}$.

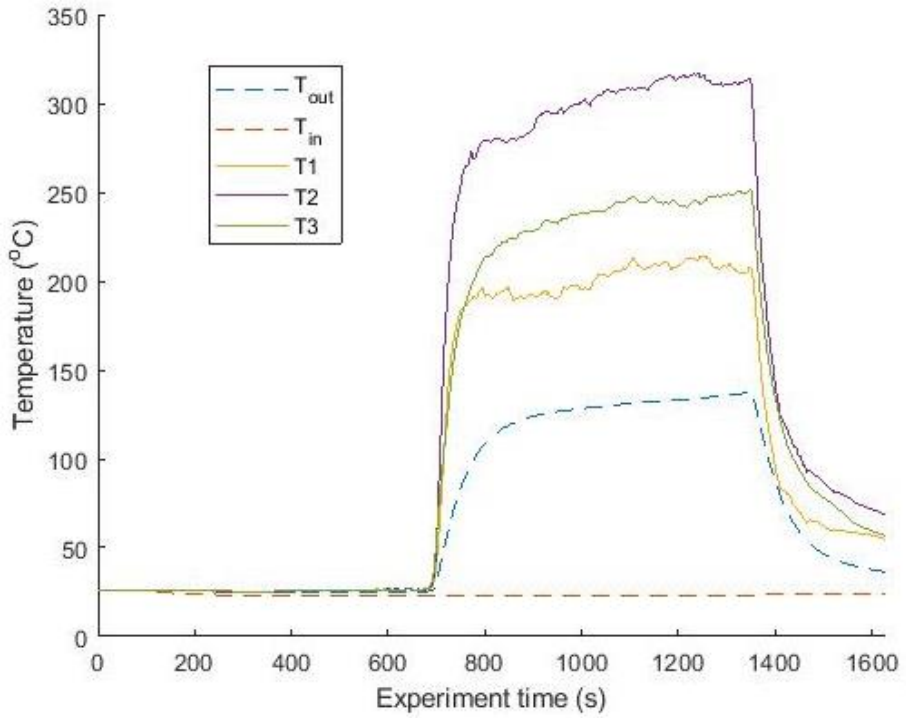


Figure 69. Experiment run using single lamp (lamp 4) with peak radiation of 200 kW $m^{-2}$ at mass flow rate of 2 g $s^{-1}$ and receiver inlet pressure of 4 bar conducted on 12/08/2022.

Referring to Figure 69, the receiver seemed to function adequately with the temperature at the receiver outlet slowly rising and reaching temperatures of close to 140 °C. Three thermocouples were placed in contact with the receiver back surface at the beginning (T1), centre (T2) and end (T3) of the receiver though these thermocouples were not completely radiation shielded as the receiver was not covered by any insulation as is clearly evident in Figure 68. The exposure of the thermocouples to radiation means that the measured solid temperature values shown in Figure 69 are overestimated.

The position of the thermocouples at the back of the receiver can be seen in Figure 70. The three thermocouples can be seen rising from the bottom and are labelled as T1, T2 and T3 moving from right (receiver flow inlet) to left (receiver flow outlet). Comparing from before and after the experiment run, besides the obvious effects of concentrated radiation on the alumina shield the receiver has also slightly oxidised on the microchannel to tube connection especially at the outlet.

In all, the first hot test was considered a successful experiment run of the pressurised receiver testbed as all subsystems from the receiver itself to the instrumentation and control were demonstrated to operate sufficiently. An issue arose with the cooling water tank, and more particularly with its chiller, as it was detected that significant water leakages occurred after a period of inactivity. This did not affect the experiments in any way as while the chiller was active the tank water temperature and exhaust air temperature were at or below room temperature. The issue was rectified in any case as logged in Table 15.

Figure 70. Receiver and radiation shield after experiment run (hot test) on 12/08/2022.

Following this initial hot test, a more elaborate experiment run was conducted at the same mass flow rate and receiver inlet pressure level but at a range of peak radiation fluxes i.e. from 200 kW $m^{-2}$ to 500 kW $m^{-2}$ at 100 kW $m^{-2}$ intervals. The radiation flux profiles/maps at each peak flux level is further elaborated on in section 3.8. This experiment run, conducted on the 22$^{nd}$ of September, is plotted as a function of important temperatures in Figure 71. The receiver and its instrumentation have remained unchanged from the previous experiment.

The receiver air outlet temperature rises as the incident radiation level rises and the regions of operation of the four radiation levels are evident from the temperature levels in Figure 71. The solid temperature of the thermocouple close to the receiver outlet (T1) rises above that of the central thermocouple (T2) despite the peak flux always occurring in the centre of the receiver. This demonstrates the cooling effect of the microchannel receiver as the thermocouple T1 is placed outside the microchannel zone. The temperatures of T1 and T2 invert at a point in the 500 kW $m^{-2}$ operating period and this is owing to the fact that the T2 (and T3 as well though this is not significant) have lost thermal contact with the solid back wall of the receiver and are fully exposed to the incident radiation as can been seen in Figure 72 and Figure 73 which depicts the receiver after the experiment run and CCD images of the receiver at different incident radiation flux levels respectively.

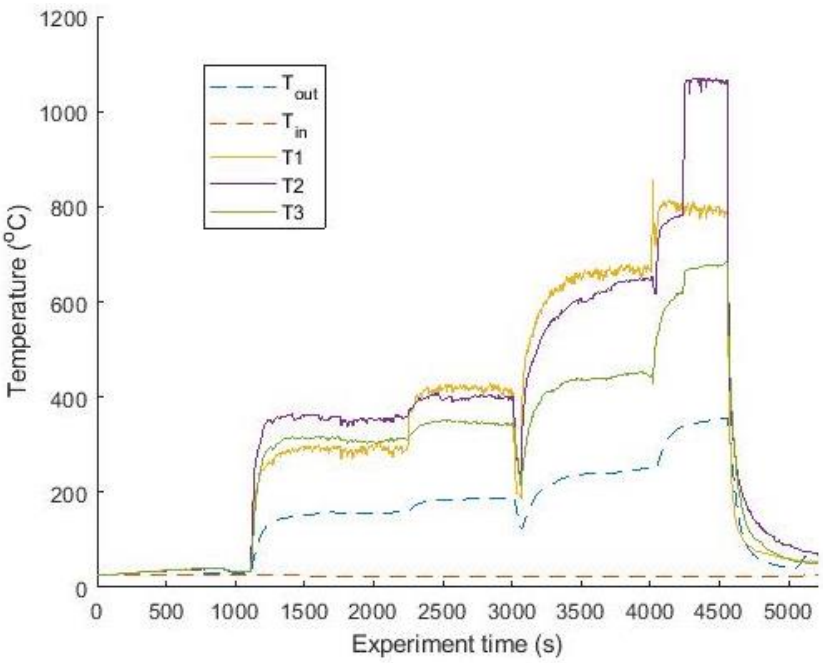


Figure 71. Experiment run using increasing peak radiation flux levels of 200 kW $m^{-2}$, 300 kW $m^{-2}$, 400 kW $m^{-2}$ and 500 kW $m^{-2}$ at mass flow rate of 2 g $s^{-1}$ and receiver inlet pressure of 4 bar conducted on 22/09/2022

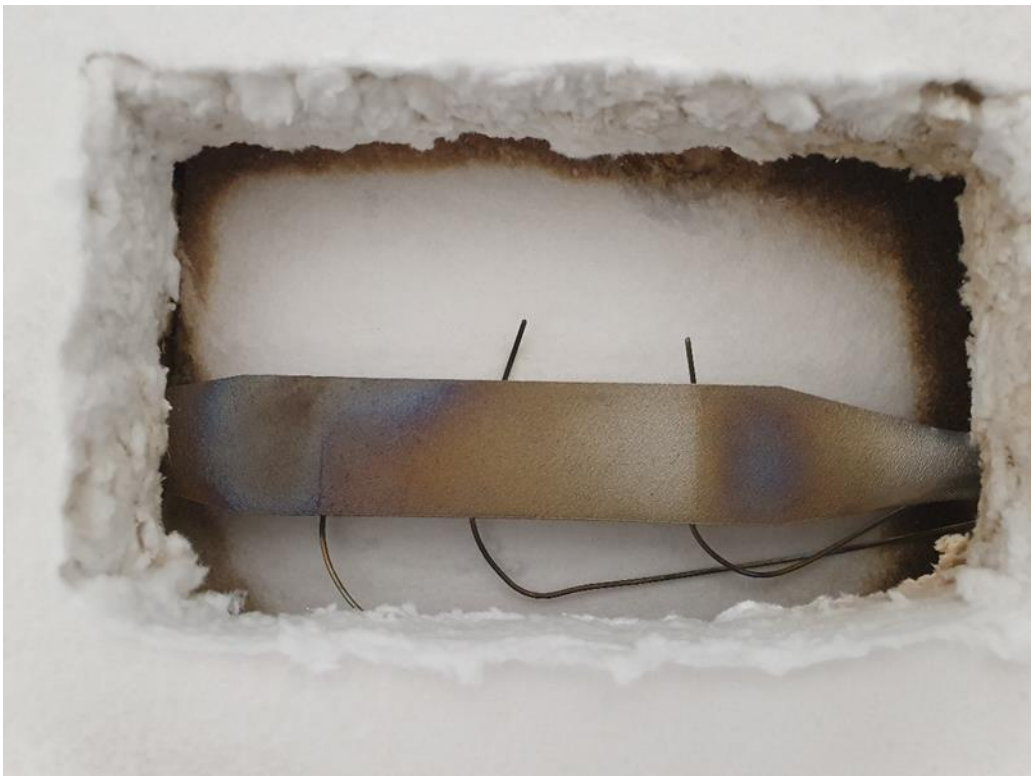

Figure 72. Receiver after experiment run (hot test) on 22/09/2022

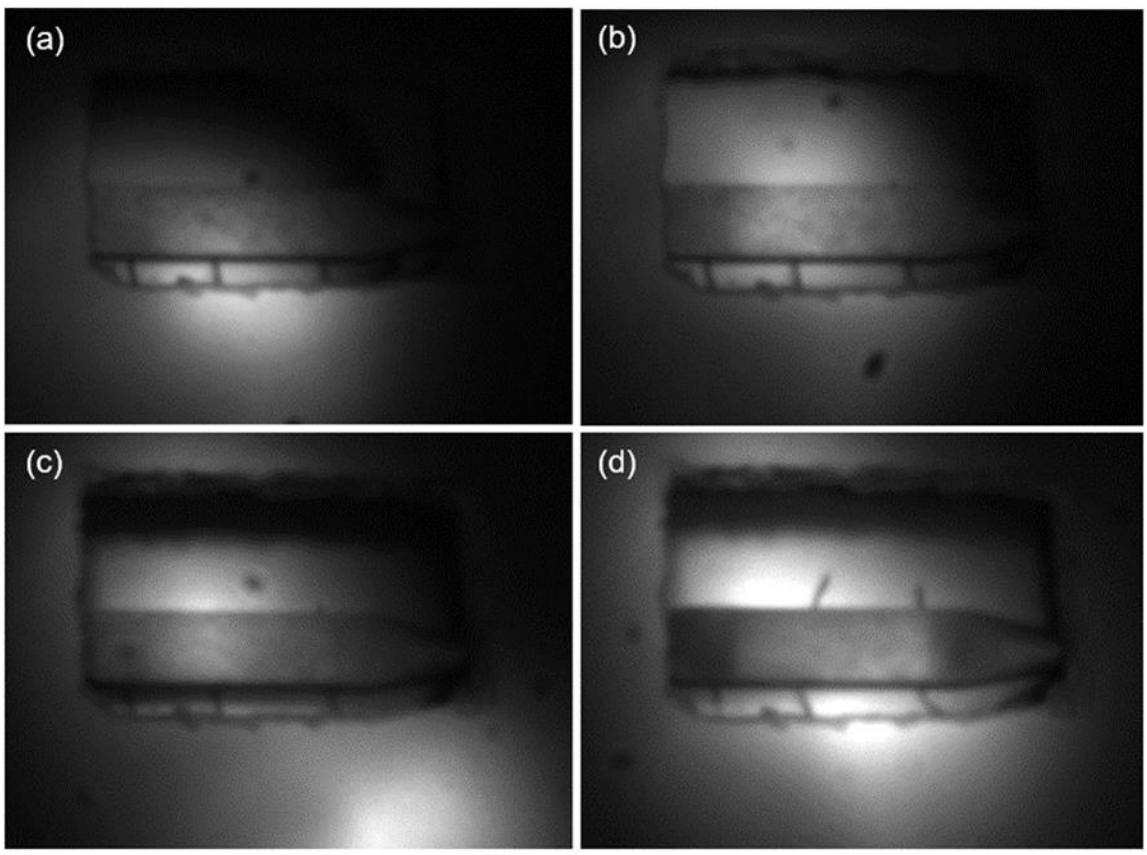


Figure 73. CCD images of receivers during experiment run on 22/09/2022 at different flux levels. (a) 200 kW $m^{-2}$; (b) 300 kW $m^{-2}$; (c) 400 kW $m^{-2}$; (d) 500 kW $m^{-2}$

The significant oxidation seen on the receiver in Figure 72 occurs when the local solid temperature of the stainless steel rises above 400 °C though the oxidation becomes significantly more pronounced at temperatures above 600 °C [147], [148]. The regions and levels of oxidation match well with expected regions of elevated temperature. Referring to Figure 74, it is clear that the most significant regions of oxidation occur outside the microchannel region (i.e. the receiver) and within the receiver the oxidation gets significantly more pronounced from the flow inlet (right) to outlet (left). While this is a good result, in terms of visually showcasing the effectiveness of the microchannels, the receiver was excessively oxidised and needed proper insulation and radiation shielding. This is especially true in case of the non-microchannel sections and the back of the receiver.

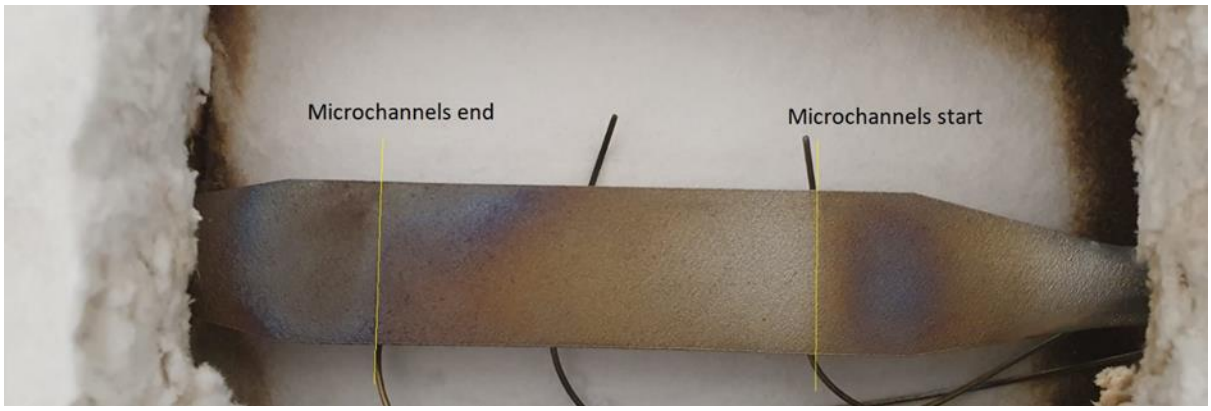


Figure 74. Depiction of microchannel region of receiver relative to oxidation regions

To this end, an insulating brick was carved out to be used as a thermal insulator to the receiver as can be seen in Figure 75.

Figure 75. Thermal insulating brick and radiation shield used for receiver insulation

With the additional thermal insulation added (Figure 28), the receiver was reinstalled in the testbed and prepared for experimentation using the same conditions as was used previously i.e. a mass flow rate of 2 g $s^{-1}$ and

receiver inlet pressure of 4 bar with a range of peak radiation fluxes i.e. from 200 kW $m^2$ to 500 kW $m^{-2}$ at 100 kW $m^{-2}$ intervals. A temperature evolution plot of the experiment run is given in Figure 77.

Figure 76. Receiver with thermal insulation as installed before experimentation on 03/10/2022

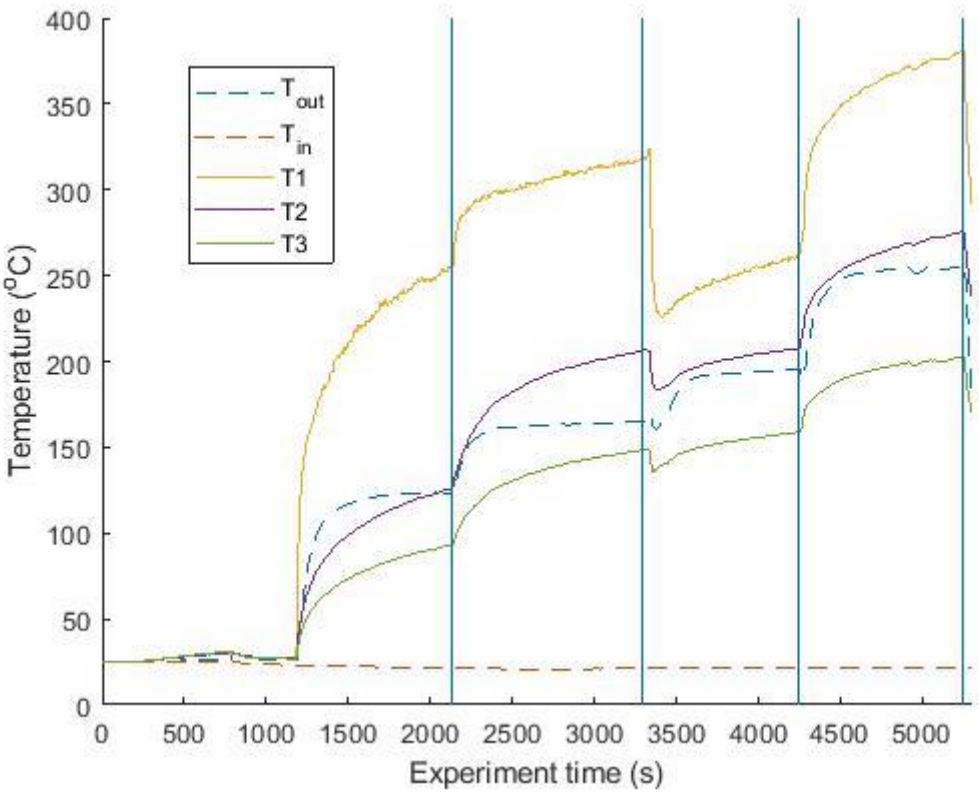


Figure 77. Temperature changes over experiment time during experiment run conducted on 03/10/2022

The temperatures, especially the solid temperatures, seen in Figure 77 are far more reasonable and within safe operating conditions of the receiver. The receiver outlet temperature stabilised to within 1% of its mean value after around 7-8 minutes since operation state conditions were reached. Hence for future experiments, 15 minutes

may be used at any operation condition with the last 5 minutes being the recorded or measurement interval used for subsequent analysis considering that, in effect, the receiver is operating in 'steady state' conditions. The experiment conducted on the 3rd of October was the first completely controlled experiment run and provided sufficient information to form guidelines and procedures to the operation of the testbed. These have been laid out in the following section 3.7. This successful experiment run was the culmination of the learnings from the previous efforts and incremental improvements from the same. Comparing the receiver before and after the experiment run (Figure 76 and Figure 78 respectively) it is clear that no significant oxidation has occurred as the receiver solid (back) temperatures were within 400 °C.

Figure 78. Receiver after experimentation on 03/10/2022

Given the large volume of experiments, the possibility of using a compressor was investigated and two trial runs were conducted. However, comparing the results when using pressurised air supplied by compressor and cylinder showed significant differences. The control parameters of mass flow rate, receiver inlet pressure and radiation fluxes were kept the same at 2 g $s^{-1}$, 4 bar and 200-500 kW $m^{-2}$ respectively.

From Figure 79 and Figure 80, it can be seen that the efficiency of the receiver using the compressor's air is higher. This can be attributed to the presence of water vapour in the air, besides argon, which only improves the heat capacitance of the air mixture. The receiver inlet temperature is also higher in the case of the compressor as the compressor slightly heats up the ambient air whereas the air from the cylinder is cooled below ambient by the expansion/throttling action of the cylinder and regulator valve. The increased inlet temperature reduces the fluid density and increases the velocity of the fluid. As discussed in chapter 2, this serves to increase the pressure drop and improve the heat transfer to the fluid.

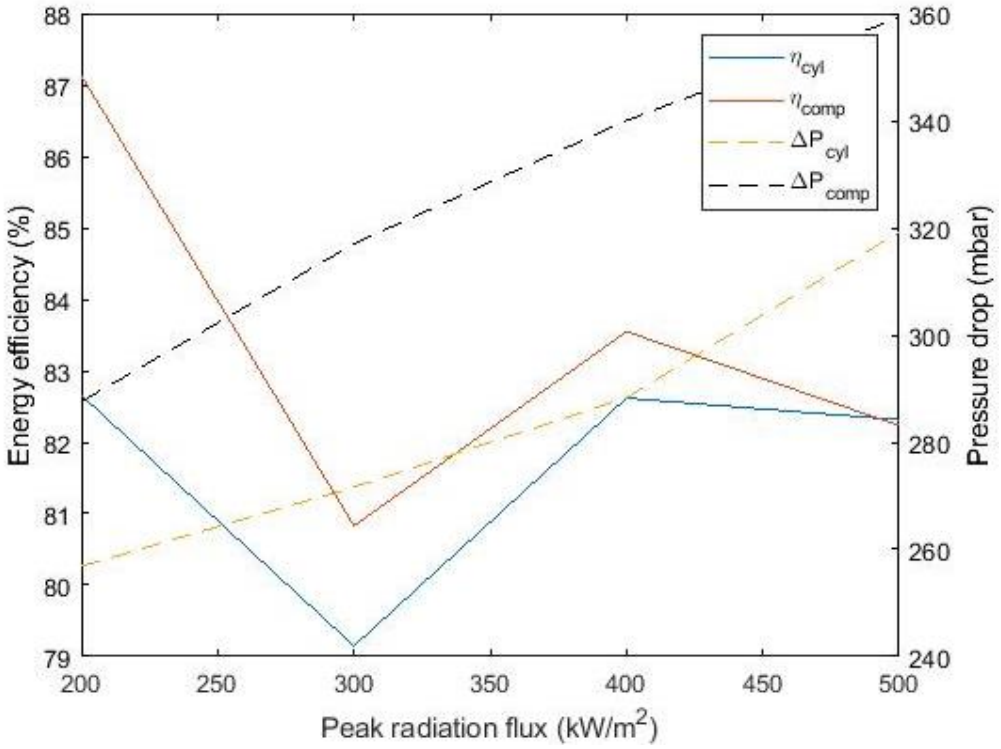


Figure 79. Energy efficiency and pressure drop as functions of peak radiation flux for experiment runs with cylinder and compressor supplied pressurised air

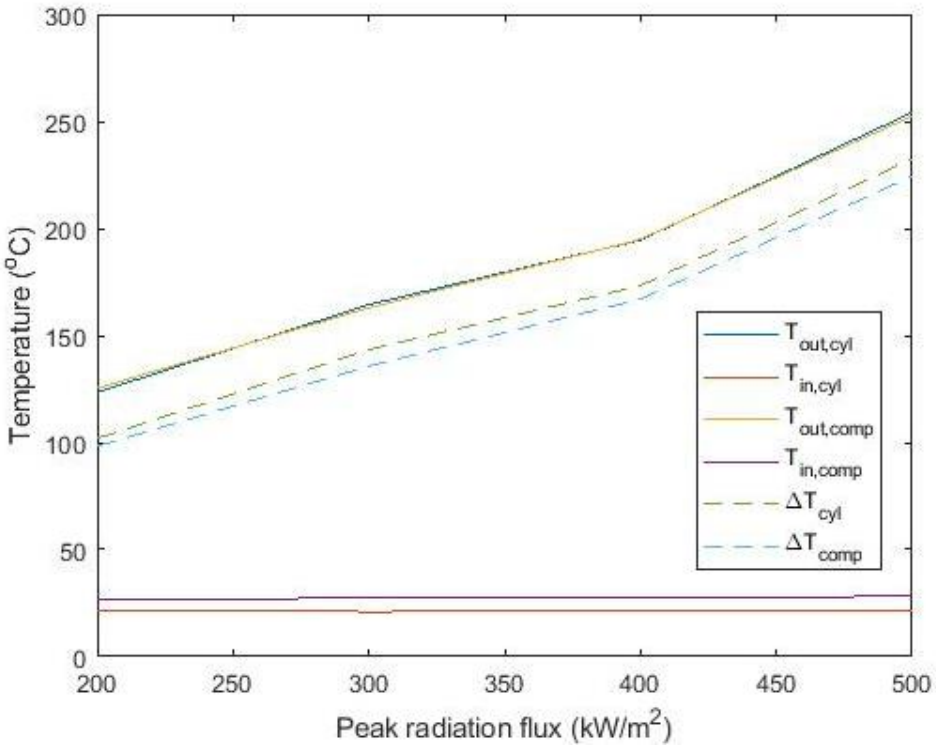


Figure 80. Air temperatures at receiver inlet and outlet as functions of peak radiation flux for experiment runs with cylinder and compressor supplied pressurised air

While the improved performance observed when using the compressor is desirable, the variability in composition on the HTF (depending on the humidity of the day), air temperature and potential of internal oxidation in the receiver channels (due to the presence of water) creates too much uncertainty in the analysis of the

performance of the receiver and it was hence decided to discontinue the use of the compressor and conduct the experimental campaign using only the dry pressurised air from the cylinders. These have a fixed composition of 79% $N_2$ and 21% $O_2$.

It should here be noted that the inlet temperature when using the cylinders is also not a constant for all experiments and varies depending on the ambient temperature and humidity. On days when the dew point temperature is high enough, there is sufficient heating from condensation on the inlet line that the receiver air inlet temperature matches the ambient (dry bulb) temperature.

Figure 81. Condensation on the pressurised air inlet line when its temperature is below the dew point temperature. This causes a rise in the receiver inlet air temperature.

Table 15. Preliminary experiment log

| Date | Status of Testbed (Changes to previous) | Experiment Plan | Result/Comment |
|---|---|---|---|
| 29/07/2022 | All instrumentation in place besides TCs<br>Testbed loop closed (complete) but without receiver and only piping in its place<br>Basic LabVIEW setup to read pressures and flowrates | **Overall objective:** Cold pressure test of the testbed to characterise its behaviour<br>**Specific objectives:** Eliminate any leaks and determine:-<br>Inlet pressure to crack anti-return valve<br>Receiver inlet to outlet pressures when static (no flow) and across range of flowmeter (0-2 g $s^{-1}$) at receiver inlet pressures of 5, 10 and 15 bar | Cracking pressure = 12 bar<br>Testing for leakage:<br>At 3 bar, negligible flow (0 g $s^{-1}$)<br>At 5 bar, negligible flow (0.02 g $s^{-1}$)<br><br>It appears that the cracking pressure depends on the tightening of the relief valve. If further strung, cracking pressure of relief valve increases.<br><br>At 10 bar some leaks appeared indicating the need for teflon at TC unions |
| 1/8/2022 | TC unions have been changed with additional Teflon. Outlet TC union had to be completely replaced as it couldn't be removed to add Teflon.<br><br>Experiment 2:<br><br>After leak detection in one of the TCs (the one that was replaced) it was removed and more teflon added | Same as previous | Static pressure test: With the flow control valve closed, the flow rate slowly decreases to zero and the system pressure rises<br><br>Small leak appears to be coming from the same TC that was replaced<br><br>----Experiment 2 ----<br><br>Flowrate of 0.008 g $s^{-1}$ at almost 10 bar<br>Flowrate of 0.01 g $s^{-1}$ at 14.6 bar<br><br>Opening the flow control valve: First sharp decrease before stabilisation of the pressure and flowrate<br><br>The pressure and flowrate take an extremely long time to stabilise. After an hour the stabilisation did not happen. |
| 3/8/2022 | Receiver added (PR1) after removing pipe that was in place to close the circuit before the receiver. A small pipe has been added to cover the remaining horizontal length as the receiver isn't long enough | **Overall objective:** Cold pressure test of the testbed with receiver to characterise its behaviour<br>**Specific objectives:** Eliminate any leaks and determine:-<br>Receiver inlet to outlet pressures when static (no flow) and across range of flowmeter (0-2 g $s^{-1}$) at receiver inlet pressures of 5, 10 and 15 bar | Leak test at around 5 bar and 8.5 bar<br><br>The system was left for 1 hour and finally stabilised at 8.5 bar with 0.008 g $s^{-1}$ flow and 28 bar cylinder pressure<br><br>Increasing the cylinder pressure to 30 bar |
| 4/8/2022 | Receiver position changed slightly to left given table movement limitation | **Overall objective:** Check dynamic pressure stability and time to stabilisation<br>**Specific objectives:** First leak test and then a dynamic pressure test at 0.75-1 g $s^{-1}$ flow and 5 bar | Leak test seems to be ok. Flow rate at 0.01 g $s^{-1}$ at 10 bar. Pressure stabilised at 9.5 bar after 20 mins approximately.<br><br>It seems the only way to have some stability of flow and pressure is to first open the flow control valve at the outlet and then vary the inlet cylinder |

| | | | |
|---|---|---|---|
| | | | valve. Starting at an unpressurised system and then pressurising it is more stable than changing the pressure of a pressurised system. |
| 11/8/2022 | Receiver set up with instrumentation installed | **Preliminary hot test:** Check how much time it takes to stabilisation besides instrumentation functioning | Mass flow of 2 g $s^{-1}$, 4 bar and 200 kW $m^{-2}$ peak flux<br>Cylinder pressure of 24 bar permits this.<br><br>Experiment run not performed due to time restrictions |
| 12/8/2022 | No change | Same as previous | Spillage of water observed overnight likely due to the suction of water in the cooling water tubes<br><br>Test conditions same as yesterday<br>Small chiller seems to be incapable of cooling water tank quickly<br><br>Chiller leak seen again and the issue is attributed to the chiller not being able to work in an open loop. A short metal pipe has been added to close the loop and transfer heat indirectly from the water tank.<br>Test carried out successfully. Only issue was that the cylinder was nearly empty at the start of the experiment and so it had to be stopped as the mass flow rate was falling |
| 22/9/2022 | Testbed and instrumentation completely set up<br>Heat exchanger (reflector) with serpentine internal tubing and flat conductive surface used for cooling exchange surface in tank | SS PR1, 4 bar, 2 g $s^{-1}$, 200-500 kW $m^{-2}$ | Experiment carried out successfully.<br>More insulation to be added for radiation shielding<br>Lamp pointing incorrect<br>Flow rate continuously rises during experiment. Has to be carefully manually reduced from main cylinder valve |
| 3/10/2022 | Insulation added to receiver<br>Exact distance between gardon centre and receiver centre calculated | SS PR1, 4 bar, 2 g $s^{-1}$, 200-500 kW $m^{-2}$ | Experiment went perfect<br>15 mins for receiver thermal equilibirum |
| 6/10/2022 | Air supply from building | SS PR1, 4 bar, 2 g $s^{-1}$, 200-500 kW $m^{-2}$ | Experiment ok |
| 7/10/2022 | Air supply from building | SS PR1, 4 bar, 1.5 g $s^{-1}$, 200-500 kW $m^{-2}$ | Experiment ok |

# 3.7. Procedures developed for a typical experiment run

## 3.7.1. Radiation flux map generation

The equipment required to generate the radiation flux profile are:

a) Gardon flux meter connected to a water chiller and data acquisition device
b) Target plate (alumina plate)
c) CCD camera with neutral density filter
d) Image processing software such as MATLAB or Python

Precautions to be followed:

a) Before switch on lamp(s) ensure that:
   - Water in the chiller is above minimum required mark
   - Water chiller to the gardon is on and has no leakages
   - There are no obstructions (wires, tubing, tools) to the movable table's free motion
   - Blower(s) of the lamp(s) to be operated is/are on
   - Radiation shield protects any sensitive equipment
   - CCD camera filter is in place
   - CCD camera exposure time setting is below (5000 us) and set to 'Manual' adjustment
   - Data acquisition software and cameras are functional
   - Switch the air extractor on (recommended but not mandatory)
b) After lamp(s) are switched on regularly check:
   - Temperature of water from chiller is not rising and within limits
   - No smoke is being evolved or burning detected

   Immediately switch off lamp(s) if issues related to any of these are detected

To generate a flux map, experimental data is required namely:

a) Peak radiation flux on measurement plane (measured by gardon)
b) CCD camera image of lamp(s) on target plane
c) CCD camera image with no lamp switched on and at same exposure time setting of camera as was used when previous image was recorded

The procedure used to acquire this information is given in Figure 82 and the steps needed to process the data to obtain the flux maps are elaborated in Figure 83.

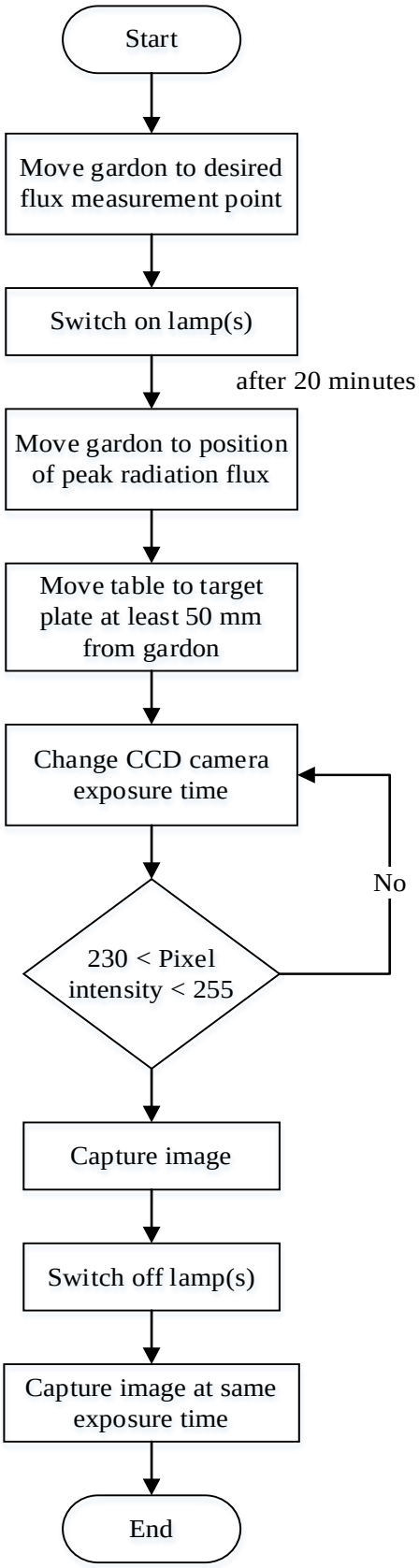


Figure 82. Procedure for experimental data acquisition for flux map generation

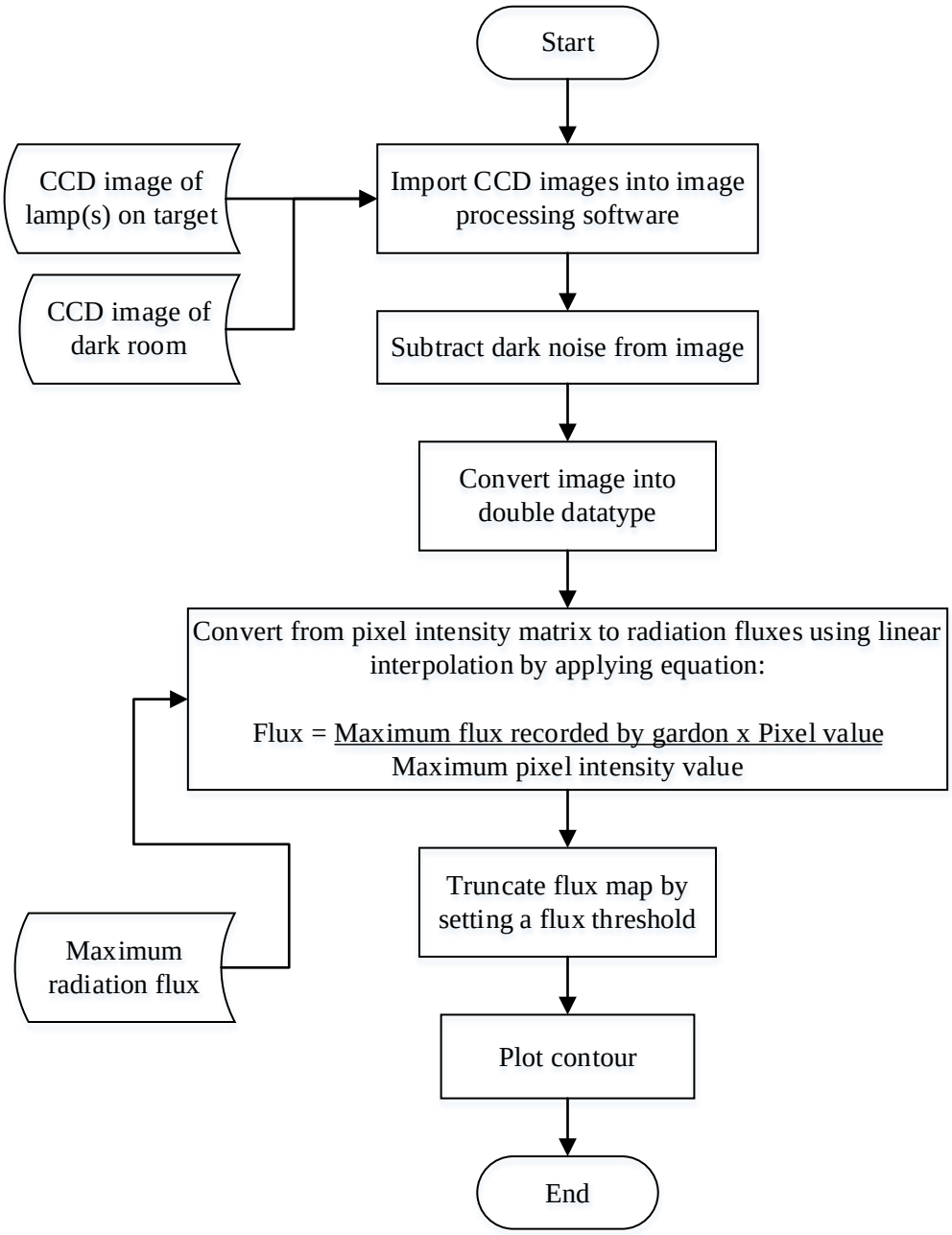


Figure 83. Data processing steps to generate radiation flux map from experimental data

### 3.7.2. Installing a new pressurised receiver/absorber (cold test)

Before a new pressurised receiver is installed there are some precautions and procedures to be followed. The precautions are:

a) Ensure the line (system) is depressurised before any changes to the testbed are made. This is done by first closing the main cylinder valve which can be identified in Figure 84a and then opening the exhaust valve shown in Figure 84b. Check if there is some pressure in the line upstream of the receiver using the LabVIEW program. If this is the case, proceed by slowly loosening the compression nut connecting the installed receiver (or piping) at either the inlet (right) or outlet (left) as indicated in Figure 85. As the nut is loosened, a hissing sound indicates that pressurised air is escaping and the line is depressurising. Continue gradually loosening the nut until it is fully removed.

Figure 84a

Figure 84b

Figure 84. Cylinder valve and Exhaust (needle) valve

b) If a receiver is being removed and replaced, ensure that it is not hot by monitoring relevant thermocouple readings in LabVIEW. The piping and surrounding insulation around the receiver may also be hot if an experiment was recently performed.

c) Inspect the entire system for open connections and fittings.

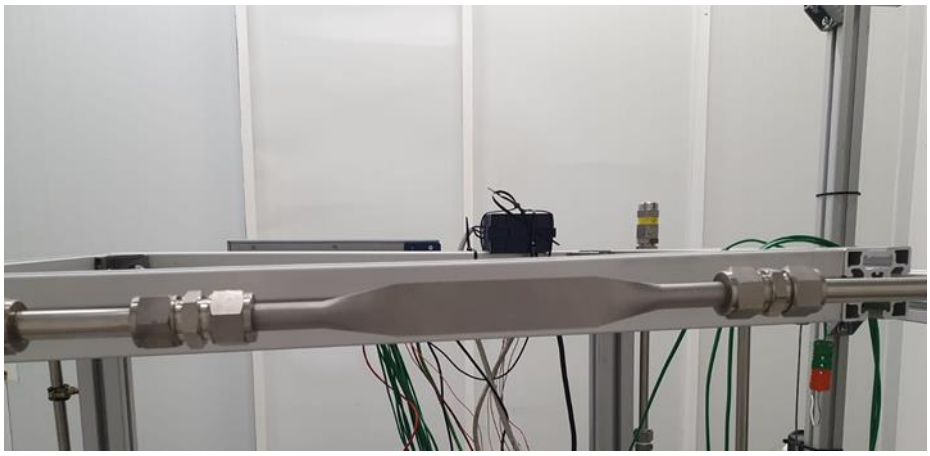

Figure 85. Compression nuts at inlet (right) and outlet (right) attaching absorber to the system piping

After installing the receiver, a static pressure test under cold conditions (without HFSS operation) must be performed to ensure there are no leakages due to incorrect installation of the receiver, defects in the receiver itself or a leakage from some other point in the system. The procedure for carrying out such a static test is presented in Figure 86.

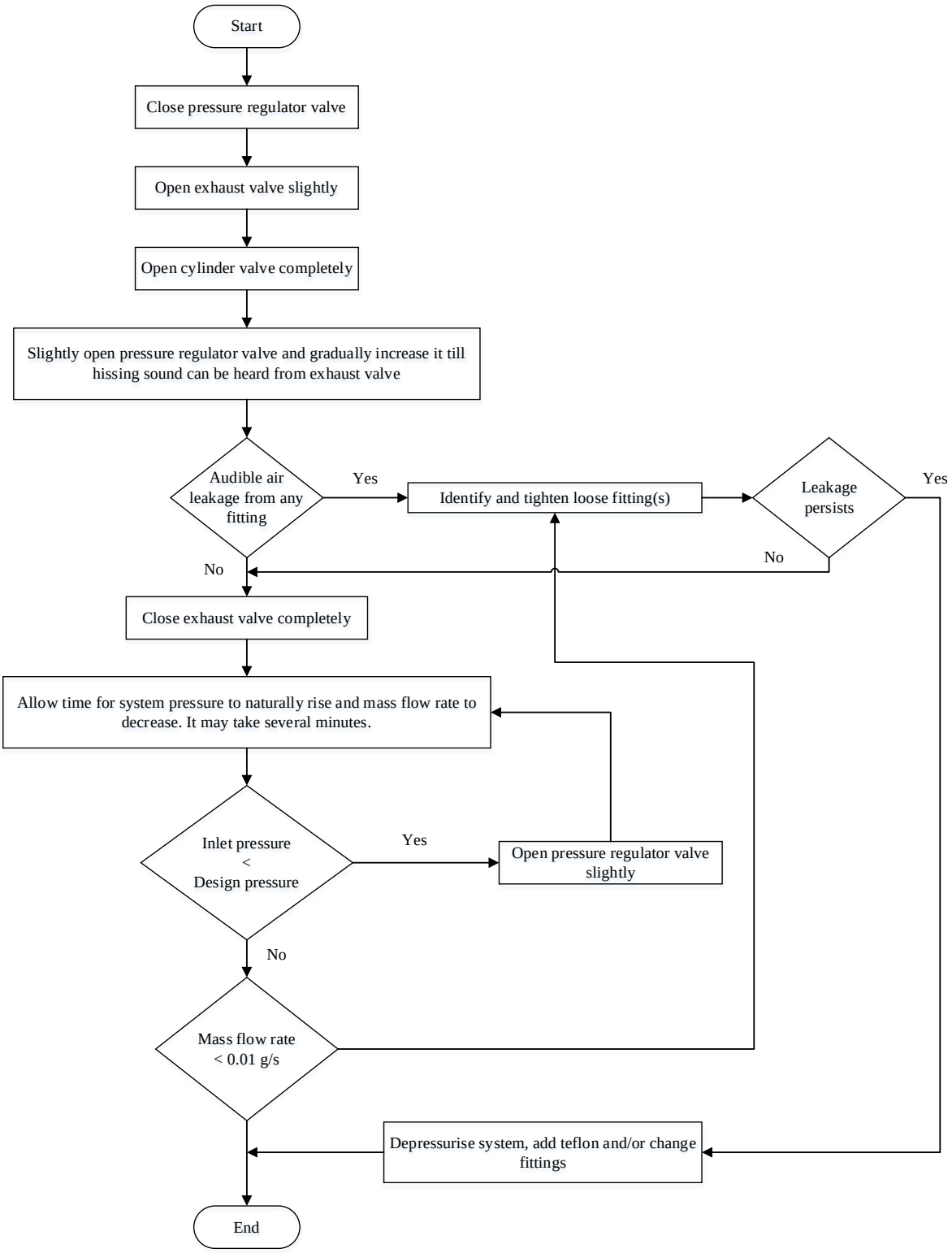


Figure 86. Procedure for conducting a cold pressure test

### 3.7.3. General operating procedure for pressurised receiver testbed

Conducting a 'hot test' or an experiment run using the KIRAN 42 HFSS carries with it several risks including blinding, burning and explosive. Hence the safety and normal operating procedures laid out here must be strictly adhered to.

Precautions to be followed:

a) Before switch on lamp(s) ensure that:
   - The receiver has been installed correctly and a cold static test, in accordance with the procedure in section 3.7.2) has been performed to pressure test the system and fix any leakages therein
   - There is sufficient pressure in the pressurised air cylinder
   - Water in the chillers are above minimum required mark
   - Water chiller to the gardon is switched on and has no leakages
   - Water chiller to the cold water tank is switched on and has no leakages
   - There are no obstructions (wires, tubing, tools) to the movable table's free motion
   - Blower(s) of the lamp(s) to be operated is/are on
   - Radiation shield protects any sensitive equipment
   - CCD camera filter is in place
   - CCD camera exposure time setting is below (5000 us) and set to 'Manual' adjustment
   - Data acquisition software and cameras are functional
   - Switch the air extractor on (recommended but not mandatory)

b) After lamp(s) are switched on regularly check:
   - Temperature of water from chiller is not rising and within limits
   - No smoke is being evolved or burning detected
   - There are no water leaks
   - The pressure in the cylinder is above 30 bar and the mass flow rate is not continuously falling

   Immediately switch off lamp(s) if issues related to any of these are detected

In addition to these precautions, there are important preliminary preparatory tasks to be accomplished before an experiment can be started. These tasks are:

a) Ascertain the experiment plan in terms of desired values and combinations of inlet pressure, mass flow rate and peak radiation flux
b) Manipulate the cylinder and exhaust valves to obtain the desired combination of mass flow rate and inlet pressure. In the current experiment setup, it is not possible to automatically control or change these and requires entry into the testbed room to make the adjustments to the exhaust valve manually. This can only be done when the lamps are off and cannot be changed during an experiment run.
c) Measure the distance between the gardon centre and the absorber centre (or wherever on the absorber the peak flux is to be) in all three axes.
d) Perform radiation flux tests with the lamp(s) required to determine the gardon positions for the desired radiation flux values on absorber. Using the previous measurements, the table positions required for the absorber sample to be in the desired radiation flux position can be calculated and determined before a 'hot test' of the absorber. This saves time and potential damage to the absorber.

After these preparatory steps have been undertaken, the experiment procedure shown in Figure 87 must be followed for any experiment run adhering constantly to the precautions listed above.

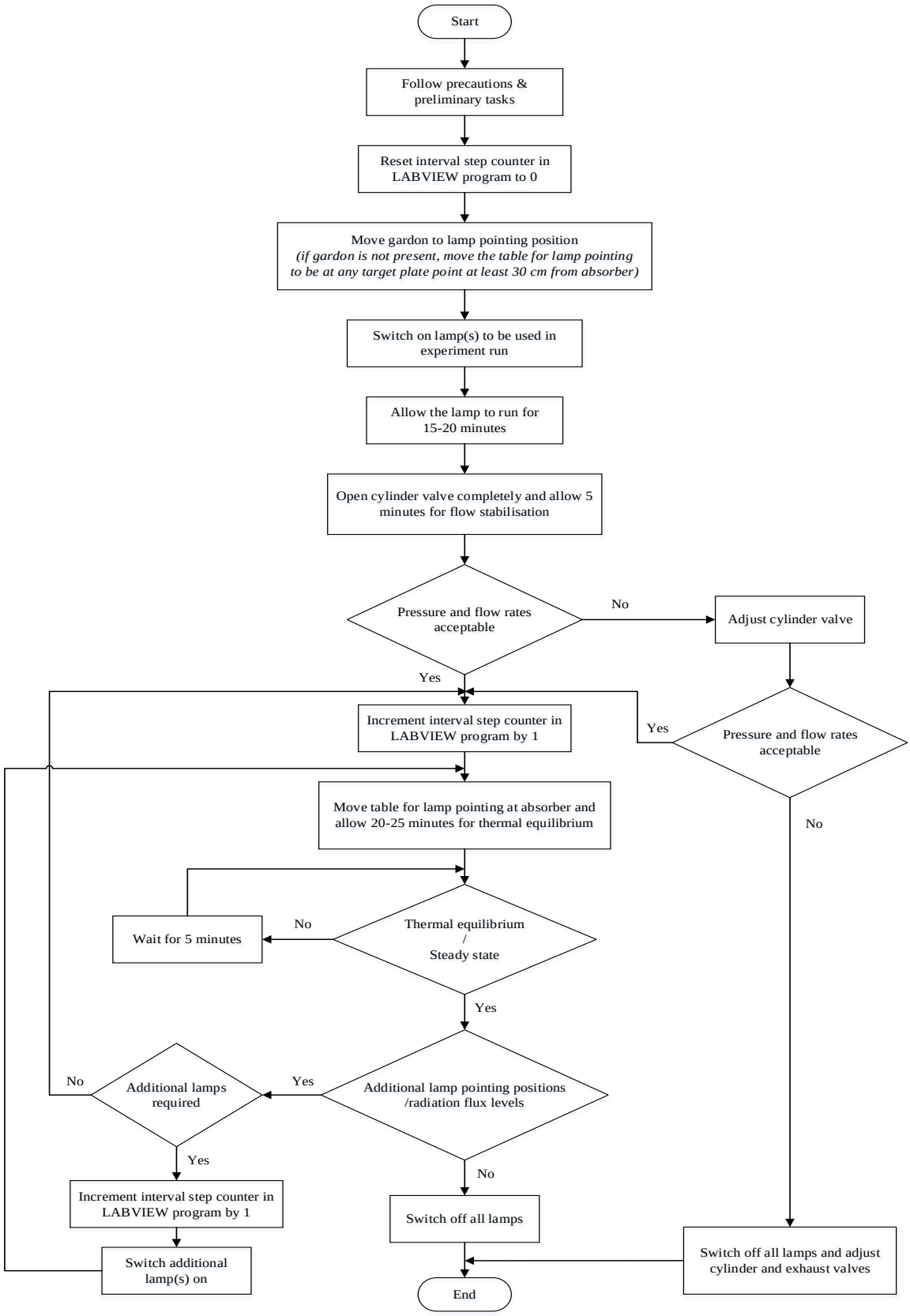


Figure 87. Experiment procedure for normal experiment run on pressurised receiver testbed.

## 3.8. Design of experiments

The operational limits of the pressurised receiver testbed have been discussed in section 3.3 and were set by some equipment capacities and design considerations. In the experiment campaign, three operating parameters have been selected to be varied in order to perform a parametric study and experimental characterisation of each of the receivers manufactured. These parameters are the peak incident flux, the mass flow rate and the receiver inlet pressure which are proposed to be controlled at the levels/points given in Table 16.

Table 16. Parametric study of three identified operating control parameters

| **Parameter** | **Unit** | **Limits** | **Proposed Datapoints** |
|---|---|---|---|
| Peak Incident flux | kW $m^{-2}$ | 200 – 2000 | 200 – 300 – 400 – 500 |
| Mass flow rate | g $s^{-1}$ | 1 – 2 | 1 – 1.50 – 2 |
| Inlet Pressure | bar | 3 – 15 | 4 – 12 |

It was initially proposed to also operate at 8 bar but this operating inlet pressure point had to be scrapped due to time constraints. The order of experimental runs proposed for each receiver to be tested is presented in Table 17.

Table 17. Experiment runs proposed for each receiver

| **Experiment Run** | **Flowrate (g $s^{-1}$)** | **Inlet Pressure (bar)** | **Incident Flux (kW $m^{-2}$)** |
|---|---|---|---|
| 1-4 | 2 | 4 | 200 – 300 – 400 - 500 |
| 5-8 | 1.5 | 4 | 200 – 300 – 400 - 500 |
| 9-12 | 1 | 4 | 200 – 300 – 400 - 500 |
| 13-16 | 2 | 12 | 200 – 300 – 400 - 500 |
| 17-20 | 1.5 | 12 | 200 – 300 – 400 - 500 |
| 21-24 | 1 | 12 | 200 – 300 – 400 - 500 |

Hence a total of 24 experiments are proposed for each receiver. The incident radiation flux profiles/maps at each of the levels proposed in Table 16 are illustrated in Figure 88 with further information about each radiation flux distribution given in Table 18. Following the procedures and guidelines elaborated in section 3.7, the experimental campaign may commence.

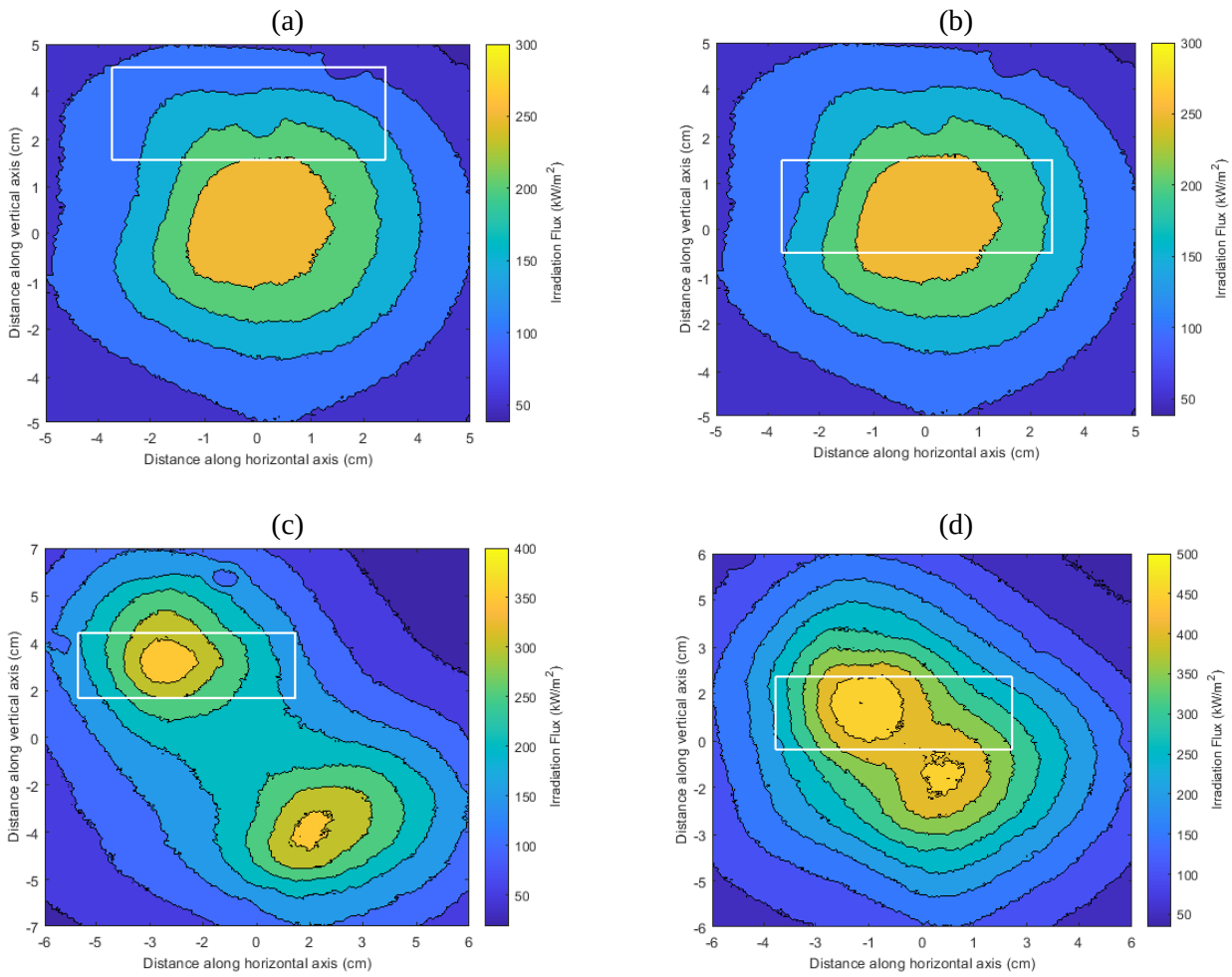


Figure 88. Incident radiation profile/map at different peak flux levels used in experimental campaign: (a) 200 kW m$^{-2}$, (b) 300 kW m$^{-2}$, (c) 400 kW m$^{-2}$, (d) 500 kW m$^{-2}$. The white rectangle represents the incident exposed surface of the receiver

Table 18. Incident radiation properties at the 4 peak flux levels used in the experiment campaign

| **Peak radiation flux (kW m$^{-2}$)** | **Mean radiation flux (kW m$^{-2}$)** | **Standard deviation (%)** | **Radiation on absorber (W)** |
|---|---|---|---|
| 200 | 161.8 | 6.8 | 252.9 |
| 300 | 232.5 | 1.4 | 370.3 |
| 400 | 273.0 | 2.1 | 434.9 |
| 500 | 388.4 | 2.9 | 611.5 |

## 3.9. Conclusions

In this chapter, the development of the pressurised receiver experimental testbed has been laid out. The design of the testbed required a careful analysis of the KIRAN 42 high flux solar simulator and its capacities. The receiver testbed was developed for the experimental characterisation of receivers under varying conditions of mass flow rate, inlet pressure and incident radiation flux/power though there are some additional operating conditions that could be varied such as the inlet temperature and gas composition. An overriding objective to the testbed's development was to inculcate flexibility in operation to permit for different operational parameter variations to wider ranges.

The pressurised receivers, which are the subjects of the proposed experiments, have also been designed in such as way so as to affirm the findings of the numerical model's analysis. Receivers with different channel height, breath and wall thickness have been designed.

After the assembly of the testbed and installation of a fabricated receiver, preliminary test runs were performed in cold and hot conditions i.e. without and with the application of the solar simulator. The learnings from these preliminary experiments shed light on the shortcomings of the testbed which were subsequently addressed. They also led to the operational experience required in order to draft operational procedures for the running of the experiments and their analysis.

Finally, the design of the experiments and the planned experimental characterisation by means of identifying key operational parameters and their operational values was elucidated.

# Chapter 4. Experimental campaign

# 4.1. Introduction

In this chapter, the results of the experimental work along with its analysis and dissection will be laid out. Following the preparation for the experiments and the experiment design that was described in chapter 3, the experiments have been performed and analysed. To facilitate comparison of the experimental results with the numerical model of the pressurised receiver that was developed in chapter 2, some modifications to the numerical model were necessitated and these alterations to the model are discussed in section 4.2.

The experimental results and analysis of the four receivers tested are presented in section 4.3 with each of its subsections dedicated to each of the receivers. After each of these receivers' performances are examined, a comparative analysis of the four receivers is performed to contrast the performance of the different geometries, across different control parameters, with one another. The experimental log of the entire campaign can be found in the appendix along with plots of each receiver's pressure leak test and photos of the receivers after each experiment run.

A sensitivity analysis is also conducted in section 4.4 to quantify the effect of key parameters such as the mass flow rate, incident radiation flux, inlet pressure, composition of air and receiver absorptance on the performance of the receivers. Over the course of the experiment campaign, as well as from the previous preliminary test runs, it was observed that these parameters had a profound impact on the performance which was the main motivation of this analysis.

The conclusions of the chapter are presented in the final section 4.5 before the appendix.

# 4.2. Modifications to numerical model for better comparison to experiments

The numerical model presented in section 2.3 cannot directly be used when contrasting its predictions with the receivers and experimental work proposed in sections 3.5 and 3.8 respectively as there are several natural phenomena that affect the results of the experiments that are otherwise not featured in the numerical model. The lack of inclusion of these real world phenomena may significantly alter the predictions made by the model and result in excessive deviation from the experimental findings. Hence modifications to the numerical model have been made in order to input these factors and better the applicability of the model.

Chief among these experimental realities that must be inculcated into the model are: (i) irradiance distribution; (ii) roughness of flow channel walls; (iii) receiver absorptivity; and (iv) additional pressure drops

In addition to these, the model was also modified to directly read the real experiment data from the measurement instrumentation (section 3.3.2) which includes input parameters such as the receiver inlet pressure and temperature, ambient temperature and mass flow rate.

## 4.2.1. Incident radiation flux distribution

The numerical model previously assumed a uniform incident radiation flux distribution across the receiver which may be a valid simplifying assumption in a numerical analysis but is not the case in this experimental campaign using the KIRAN 42 HFSS (described in section 3.2.2) as a light source without a radiation homogeniser. As the numerical model divides the receiver into heat collector elements (HCEs) along the flow direction/receiver length, the model was slightly modified to allow for the input of different incident radiation power for each HCE. The incident radiation flux on the receiver, obtained by the procedure elaborated in section 3.7.1, has been integrated along the receiver breadth for each HCE (i.e. pixel along the receiver breadth in the flux map image) to determine the incident radiation on each HCE. The number of HCEs depends on the pixel matrix

that comprises the flux map image and more specifically the number of pixels in the direction along the receiver length. As the number of HCEs is a controllable input in the model, the incident radiation per HCE obtained from the flux map processing can be easily fed into the receiver model. The processing of the flux maps into incident radiation distributions along the receiver length is shown in Figure 89.

### 4.2.2. Roughness of flow channel walls

The inherent flexibility of the numerical model facilitates the use of whichever empirical or semi-empirical correlation best suits the situation at hand. In the case of the experimental receivers, it was clear from the off that the 'smooth channel' assumption employed earlier would not be suitable as surface roughness and imperfections due to additive manufacturing is a well-documented phenomenon [149], [150]. Previous studies on the roughness of AISI 326L steel pieces produced by 3D printing reported roughness values (Ra) of around 15 um [151], [152].

The addition of channel wall roughness to the model increases the pressure drop of the HTF due to increased friction with the channel but this increased friction and turbulence also results in better heat transfer to the HTF [99]. New correlations for the pressure drop and heat transfer modelling must be implemented in the numerical model to account for the surface roughness.

The pressure drop correlation used is the Nikuradse equation [153] which is given in equation (24);

$$\frac{1}{\sqrt{f_D}} = 3.48 - 1.737 \log\left(\frac{\varepsilon}{r_h}\right) , \tag{24}$$

Where $\varepsilon$ is the surface roughness value (Ra) and $r_h$ is the hydraulic radius.

The heat transfer correlation used is the Martinelli equation [154] which is expressed in equation (25);

$$Nu = \frac{Re\ Pr\ \sqrt{f_F/2}}{5\left[Pr + \log(1 + 5\ Pr) + 0.5 \log\left(\frac{Re\ \sqrt{\frac{f_F}{2}}}{60}\right)\right]} , \tag{25}$$

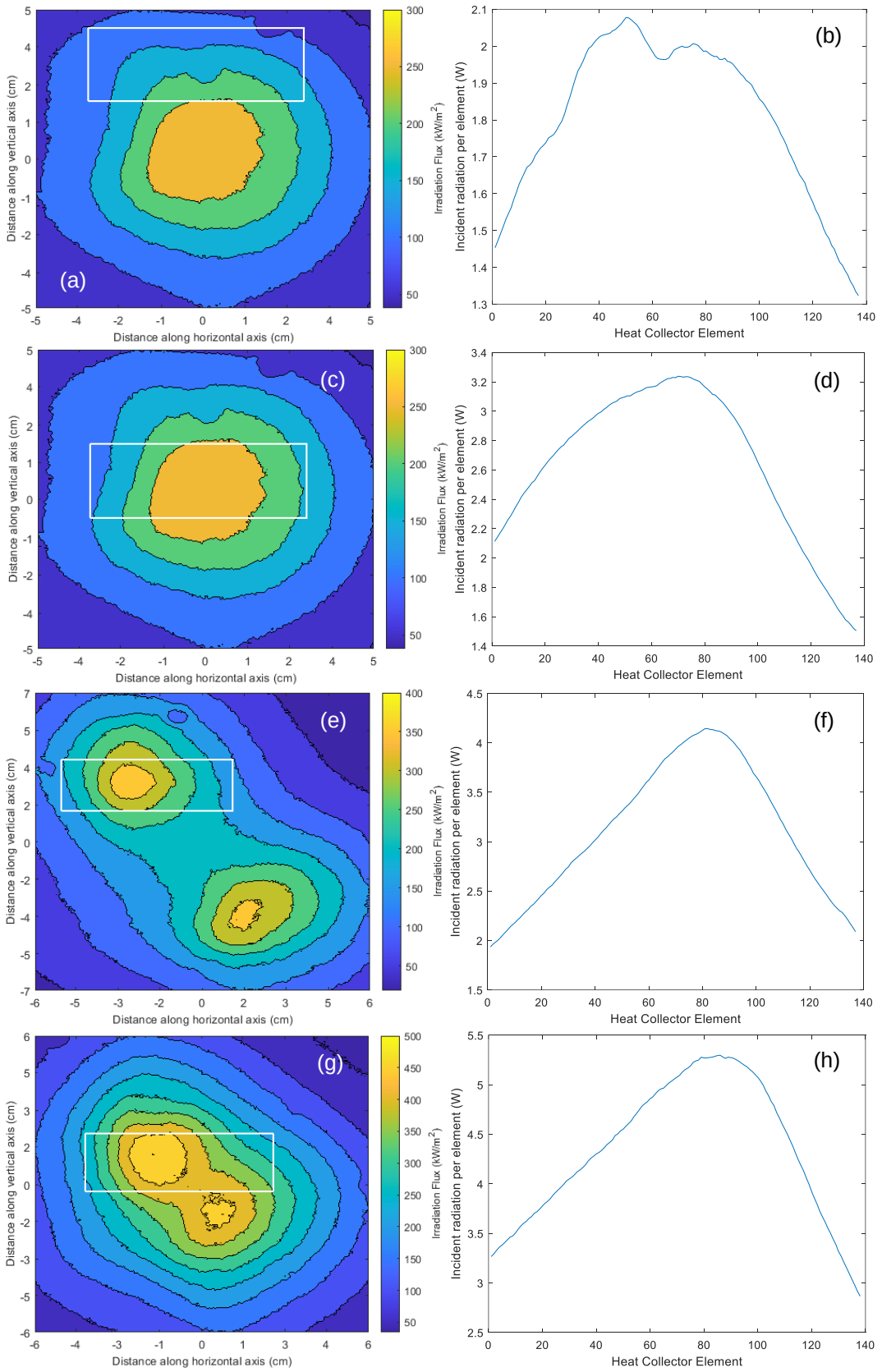


Figure 89. Irradiance map processing to determine incident radiation on each HCE for the different peak flux levels used in the experimental campaign. Images on left show the flux map with receiver marked in white rectangle and images on right show incident radiation per HCE from receiver inlet to outlet. (a, b) 200 kW m$^{-2}$, (c, d) 300 kW m$^{-2}$; (e, f) 400 kW m$^{-2}$; and (g, h) 500 kW m$^{-2}$

### 4.2.3. Receiver absorptivity

The receivers used in the experiments were of unoxidised and otherwise untreated stainless steel (AISI 316L). As was observed during the preliminary hot tests (section 3.6.2), at elevated temperatures an oxide layer develops which drastically alters its absorptivity. To quantify this, spectroscopy measurements were conducted thrice on the inlet, central and outlet sections of the receiver after the conclusion of the experiments. The result of such a measurement on an unoxidised receiver sample, tested as received from the supplier i.e. before any high temperature experiment had been performed on it, can be seen in Figure 90.

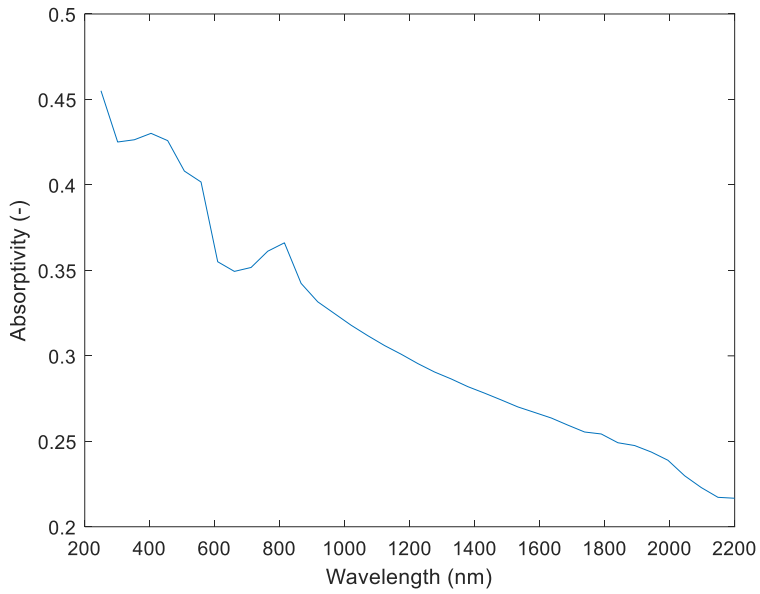


Figure 90. Absorptivity of unoxidised receiver sample as received from supplier.

Combining the absorptivity measurements with the xenon arc lamp emission spectrum, shown in Figure 91(a), results in the absorbed radiation profile plotted in Figure 91(b). The term absorptance, henceforth, refers to the weighted Xe arc spectrum absorptance. Three repetitions of spectroscopy tests were performed resulting in three absorptance values the average of which is chosen as the final value. The results of these tests are given in Table 19.

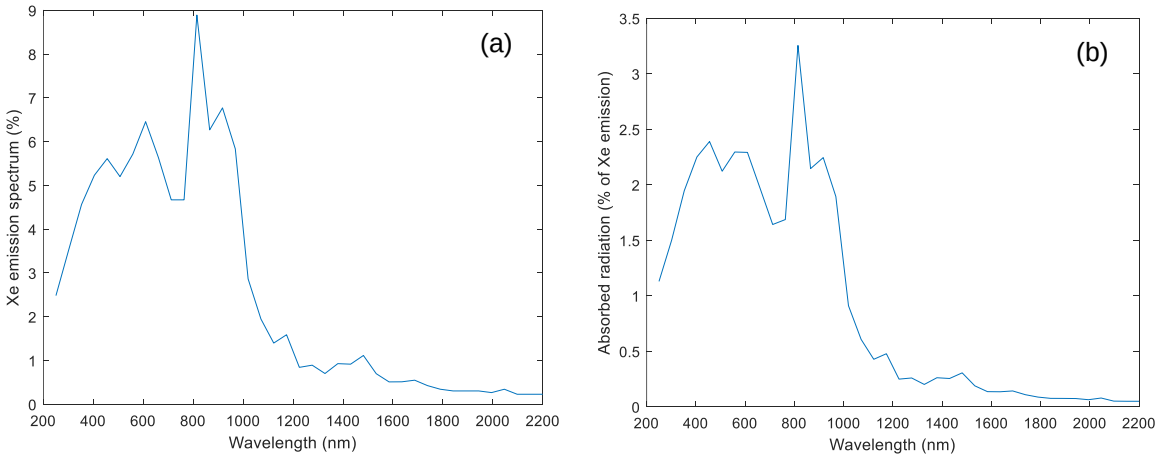


Figure 91. Absorbed radiation analysis: (a) Xenon lamp emission spectrum; (b) Absorbed radiation by receiver

Table 19. Absorptance of unoxidised receiver.

| Test | Absorptance (-) |
|---|---|
| #1 | 0.3604 |
| #2 | 0.3470 |
| #3 | 0.3532 |
| Average absorptance | 0.3536 |
| Standard deviation | 0.0067 |

### 4.2.4. Additional pressure drops

Referring to the pressurised receiver testbed layout in Figure 58, there are additional sources of loss of pressure in the system, in addition to the receiver itself, from the inlet pressure sensor to the outlet pressure sensor. These are the pipe sections and sudden contraction and expansion zones at the receiver inlet and outlet respectively which can be estimated [155] by equation (26):

$$\Delta p = \Delta p_{pipe} + \Delta p_c + \Delta p_e \ = \frac{1}{2}\rho\, v^2 \left( f_D \, \frac{L_{pipe}}{D_{h_{pipe}}} + K_c + K_e \right), \tag{26}$$

where $\Delta p_{pipe}$ refers to the pressure drop in the pipe section; $\Delta p_c$ and $\Delta p_e$ are the pressure drop due to contraction and expansion, respectively; $L_{pipe}$ refers to the length of the pipe section; and $K_c$ and $K_e$ are the contraction and expansion coefficients [155].

## 4.3. Experiment characterisation of receivers

The experiments, performed as designed and discussed in section 3.8, produced interesting findings that will be presented and contrasted with the numerical model in this section. Each of the four stainless steel receivers experimented upon in this study will be elucidated in a separate subsection. As all the receivers are composed of stainless steel (AISI 316L) the same value of high temperature thermal emittance is provided to numerical model based on previous research into the same [147], [148].

### 4.3.1. Pressurised receiver 1 (PR1)

The pressurised receiver 1 (PR1) before and after the experimentation can be seen in Figure 92. As is clearly evident, significant oxidation has taken place due to the high temperatures achieved at the surface which have discoloured the receiver. The progression of the oxidation on the receiver is showcased in the photos of the receiver taken after an experiment run which can be found in the appendix.

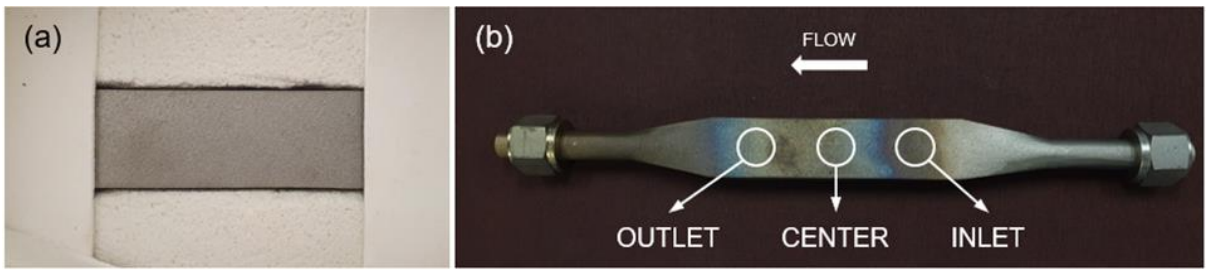


Figure 92. PR1 with inlet to right and outlet at left: (a) before experiments, (b) after experiment.

It is normally expected for the outlet section of the receiver to be more oxidised i.e. darker than the inlet section as this section will experience the higher surface temperature. However, this is not what is observed in Figure 92(b) as the oxide coating, especially near the outlet, was removed due to uneven thermal expansion of the substrate metal and the oxide layer during an experiment run with a very high heating rate. Observing Figure 131 in the appendix will clearly depict this phenomenon of oxide layer removal and scorching of the receiver. After this, subsequent experiments were conducted in such a way so as to control the rate of receiver surface temperature rise.

Before the experiments were performed, a leak test was conducted to ensure that the receiver was installed correctly. A depiction of this leak test in terms of mass flow rate and system pressure, is given in the appendix. An absorptivity test was conducted after the conclusion of the experiments on PR1 and the results of the same can be found in Table 20. The experimental characterization was performed varying the inlet control parameters as shown in Table 21. Closed circuit camera (CCD) images of the receiver taken at each peak flux level are presented in Figure 93.

Table 20. Absorptance measurements of PR1 after experiments.

| Zone | Absorptance (-) | | | |
|---|---|---|---|---|
| | Measurement #1 | Measurement #2 | Measurement #3 | Retained value |
| Inlet | 0.7185 | 0.7068 | 0.7021 | 0.744±0.018 |
| Centre | 0.7252 | 0.7174 | 0.7274 | 0.723±0.005 |
| Outlet | 0.7422 | 0.7628 | 0.7264 | 0.709±0.009 |

Table 21. Input parameters for experiments with PR1

| Design setpoints | | | Experimental parameter | |
|---|---|---|---|---|
| Peak flux (kW $m^{-2}$) | Inlet pressure (bar) | Mass flow rate (g $s^{-1}$) | Inlet pressure (bar) | Mass flow rate (g $s^{-1}$) |
| 0 | 4 | 1.0 | 4.03±0.04 | 1.019±0.005 |
| 0 | 4 | 1.5 | 4.07±0.05 | 1.478±0.011 |
| 0 | 4 | 2.0 | 3.93±0.06 | 1.928±0.019 |
| 200 | 4 | 1.0 | 3.98±0.04 | 1.006±0.007 |
| 200 | 4 | 1.5 | 4.20±0.05 | 1.506±0.017 |
| 200 | 4 | 2.0 | 4.17±0.08 | 2.02±0.04 |
| 300 | 4 | 1.0 | 3.94±0.04 | 1.000±0.006 |
| 300 | 4 | 1.5 | 4.21±0.05 | 1.504±0.014 |
| 300 | 4 | 2.0 | 4.17±0.08 | 2.01±0.04 |
| 400 | 4 | 1.0 | 3.96±0.05 | 1.001±0.016 |
| 400 | 4 | 1.5 | 4.21±0.04 | 1.504±0.014 |
| 400 | 4 | 2.0 | 4.15±0.08 | 2.00±0.04 |
| 500 | 4 | 1.0 | 4.00±0.05 | 1.007±0.009 |
| 500 | 4 | 1.5 | 4.21±0.05 | 1.502±0.017 |
| 500 | 4 | 2.0 | 4.19±0.06 | 2.006±0.034 |
| 0 | 12 | 1.0 | 11.97±0.07 | 1.004±0.005 |
| 0 | 12 | 1.5 | 11.74±0.08 | 1.505±0.011 |
| 0 | 12 | 2.0 | 12.23±0.07 | 1.94±0.02 |
| 200 | 12 | 1.0 | 12.05±0.07 | 1.006±0.007 |
| 200 | 12 | 1.5 | 11.79±0.08 | 1.504±0.014 |
| 200 | 12 | 2.0 | 12.23±0.08 | 2.00±0.03 |
| 300 | 12 | 1.0 | 12.08±0.07 | 1.008±0.006 |
| 300 | 12 | 1.5 | 11.77±0.07 | 1.502±0.013 |
| 300 | 12 | 2.0 | 12.04±0.07 | 2.00±0.02 |
| 400 | 12 | 1.0 | 11.81±0.07 | 1.005±0.006 |
| 400 | 12 | 1.5 | 11.75±0.07 | 1.500±0.013 |
| 400 | 12 | 2.0 | 11.94±0.07 | 2.01±0.02 |
| 500 | 12 | 1.0 | 11.78±0.07 | 1.003±0.006 |
| 500 | 12 | 1.5 | 11.75±0.08 | 1.495±0.018 |
| 500 | 12 | 2.0 | 12.12±0.08 | 2.01±0.02 |

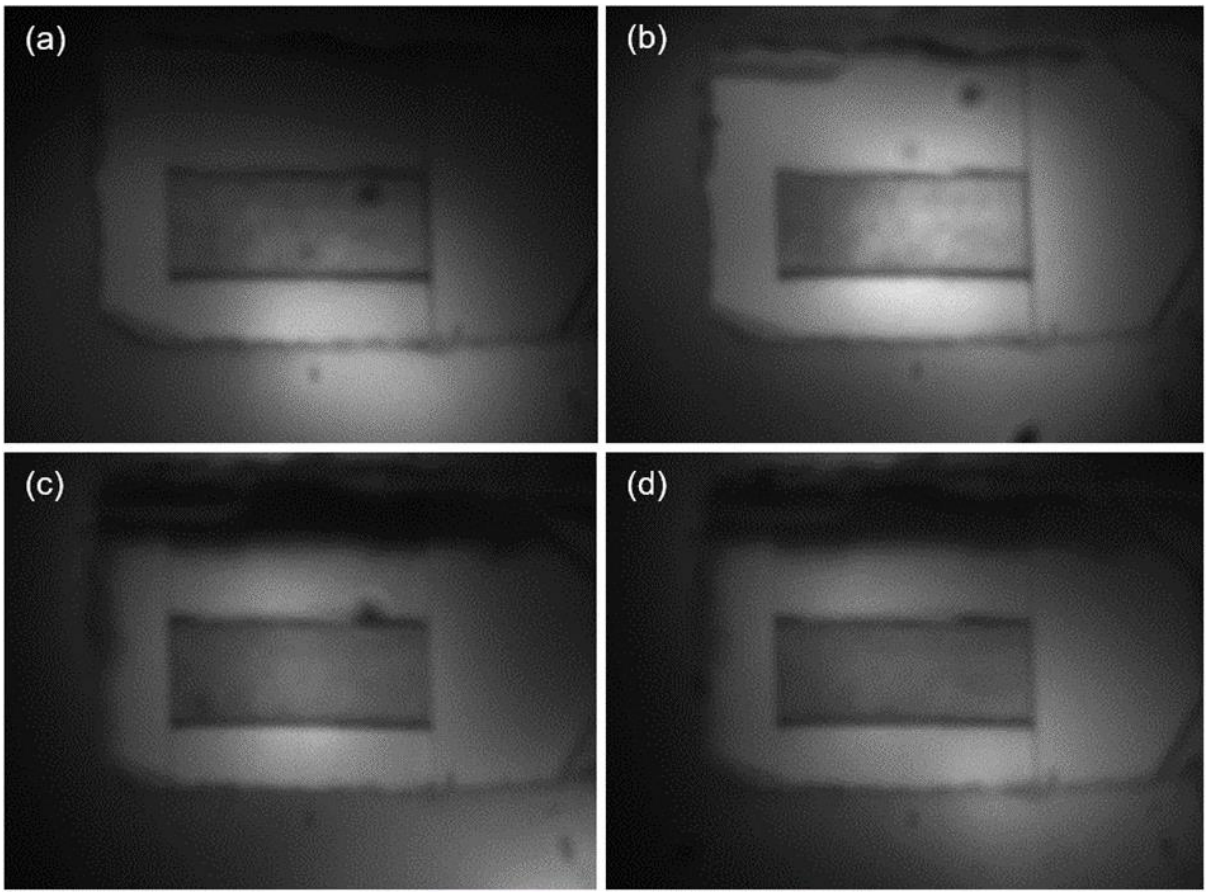


Figure 93. CCD images of PR1 during experimentation at different flux levels: (a) 200 kW $m^{-2}$, (b) 300 kW $m^{-2}$, (c) 400 kW $m^{-2}$, (d) 500 kW $m^{-2}$.

The results of the experiments, in terms of pressure drop and outlet temperature, are plotted in Figure 94. Observing Figure 94, the pressure drop rises with increasing incident radiation levels. This is because of the increase in the channel velocity with higher fluid temperatures, and hence lower densities, expected when the incident radiation level rises. Higher channel velocities cause higher pressure drops. On the other hand, at greater inlet pressure levels the pressure drop falls which can be attributed to the larger density at elevated pressures and thus the smaller channel velocity resulting in a lower pressure drop. Higher mass flow rates cause greater channel velocities, if the cross sectional flow area is constant, and this explains the increased pressure drops at higher flow rates.

The outlet temperature is expected to rise with higher incident radiation values as the heat input to the HTF is greater. The mass flow rate is indirectly related to the outlet temperature as a lower flow rate must be compensated by a higher outlet temperature, assuming that the heat transferred to the HTF is the same. Increased inlet pressures seem to slightly increase the outlet temperature as the effect of the higher density offsets the associated fall in channel flow velocity to improve the heat transfer to the fluid.

The numerical model generally seems to line up reasonably well with the experimental data. The pressure drops coincide well given that the exact value of surface roughness, which plays an important role in the pressure drop, is unknown. There are more significant deviations in the outlet temperature profiles which can be explained when the absorptance of the receiver is considered. The absorptance has a strong impact on the heat transfer to the HTF and hence its outlet temperature. While in reality the absorptance of the receiver changes continuously,

as it is unoxidised and untreated, its absorptance has only been measured once at the end of the experiments on the receiver (see Table 20) and it is this single value that has been fed to the model. This is why the outlet temperature at higher flow rates and lower fluxes (when the receiver was relatively less oxidised and had a lower absorptance) was lower than that predicted by the numerical model which used a higher absorptance.

There is also a divergence of the numerical model's outlet temperature from the experimental one at higher fluxes which may have to do with imperfections in the insulation of the receiver allowing for increased exposure (especially of the top surface) to incident radiation. This effect is particularly enhanced when two lamps, one from above as discussed in section 3.8, are used.

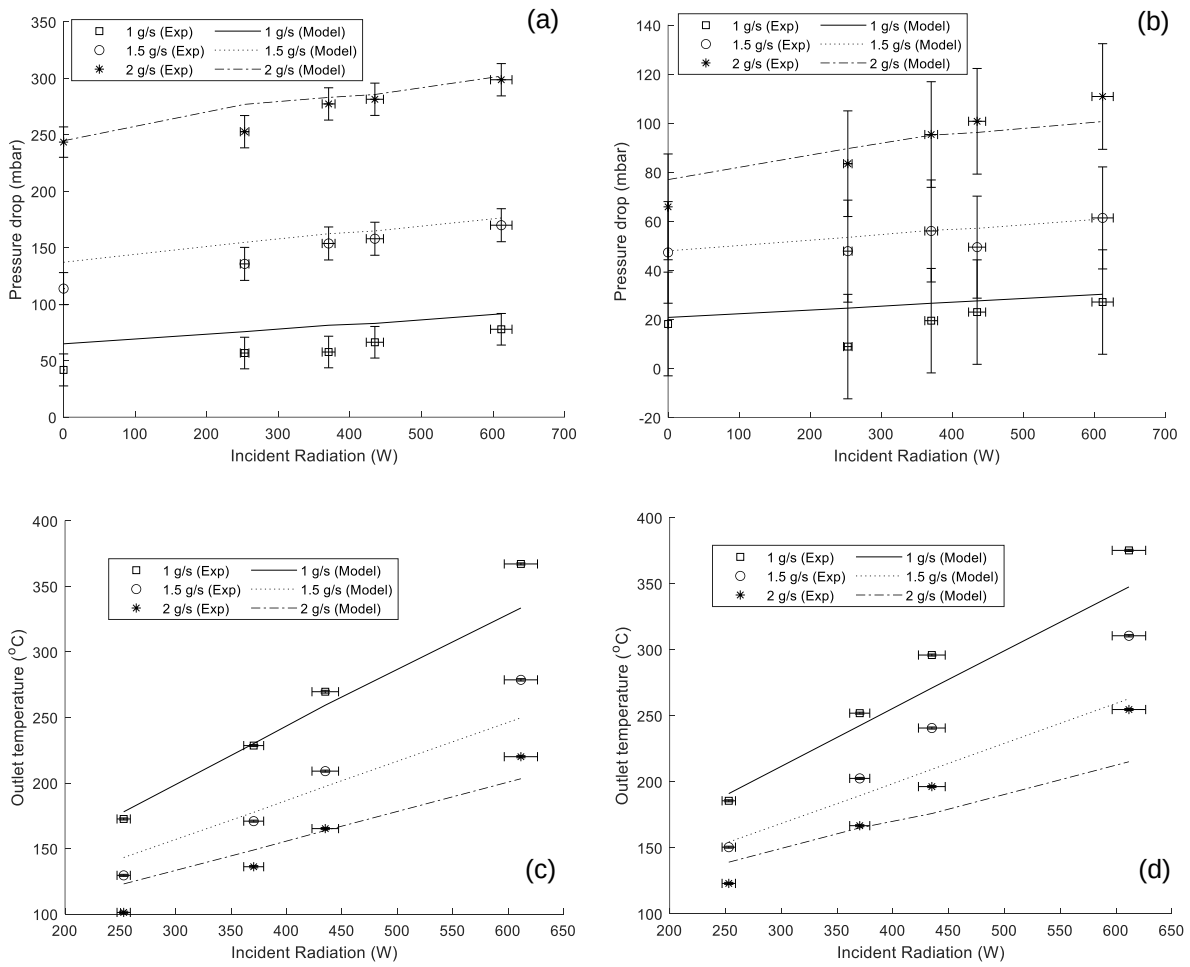


Figure 94. Experimental results compared with numerical model. (a) Pressure drop at inlet pressure of 4 bar, (b) Pressure drop at inlet pressure of 12 bar, (c) Outlet temperature of air at inlet pressure of 4 bar, (d) Outlet temperature of air at inlet pressure of 12 bar

### 4.3.2. Pressurised receiver 2 (PR2)

The pressurised receiver 2 (PR2) before and after the experimentation can be seen in Figure 95. As is clearly evident, significant oxidation has taken place due to the high temperatures achieved at the surface which have discoloured the receiver. The progression of the oxidation on the receiver is showcased in the photos of the receiver taken after an experiment run which can be found in the appendix.


Figure 95. PR2 with inlet to right and outlet at left: (a) before experiments, (b) after experiments.

It is normally expected for the outlet section of the receiver to be more oxidised i.e. darker than the inlet section as this section will experience the higher surface temperature, which is observed in Figure 95(b).

Before the experiments were performed, a leak test was conducted to ensure that the receiver was installed correctly. A depiction of this leak test in terms of mass flow rate and system pressure, is given in the appendix. An absorptivity test was conducted on the spectrometer after the conclusion of the experiments on PR2 and the results of the same can be found in Table 22. The experimental characterisation was performed varying the inlet control parameters as shown in Table 23. The experiments at 500 kW $m^{-2}$ peak incident radiation flux at a mass flow rate of 1 g $s^{-1}$ were attempted but aborted as the receiver surface temperature rose above 600 °C. Closed circuit camera (CCD) images of the receiver taken at each peak flux level are presented in Figure 96.

Table 22. Absorptance measurements of PR2 after experiments

| Zone | Absorptance (-) | | | |
|---|---|---|---|---|
| | **Measurement #1** | **Measurement #2** | **Measurement #3** | **Retained value** |
| Inlet | 0.5844 | 0.6261 | 0.6349 | 0.615±0.03 |
| Centre | 0.7520 | 0.7451 | 0.7507 | 0.749±0.004 |
| Outlet | 0.7677 | 0.7629 | 0.7651 | 0.765±0.002 |

Table 23. Input parameters for experiments with PR2

| Design setpoints | | | Experimental parameter | |
|---|---|---|---|---|
| **Mass flow rate ($g\ s^{-1}$)** | **Inlet pressure (bar)** | **Mass flow rate ($g\ s^{-1}$)** | **Inlet pressure (mbar)** | **Mass flow rate ($g\ s^{-1}$)** |
| 0 | 4 | 1.0 | 4.13±0.04 | 1.006±0.006 |
| 0 | 4 | 1.5 | 3.85±0.05 | 1.503±0.012 |
| 0 | 4 | 2.0 | 4.22±0.03 | 2.03±0.02 |
| 200 | 4 | 1.0 | 4.10±0.04 | 1.000±0.008 |
| 200 | 4 | 1.5 | 3.85±0.04 | 1.500±0.012 |
| 200 | 4 | 2.0 | 4.22±0.04 | 2.01±0.02 |
| 300 | 4 | 1.0 | 4.11±0.05 | 1.001±0.008 |
| 300 | 4 | 1.5 | 3.85±0.04 | 1.498±0.013 |
| 300 | 4 | 2.0 | 4.23±0.04 | 2.01±0.02 |
| 400 | 4 | 1.0 | 4.10±0.04 | 0.999±0.008 |
| 400 | 4 | 1.5 | 3.82±0.04 | 1.492±0.014 |
| 400 | 4 | 2.0 | 4.23±0.04 | 2.01±0.02 |
| 500 | 4 | 1.0 | - | - |
| 500 | 4 | 1.5 | 3.86±0.04 | 1.501±0.013 |
| 500 | 4 | 2.0 | 4.22±0.04 | 1.99±0.02 |
| 0 | 12 | 1.0 | 12.12±0.06 | 1.014±0.006 |
| 0 | 12 | 1.5 | 11.90±0.06 | 1.507±0.012 |
| 0 | 12 | 2.0 | 12.48±0.07 | 1.99±0.02 |
| 200 | 12 | 1.0 | 11.75±0.08 | 0.985±0.006 |
| 200 | 12 | 1.5 | 11.73±0.09 | 1.492±0.014 |
| 200 | 12 | 2.0 | 11.97±0.07 | 2.02±0.03 |
| 300 | 12 | 1.0 | 11.87±0.07 | 0.995±0.006 |
| 300 | 12 | 1.5 | 11.79±0.08 | 1.498±0.014 |
| 300 | 12 | 2.0 | 11.91±0.07 | 2.01±0.02 |
| 400 | 12 | 1.0 | 11.75±0.07 | 0.981±0.006 |
| 400 | 12 | 1.5 | 11.87±0.07 | 1.501±0.013 |
| 400 | 12 | 2.0 | 11.90±0.09 | 2.01±0.02 |
| 500 | 12 | 1.0 | - | - |
| 500 | 12 | 1.5 | 11.90±0.07 | 1.503±0.012 |
| 500 | 12 | 2.0 | 11.83±0.09 | 1.99±0.02 |

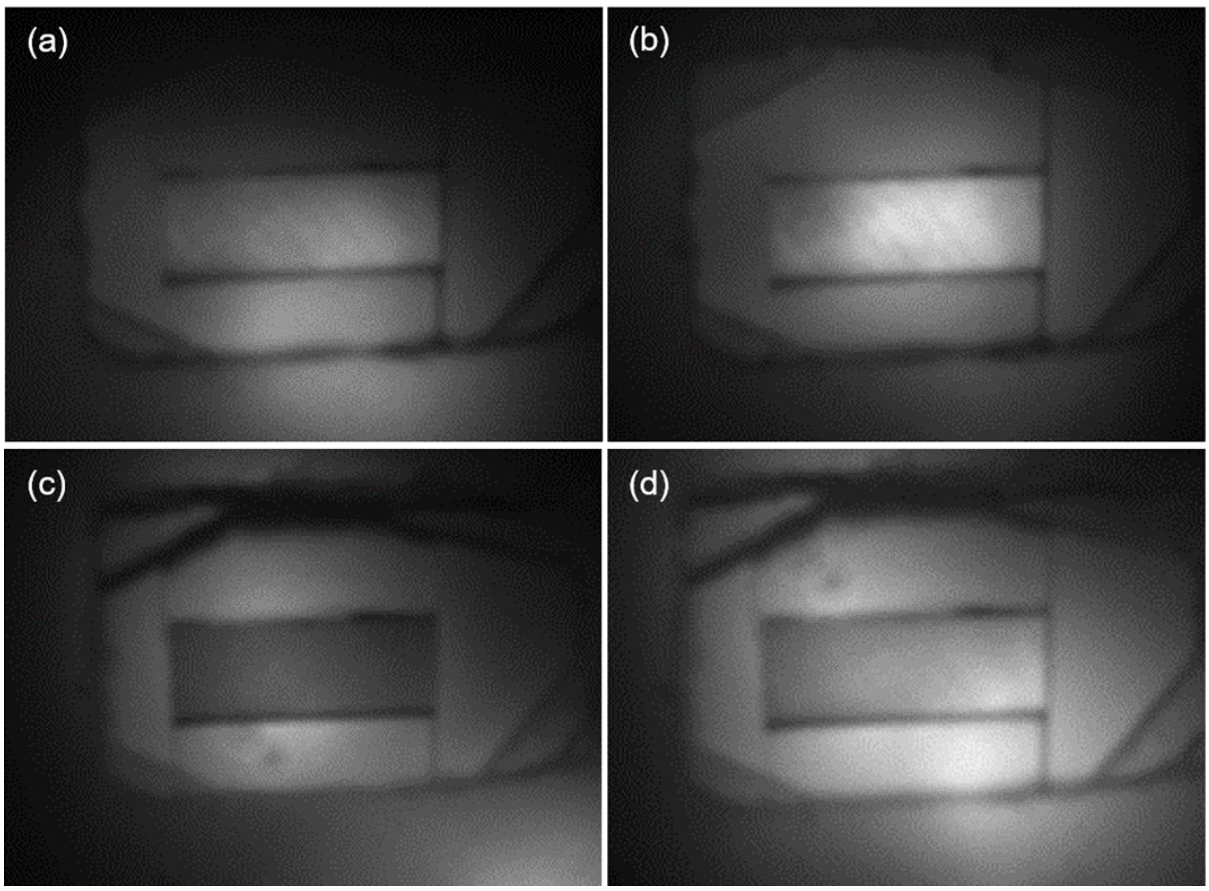


Figure 96. CCD images of PR2 during experimentation at different flux levels: (a) 200 kW $m^{-2}$, (b) 300 kW $m^{-2}$, (c) 400 kW $m^{-2}$, (d) 500 kW $m^{-2}$.

The results of the experiments, in terms of pressure drop and outlet temperature, are plotted in Figure 97. Observing Figure 97, the general trends of the pressure drop and outlet temperature are the same as seen with PR1. The pressure drop increases with higher mass flow rates and incident radiation power as the channel velocity increases in both these instances resulting in higher pressure drops. At the same time it falls at elevated pressures due to increased density levels and lower associated channel velocities. The outlet temperature behaves as predicted with it rising with rising incident flux levels and falling at higher mass flow rates. The effect of higher inlet pressures is to increase the outlet temperature by bettering the heat transfer to the HTF due to the higher densities.

The numerical model generally seems to match reasonably well with the experimental data. The pressure drops coincide well given that the exact value of surface roughness, which plays an important role in the pressure drop, is unknown. There are more significant deviations in the outlet temperature profiles which, as explained previously, are reasonable when the absorptance of the receiver is considered. The absorptance has a strong impact on the heat transfer to the HTF and hence its outlet temperature. While in reality the absorptance of the receiver changes continuously, as it is unoxidised and untreated, its absorptance has only been measured once at the end of the experiments on the receiver (see Table 22) and it is this single value that has been fed to the model. This is why the outlet temperature at higher flow rates and lower fluxes (when the receiver was relatively less oxidised and had a lower absorptance) was lower than that predicted by the numerical model which used a higher absorptance.

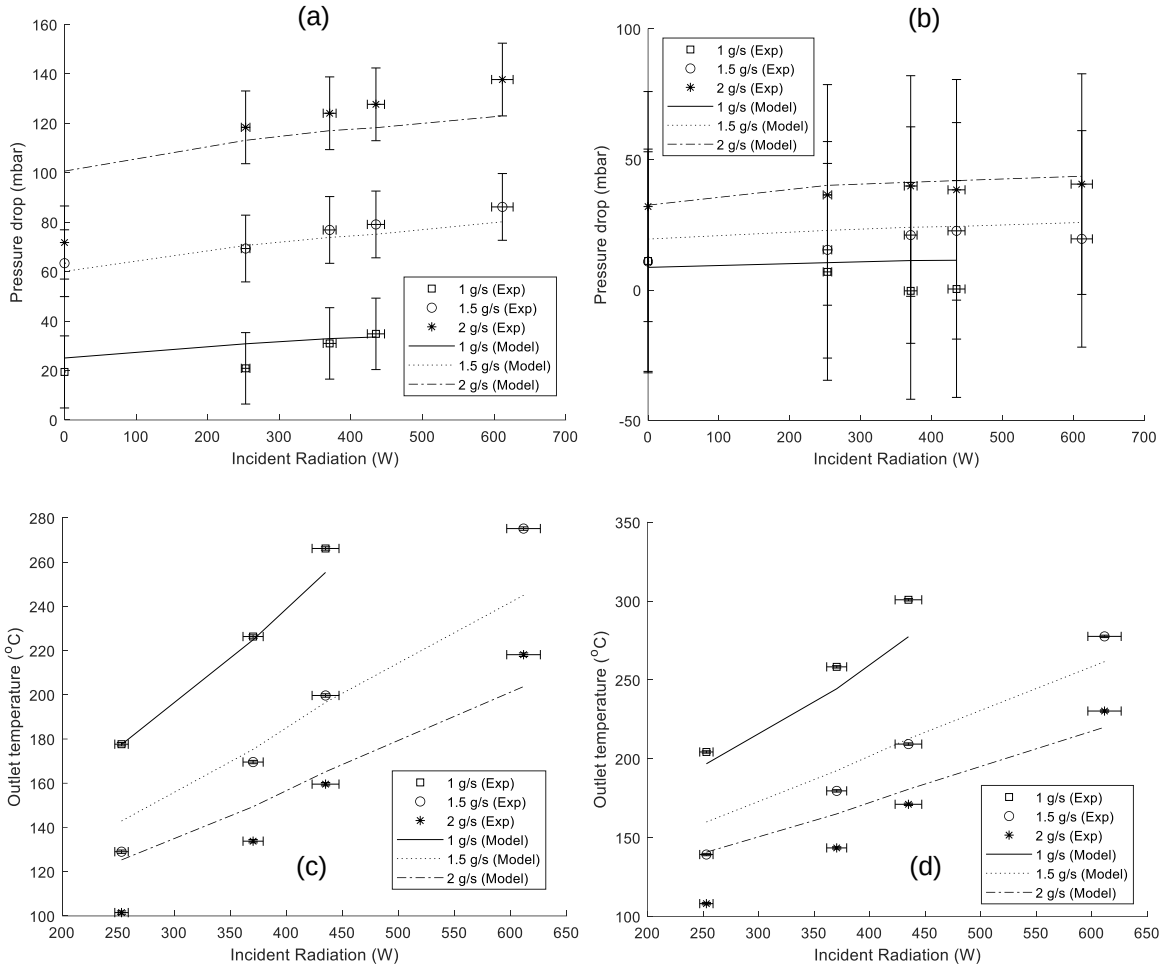


Figure 97. Experimental results compared with numerical model: (a) Pressure drop at inlet pressure of 4 bar, (b) Pressure drop at inlet pressure of 12 bar, (c) Outlet temperature of air at inlet pressure of 4 bar, (d) Outlet temperature of air at inlet pressure of 12 bar

There is also a divergence of the numerical model's outlet temperature from the experimental one at higher fluxes which may have to do with imperfections in the insulation of the receiver allowing for increased exposure (especially of the top surface) to incident radiation. This effect is particularly enhanced when two lamps, one from above as discussed in section 3.8, are used.

### 4.3.3. Pressurised receiver 3 (PR3)

The pressurised receiver 3 (PR3) before and after the experimentation can be seen in Figure 98. As is clearly evident, significant oxidation has taken place due to the high temperatures achieved at the surface which have discoloured the receiver. The progression of the oxidation on the receiver is showcased in the photos of the receiver taken after an experiment run which can be found in the appendix.

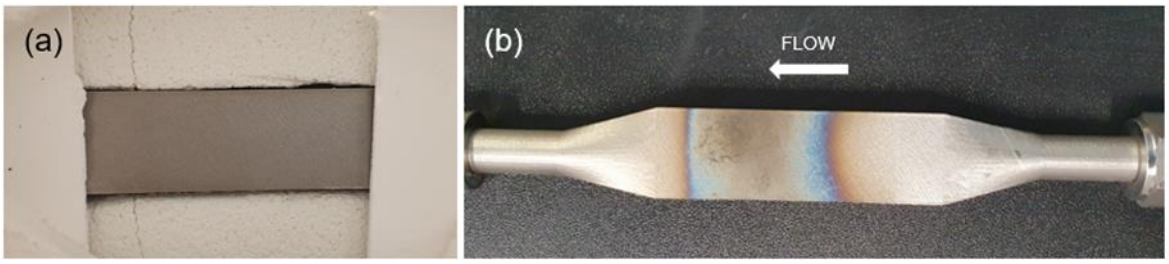


Figure 98. PR3 with inlet to right and outlet at left: (a) before experiments, (b) after experiments.

It is normally expected for the outlet section of the receiver to be more oxidised i.e. darker than the inlet section as this section will experience the higher surface temperature, which is observed in Figure 98(b). Before the experiments were performed, a leak test was conducted to ensure that the receiver was installed correctly. The leak test, in terms of mass flow rate and system pressure, is given in the appendix. One of the pipe sections of the receiver was slightly deformed which affected its circularity and prevented it from fully sealing with the compression nut. Hence a small leak was detected on one of the pipe connections which was placed at the outlet of the receiver so as not to affect the mass flow rate into the receiver.

An absorptivity test was conducted on the spectrometer after the conclusion of the experiments on PR3 and the results of the same can be found in Table 24. The experimental characterisation was performed varying the inlet control parameters as shown in Table 25. The experiments at 500 kW $m^{-2}$ peak incident radiation flux at a mass flow rate of 1 g $s^{-1}$ were attempted but aborted as the receiver back surface temperature rose above 600 °C. Closed circuit camera (CCD) images of the receiver taken at each peak flux level are presented in Figure 99.

Table 24. Absorptance measurements of PR3 after experiments

| Zone | Absorptance (-) | | | |
|---|---|---|---|---|
| | **Measurement #1** | **Measurement #2** | **Measurement #3** | **Retained value** |
| Inlet | 0.4318 | 0.4293 | 0.5272 | 0.46±0.06 |
| Centre | 0.8084 | 0.8083 | 0.8434 | 0.82±0.02 |
| Outlet | 0.8418 | 0.8781 | 0.8723 | 0.86±0.02 |

Table 25. Input parameters for experiments with PR3

| Design setpoints | | | Experimental parameter | |
|---|---|---|---|---|
| **Mass flow rate ($g\ s^{-1}$)** | **Inlet pressure (bar)** | **Mass flow rate ($g\ s^{-1}$)** | **Inlet pressure (mbar)** | **Mass flow rate ($g\ s^{-1}$)** |
| 0 | 4 | 1.0 | 3.68±0.03 | 1.006±0.008 |
| 0 | 4 | 1.5 | 3.94±0.04 | 1.503±0.014 |
| 0 | 4 | 2.0 | 4.18±0.04 | 2.02±0.02 |
| 200 | 4 | 1.0 | 3.65±0.04 | 1.002±0.008 |
| 200 | 4 | 1.5 | 3.88±0.05 | 1.491±0.015 |
| 200 | 4 | 2.0 | 4.17±0.05 | 2.01±0.02 |
| 300 | 4 | 1.0 | 3.64±0.04 | 0.999±0.009 |
| 300 | 4 | 1.5 | 3.87±0.05 | 1.487±0.016 |
| 300 | 4 | 2.0 | 4.17±0.04 | 2.01±0.02 |
| 400 | 4 | 1.0 | 3.67±0.03 | 1.007±0.007 |
| 400 | 4 | 1.5 | 3.93±0.04 | 1.496±0.015 |
| 400 | 4 | 2.0 | 4.17±0.04 | 2.01±0.02 |
| 500 | 4 | 1.0 | - | - |
| 500 | 4 | 1.5 | 3.94±0.04 | 1.501±0.013 |
| 500 | 4 | 2.0 | 4.15±0.05 | 2.00±0.02 |
| 0 | 12 | 1.0 | 11.43±0.06 | 1.004±0.006 |
| 0 | 12 | 1.5 | 11.94±0.06 | 1.508±0.014 |
| 0 | 12 | 2.0 | 11.87±0.06 | 2.01±0.02 |
| 200 | 12 | 1.0 | 11.20±0.08 | 0.988±0.007 |
| 200 | 12 | 1.5 | 11.86±0.09 | 1.501±0.013 |
| 200 | 12 | 2.0 | 11.741±009 | 1.99±0.02 |
| 300 | 12 | 1.0 | 11.37±0.07 | 1.003±0.008 |
| 300 | 12 | 1.5 | 11.82±0.08 | 1.496±0.013 |
| 300 | 12 | 2.0 | 11.67±0.09 | 1.98±0.02 |
| 400 | 12 | 1.0 | 11.36±0.07 | 1.004±0.007 |
| 400 | 12 | 1.5 | 11.84±0.07 | 1.495±0.013 |
| 400 | 12 | 2.0 | 11.71±0.10 | 1.99±0.02 |
| 500 | 12 | 1.0 | - | - |
| 500 | 12 | 1.5 | 11.87±0.07 | 1.498±0.012 |
| 500 | 12 | 2.0 | 11.81±0.07 | 2.00±0.02 |

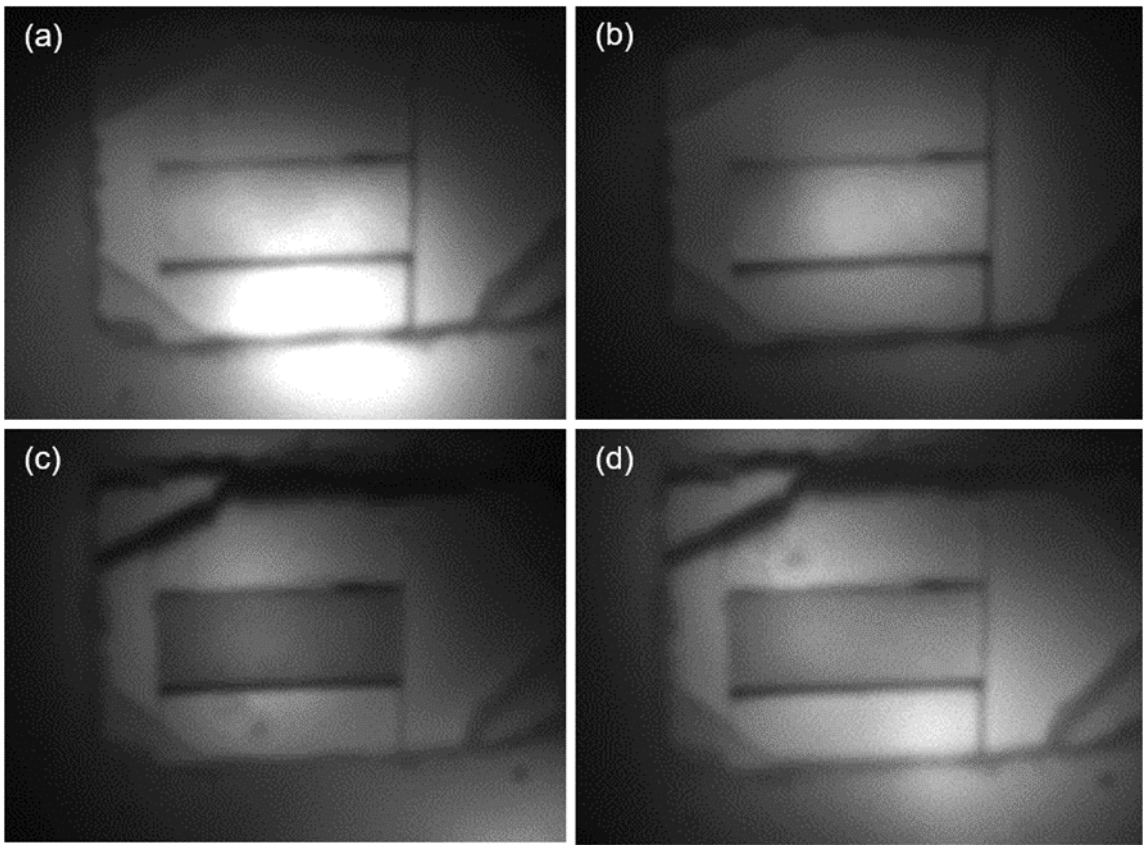


Figure 99. CCD images of PR3 during experimentation at different flux levels: (a) 200 kW $m^{-2}$, (b) 300 kW $m^{-2}$, (c) 400 kW $m^{-2}$, (d) 500 kW $m^{-2}$.

The results of the experiments, in terms of pressure drop and outlet temperature, are plotted in Figure 100. Observing Figure 100, the pressure drop and temperature at the outlet behaves as predicted an observed with the other receivers. In other words, the pressure drop is directly related to the mass flow rate and incident radiation power and simultaneously inversely related to the inlet pressure level. Since both the mass flow rate and incident radiation level act to increase the channel velocity when they rise, the pressure drop, which itself is proportional to the channel velocity, follows suit and also rises. Conversely, the channel velocity drops with increased inlet pressure which causes the pressure drop to fall. The outlet temperature rises with greater incident radiation levels due to increased heat available to be transferred to the fluid. It also grows with greater pressure levels as the heat transfer properties of the HTF are enhanced at higher pressures and densities. The mass flow rate is indirectly related to the outlet temperature as a fall in the mass flow rate results in a rise in the outlet temperature.

The numerical model generally seems to line up reasonably well with the experimental data. The pressure drops coincide well given that the exact value of surface roughness, which plays an important role in the pressure drop, is unknown. There are more significant deviations in the outlet temperature profiles which can be explained when the absorptance of the receiver is considered. The absorptance has a strong impact on the heat transfer to the HTF and hence its outlet temperature. While in reality the absorptance of the receiver changes continuously, as it is unoxidised and untreated, its absorptance has only been measured once at the end of the experiments on the receiver (see Table 24) and it is this single value that has been fed to the model. This is why the outlet temperature at higher flow rates and lower fluxes (when the receiver was relatively less oxidised and had a lower absorptance) was lower than that predicted by the numerical model which used a higher absorptance.

There is also a divergence of the numerical model's outlet temperature from the experimental one at higher fluxes which may have to do with imperfections in the insulation of the receiver allowing for increased exposure (especially of the top surface) to incident radiation. This effect is particularly enhanced when two lamps, one from above as discussed in section 3.8, are used.

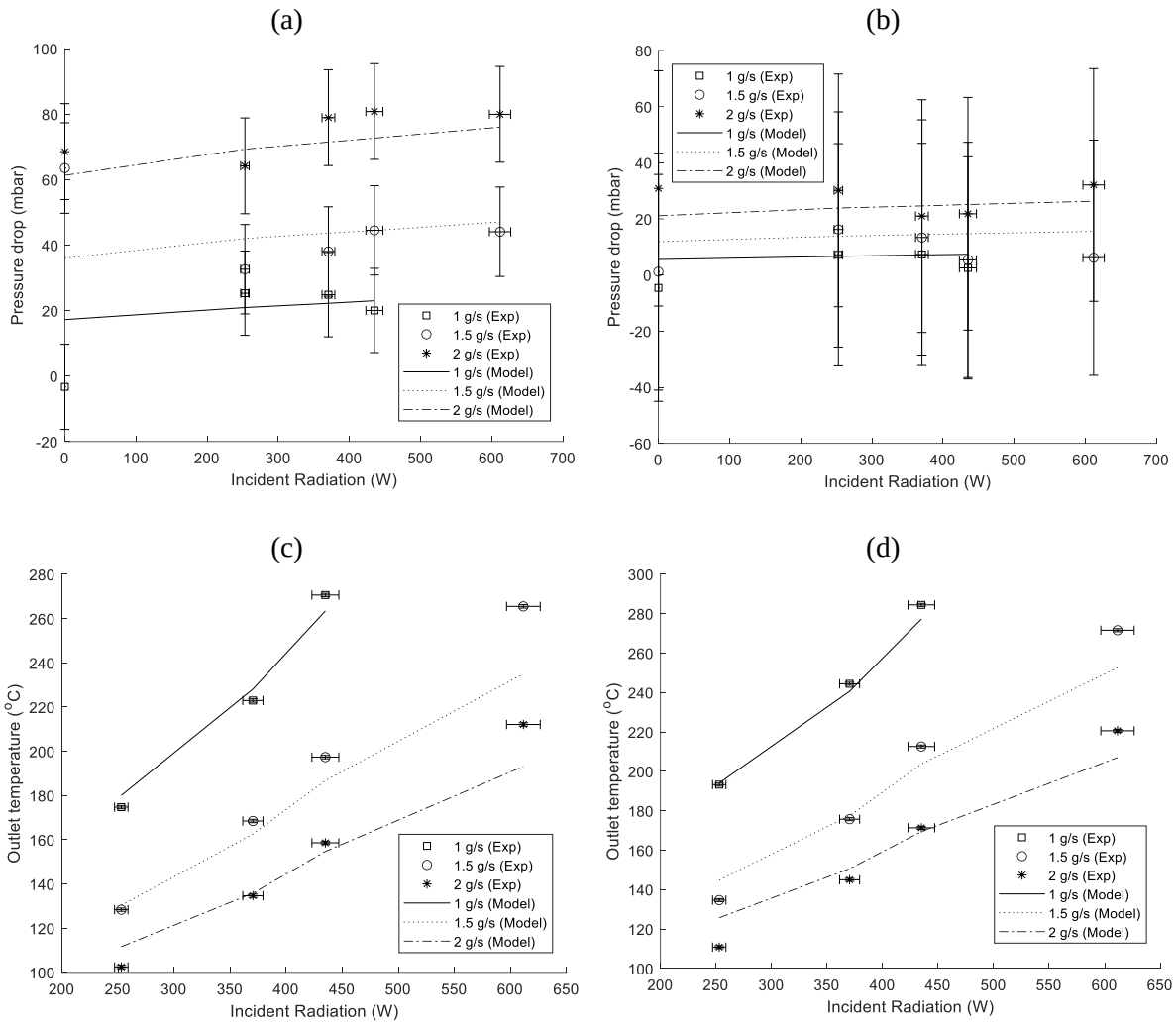


Figure 100. Experimental results compared with numerical model: (a) Pressure drop at inlet pressure of 4 bar, (b) Pressure drop at inlet pressure of 12 bar, (c) Outlet temperature of air at inlet pressure of 4 bar, (d) Outlet temperature of air at inlet pressure of 12 bar

### 4.3.4. Pressurised receiver 4 (PR4)

The pressurised receiver 4 (PR4) before and after the experimentation can be seen in Figure 101. As is clearly evident, significant oxidation has taken place due to the high temperatures achieved at the surface which have discoloured the receiver. The progression of the oxidation on the receiver is showcased in the photos of the receiver taken after an experiment run which can be found in the appendix.


Figure 101. PR4 with inlet to right and outlet at left: (a) before experiments, (b) after experiments

It is normally expected for the outlet section of the receiver to be more oxidised i.e. darker than the inlet section as this section will experience the higher surface temperature, which is observed in Figure 101(b).

Before the experiments were performed, a leak test was conducted to ensure that the receiver was installed correctly. A depiction of this leak test in terms of mass flow rate and system pressure, is given in the appendix.

An absorptivity test was conducted on the spectrometer after the conclusion of the experiments on PR4 and the results of the same can be found in Table 26. The experimental characterisation was performed varying the inlet control parameters as shown in Table 27. Noting that when the previous receivers were most oxidised when attempting to operate them at 500 kW $m^{-2}$ peak incident radiation flux and at 1 g $s^{-1}$ mass flow rate, it was decided to not attempt to operate at this experiment design setpoint and to observe the effect on the oxidation levels of PR4 as compared with the other receivers. As in clear from photos of the receivers after the entire set of experiments have been completed on them, PR4 is the least oxidised. Closed circuit camera (CCD) images of the receiver taken at each peak flux level are presented in Figure 102.

Table 26. Absorptance measurements of PR4 after experiments.

| Zone | Absorptance (-) | | | |
|---|---|---|---|---|
| | **Measurement #1** | **Measurement #2** | **Measurement #3** | **Retained value** |
| Inlet | 0.4257 | 0.4241 | 0.4205 | 0.423±0.003 |
| Centre | 0.5650 | 0.5793 | 0.6108 | 0.59±0.02 |
| Outlet | 0.6591 | 0.6397 | 0.6215 | 0.640±0.019 |

Table 27. Input parameters for experiments with PR4.

| Design setpoints | | | Experimental parameter | |
|---|---|---|---|---|
| **Peak flux (kW m$^{-2}$)** | **Inlet pressure (bar)** | **Mass flow rate (g s$^{-1}$)** | **Inlet pressure (bar)** | **Mass flow rate (g s$^{-1}$)** |
| 0 | 4 | 1.0 | 3.86±0.02 | 1.004±0.005 |
| 0 | 4 | 1.5 | 3.81±0.04 | 1.503±0.012 |
| 0 | 4 | 2.0 | 3.86±0.06 | 2.01±0.02 |
| 200 | 4 | 1.0 | 3.84±0.03 | 1.00±0.07 |
| 200 | 4 | 1.5 | 3.79±0.04 | 1.498±0.013 |
| 200 | 4 | 2.0 | 3.89±0.04 | 2.00±0.02 |
| 300 | 4 | 1.0 | 3.79±0.05 | 0.991±0.009 |
| 300 | 4 | 1.5 | 3.82±0.05 | 1.494±0.014 |
| 300 | 4 | 2.0 | 3.89±0.04 | 2.00±0.02 |
| 400 | 4 | 1.0 | 3.83±0.04 | 0.997±0.006 |
| 400 | 4 | 1.5 | 3.81±0.04 | 1.497±0.013 |
| 400 | 4 | 2.0 | 3.88±0.05 | 2.00±0.02 |
| 500 | 4 | 1.0 | - | - |
| 500 | 4 | 1.5 | 3.84±0.04 | 1.503±0.013 |
| 500 | 4 | 2.0 | 3.90±0.04 | 2.00±0.02 |
| 0 | 12 | 1.0 | 11.79±0.07 | 1.002±0.007 |
| 0 | 12 | 1.5 | 11.77±0.07 | 1.502±0.011 |
| 0 | 12 | 2.0 | 12.02±0.06 | 2.01±0.02 |
| 200 | 12 | 1.0 | 11.73±0.06 | 1.000±0.006 |
| 200 | 12 | 1.5 | 11.72±0.08 | 1.493±0.014 |
| 200 | 12 | 2.0 | 11.86±0.10 | 1.98±0.02 |
| 300 | 12 | 1.0 | 11.68±0.07 | 0.998±0.006 |
| 300 | 12 | 1.5 | 11.83±0.07 | 1.504±0.012 |
| 300 | 12 | 2.0 | 11.94±0.07 | 1.99±0.02 |
| 400 | 12 | 1.0 | 11.60±0.07 | 0.988±0.005 |
| 400 | 12 | 1.5 | 11.84±0.07 | 1.498±0.012 |
| 400 | 12 | 2.0 | 12.15±0.07 | 2.00±0.02 |
| 500 | 12 | 1.0 | - | - |
| 500 | 12 | 1.5 | 11.80±0.09 | 1.494±0.015 |
| 500 | 12 | 2.0 | 12.14±0.07 | 2.00±0.02 |

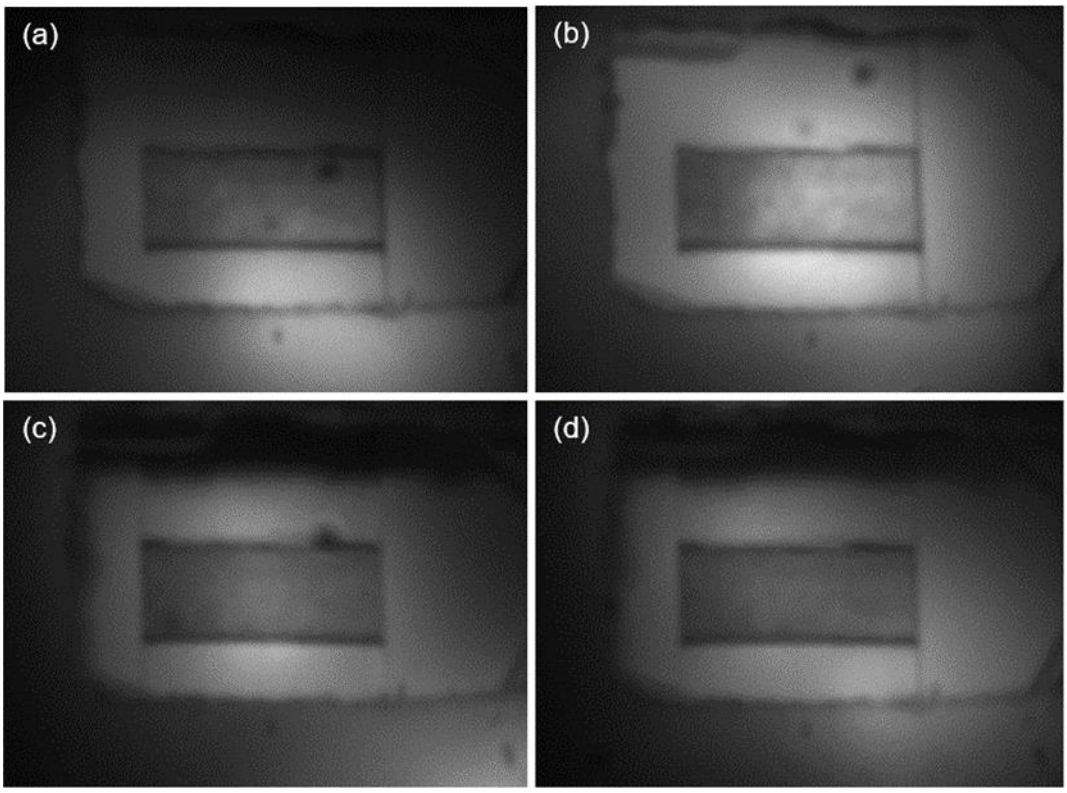


Figure 102. CCD images of PR4 during experimentation at different flux levels: (a) 200 kW $m^{-2}$, (b) 300 kW $m^{-2}$, (c) 400 kW $m^{-2}$, (d) 500 kW $m^{-2}$.

The results of the experiments, in terms of pressure drop and outlet temperature, are plotted in Figure 103. Observing Figure 103, the same trends of pressure drop and outlet temperature seen with the previous receivers is also observed here. The pressure drop varies proportionally with the incident radiation level and the mass flow rate while it is inversely proportional to the inlet pressure. This directly follows the influence of each of these parameters with the channel velocity. The outlet temperature, on the other hand, rises with lower mass flow rates and higher incident radiation levels and inlet pressure conditions.

The numerical model generally seems to line up reasonably well with the experimental data. The pressure drops coincide well given that the exact value of surface roughness, which plays an important role in the pressure drop, is unknown. There are more significant deviations in the outlet temperature profiles, especially at higher fluxes, which can be partially explained when the absorptance of the receiver is considered. The absorptance has a strong impact on the heat transfer to the HTF and hence its outlet temperature. While in reality the absorptance of the receiver changes continuously, as it is unoxidised and untreated, its absorptance has only been measured once at the end of the experiments on the receiver (see Table 26) and it is this single value that has been fed to the model. This is why the outlet temperature at higher flow rates and lower fluxes (when the receiver was relatively less oxidised and had a lower absorptance) was lower than that predicted by the numerical model which used a higher absorptance.

There is also a divergence of the numerical model's outlet temperature from the experimental one at higher fluxes which may have to do with imperfections in the insulation of the receiver allowing for increased exposure (especially of the top surface) to incident radiation. This effect is particularly enhanced when two lamps, one from above as discussed in section 3.8, are used.

As noted in the experiment log, the experiment runs with the PR4 receiver were performed in a slightly different manner in which the cylinder was changed in the middle of the experiment run by pointing the lamps away from the receiver and replacing a spent cylinder and then continuing the experiment run while gradually reheating the receiver. This was contrary to previous experiments in which the experiment run would stop if a cylinder was spent and a new run would resume after the cylinder was replaced.

The advantage of replacing a cylinder during an experiment run is in the experiment time required as the operator would not have to wait 30 minutes for the lamps to cool before restarting the experiment. However, a potential drawback in this method, especially given the absence of a purge valve, is the potential of entry of ambient air into the cylinder valve during the cylinder change. The infiltration of moisture and argon into the air supply to the receiver could also have increased the outlet temperatures observed in the experiments at higher fluxes.

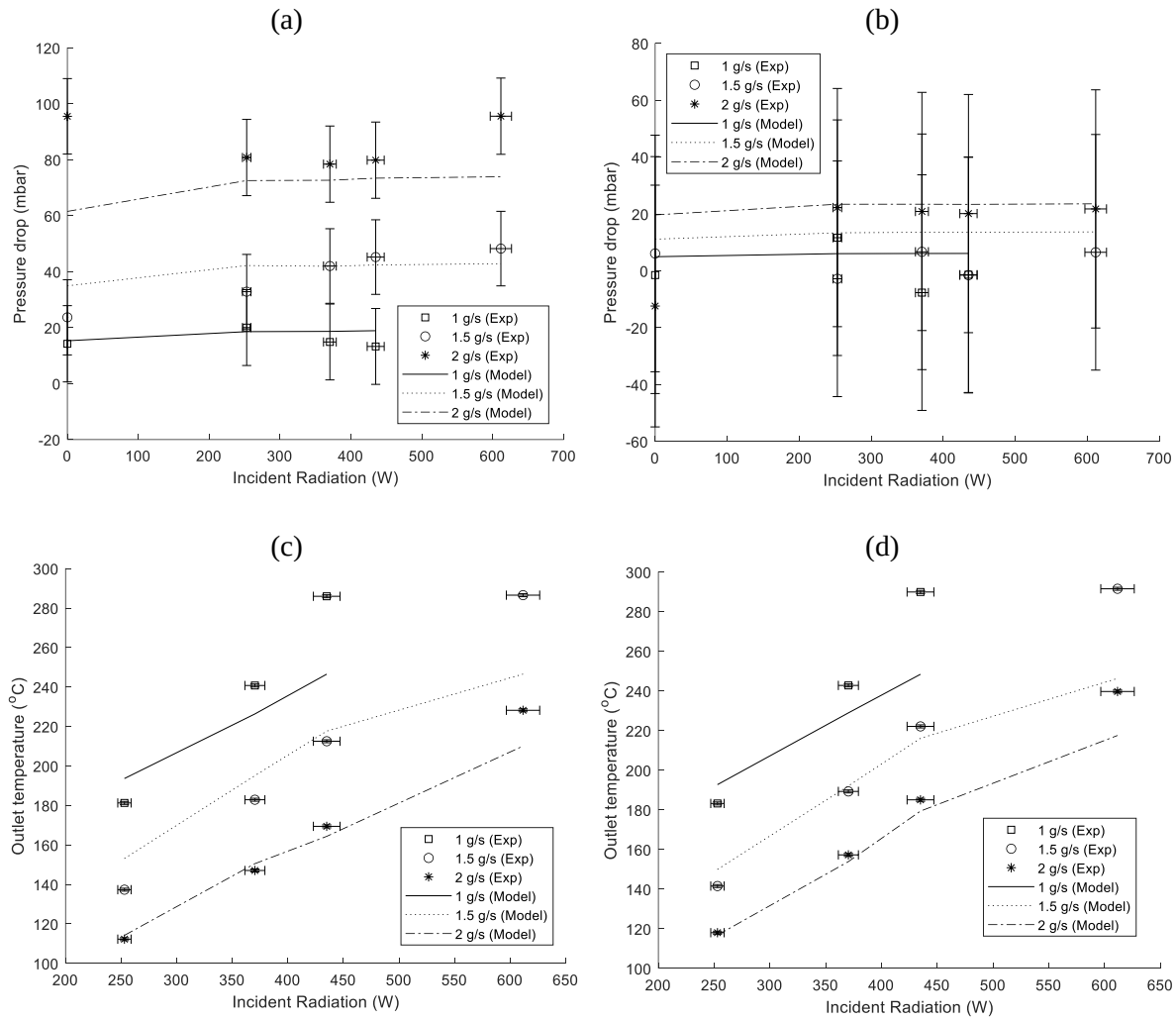


Figure 103. Experimental results compared with numerical model: (a) Pressure drop at inlet pressure of 4 bar, (b) Pressure drop at inlet pressure of 12 bar, (c) Outlet temperature of air at inlet pressure of 4 bar, (d) Outlet temperature of air at inlet pressure of 12 bar

### 4.3.5. Comparison of the receivers

Before the performance results of the four receivers (summarised in Table 14) are compared and discussed, it must be borne in mind that the results presented here have a degree of uncertainty and error which is in the inherent nature of experimental analyses. The following tables present the outlet temperatures (Table 28) and pressure drop (Table 29) of the receivers at different operating conditions.

Table 28. Results table: Receiver outlet temperature

| Control parameter | | | Outlet temperature | | | |
|---|---|---|---|---|---|---|
| **Peak flux (kW m$^{-2}$)** | **Inlet pressure (bar)** | **Mass flow rate (g s$^{-1}$)** | **PR1 (°C)** | **PR2 (°C)** | **PR3 (°C)** | **PR4 (°C)** |
| 0 | 4 | 1.0 | 27 | 20 | 21 | 21 |
| 0 | 4 | 1.5 | 36 | 19 | 21 | 21 |
| 0 | 4 | 2.0 | 27 | 21 | 21 | 26 |
| 200 | 4 | 1.0 | 173 | 178 | 175 | 181 |
| 200 | 4 | 1.5 | 130 | 129 | 128 | 137 |
| 200 | 4 | 2.0 | 101 | 102 | 102 | 112 |
| 300 | 4 | 1.0 | 229 | 226 | 223 | 241 |
| 300 | 4 | 1.5 | 171 | 170 | 168 | 183 |
| 300 | 4 | 2.0 | 136 | 134 | 135 | 147 |
| 400 | 4 | 1.0 | 270 | 266 | 271 | 286 |
| 400 | 4 | 1.5 | 209 | 200 | 197 | 213 |
| 400 | 4 | 2.0 | 165 | 160 | 159 | 169 |
| 500 | 4 | 1.0 | 367 | - | - | - |
| 500 | 4 | 1.5 | 279 | 275 | 266 | 287 |
| 500 | 4 | 2.0 | 220 | 218 | 212 | 228 |
| 0 | 12 | 1.0 | 34 | 27 | 22 | 21 |
| 0 | 12 | 1.5 | 26 | 21 | 21 | 19 |
| 0 | 12 | 2.0 | 29 | 21 | 19 | 23 |
| 200 | 12 | 1.0 | 186 | 204 | 193 | 183 |
| 200 | 12 | 1.5 | 150 | 139 | 135 | 142 |
| 200 | 12 | 2.0 | 123 | 108 | 111 | 118 |
| 300 | 12 | 1.0 | 252 | 258 | 244 | 243 |
| 300 | 12 | 1.5 | 203 | 180 | 176 | 189 |
| 300 | 12 | 2.0 | 167 | 143 | 145 | 157 |
| 400 | 12 | 1.0 | 296 | 301 | 284 | 290 |
| 400 | 12 | 1.5 | 241 | 209 | 213 | 222 |
| 400 | 12 | 2.0 | 196 | 171 | 171 | 185 |
| 500 | 12 | 1.0 | 375 | - | - | - |
| 500 | 12 | 1.5 | 311 | 278 | 272 | 292 |
| 500 | 12 | 2.0 | 255 | 230 | 221 | 240 |

As was noted and explained in the individual analysis of the receivers, the outlet temperature rises with increasing incident radiation power and inlet pressure while it falls with higher mass flow rates. These trends hold true irrespective of the receiver being analysed. Comparing the four receivers, the outlet temperature is, generally, highest in PR1 as is expected given that it has the smallest sized channels and hence the best thermal efficiency with other conditions being equal. Smaller channels result in higher channel velocities and better heat transfer coefficients which ultimately results in greater outlet temperatures.

Conversely, PR3 has the lowest outlet temperatures as the increased channel breadth results in a higher thermal resistance of the receiver as the reduced solid area, or alternatively higher fluid contact area, along the receiver breadth serve to the detriment of the thermal resistance. This observation is consistent with the findings of the numerical model presented in Chapter 2 that demonstrated the reduction in thermal performance of receivers with higher breadth flow channels as the HTF offers a higher thermal resistance path than the solid walls.

The two receivers with the higher channel height (PR2 and PR4) have similar outlet temperatures though it seems that PR4 with thinner channel walls has slightly greater outlet temperatures at low pressures and slightly lower outlet temperatures at elevated pressures and low mass flow rates. This illustrates the significant influence of the thermal resistance of the fluid to the overall performance and optimum geometry of the receiver for a particular pressure and mass flow rate. At low pressures and high mass flow rates, the channel velocity is high enough to bring down the thermal resistance of the fluid to the extent that thinner channel walls may be preferred as thicker walls and conduction through the solid wall becomes unfavourable.

On the other hand, at larger pressures and lower mass flow rates, the channel velocity is brought down and results in a rise in the fluid's thermal resistance to the extent that heat transfer through the solid wall is preferred and hence receivers with thicker channel walls perform better.

Independent of receiver geometry, the pressure drop follows the same trends with regards to the incident radiation power, mass flow rate and inlet pressure as was observed in in the individual receiver analysis. For each receiver, the pressure drop is rises with increasing incident radiation power and mass flow rate while it falls at larger pressure levels. From Table 29 it is clearly evident that PR1 consistently has the highest pressure drop which is unsurprising as it has the smallest channels and hence the largest channel velocity which directly affects the pressure drop. As PR2, PR3 and PR4 all have the same wetted area, the measured pressure drops are quite similar to one another as the only influence on their pressure drop would be the heat conducted through the receiver bulk and hence transmitted to the fluid. Of course, the surface roughness of each receiver may not be the same and that has an outsized effect on the pressure drop but this roughness is unknown and is assumed equal for the sake of this discussion. It should be noted that the measured pressure drop of PR3 is an exaggerated value as a very small leak was detected at the receiver outlet which, unfortunately, could not be fully sealed.

PR2 seems to have a generally higher pressure loss value than PR4, though the only difference between the two receivers is in their channel wall thickness. The thicker walls of PR2 conduct more heat via the channels walls through the depth/height of the receiver and hence the solid wall-fluid interface temperature is higher than in the case of PR4 in which the transfer of heat through the receiver bulk is more favoured through the fluid. This results in a thicker boundary layer in the case of PR2 which explains why a slightly higher pressure drop is observed.

At higher inlet pressures, the pressure drop is expectedly lower as the channel velocity is correspondingly lower due to the larger fluid density. The relative pressure drop is always below 1% at 12 bar inlet pressures but rises to around 2.5% when the inlet pressure is 4 bar. At its peak, for the PR1 receiver operating at 4 bar, peak incident radiation flux of 500 kW $m^{-2}$ and a mass flow rate of 2 g $s^{-1}$, the pressure drop is 7.5%.

Table 29. Results table: Receiver pressure drop.

| Control parameter | | | Pressure drop | | | |
|---|---|---|---|---|---|---|
| **Peak flux (kW m$^{-2}$)** | **Inlet pressure (bar)** | **Mass flow rate (g s$^{-1}$)** | **PR1 (mbar)** | **PR2 (mbar)** | **PR3 (mbar)** | **PR4 (mbar)** |
| 0 | 4 | 1.0 | 42 | 19 | - | 14 |
| 0 | 4 | 1.5 | 114 | 63 | 64 | 24 |
| 0 | 4 | 2.0 | 244 | 72 | 69 | 96 |
| 200 | 4 | 1.0 | 57 | 21 | 25 | 20 |
| 200 | 4 | 1.5 | 136 | 69 | 33 | 33 |
| 200 | 4 | 2.0 | 253 | 118 | 64 | 81 |
| 300 | 4 | 1.0 | 58 | 31 | 25 | 15 |
| 300 | 4 | 1.5 | 154 | 77 | 38 | 42 |
| 300 | 4 | 2.0 | 277 | 124 | 79 | 78 |
| 400 | 4 | 1.0 | 66 | 35 | 20 | 13 |
| 400 | 4 | 1.5 | 158 | 79 | 45 | 45 |
| 400 | 4 | 2.0 | 281 | 128 | 81 | 80 |
| 500 | 4 | 1.0 | 78 | 0 | 0 | 0 |
| 500 | 4 | 1.5 | 170 | 86 | 44 | 48 |
| 500 | 4 | 2.0 | 299 | 138 | 80 | 96 |
| 0 | 12 | 1.0 | - | - | - | - |
| 0 | 12 | 1.5 | 47 | 11 | 1 | 6 |
| 0 | 12 | 2.0 | 66 | 32 | 31 | -12 |
| 200 | 12 | 1.0 | 9 | 7 | 7 | 12 |
| 200 | 12 | 1.5 | 48 | 15 | 16 | -3 |
| 200 | 12 | 2.0 | 84 | 36 | 30 | 22 |
| 300 | 12 | 1.0 | 20 | 0 | 7 | -8 |
| 300 | 12 | 1.5 | 56 | 21 | 13 | 7 |
| 300 | 12 | 2.0 | 95 | 40 | 21 | 21 |
| 400 | 12 | 1.0 | 23 | - | - | - |
| 400 | 12 | 1.5 | 49 | 23 | 5 | - |
| 400 | 12 | 2.0 | 101 | 38 | 22 | 20 |
| 500 | 12 | 1.0 | 27 | 0 | 0 | 0 |
| 500 | 12 | 1.5 | 61 | 20 | 6 | 7 |
| 500 | 12 | 2.0 | 111 | 41 | 32 | 22 |

The energy and thermal efficiencies of the receivers at the different operating conditions used in the experimental campaign are tabulated in Table 30. As mentioned previously in section 4.2.3, the absorptances of the receivers at each set of operating conditions changes as the previously unoxidised and otherwise untreated receivers oxidise with the elevated surfaces temperatures. These individual operating condition specific receiver absorptances were not measured and instead the receiver absorptance was only measured after the entire set of experiments on the receiver were completed. This makes direct comparisons between receivers or observing trends and behaviours in each receiver unreliable if not next to impossible though some learnings can be gleaned from Table 30.

Table 30. Results table: Energy and thermal efficiency

| Control parameter | | | Energy Efficiency | | | | Thermal Efficiency | | | |
|---|---|---|---|---|---|---|---|---|---|---|
| **Peak flux (kW m$^{-2}$)** | **Inlet pressure (bar)** | **Mass flow rate (g s$^{-1}$)** | **PR1 (%)** | **PR2 (%)** | **PR3 (%)** | **PR4 (%)** | **PR1 (%)** | **PR2 (%)** | **PR3 (%)** | **PR4 (%)** |
| 200 | 4 | 1.0 | 59.9 | 64.2 | 62.9 | 65.5 | 68.5 | 78.7 | 74.7 | 75.0 |
| 200 | 4 | 1.5 | 62.6 | 67.2 | 66.0 | 71.0 | 71.6 | 82.5 | 78.4 | 81.3 |
| 200 | 4 | 2.0 | 61.8 | 67.8 | 68.4 | 76.2 | 70.7 | 83.1 | 81.2 | 87.2 |
| 300 | 4 | 1.0 | 56.2 | 57.5 | 56.3 | 60.9 | 64.3 | 70.5 | 66.9 | 69.7 |
| 300 | 4 | 1.5 | 60.1 | 62.8 | 61.7 | 67.3 | 68.7 | 77.0 | 73.3 | 77.0 |
| 300 | 4 | 2.0 | 61.6 | 64.5 | 64.6 | 72.0 | 70.5 | 79.1 | 76.8 | 82.3 |
| 400 | 4 | 1.0 | 57.5 | 58.2 | 59.6 | 62.8 | 65.8 | 71.4 | 70.8 | 71.9 |
| 400 | 4 | 1.5 | 64.6 | 63.7 | 63.0 | 67.9 | 73.9 | 78.1 | 74.8 | 77.8 |
| 400 | 4 | 2.0 | 66.0 | 66.8 | 66.2 | 71.4 | 75.5 | 81.9 | 78.6 | 81.7 |
| 500 | 4 | 1.0 | 58.1 | - | - | - | 66.5 | - | - | - |
| 500 | 4 | 1.5 | 63.6 | 64.7 | 62.2 | 67.6 | 72.8 | 79.3 | 73.9 | 77.3 |
| 500 | 4 | 2.0 | 65.6 | 66.6 | 64.6 | 70.6 | 75.0 | 81.7 | 76.7 | 80.8 |
| 200 | 12 | 1.0 | 66.5 | - | 69.7 | 66.9 | 76.2 | 90.3 | 82.8 | 76.6 |
| 200 | 12 | 1.5 | 78.0 | 72.9 | 70.6 | 75.3 | 89.3 | 89.4 | 83.8 | 86.1 |
| 200 | 12 | 2.0 | 79.1 | 73.8 | 75.7 | 79.1 | 90.5 | 90.5 | 89.8 | 90.5 |
| 300 | 12 | 1.0 | 64.3 | 65.8 | 62.7 | 62.3 | 73.6 | 80.7 | 74.5 | 71.3 |
| 300 | 12 | 1.5 | 75.2 | 66.9 | 65.3 | 71.7 | 86.0 | 82.0 | 77.5 | 82.1 |
| 300 | 12 | 2.0 | 78.8 | 70.3 | 70.4 | 76.3 | 90.2 | 86.2 | 83.6 | 87.3 |
| 400 | 12 | 1.0 | 65.3 | 65.1 | 62.9 | 63.6 | 74.7 | 79.9 | 74.7 | 72.7 |
| 400 | 12 | 1.5 | 77.4 | 67.5 | 68.2 | 72.2 | 88.6 | 82.9 | 81.0 | 82.6 |
| 400 | 12 | 2.0 | 82.8 | 72.9 | 72.4 | 78.9 | 94.7 | 89.4 | 86.0 | 90.3 |
| 500 | 12 | 1.0 | 60.2 | - | - | - | 68.8 | - | - | - |
| 500 | 12 | 1.5 | 72.8 | 65.6 | 63.6 | 69.0 | 83.3 | 80.5 | 75.5 | 78.9 |
| 500 | 12 | 2.0 | 79.2 | 71.1 | 68.2 | 74.9 | 90.6 | 87.2 | 81.0 | 85.7 |

It was observed, and is clear from analysing the photos of the receivers after each experiment run (section A9) and the experiment log (section A7) in the appendix, that the heaviest oxidation only occurred at higher fluxes and low mass flow rates. More specifically at mass flow rates of 1 g s$^{-1}$, and to a lesser extent 1.5 g s$^{-1}$, and incident radiation peak fluxes of 400-500 kW m$^{-2}$, the receiver underwent severe oxidation which altered all subsequent experiments on the same receiver. As the experiment plan called for experiments at the lower pressure level (4 bar) to be conducted first, the oxidation on the receiver, and hence its absorptance, during the 12 bar experiment runs were greater leading to better energy efficiencies at higher pressures in Table 30 for all receivers. Regarding the thermal efficiency, since the value of receiver absorptance used in the calculation of this efficiency is one was only measured at the end of all the experiment runs on the receiver, this absorptance will certainly be larger than the actual absorptance for many of the operating condition sets. This is especially true for the earliest experiments with the receiver i.e. the low pressure (4 bar) experiment runs. Referring to the equation of thermal efficiency (equation (7)), the thermal efficiency falls as absorptance rises. Hence the thermal efficiencies at inlet pressures of 4 bar are penalised most by considering their absorptances to be higher than they should be.

On the other hand, this same consideration leads to the conclusion that the thermal efficiencies reported in Table 30 can only be smaller and not larger than the true thermal efficiencies and thus the maximum value of thermal efficiency observed for each receiver is significant. The highest thermal efficiency noted is that of PR1 at

94.7%. PR3 appears to be the worst performing receiver, as predicted by the numerical model, with no operating condition set seeing it cross the 90% threshold. The other two receivers have thermal efficiencies just above 90% for multiple operating condition sets though these efficiencies are too close together in value to make any definitive comparative assessment.

Encouragingly, the pressure drop at the highest thermal efficiency is just 0.84% of the inlet pressure and similar values of relative pressure drop are observed at thermal efficiencies above 90% for the PR1 receiver. Though the thermal efficiencies of the PR2 and PR4 are slightly lower than those corresponding to PR1, the pressure drops are an order of magnitude lower with relative pressure drops below 0.30% of the inlet pressure. This not only experimentally demonstrates that the receivers achieve a high thermal efficiency without excessive pressure drop but also indicates that, as predicted by the numerical model, an optimum receiver geometrical configuration has taller and narrower channels.

## 4.4. Sensitivity analysis

The influence of experimental errors on the final results was evident even before detailed post-processing of the experimental data was performed. These were the findings from the preliminary tests (section 3.6) besides the experiment campaign. To quantify the effects of these experimental errors and uncertainties, a sensitivity analysis was performed to assess the impact of deviations from the setpoint of the following key parameters:

- Mass flow rate
- Incident radiation flux
- Inlet pressure
- Air composition
- Absorptance

The pressurised receiver model of the PR1 geometry, modified to include the surface roughness effect, has been used to perform this sensitivity analysis. A uniform incident radiation flux distribution and absorptance are assumed across the receiver exposed/incident surface.

The performance indicators assessed are the thermal efficiency, energy efficiency, outlet temperature and pressure drop of the receiver. A basic curve fitting is applied to the distributions obtained from the numerical model to better understand the relationship between the performance indicator in question and the studied input parameter.

### 4.4.1. Effect of mass flow rate

The numerical model assumed a uniform incident flux of 400 kW $m^{-2}$, inlet pressure of 12 bar and an absorptance of 0.7 to evaluate the effect of the mass flow rate. The mass flow rate is varied from 1 to 3 g $s^{-1}$ in intervals of 0.25 g $s^{-1}$. The results of this analysis are presented in Figure 104.

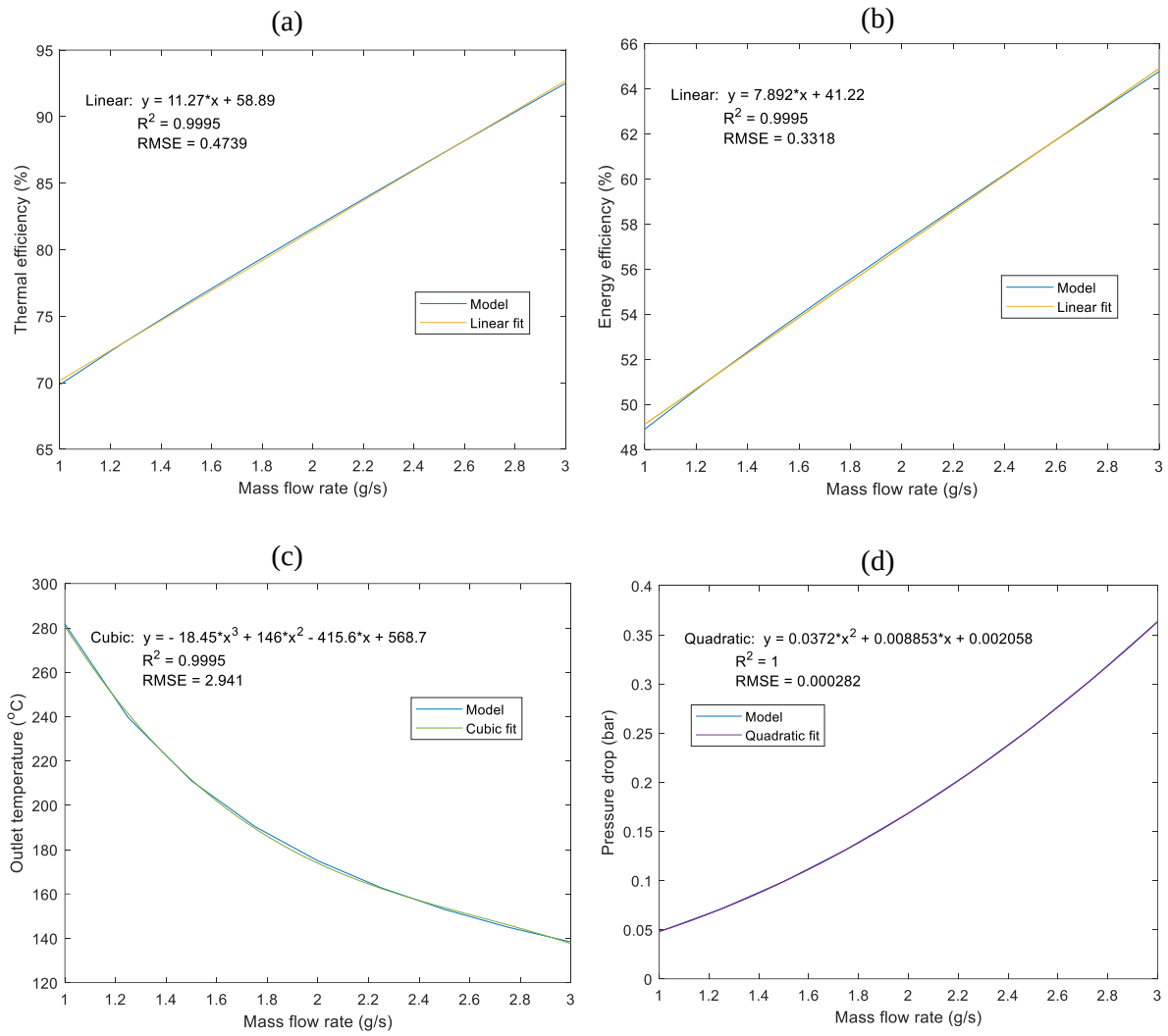


Figure 104. Influence of mass flow rate variation on receiver performance indicators: (a) Thermal efficiency, (b) Energy efficiency, (c) Outlet temperature, (d) Pressure drop

As can be observed from the fitted curves in Figure 104, the behaviour of the thermal and energy efficiencies with varying mass flow rate is linear while the outlet temperature and pressure drop curves are cubic and quadratic respectively. This highlights the significance of the mass flow rate on the general performance of the receiver. More sensitive automatic mass flow controllers must be employed in future experimental works to better control this crucial parameter to minimise the effect of its variability on the output performance indicators and permit better comparative analyses with less error.

### 4.4.2. Effect of incident radiation flux

The numerical model assumed a constant mass flow rate of 2 g $s^{-1}$, inlet pressure of 12 bar and an absorptance of 0.7 to evaluate the effect of the incident radiation flux. The flux is varied from 200 to 500 kW $m^{-2}$ in intervals of 50 kW $m^{-2}$. The results of this analysis are presented in Figure 105.

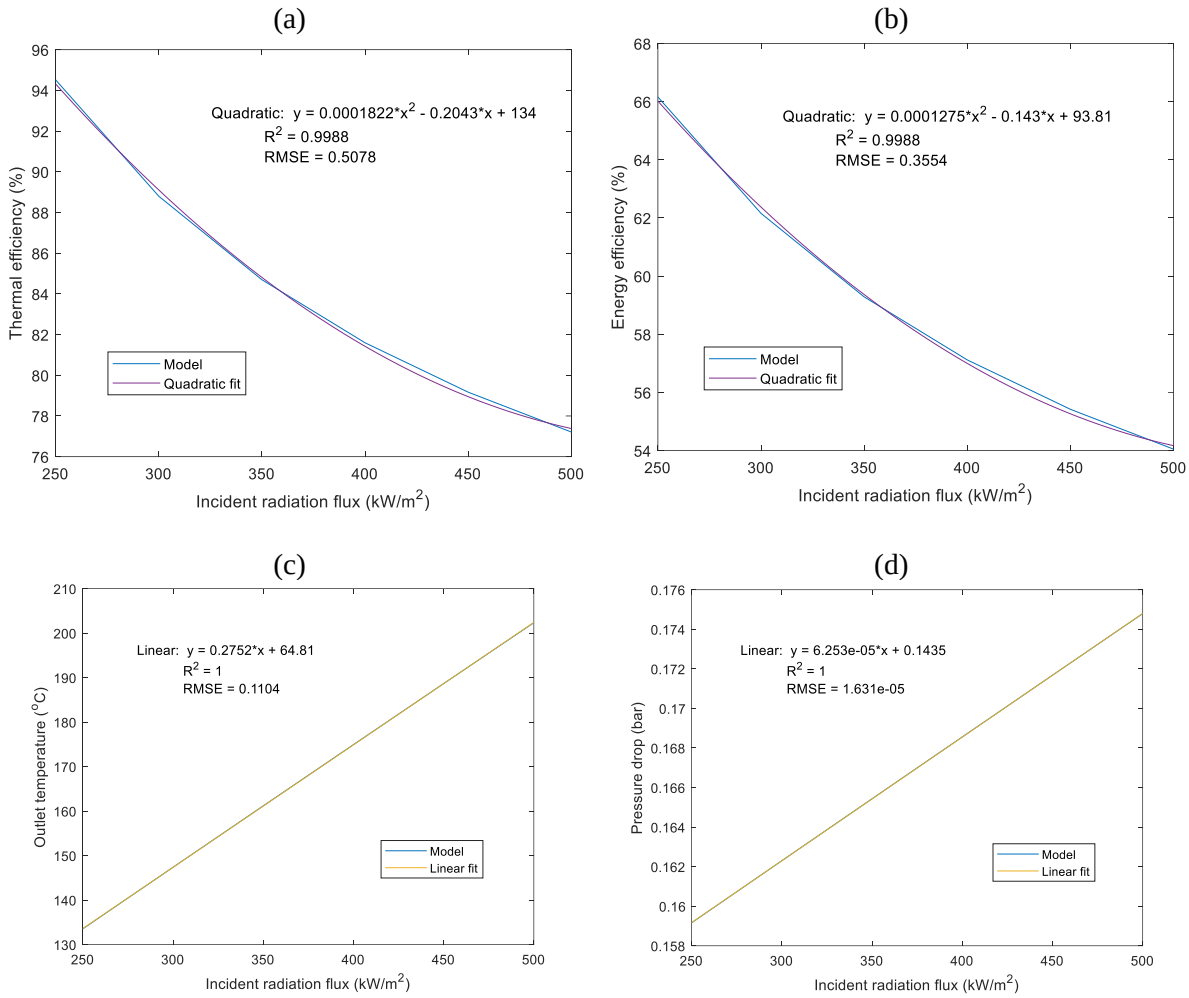


Figure 105. Influence of incident radiation flux variation on receiver performance indicators: (a) Thermal efficiency, (b) Energy efficiency, (c) Outlet temperature, (d) Pressure drop

As can be observed from the fitted curves in Figure 105, the outlet temperature and pressure drop vary linearly with variations in the mass flow rate while the thermal and energy efficiencies curves are both quadratic. The pressure drop is weakly related to the incident radiation flux as can be seen in Figure 105(d) and this is generally consistent with the experimental results seen in section 4.3. Contrarily, the outlet temperature has a far stronger relation with the incident radiation flux as is expected intuitively as well as is seen in the experiments.

### 4.4.3. Effect of inlet pressure

The inlet pressure was difficult to maintain constant during the experiments as the only control was manually from the cylinder valve once the experiment run began as described in section 3.3.1. As the compressed air cylinder discharged, its outlet pressure decreased continuously and its valve had to hence be slightly adjusted accordingly. It was hence ascertained as a highly variable 'control' parameter and required a sensitivity analysis to determine the effects of its variability. A uniform incident flux of 400 kW $m^{-2}$, mass flow rate of 2 g $s^{-1}$ and an absorptance of 0.7 was used in the model. The inlet pressure is varied from 3 to 15 bar in intervals of 0.5 bar. The results of this analysis are presented in Figure 106.

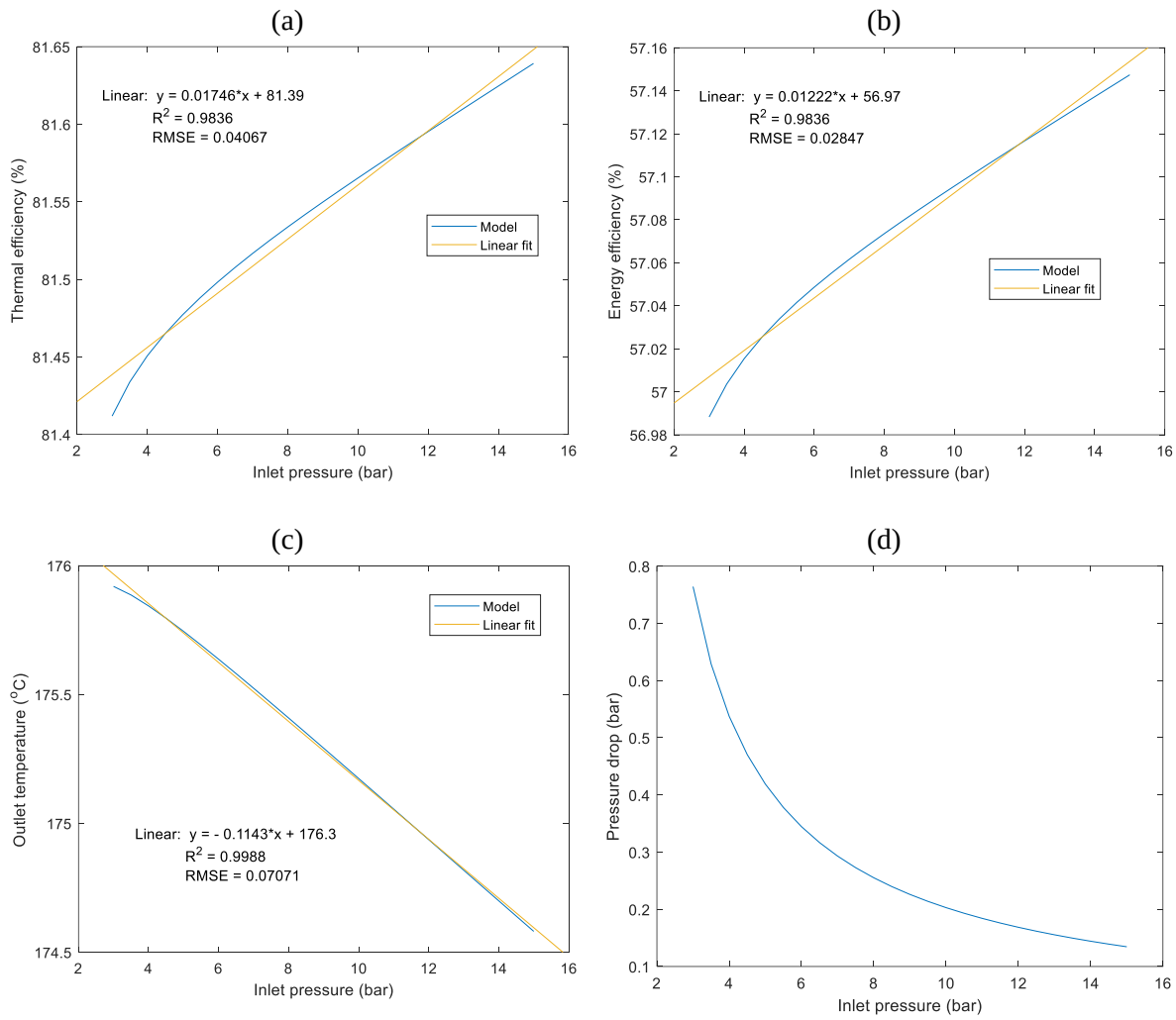


Figure 106. Influence of incident radiation flux variation on receiver performance indicators: (a) Thermal efficiency, (b) Energy efficiency, (c) Outlet temperature, (d) Pressure drop

As can be observed from the fitted curves in Figure 106, the outlet temperature as well as both efficiencies vary linearly with changing inlet pressure especially above pressures of 5 bar.

### 4.4.4. Effect of air composition

It was seen in the preliminary experiments with air supplied from a compressor (section 3.6.2) as well as with receiver PR4 that the air composition plays an important role in the performance od the receiver. The numerical model to analyse this assumed a uniform incident flux of 400 kW $m^{-2}$, inlet pressure of 12 bar and an absorptance of 0.7 while varying the $N_2$ concentration in a $N_2$:$O_2$ mixture from 77.5% to 79% in intervals of 0.1%. The results of this analysis are presented in Figure 107.

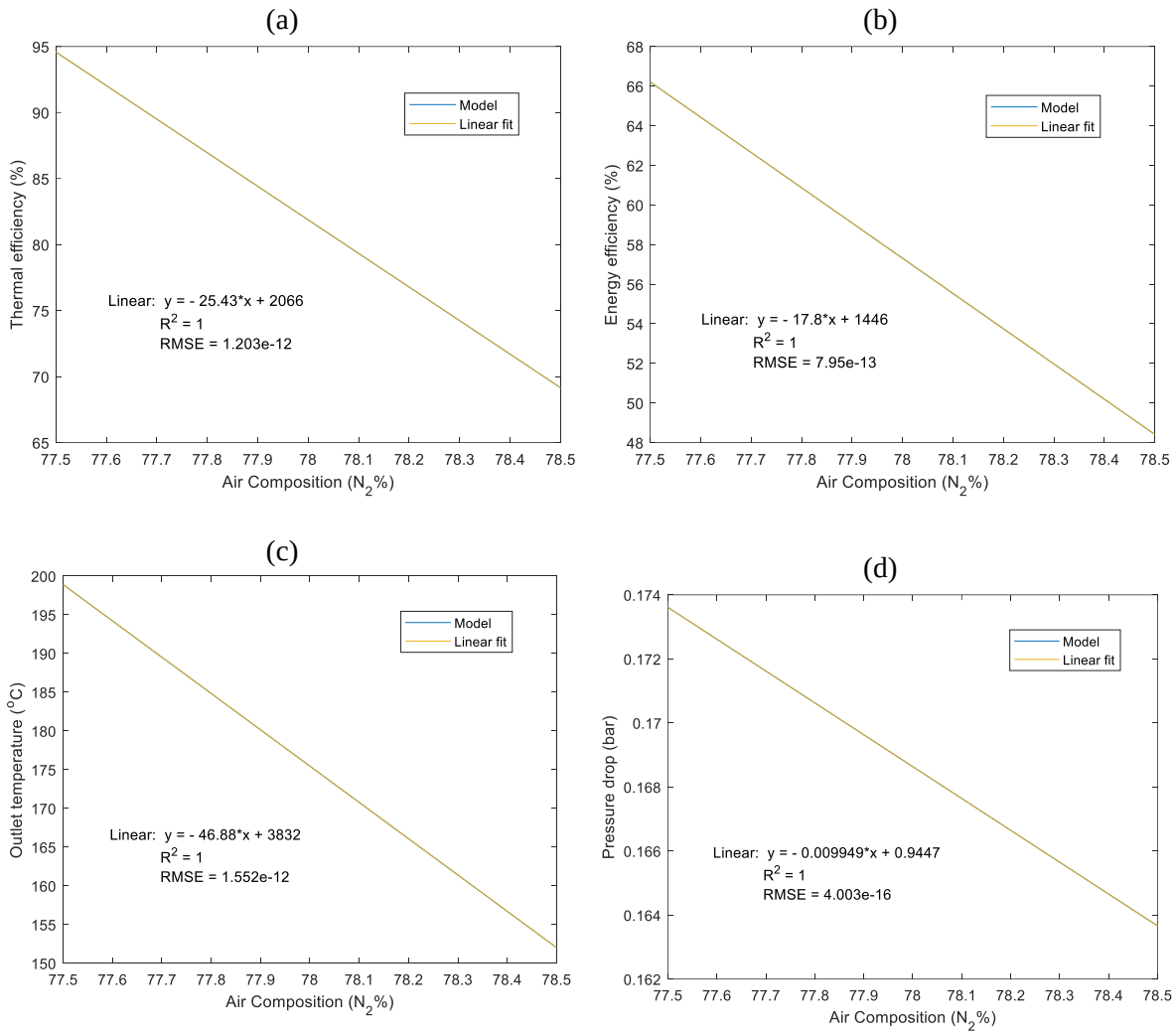


Figure 107. Influence of air composition (% of $N_2$ in dry air) on receiver performance indicators: (a) Thermal efficiency, (b) Energy efficiency, (c) Outlet temperature, (d) Pressure drop

As can be observed from the fitted curves in Figure 107, the behaviour of the performance indicators all vary linearly and are indirectly related to the percentage of Nitrogen in the air mix. While the effect of the air composition doesn't appear to affect the pressure drop significantly, it has a far more profound impact on the thermal performance indicators selected.

### 4.4.5. Effect of absorptance

The numerical model assumed a uniform incident flux of 400 kW $m^{-2}$, inlet pressure of 12 bar and a mass flow rate of 2 g $s^{-1}$ to evaluate the effect of the absorptance. The absorptance itself is varied from 50% to 70% in intervals of 5%. The results of this analysis are presented in Figure 108.

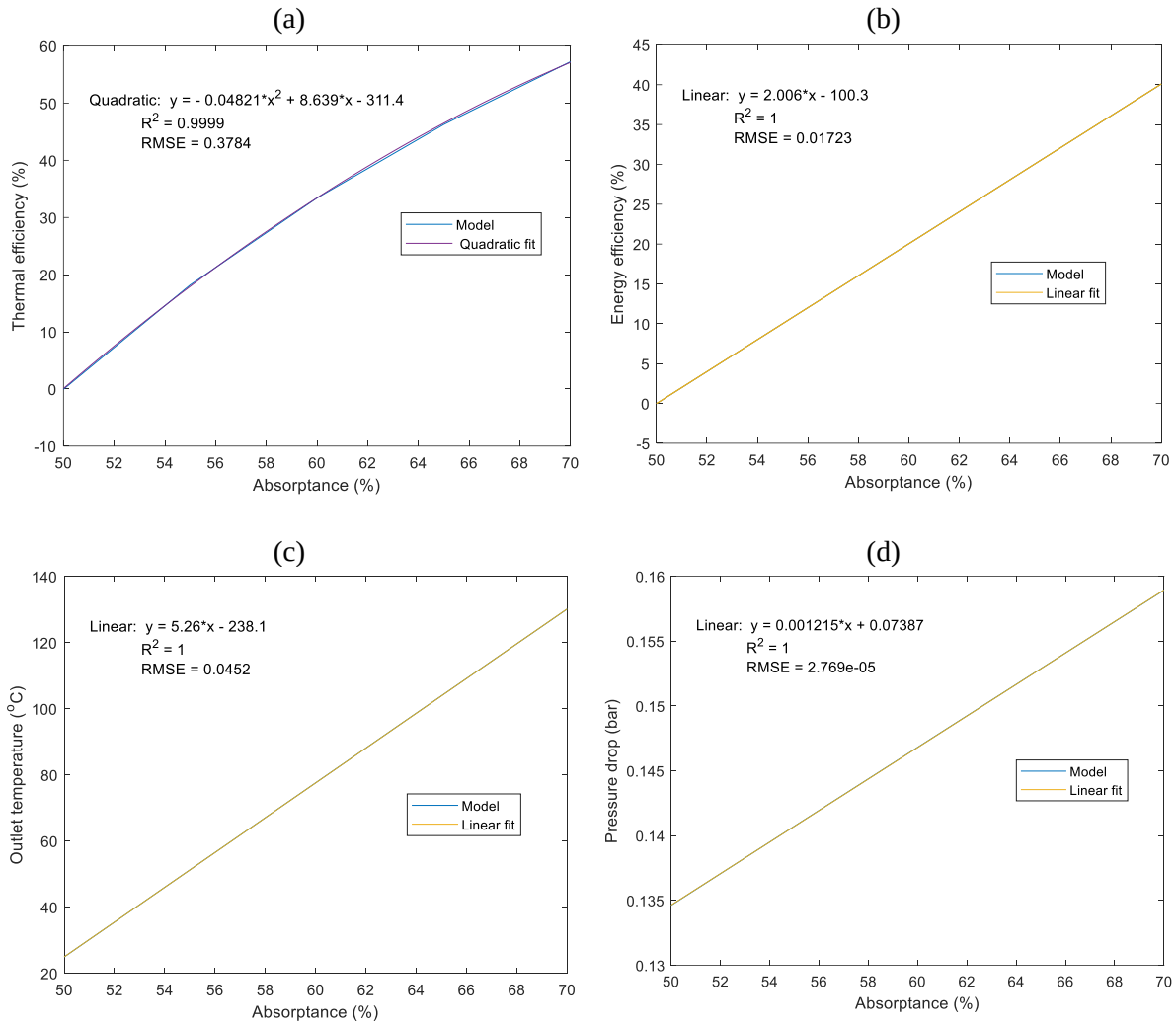


Figure 108. Influence of absorptance on receiver performance indicators: (a) Thermal efficiency, (b) Energy efficiency, (c) Outlet temperature, (d) Pressure drop

As can be observed from the fitted curves in Figure 108, the behaviour of the thermal efficiency with varying absorptance is quadratic while the other indicators have a linear relation. All performance indicators here are directly related to the absorptance though the pressure drop is more weakly proportional than the other indicators.

## 4.5. Conclusions

In this chapter the results of the experimental campaign on the four pressurised receivers were presented and elaborated. As one of the important objectives of the experimental work was to validate some of the findings of the numerical model, it was imperative that the numerical model was modified and adapted to be able to be employed in the prediction of the experimental results. The modifications were made to better the applicability of the model to input physical realities such as the inhomogeneity of the incident radiation flux, surface roughness of the flow channels, variable absorptivity of the receiver due to uneven surface oxidation and additional pressure losses in the system.

The experimental campaign, which consisted of experiments on all four receivers, entailed varying the controlled parameters of the incident radiation power (peak radiation flux), mass flow rate and receiver inlet pressure. The main output performance indicators, directly measured by the calorimetric test loop, were the receiver outlet temperature, pressure drop, energy and thermal efficiency. A maximum thermal efficiency of 94.7% was achieved in the PR1 receiver at a mass flow rate of 2 g $s^{-1}$, an inlet pressure of 12 bar and a peak incident flux of 400 kW $m^{-2}$. The pressure drop at this operating point was 0.84% of the inlet pressure which is remarkably low for such a high corresponding thermal efficiency value as compared with the state of the art. Thermal efficiencies above 90% were also observed with the PR2 and PR4 receivers and their corresponding pressure drops were far lower than those of PR1 at below 0.30% of the inlet pressure. These observations showcase the improved performance of the pressurised receiver concept as they boast high thermal efficiencies and low pressure drops. Moreover, the significant decrease in the relative pressure drops while only slightly penalising the thermal efficiencies, in the case of PR2 and PR4 as compared with PR1, indicate that the optimum flow channel geometry might be one with taller and narrower channels. Temperature rises of above 350 °C were also attained at the maximum peak incident flux level of 500 kW $m^{-2}$ and the lowest mass flow rate of 1 g $s^{-1}$.

The behaviour of the analysed performance indicators corresponded well with the predictions of the receiver numerical model, within the limits of error. Moreover, the comparative analysis of the receivers experimentally demonstrated what the numerical model predicted i.e. better heat transfer to the fluid in smaller channels and the preference for channels with increased channel height and thicker walls at the right combination of mass flow rate and inlet pressure.

A major source of uncertainty in the experimental analysis was inadequate quantification of the absorptance of the receiver. This issue could have been mitigated by either measuring the receiver's absorptance after each experiment run or pre-treating the receiver so as to have a near constant absorptance with the latter option preferred for simplicity and experiment time saving. A mass flow controller to automatically and more accurately control the mass flow rate would also be a valuable improvement to the testbed to reduce the error related with the same. Unwanted illumination of the side walls of the receiver was also identified during the experimentation which can be avoided by better design of the receiver insulation. The receiver and insulation could also be better designed so as to allow for the ready introduction of thermocouples that can be easily added and removed, as required, to reliably measure the receiver's solid temperature.

A sensitivity analysis was also performed to quantify the effects of the variability of the mass flow rate, incident radiation flux, inlet pressure, composition of air and absorptance of the receiver. This performance indicators evaluated in this analysis were the thermal efficiency, energy efficiency, outlet temperature and pressure drop.

# Chapter 5. Summary, conclusions and future work

Concentrated solar thermal energy systems are a promising sustainable energy technology that can be harnessed by a diverse range of applications from power generation to industrial process heating. One of the most critical components of any concentrated solar thermal technology is its receiver whose primary objective is to most efficiently convert the incident solar radiation to heat which is typically in the form of heat transferred to a working fluid circulating in the receiver. In this thesis, the use of compact flow channel geometries in solar receivers was proposed and analysed as a method to improve the receiver efficiency.

Performance enhancement owing to the use of compact flow channel geometries, especially when the working fluid is a gas, is a well understood and applied concept in the actively commercial field of compact heat exchangers. It is envisaged that by employing these concepts in the design of solar receivers, a betterment in the performance and efficiencies of these receivers, as compared to the state of the art, may be achieved.

Pressurised gases receivers in particular have been identified and analysed, though the application of compact flow channel geometries is not limited to only gas receivers, as the use of pressurised gases offers unique advantages including high temperature and pressure operability, stability, non-toxicity and inexpensiveness.

Chapter 1 introduces topics relevant to the development of the thesis including an overview of concentrated solar thermal technologies with subtopics of heat transfer fluids typically used in receivers and selected applications of concentrated solar and their respective requirements. Though the concepts of compact flow channel geometries can be applied to other concentrated solar thermal technology types, central receivers (or solar tower receivers) have been analysed in this work. Compact heat exchangers and their suitability for use in solar receivers is also discussed in chapter 1 followed by a review of the state of the art in solar receivers using pressurised gases and potential performance indicators that could be used to evaluate such receivers. Among these discussed performance indicators, exergy efficiency was identified as being a potent tool for optimisation in design and evaluation of performance of receivers as it includes both the useful heat gain from incident solar radiation as well as the undesired pressure drop.

In order to evaluate the performance of pressurised gas receivers using compact flow channel geometries, a numerical model of the same had to first be developed and this is the focus of chapter 2. The development of the simplified receiver numerical model was conducted in such a way as to facilitate the addition of different flow channel geometries and allow for variation in their respective geometrical parameters. Six flow channel geometries were analysed in this numerical work namely the plain rectangular, plain triangular, offset strip fin, wavy fin, perforated fin and louvred fin geometries. A parametric study varying four common geometrical parameters common to all the above flow channel geometries was also performed in order to identify the receiver geometric configuration with the best performance in terms of energy and exergy efficiency. The pressurised receivers were analysed in application to a $sCO_2$ power plant. It was observed that the perforated fin receiver has the best exergy efficiency followed by the plain rectangular and wavy fin respectively. The increased pressure drop due to smaller channel sizes sets a minimum limit to this size though the heat transfer is improved with smaller channel sizes. An increase in the channel height, to a limit, reduces the pressure drop while not excessively penalising the heat transfer through the receiver if the channel wall thickness is sufficiently thick as the heat transfer resistance through the solid wall is far lower than that through the gas in the channels. Hence by having narrower and thicker walled channels, the thermal resistance through the receiver bulk is reduced, or conversely the heat transfer to the fluid is improved, while also reducing the pressure drop.

This significant finding of the numerical modelling and parametric analysis was proposed to be tested and validated experimentally. This called for the development for a pressurised receiver testbed besides pressurised receiver samples to be experimented upon. Chapter 3 deals with the design and development of the

experimental testbed and the use of the KIRAN 42 high flux solar simulator as a radiation heat source in the experiments. The pressurised receiver samples were designed and fabricated using 3D printing and were of the plain rectangular geometry. The four receiver geometry variations were designed in such a way as to test the validity of the findings of the numerical model with regards to the influence of the channel height, breadth, thickness and number of vertical channels in the receiver's performance. Preliminary test runs after the assembly of the testbed with an installed receiver highlighted some glaring shortcomings of the setup, most of which could be addressed. These test runs also provided operational experience that enabled the drafting of operational procedures for the pressurised receiver testbed.

The design of experiments called for the variation of three principal operational parameters, namely the mass flow rate, inlet pressure and peak incident radiation flux and analysing the influence of these three parameters on the performance of the receivers. It was observed that the predictions of the numerical model largely lined up well the experimental results. The receiver with the smallest channels has the highest thermal efficiency of 94.7% which is higher than that of several state-of-the-art receivers whose thermal efficiencies do not cross 90%. Besides this high thermal efficiency, the corresponding pressure drop is also low at only 0.84% of the inlet pressure which is far better than the state of the art at similar thermal efficiencies. On the other hand, besides the smallest channel sized receiver, the two receivers with increased channel height were also observed with slightly inferior thermal efficiencies, though still over 90%, and even lower relative pressure drops of around 0.30%.

These experimental results illustrate not only the improved performance of the conceptualised pressured receivers in terms of high thermal efficiencies at small pressure drops but also indicate that the optimum receiver flow channel geometrical configuration may have taller and narrower channels. The influence of the channel wall thickness, differentiating the two receivers with increased channel height, is not so clear. What is more easily evident though is the deterioration in performance of the receiver with the increased channel breadth. All these findings are precisely as predicted by the numerical model.

A major source of error in the experimental analysis is the absorptance of the receivers themselves. The receivers, manufactured of stainless steel, were untreated and unoxidised before experimentation. As steels typically oxidised, and darken, at elevated temperatures, the true absorptance of the receivers at every operating parameter set, which was only measured after all the experiments on it had been completed, was an unknown quantity.

Given this and other sources of errors, it was proposed to perform a sensitivity analysis to evaluate and quantify the effect of the variation of the absorptance, mass flow rate, radiation power, air composition and inlet pressure. The performance indicators evaluated in this study were the outlet temperature, pressure drop, energy and thermal efficiencies. As was observed during the experiment runs, the sensitivity analysis using the numerical model confirmed that these factors substantially affect the performance of the receivers.

The thesis has numerically and experimentally advanced the case for the use of compact flow channel geometries in pressurised gas receivers. There are several lines of research into furthering its development. The receiver numerical model, having been developed, can be employed to study in more depth the optimum set of operating conditions including heat transfer fluid, mass flow rates, inlet pressures, incident radiation flux profiles, absorptances etc. Alternative receiver configurations and combinations, external light trapping structures and the effect of coatings and surface treatments can relatively easily been simulated by the receiver model.

While it has been employed for steady state analysis, the receiver model can readily be exploited for use in transient simulation analysis to evaluate the performance of different receiver concepts under varying operational conditions over an extended period of time.

The pressurised receiver testbed can also be further utilised to evaluate the performance of receivers of various materials or with different surface treatments under varying conditions of mass flow rate, inlet pressure, working gas, incident radiation levels etc. As was mentioned previously, the receiver testbed was designed for flexibility in operation and can permit several parametric studies to be performed on it. Receiver sizes and configurations can also be tested within limits.

# References

[1] ‘World Energy Outlook 2020’. International Energy Agency (IEA).
[2] ‘Energy Outlook: 2020 edition’. BP, 2020.
[3] ‘Renewables Global Status Report’, REN21.
[4] S. Teske, T. Pregger, S. Simon, and T. Naegler, ‘High renewable energy penetration scenarios and their implications for urban energy and transport systems’, *Curr. Opin. Environ. Sustain.*, vol. 30, pp. 89–102, Feb. 2018, doi: 10.1016/j.cosust.2018.04.007.
[5] D. Bogdanov, A. Gulagi, M. Fasihi, and C. Breyer, ‘Full energy sector transition towards 100% renewable energy supply: Integrating power, heat, transport and industry sectors including desalination’, *Appl. Energy*, vol. 283, p. 116273, Feb. 2021, doi: 10.1016/j.apenergy.2020.116273.
[6] E. Pursiheimo, H. Holttinen, and T. Koljonen, ‘Inter-sectoral effects of high renewable energy share in global energy system’, *Renew. Energy*, vol. 136, pp. 1119–1129, Jun. 2019, doi: 10.1016/j.renene.2018.09.082.
[7] R. A. Verzijlbergh, L. J. De Vries, G. P. J. Dijkema, and P. M. Herder, ‘Institutional challenges caused by the integration of renewable energy sources in the European electricity sector’, *Renew. Sustain. Energy Rev.*, vol. 75, pp. 660–667, Aug. 2017, doi: 10.1016/j.rser.2016.11.039.
[8] J. A. Duffie and W. A. Beckman, *Solar engineering of thermal processes*, 4. ed. New York: Wiley, 2013.
[9] T. Eglinton, J. Hinkley, A. Beath, and M. Dell’Amico, ‘Potential Applications of Concentrated Solar Thermal Technologies in the Australian Minerals Processing and Extractive Metallurgical Industry’, *JOM*, vol. 65, no. 12, pp. 1710–1720, Dec. 2013, doi: 10.1007/s11837-013-0707-z.
[10] S. Abanades, S. Rodat, and H. Boujjat, ‘Solar Thermochemical Green Fuels Production: A Review of Biomass Pyro-Gasification, Solar Reactor Concepts and Modelling Methods’, *Energies*, vol. 14, no. 5, p. 1494, Mar. 2021, doi: 10.3390/en14051494.
[11] W. Grasse, H. P. Hertlein, C.-J. Winter, and G. W. Braun, ‘Thermal Solar Power Plants Experience’, in *Solar Power Plants*, C.-J. Winter, R. L. Sizmann, and L. L. Vant-Hull, Eds. Berlin, Heidelberg: Springer Berlin Heidelberg, 1991, pp. 215–282. doi: 10.1007/978-3-642-61245-9_7.
[12] P. Falcone, ‘A handbook for solar central receiver design’, SAND-86-8009, 6545992, ON: DE87009985, Dec. 1986. doi: 10.2172/6545992.
[13] E. Zarza-Moya, ‘Concentrating Solar Thermal Power’, in *A Comprehensive Guide to Solar Energy Systems*, Elsevier, 2018, pp. 127–148. doi: 10.1016/B978-0-12-811479-7.00007-5.
[14] C. K. Ho, ‘Advances in central receivers for concentrating solar applications’, *Sol. Energy*, vol. 152, pp. 38–56, Aug. 2017, doi: 10.1016/j.solener.2017.03.048.
[15] R. Thonig and J. Lilliestam, ‘CSP.guru 2022-07-01’. Zenodo, Jul. 01, 2022. doi: 10.5281/ZENODO.7010643.
[16] U. Pelay, L. Luo, Y. Fan, D. Stitou, and M. Rood, ‘Thermal energy storage systems for concentrated solar power plants’, *Renew. Sustain. Energy Rev.*, vol. 79, pp. 82–100, Nov. 2017, doi: 10.1016/j.rser.2017.03.139.
[17] W.-D. Steinmann and C. Prieto, ‘Thermal storage for concentrating solar power plants’, in *Advances in Thermal Energy Storage Systems*, Elsevier, 2021, pp. 673–697. doi: 10.1016/B978-0-12-819885-8.00024-3.
[18] E. González-Roubaud, D. Pérez-Osorio, and C. Prieto, ‘Review of commercial thermal energy storage in concentrated solar power plants: Steam vs. molten salts’, *Renew. Sustain. Energy Rev.*, vol. 80, pp. 133–148, Dec. 2017, doi: 10.1016/j.rser.2017.05.084.
[19] S. Kuravi, J. Trahan, D. Y. Goswami, M. M. Rahman, and E. K. Stefanakos, ‘Thermal energy storage technologies and systems for concentrating solar power plants’, *Prog. Energy Combust. Sci.*, vol. 39, no. 4, pp. 285–319, Aug. 2013, doi: 10.1016/j.pecs.2013.02.001.

[20] B. Brand, A. Boudghene Stambouli, and D. Zejli, 'The value of dispatchability of CSP plants in the electricity systems of Morocco and Algeria', *Energy Policy*, vol. 47, pp. 321–331, Aug. 2012, doi: 10.1016/j.enpol.2012.04.073.

[21] A. M. Yasin, 'The Impact of Dispatchability of Parabolic Trough CSP Plants over PV Power Plants in Palestinian Territories', *Int. J. Photoenergy*, vol. 2019, pp. 1–14, Oct. 2019, doi: 10.1155/2019/4097852.

[22] F. M. Aprà, S. Smit, R. Sterling, and T. Loureiro, 'Overview of the Enablers and Barriers for a Wider Deployment of CSP Tower Technology in Europe', *Clean Technol.*, vol. 3, no. 2, pp. 377–394, Apr. 2021, doi: 10.3390/cleantechnol3020021.

[23] G. J. Kolb, 'Economic evaluation of solar-only and hybrid power towers using molten-salt technology', *Sol. Energy*, vol. 62, no. 1, pp. 51–61, Jan. 1998, doi: 10.1016/S0038-092X(97)00075-3.

[24] A. Gil *et al.*, 'State of the art on high temperature thermal energy storage for power generation. Part 1—Concepts, materials and modellization', *Renew. Sustain. Energy Rev.*, vol. 14, no. 1, pp. 31–55, Jan. 2010, doi: 10.1016/j.rser.2009.07.035.

[25] K. S. do Couto Aktay, R. Tamme, and H. Müller-Steinhagen, 'Thermal Conductivity of High-Temperature Multicomponent Materials with Phase Change', *Int. J. Thermophys.*, vol. 29, no. 2, pp. 678–692, Apr. 2008, doi: 10.1007/s10765-007-0315-7.

[26] P. Pardo, A. Deydier, Z. Anxionnaz-Minvielle, S. Rougé, M. Cabassud, and P. Cognet, 'A review on high temperature thermochemical heat energy storage', *Renew. Sustain. Energy Rev.*, vol. 32, pp. 591–610, Apr. 2014, doi: 10.1016/j.rser.2013.12.014.

[27] P. Kurup and C. Turchi, 'Initial Investigation into the Potential of CSP Industrial Process Heat for the Southwest United States', National Renewable Energy Laboratory, NREL/TP-6A20-64709, Nov. 2015.

[28] M. Romero and J. González-Aguilar, 'Solar thermal CSP technology: Solar thermal CSP technology', *Wiley Interdiscip. Rev. Energy Environ.*, vol. 3, no. 1, pp. 42–59, Jan. 2014, doi: 10.1002/wene.79.

[29] P. W. Heller, Ed., *The performance of concentrated solar power (CSP) systems: analysis, measurement and assessment*. Cambridge, MA: Woodhead Publishing, an imprint of Elsevier, 2017.

[30] R. P. Merchán, M. J. Santos, A. Medina, and A. Calvo Hernández, 'High temperature central tower plants for concentrated solar power: 2021 overview', *Renew. Sustain. Energy Rev.*, vol. 155, p. 111828, Mar. 2022, doi: 10.1016/j.rser.2021.111828.

[31] M. Blanco and L. Ramirez Santigosa, Eds., *Advances in concentrating solar thermal research and technology*. Oxford: Woodhead Publishing, 2017.

[32] M. Romero, R. Buck, and J. E. Pacheco, 'An Update on Solar Central Receiver Systems, Projects, and Technologies', *J. Sol. Energy Eng.*, vol. 124, no. 2, pp. 98–108, May 2002, doi: 10.1115/1.1467921.

[33] J. S. M. Jebamalai, 'Receiver Design Methodology for Solar Tower Power Plants', KTH University, 2016.

[34] A. Lenert, Y. Nam, and E. N. Wang, 'HEAT TRANSFER FLUIDS', *Annu. Rev. Heat Transf.*, vol. 15, no. 15, pp. 93–129, 2012, doi: 10.1615/AnnualRevHeatTransfer.2012004122.

[35] M. Mehos, C. Turchi, J. Vidal, M. Wagner, and Z. Ma, 'Concentrating Solar Power Gen3 Demonstration Roadmap', *Renew. Energy*, p. 140, 2017.

[36] C. Lang and B. Lee, 'Heat Transfer Fluid Life Time Analysis of Diphenyl Oxide/Biphenyl Grades for Concentrated Solar Power Plants', *Energy Procedia*, vol. 69, pp. 672–680, May 2015, doi: 10.1016/j.egypro.2015.03.077.

[37] L. Moens and D. Blake, 'Mechanism of Hydrogen Formation in Solar Paraboic Trough Receivers', NREL/TP-510-42468, 924987, Feb. 2008. doi: 10.2172/924987.

[38] S. Bell, T. Steinberg, and G. Will, ‘Corrosion mechanisms in molten salt thermal energy storage for concentrating solar power’, *Renew. Sustain. Energy Rev.*, vol. 114, p. 109328, Oct. 2019, doi: 10.1016/j.rser.2019.109328.
[39] C. K. Ho and B. D. Iverson, ‘Review of high-temperature central receiver designs for concentrating solar power’, *Renew. Sustain. Energy Rev.*, vol. 29, pp. 835–846, Jan. 2014, doi: 10.1016/j.rser.2013.08.099.
[40] M. Sedighi *et al.*, ‘Design of high-temperature atmospheric and pressurised gas-phase solar receivers: A comprehensive review on numerical modelling and performance parameters’, *Sol. Energy*, vol. 201, pp. 701–723, May 2020, doi: 10.1016/j.solener.2020.03.025.
[41] A. L. Ávila-Marín, ‘Volumetric receivers in Solar Thermal Power Plants with Central Receiver System technology: A review’, *Sol. Energy*, vol. 85, no. 5, pp. 891–910, May 2011, doi: 10.1016/j.solener.2011.02.002.
[42] F. Gomez-Garcia, J. González-Aguilar, G. Olalde, and M. Romero, ‘Thermal and hydrodynamic behavior of ceramic volumetric absorbers for central receiver solar power plants: A review’, *Renew. Sustain. Energy Rev.*, vol. 57, pp. 648–658, May 2016, doi: 10.1016/j.rser.2015.12.106.
[43] R. Capuano *et al.*, ‘Numerical models of advanced ceramic absorbers for volumetric solar receivers’, *Renew. Sustain. Energy Rev.*, vol. 58, pp. 656–665, May 2016, doi: 10.1016/j.rser.2015.12.068.
[44] D. D’Souza, M. J. Montes, M. Romero, and J. González-Aguilar, ‘Energy and exergy analysis of microchannel central solar receivers for pressurised fluids’, *Appl. Therm. Eng.*, vol. 219, p. 119638, Jan. 2023, doi: 10.1016/j.applthermaleng.2022.119638.
[45] J. Muñoz-Anton, M. Biencinto, E. Zarza, and L. E. Díez, ‘Theoretical basis and experimental facility for parabolic trough collectors at high temperature using gas as heat transfer fluid’, *Appl. Energy*, vol. 135, pp. 373–381, Dec. 2014, doi: 10.1016/j.apenergy.2014.08.099.
[46] E. Almatrafi, A. Khaliq, and T. Alquthami, ‘Thermodynamic investigation of a novel cooling-power cogeneration system driven by solar energy’, *Int. J. Refrig.*, vol. 138, pp. 244–258, Jun. 2022, doi: 10.1016/j.ijrefrig.2022.03.017.
[47] M. Sedighi, R. V. Padilla, R. A. Taylor, M. Lake, I. Izadgoshasb, and A. Rose, ‘High-temperature, point-focus, pressurised gas-phase solar receivers: A comprehensive review’, *Energy Convers. Manag.*, vol. 185, pp. 678–717, Apr. 2019, doi: 10.1016/j.enconman.2019.02.020.
[48] E. Bellos, C. Tzivanidis, K. A. Antonopoulos, and I. Daniil, ‘The use of gas working fluids in parabolic trough collectors – An energetic and exergetic analysis’, *Appl. Therm. Eng.*, vol. 109, pp. 1–14, Oct. 2016, doi: 10.1016/j.applthermaleng.2016.08.043.
[49] E. Bellos, C. Tzivanidis, and K. A. Antonopoulos, ‘A detailed working fluid investigation for solar parabolic trough collectors’, *Appl. Therm. Eng.*, vol. 114, pp. 374–386, Mar. 2017, doi: 10.1016/j.applthermaleng.2016.11.201.
[50] K. Lovegrove and W. Stein, *Concentrating solar power technology: principles, developments, and applications*, Second edition. Duxford: Elsevier Woodhead Publishing, 2021.
[51] S. M. Besarati and D. Y. Goswami, ‘Supercritical CO2 and other advanced power cycles for concentrating solar thermal (CST) systems’, in *Advances in Concentrating Solar Thermal Research and Technology*, Elsevier, 2017, pp. 157–178. doi: 10.1016/B978-0-08-100516-3.00008-3.
[52] C. S. Turchi, Z. Ma, T. W. Neises, and M. J. Wagner, ‘Thermodynamic Study of Advanced Supercritical Carbon Dioxide Power Cycles for Concentrating Solar Power Systems’, *J. Sol. Energy Eng.*, vol. 135, no. 4, p. 041007, Nov. 2013, doi: 10.1115/1.4024030.

[53] V. Dostal, P. Hejzlar, and M. J. Driscoll, ‘The Supercritical Carbon Dioxide Power Cycle: Comparison to Other Advanced Power Cycles’, *Nucl. Technol.*, vol. 154, no. 3, pp. 283–301, Jun. 2006, doi: 10.13182/NT06-A3734.

[54] S. M. Besarati and D. Yogi Goswami, ‘Analysis of Advanced Supercritical Carbon Dioxide Power Cycles With a Bottoming Cycle for Concentrating Solar Power Applications’, *J. Sol. Energy Eng.*, vol. 136, no. 1, p. 010904, Feb. 2014, doi: 10.1115/1.4025700.

[55] J. I. Linares, M. J. Montes, A. Cantizano, and C. Sánchez, ‘A novel supercritical CO2 recompression Brayton power cycle for power tower concentrating solar plants’, *Appl. Energy*, vol. 263, p. 114644, Apr. 2020, doi: 10.1016/j.apenergy.2020.114644.

[56] ‘Solar Heat for Industrial Processes’. IRENA, Jan. 2015. [Online]. Available: www.irena.org/Publications

[57] C. A. Schoeneberger, C. A. McMillan, P. Kurup, S. Akar, R. Margolis, and E. Masanet, ‘Solar for industrial process heat: A review of technologies, analysis approaches, and potential applications in the United States’, *Energy*, vol. 206, p. 118083, Sep. 2020, doi: 10.1016/j.energy.2020.118083.

[58] Q. Li, G. Flamant, X. Yuan, P. Neveu, and L. Luo, ‘Compact heat exchangers: A review and future applications for a new generation of high temperature solar receivers’, *Renew. Sustain. Energy Rev.*, vol. 15, no. 9, pp. 4855–4875, Dec. 2011, doi: 10.1016/j.rser.2011.07.066.

[59] S. S. Mehendale, A. M. Jacobi, and R. K. Shah, ‘Fluid Flow and Heat Transfer at Micro- and Meso-Scales With Application to Heat Exchanger Design’, *Appl. Mech. Rev.*, vol. 53, no. 7, pp. 175–193, Jul. 2000, doi: 10.1115/1.3097347.

[60] S. Kakaç, H. Liu, and A. Pramuanjaroenkij, *Heat Exchangers: Selection, Rating, and Thermal Design, Third Edition*. Hoboken: CRC Press, 2012.

[61] L. Sheik Ismail, R. Velraj, and C. Ranganayakulu, ‘Studies on pumping power in terms of pressure drop and heat transfer characteristics of compact plate-fin heat exchangers—A review’, *Renew. Sustain. Energy Rev.*, vol. 14, no. 1, pp. 478–485, Jan. 2010, doi: 10.1016/j.rser.2009.06.033.

[62] K. W. M and L. A. L, *Compact Heat Exchangers (3rd Edition)*. 2018. Accessed: Aug. 16, 2021. [Online]. Available: https://app.knovel.com/hotlink/toc/id:kpCHEE0002/compact-heat-exchangers

[63] W. W. Focke and P. G. Knibbe, ‘Flow visualization in parallel-plate ducts with corrugated walls’, *J. Fluid Mech.*, vol. 165, no. 1, p. 73, Apr. 1986, doi: 10.1017/S0022112086003002.

[64] Alfa Laval, ‘How gasketed plate heat exchangers work’, *Gasketed plate heat exchangers*. https://www.alfalaval.com/microsites/gphe/tools/how-gphes-work/

[65] B. Thonon And E. Breuil, ‘Compact Heat Exchanger Technologies For The HTRs Recuperator Application’, International Atomic Energy Agency, Vienna, Austria, IAEA-Tecdoc--1238, Nov. 2000.

[66] L. Chai and S. A. Tassou, ‘A review of printed circuit heat exchangers for helium and supercritical CO2 Brayton cycles’, *Therm. Sci. Eng. Prog.*, vol. 18, p. 100543, Aug. 2020, doi: 10.1016/j.tsep.2020.100543.

[67] M. J. Montes, J. I. Linares, R. Barbero, and A. Rovira, ‘Proposal of a new design of source heat exchanger for the technical feasibility of solar thermal plants coupled to supercritical power cycles’, *Sol. Energy*, vol. 211, pp. 1027–1041, Nov. 2020, doi: 10.1016/j.solener.2020.10.042.

[68] J. E. Hesselgreaves, R. Law, and D. Reay, *Compact Heat Exchangers: Selection, Design and Operation*. Butterworth-Heinemann, 2016.

[69] S. Mellouli, F. Askri, H. Dhaou, A. Jemni, and S. Ben Nasrallah, ‘A novel design of a heat exchanger for a metal-hydrogen reactor’, *Int. J. Hydrog. Energy*, vol. 32, no. 15, pp. 3501–3507, Oct. 2007, doi: 10.1016/j.ijhydene.2007.02.039.

[70] X. Sun, X. Zhang, R. Christensen, and M. Anderson, ‘Compact Heat Exchanger Design and Testing for Advanced Reactors and Advanced Power Cycles’, 13–5101, 1437159, Mar. 2018. doi: 10.2172/1437159.
[71] A. Katz, S. R. Aakre, M. H. Anderson, and D. Ranjan, ‘Experimental investigation of pressure drop and heat transfer in high temperature supercritical CO2 and helium in a printed-circuit heat exchanger’, *Int. J. Heat Mass Transf.*, vol. 171, p. 121089, Jun. 2021, doi: 10.1016/j.ijheatmasstransfer.2021.121089.
[72] P. S. McNeff and B. K. Paul, ‘Manufacturing Process Design of a Microchannel Solar Receiver using Electrically-Assisted Embossing’, *Procedia Manuf.*, vol. 48, pp. 187–196, 2020, doi: 10.1016/j.promfg.2020.05.037.
[73] Q. Li, N. G. de Tourville, I. Yadroitsev, X. Yuan, and G. Flamant, ‘Micro-channel pressurized-air solar receiver based on compact heat exchanger concept’, *Sol. Energy*, vol. 91, pp. 186–195, May 2013, doi: 10.1016/j.solener.2013.02.004.
[74] K. Drost, ‘High Flux Microchannel Receiver Development with Adap-tive Flow Control’, Final Report, 1347906, Aug. 2015. doi: 10.2172/1347906.
[75] T. L’Estrange, ‘Title: Experimental Characterization of a Supercritical Carbon Dioxide Microchannel Solar Thermal Receiver’, Oregon State, 2015.
[76] J. Karni, A. Kribus, B. Ostraich, and E. Kochavi, ‘A High-Pressure Window for Volumetric Solar Receivers’, *J. Sol. Energy Eng.*, vol. 120, no. 2, pp. 101–107, May 1998, doi: 10.1115/1.2888051.
[77] T. Neises and C. Turchi, ‘A Comparison of Supercritical Carbon Dioxide Power Cycle Configurations with an Emphasis on CSP Applications’, *Energy Procedia*, vol. 49, pp. 1187–1196, 2014, doi: 10.1016/j.egypro.2014.03.128.
[78] ‘Thermo-economic optimization of an air driven supercritical CO2 Brayton power cycle for concentrating solar power plant with packed bed thermal energy storage’, *Sol. Energy*, vol. 211, pp. 1373–1391, Nov. 2020, doi: 10.1016/j.solener.2020.10.069.
[79] European Commission and Directorate General for Research, *SOLGATE: solar hybrid gas turbine electric power system*. Luxembourg: EUR-OP, 2005.
[80] L. Amsbeck, R. Buck, P. Heller, J. Jedamski, and R. Uhlig, ‘DEVELOPMENT OF A TUBE RECEIVER FOR A SOLAR-HYBRID MICROTURBINE SYSTEM’, presented at the SolarPACES, Mar. 2008.
[81] European Commission, ‘SOLHYCO (Solar-Hybrid Power and Cogeneration Plants)’, Mar. 2011.
[82] R. Korzynietz *et al.*, ‘Solugas – Comprehensive analysis of the solar hybrid Brayton plant’, *Sol. Energy*, vol. 135, pp. 578–589, Oct. 2016, doi: 10.1016/j.solener.2016.06.020.
[83] J. D. Ortega, J. M. Christian, and C. K. Ho, ‘Design and Testing of a Novel Bladed Receiver’, p. 9, 2017.
[84] C. K. Ho *et al.*, ‘Fractal-Like Materials Design with Optimized Radiative Properties for High-Efficiency Solar Energy Conversion’, SAND2016--9526, 1431480, Sep. 2016. doi: 10.2172/1431480.
[85] H.-S. Cho, H.-J. Lee, J.-K. Kim, S.-N. Lee, and Y.-H. Kang, ‘Design and Performance Evaluation of Solar Air Receivers’, *J. Korean Sol. Energy Soc.*, vol. 32, no. spc3, pp. 207–212, Jun. 2012, doi: 10.7836/kses.2012.32.spc3.207.
[86] I. Hischier, D. Hess, W. Lipiński, M. Modest, and A. Steinfeld, ‘Heat Transfer Analysis of a Novel Pressurized Air Receiver for Concentrated Solar Power via Combined Cycles’, *J. Therm. Sci. Eng. Appl.*, vol. 1, no. 4, p. 041002, Dec. 2009, doi: 10.1115/1.4001259.
[87] I. Hischier, P. Leumann, and A. Steinfeld, ‘Experimental and Numerical Analyses of a Pressurized Air Receiver for Solar-Driven Gas Turbines’, *J. Sol. Energy Eng.*, vol. 134, no. 2, p. 021003, May 2012, doi: 10.1115/1.4005446.

[88] P. Poživil, N. Ettlin, F. Stucker, and A. Steinfeld, ‘Modular Design and Experimental Testing of a 50 kWth Pressurized-Air Solar Receiver for Gas Turbines’, *J. Sol. Energy Eng.*, vol. 137, no. 3, p. 031002, Jun. 2015, doi: 10.1115/1.4028918.
[89] W. Wang, H. Xu, B. Laumert, and T. Strand, ‘An inverse design method for a cavity receiver used in solar dish Brayton system’, *Sol. Energy*, vol. 110, pp. 745–755, Dec. 2014, doi: 10.1016/j.solener.2014.10.019.
[90] W. Wang, B. Laumert, H. Xu, and T. Strand, ‘Conjugate heat transfer analysis of an impinging receiver design for a dish-Brayton system’, *Sol. Energy*, vol. 119, pp. 298–309, Sep. 2015, doi: 10.1016/j.solener.2015.07.013.
[91] W. Wang, B. Wang, L. Li, B. Laumert, and T. Strand, ‘The effect of the cooling nozzle arrangement to the thermal performance of a solar impinging receiver’, *Sol. Energy*, vol. 131, pp. 222–234, Jun. 2016, doi: 10.1016/j.solener.2016.02.052.
[92] W. Wang and B. Laumert, ‘Effect of cavity surface material on the concentrated solar flux distribution for an impinging receiver’, *Sol. Energy Mater. Sol. Cells*, vol. 161, pp. 177–182, Mar. 2017, doi: 10.1016/j.solmat.2016.12.008.
[93] W. Wang, *Development of an Impinging Receiver for Solar Dish-Brayton Systems*. Stockholm: KTH Royal Institute of Technology, 2015. Accessed: Aug. 16, 2021. [Online]. Available: http://urn.kb.se/resolve?urn=urn:nbn:se:kth:diva-177531
[94] W. Wang, A. Malmquist, L. Aichmayer, and B. Laumert, ‘Transient performance of an impinging receiver: An indoor experimental study’, *Energy Convers. Manag.*, vol. 158, pp. 193–200, Feb. 2018, doi: 10.1016/j.enconman.2017.12.070.
[95] A. Bejan, ‘The thermodynamic design of heat and mass transfer processes and devices’, *Int. J. Heat Fluid Flow*, vol. 8, no. 4, pp. 258–276, Dec. 1987, doi: 10.1016/0142-727X(87)90062-2.
[96] A. Bejan, ‘Entropy generation minimization: The new thermodynamics of finite-size devices and finite-time processes’, *J. Appl. Phys.*, vol. 79, no. 3, pp. 1191–1218, Feb. 1996, doi: 10.1063/1.362674.
[97] S. A. Ashrafizadeh, ‘Application of Second Law Analysis in Heat Exchanger Systems’, *Entropy*, vol. 21, no. 6, p. 606, Jun. 2019, doi: 10.3390/e21060606.
[98] J. E. Parrott, ‘Theoretical upper limit to the conversion efficiency of solar energy’, *Sol. Energy*, vol. 21, no. 3, pp. 227–229, 1978, doi: 10.1016/0038-092X(78)90025-7.
[99] J. P. Holman, *Heat transfer*, 10th ed. Boston: McGraw Hill Higher Education, 2010.
[100] ‘ISO 16528-1:2007 Boilers and pressure vessels — Part 1: Performance requirements’. International Organization for Standardization, Aug. 2007.
[101] ‘EN 13445 part 1 - 5 Unfired pressure vessels’. CEN/CENELEC, Nov. 30, 2021.
[102] *2021 ASME boiler & pressure vessel code*, 2021 edition. New York, NY: American Societ of Mechanical Engineers, 2021.
[103] M. J. Montes, J. I. Linares, D. D’Souza, J. Gonzalez-Aguilar, and M. Romero, ‘A new design of central solar receiver for pressurised gases and supercritical fluids’, *Energy*.
[104] R. Forristall, ‘Heat Transfer Analysis and Modeling of a Parabolic Trough Solar Receiver Implemented in Engineering Equation Solver’, NREL/TP-550-34169, 15004820, Oct. 2003. doi: 10.2172/15004820.
[105] M. J. Montes, R. Barbero, R. Abbas, and A. Rovira, ‘Performance model and thermal comparison of different alternatives for the Fresnel single-tube receiver’, *Appl. Therm. Eng.*, vol. 104, pp. 162–175, Jul. 2016, doi: 10.1016/j.applthermaleng.2016.05.015.
[106] S. M. Besarati, D. Yogi Goswami, and E. K. Stefanakos, ‘Development of a Solar Receiver Based on Compact Heat Exchanger Technology for Supercritical Carbon Dioxide Power Cycles’, *J. Sol. Energy Eng.*, vol. 137, no. 3, p. 031018, Jun. 2015, doi: 10.1115/1.4029861.
[107] Xiaojin Wei and Y. Joshi, ‘Optimization study of stacked micro-channel heat sinks for micro-electronic cooling’, *IEEE Trans. Compon. Packag. Technol.*, vol. 26, no. 1, pp. 55–61, Mar. 2003, doi: 10.1109/TCAPT.2003.811473.

[108] N. Lei, 'The Thermal Characteristics Of Multilayer Minichannel Heat Sinks In Single-Phase And Two-Phase Flow', Doctoral, University of Arizona, 2006.
[109] M. Huber, A. Harvey, E. Lemmon, G. Hardin, I. Bell, and M. McLinden, 'NIST Reference Fluid Thermodynamic and Transport Properties Database (REFPROP) Version 10 - SRD 23'. National Institute of Standards and Technology, 2018. doi: 10.18434/T4/1502528.
[110] S. Sullivan, 'High-Efficiency Low-Cost Solar Receiver for use in a Supercritical CO2 Recompression Cycle Brayton', Brayton Energy, LLC, Portsmouth, NH 03842, Jun. 2016.
[111] H. E. McCoy and J. F. King, 'Mechanical properties of Inconel 617 and 618', ORNL/TM--9337, 711763, Feb. 1985. doi: 10.2172/711763.
[112] K. Venkatesan, A. T. Mathew, S. Devendiran, N. M. Ghazaly, S. Sanjith, and R. Raghul, 'Machinability study and multi-response optimization of cutting force, Surface roughness and tool wear on CNC turned Inconel 617 superalloy using Al2O3 Nanofluids in Coconut oil', *Procedia Manuf.*, vol. 30, pp. 396–403, 2019, doi: 10.1016/j.promfg.2019.02.055.
[113] J. Yellowhair, C. K. Ho, J. D. Ortega, J. M. Christian, and C. E. Andraka, 'Testing and optical modeling of novel concentrating solar receiver geometries to increase light trapping and effective solar absorptance', presented at the SPIE Optics + Photonics for Sustainable Energy, San Diego, California, United States, Sep. 2015, p. 95590A. doi: 10.1117/12.2186647.
[114] J. R. Howell, M. P. Mengüç, K. J. Daun, and R. Siegel, *Thermal radiation heat transfer*, Seventh edition. Boca Raton: CRC Press, 2021.
[115] K. Altfeld, W. Leiner, and M. Fiebig, 'Second law optimization of flat-plate solar air heaters Part I: The concept of net exergy flow and the modeling of solar air heaters', *Sol. Energy*, vol. 41, no. 2, pp. 127–132, 1988, doi: 10.1016/0038-092X(88)90128-4.
[116] M. K. Sahu and R. K. Prasad, 'Exergy based performance evaluation of solar air heater with arc-shaped wire roughened absorber plate', *Renew. Energy*, vol. 96, pp. 233–243, Oct. 2016, doi: 10.1016/j.renene.2016.04.083.
[117] *COMSOL Multiphysics*®. Stockholm, Sweden: COMSOL AB. [Online]. Available: www.comsol.com
[118] S. Luque, S. Santiago, F. Gómez-García, M. Romero, and J. González-Aguilar, 'A new calorimetric facility to investigate radiative-convective heat exchangers for concentrated solar power applications: A New Facility to Investigate Heat Exchangers for CSP Applications', *Int. J. Energy Res.*, vol. 42, no. 3, pp. 966–976, Mar. 2018, doi: 10.1002/er.3859.
[119] D. G. Erbs, S. A. Klein, and J. A. Duffie, 'Estimation of the diffuse radiation fraction for hourly, daily and monthly-average global radiation', *Sol. Energy*, vol. 28, no. 4, pp. 293–302, 1982, doi: 10.1016/0038-092X(82)90302-4.
[120] W. Wang, 'Simulate a "Sun" for Solar Research: A Literature Review of Solar Simulator Technology', KTH University, Stockholm, Sweden, 2014. [Online]. Available: http://kth.diva-portal.org/smash/get/diva2:756274/FULLTEXT01.pdf
[121] A. Gallo, A. Marzo, E. Fuentealba, and E. Alonso, 'High flux solar simulators for concentrated solar thermal research: A review', *Renew. Sustain. Energy Rev.*, vol. 77, pp. 1385–1402, Sep. 2017, doi: 10.1016/j.rser.2017.01.056.
[122] J. Sarwar, G. Georgakis, R. LaChance, and N. Ozalp, 'Description and characterization of an adjustable flux solar simulator for solar thermal, thermochemical and photovoltaic applications', *Sol. Energy*, vol. 100, pp. 179–194, Feb. 2014, doi: 10.1016/j.solener.2013.12.008.
[123] A. Steinfeld, 'Exchange factor between two spheres placed at the foci of a specularly reflecting ellipsoidal cavity', *Int. Commun. Heat Mass Transf.*, vol. 18, no. 1, pp. 19–26, Jan. 1991, doi: 10.1016/0735-1933(91)90004-N.

[124] M. Tawfik, X. Tonnellier, and C. Sansom, 'Light source selection for a solar simulator for thermal applications: A review', *Renew. Sustain. Energy Rev.*, vol. 90, pp. 802–813, Jul. 2018, doi: 10.1016/j.rser.2018.03.059.
[125] D. Jaworske, K. Jefferies, and L. Mason, 'Alignment and initial operation of an advanced solar simulator', in *34th Aerospace Sciences Meeting and Exhibit*, Reno,NV,U.S.A., Jan. 1996. doi: 10.2514/6.1996-102.
[126] R. J. Matson, K. A. Emery, and R. E. Bird, 'Terrestrial solar spectra, solar simulation and solar cell short-circuit current calibration: A review', *Sol. Cells*, vol. 11, no. 2, pp. 105–145, Mar. 1984, doi: 10.1016/0379-6787(84)90022-X.
[127] D. Bickler, 'The simulation of solar radiation', *Sol. Energy*, vol. 6, no. 2, pp. 64–68, Apr. 1962, doi: 10.1016/0038-092X(62)90006-3.
[128] B. M. Ekman, G. Brooks, and M. Akbar Rhamdhani, 'Development of high flux solar simulators for solar thermal research', *Sol. Energy Mater. Sol. Cells*, vol. 141, pp. 436–446, Oct. 2015, doi: 10.1016/j.solmat.2015.06.016.
[129] Y. Okuhara, T. Kuroyama, T. Tsutsui, K. Noritake, and T. Aoshima, 'A Solar Simulator for the Measurement of Heat Collection Efficiency of Parabolic Trough Receivers', *Energy Procedia*, vol. 69, pp. 1911–1920, May 2015, doi: 10.1016/j.egypro.2015.03.185.
[130] I. Alxneit and H. Schmit, 'Spectral Characterization of PSI's High-Flux Solar Simulator', *J. Sol. Energy Eng.*, vol. 134, no. 1, p. 011013, Feb. 2012, doi: 10.1115/1.4005249.
[131] W. Platzer and C. Hildebrandt, 'Absorber materials for solar thermal receivers in concentrating solar power (CSP) systems', in *Concentrating Solar Power Technology*, Elsevier, 2012, pp. 469–494. doi: 10.1533/9780857096173.3.469.
[132] J. Li, J. Gonzalez-Aguilar, C. Pérez-Rábago, H. Zeaiter, and M. Romero, 'Optical Analysis of a Hexagonal 42kWe High-flux Solar Simulator', *Energy Procedia*, vol. 57, pp. 590–596, 2014, doi: 10.1016/j.egypro.2014.10.213.
[133] J. Li, J. Gonzalez-Aguilar, and M. Romero, 'Line-concentrating Flux Analysis of 42kWe High-flux Solar Simulator', *Energy Procedia*, vol. 69, pp. 132–137, May 2015, doi: 10.1016/j.egypro.2015.03.016.
[134] S. Luque, J. González-Aguilar, and M. Romero, 'Design of a Calorimetric Facility to Assess Volumetric Receivers Employing a 42 KW High Flux Solar Simulator', in *Proceedings of SWC2017/SHC2017*, Abu Dhabi, 2017, pp. 1–10. doi: 10.18086/swc.2017.04.10.
[135] J. Gonzalez-Aguilar, Z. Zeaiter, and M. Romero, 'Estudio de procesos a altos flujos de radiación y altas temperaturas', *ERA Solar*, vol. 181, Aug. 2014.
[136] M. Sanchez, J. Gonzalez-Aguilar, and M. Romero, 'Determinación De Estrategias De Apunte En Un Simulador Solar De Alto Flujo', presented at the XVI Congreso Ibérico y XII Congreso Iberoamericano de Energía Solar, Madrid, Jun. 2018. [Online]. Available: https://agenda.uib.es/_files/_event/_15227/_editorFiles/file/PDFS!!!!!/Determinaci%C3%B3n%20de%20estrategias%20de%20apunte%20en%20un%20simulador%20solar%20de%20alto%20flujo.pdf
[137] W. B. Stine and R. W. Harrigan, *Solar energy fundamentals and design: with computer applications*. New York: Wiley, 1985.
[138] R. Pitz-Paal, B. Hoffschmidt, M. Böhmer, and M. Becker, 'Experimental and numerical evaluation of the performance and flow stability of different types of open volumetric absorbers under non-homogeneous irradiation', *Sol. Energy*, vol. 60, no. 3–4, pp. 135–150, Mar. 1997, doi: 10.1016/S0038-092X(97)00007-8.
[139] M. Becker *et al.*, 'Theoretical and numerical investigation of flow stability in porous materials applied as volumetric solar receivers', *Sol. Energy*, vol. 80, no. 10, pp. 1241–1248, Oct. 2006, doi: 10.1016/j.solener.2005.11.006.

[140] A. L. Ávila-Marín, ‘Volumetric receivers in Solar Thermal Power Plants with Central Receiver System technology: A review’, *Sol. Energy*, vol. 85, no. 5, Art. no. 5, May 2011, doi: 10.1016/j.solener.2011.02.002.
[141] S. Luque, G. Menéndez, M. Roccabruna, J. González-Aguilar, L. Crema, and M. Romero, ‘Exploiting volumetric effects in novel additively manufactured open solar receivers’, *Sol. Energy*, vol. 174, pp. 342–351, Nov. 2018, doi: 10.1016/j.solener.2018.09.030.
[142] S. Luque, S. Santiago, F. Gómez-García, M. Romero, and J. González-Aguilar, ‘A new calorimetric facility to investigate radiative-convective heat exchangers for concentrated solar power applications: A New Facility to Investigate Heat Exchangers for CSP Applications’, *Int. J. Energy Res.*, vol. 42, no. 3, Art. no. 3, Mar. 2018, doi: 10.1002/er.3859.
[143] I. Alxneit and G. Dibowski, ‘R12.5 Solar Simulator Evaluation Report - Project SFERA’, Aug. 2011.
[144] H. W. Coleman and W. G. Steele, *Experimentation, validation, and uncertainty analysis for engineers*, Fourth edition. Hoboken, NJ, USA: Wiley, 2018.
[145] ‘ISO/IEC Guide 98:1993 Guide to the expression of uncertainty in measurement (GUM)’. ISO, Jan. 1993.
[146] M. Dana, I. Zetkova, P. Hanzl, and O. Hronek, ‘Accuracy of Holes Created by 3D Printing (DMLS)’, in *DAAAM Proceedings*, 1st ed., vol. 1, B. Katalinic, Ed. DAAAM International Vienna, 2017, pp. 0467–0473. doi: 10.2507/28th.daaam.proceedings.065.
[147] R. Wonneberger *et al.*, ‘Oxidation of stainless steel 316L – Oxide grains with pronounced inhomogeneous composition’, *Corros. Sci.*, vol. 149, pp. 178–184, Apr. 2019, doi: 10.1016/j.corsci.2018.12.035.
[148] X. Huang *et al.*, ‘Oxidation behavior of 316L austenitic stainless steel in high temperature air with long-term exposure’, *Mater. Res. Express*, vol. 7, no. 6, p. 066517, Jun. 2020, doi: 10.1088/2053-1591/ab96fa.
[149] I. Gibson, D. Rosen, and B. Stucker, *Additive Manufacturing Technologies*. New York, NY: Springer New York, 2015. doi: 10.1007/978-1-4939-2113-3.
[150] R. J. Hebert, ‘Viewpoint: metallurgical aspects of powder bed metal additive manufacturing’, *J. Mater. Sci.*, vol. 51, no. 3, pp. 1165–1175, Feb. 2016, doi: 10.1007/s10853-015-9479-x.
[151] P. Masek, T. Fornusek, P. Zeman, M. Bucko, J. Smolik, and P. Heinrich, ‘MACHINABILITY THE AISI 316 STAINLESS STEEL AFTER PROCESSING BY VARIOUS METHODS OF 3D PRINTING’, *MM Sci. J.*, vol. 2019, no. 04, pp. 3338–3346, Nov. 2019, doi: 10.17973/MMSJ.2019_11_2019091.
[152] P. Tyagi, T. Goulet, C. Riso, and F. Garcia-Moreno, ‘Reducing surface roughness by chemical polishing of additively manufactured 3D printed 316 stainless steel components’, *Int. J. Adv. Manuf. Technol.*, vol. 100, no. 9–12, pp. 2895–2900, Feb. 2019, doi: 10.1007/s00170-018-2890-0.
[153] J. Nikuradse, ‘LAWS OF FLOW IN ROUGH PIPES’. 1933.
[154] W. M. Rohsenow, J. P. Hartnett, and Y. I. Cho, Eds., *Handbook of heat transfer*, 3rd ed. New York: McGraw-Hill, 1998.
[155] W. M. Kays and A. L. London, ‘Compact heat exchangers’, Jan. 1984, Accessed: Jun. 29, 2021. [Online]. Available: https://www.osti.gov/biblio/6132549
[156] N. A. A. Qasem and S. M. Zubair, ‘Compact and microchannel heat exchangers: A comprehensive review of air-side friction factor and heat transfer correlations’, *Energy Convers. Manag.*, vol. 173, pp. 555–601, Oct. 2018, doi: 10.1016/j.enconman.2018.06.104.
[157] A. Diani, S. Mancin, C. Zilio, and L. Rossetto, ‘Experimental and numerical analyses of different extended surfaces’, *J. Phys. Conf. Ser.*, vol. 395, p. 012045, Nov. 2012, doi: 10.1088/1742-6596/395/1/012045.

[158] M. V. V. Mortean and M. B. H. Mantelli, ‘Nusselt number correlation for compact heat exchangers in transition regimes’, *Appl. Therm. Eng.*, vol. 151, pp. 514–522, Mar. 2019, doi: 10.1016/j.applthermaleng.2019.02.017.
[159] V. Gnielinski, ‘New equations for heat and mass transfer in turbulent pipe and channel flow’, *Int. Chem. Eng.*, vol. 16, no. 2, Art. no. 2, 1976.
[160] M. Khoshvaght Aliabadi, F. Hormozi, and E. Hosseini Rad, ‘New correlations for wavy plate-fin heat exchangers: different working fluids’, *Int. J. Numer. Methods Heat Fluid Flow*, vol. 24, no. 5, Art. no. 5, Jan. 2014, doi: 10.1108/HFF-09-2012-0195.
[161] S. Mochizuki, Y. Yagi, and W.-J. Yang, ‘Transport Phenomena in Stacks of Interrupted Parallel-Plate Surfaces’, *Exp. Heat Transf.*, vol. 1, no. 2, Art. no. 2, Jan. 1987, doi: 10.1080/08916158708946336.
[162] J. Deng, ‘Improved correlations of the thermal-hydraulic performance of large size multi-louvered fin arrays for condensers of high power electronic component cooling by numerical simulation’, *Energy Convers. Manag.*, vol. 153, pp. 504–514, Dec. 2017, doi: 10.1016/j.enconman.2017.09.066.
[163] M. R. Shaeri, M. Yaghoubi, and K. Jafarpur, ‘Heat transfer analysis of lateral perforated fin heat sinks’, *Appl. Energy*, vol. 86, no. 10, Art. no. 10, Oct. 2009, doi: 10.1016/j.apenergy.2008.12.029.
[164] T. K. Ibrahim, A. T. Al-Sammarraie, M. S. M. Al-Jethelah, W. H. Al-Doori, M. R. Salimpour, and H. Tao, ‘The impact of square shape perforations on the enhanced heat transfer from fins: Experimental and numerical study’, *Int. J. Therm. Sci.*, vol. 149, p. 106144, Mar. 2020, doi: 10.1016/j.ijthermalsci.2019.106144.
[165] A. Diani, S. Mancin, C. Zilio, and L. Rossetto, ‘An assessment on air forced convection on extended surfaces: Experimental results and numerical modeling’, *Int. J. Therm. Sci.*, vol. 67, pp. 120–134, May 2013, doi: 10.1016/j.ijthermalsci.2012.11.012.

# Appendix

The appendix contains a table with relevant geometrical, operational and performance related parameters related to the state of the art in indirectly irradiated pressurised gas receivers (section A.1), the semi-empirical correlations used to determine the heat transfer coefficients (section A.2) and pressure drops (section A.3) in each of the compact heat exchanger geometries used in the analysis. The exergy efficiency and energy efficiency contour plots of the plain triangular fin (PTF) receiver, wavy fin (WF) receiver, offset strip fin (OSF) receiver, perforated fin (PF) receiver and louvred fin (LF) receiver can also be found in this appendix (section A.4 and A.5 respectively).

Additionally, photos of the pressurised receiver testbed and its individual components and instrumentation besides other important measurement devices used in this work are presented in section A.6. The detailed experiment log of the entire experimental campaign can be found in section A.7 and images of the leak tests of the receivers and photos of each receiver at the end of an experiment run shown in section A.8 and section A.9 respectively.

# A.1. Indirectly irradiated pressurised gas receivers

Table 31. Technical specifications of indirectly irradiated pressurised gas receivers

t = thermal, D = Design Point, * refers to calculated values based on assumptions

| **Receiver** | **Material** | **Incident Power/ Flux ($q$)** | **Radiation Energy ($\dot{Q}$)** | $\dot{m}$ | $T_{out}$ | $T_{in}$ | $P_{in}$ | $\Delta P_{rec}$ | $\eta_{th}$ | $D_h$ | $L$ |
|---|---|---|---|---|---|---|---|---|---|---|---|
| | | kW m$^{-2}$ | kW | kg s$^{-1}$ | °C | °C | bar | mbar | | mm | mm |
| SOLGATE | - | 500 | 900-1000 | 1.327 | 350-550 | 290 | 6.5 | 100 -120 | 75% | 28 | 2300 |
| SOLHYCO | Inconel 600 | 328.2 | 181.9 (thermal)<br>234.6 | 0.8 | 749–783<br>800 (D) | 600 | 3.75 | 67–72 | 38–45%<br>67.7-77% (D) | 22.48 | 2500 |
| SOLUGAS | Inconel 617 | 393.5* | 3200 (t)(D) | 5.75 | 800 | 300–350 | 9 | < 250 (D)<br>2% $P_{in}$ or 200 | 73% (D)<br>71.3-78.1% | 19.6 | 5000 |
| RPC Cavity Receiver (low power) | SiSiC | 1870-4360 | 1.32-3.08 | 0.8-2.09 x10$^{-3}$ | 420–1060 | 300 | 5 (abs) | 10 | 35-77% | | |
| RPC Cavity Receiver (high power) | SiSiC | 2500 | < 47 | 10-150 x10$^{-3}$ | 300-1200 | 300 | 2-6 | 1-54 | 60% | | |
| Impinging cavity Receiver (preliminary) | Austenitic stainless steel 253 MA | 277 | | 0.015-0.03 | ΔT = 160−253 at ambient inlet (≈ 15) | | 3 | 1-2.5 | 43-53% | 40 | 390 |
| Impinging cavity Receiver | Austenitic stainless steel 253 MA | | 19.7 | 0.022-0.026 | 800 | 674 | 3 | | 74.1% | 40 | 390 |
| Flat Panel | Inconel 625 | 20-70 | 14.83* | 0.1 | 650 | 400 | 8.3 | 10% (D)<br>290 | 75-80% | 9.398 | |
| Bladed | Inconel 625 | 45 | 14.83 | 0.1 | 650 | 400 | 8.3 | 800 | 80-85% | 9.398 | |
| Embedded circumferential | | 254-861 | 3.4-11.6 | 1.85-2.65 x10$^{-2}$ | 520 | 135 | 3.81–3.9 | 1570–1940 | 83–96% | 36 | 2120 |
| Embedded axial | | 247-837 | 3.6-12.1 | 2.05-2.81 x10$^{-2}$ | 450 | 150 | 3.85–4.05 | 410–550 | 78–96% | 38.636 | 388 |
| Microchannel Receiver | Inconel 625 | 200–350 | 0.7 | 0.431–0.862 x10$^{-3}$ | ΔT = 100–360 | | 4 | 750 | 64.28* | 1.5 | 30 |

## A.2. Heat transfer correlations (channel flow)

Heat transfer correlations, in terms of Colburn factor (j) or Nusselt Number (Nu), are presented in Table 32, for the different compact geometries analysed in this work, at different operating conditions.

Table 32. Heat transfer correlations, in terms of Colburn factor (j) or Nusselt Number (Nu) for the different compact geometries analysed

| Receiver | Validity | Correlation | Reference |
|---|---|---|---|
| Plain Rectangular Fin | $2700 < Re_{D_h} < 10100$ | $j = 0.609\ Re_{D_h}^{-0.493} \left(\frac{t}{H_c}\right)^{-0.011} \left(\frac{p}{H_c}\right)^{-0.071} \left(\frac{L_e}{D_h}\right)^{-0.298}$ | [156],[157] |
| | $Re_{D_h} > 10100$ $0.5 < Pr_{D_h} < 2000$ | $Nu_{D_h} = \frac{f_D}{2}(Re_{D_h} - 1000)Pr_{D_h} \left(1 + 12.7\left(\frac{f_D}{2}\right)^{0.5}\left(Pr_{D_h}^{\frac{2}{3}} - 1\right)\right)^{-1} \left(1 + \left(\frac{D_h}{L_e}\right)^{\frac{2}{3}}\right)$ | [158],[159] |
| Plain Triangular Fin | $Re_{D_h} > 2300$ $0.5 < Pr_{D_h} < 2000$ | $Nu_{D_h} = \frac{f_D}{2}\left(Re_{D_h} - 1000\right) Pr_{D_h} \left(1 + 12.7\left(\frac{f_D}{2}\right)^{0.5}\left(Pr_{D_h}^{\frac{2}{3}} - 1\right)\right)^{-1} \left(1 + \left(\frac{D_h}{L_e}\right)^{\frac{2}{3}}\right)$ | [158],[159] |
| Wavy Fin | $Re_{D_h} < 1900$ | $j = 0.2951\ Re_{D_h}^{-0.1908} \left(\frac{p}{D_h}\right)^{0.7356} \left(\frac{H_c}{D_h}\right)^{0.1378} \left(\frac{t}{D_h}\right)^{0.0485} \left(\frac{2A}{D_h}\right)^{0.2467} \left(\frac{L}{D_h}\right)^{-0.4976}$ | [160] |
| | $Re_{D_h} > 1900$ | $j = 0.7293\ Re_{D_h}^{-0.3637} \left(\frac{p}{D_h}\right)^{0.7966} \left(\frac{H_c}{D_h}\right)^{0.2398} \left(\frac{L}{D_h}\right)^{-0.4979} \left(\frac{t}{D_h}\right)^{0.0402} \left(\frac{2A}{D_h}\right)^{0.2012} \left(\frac{L_e}{D_h}\right)^{-0.3026}$ | |
| Offset strip Fin | $Re_{D_h} < 2000$ | $j = 1.37\ Re_{D_h}^{-0.67} \left(\frac{L_s}{D_h}\right)^{-0.25} \left(\frac{B_c}{H_c}\right)^{-0.184}$ | [161] |
| | $Re_{D_h} \geq 2000$ | $j = 1.17\ Re_{D_h}^{-0.36} \left(\frac{L_s}{D_h} + 3.75\right)^{-1} \left(\frac{t}{D_h}\right)^{0.089}$ | |
| Louvred (Triangular) Fin | | $j = 0.65842 \left(\frac{L_e}{L_l\ Re_L\ Pr_{D_h}}\right)^{0.6317} \left(\frac{L_l}{H_c}\right)^{-0.4825} \left(\frac{L_e}{H_c}\ tan(L_a)\right)^{-0.433} \left(\frac{L_s}{t}\right)^{-1.1902}$ | [162] |
| Perforated (Rectangular) Fin | $Nu_{SF}$ (solid fin) is calculated as is done with Plain Rectangular Fin | | [163],[164] |
| | $P_d > 0.04$ | $Nu_{PF} = Nu_{SF}\ 1.296\ \ Re_{D_{SF}}^{-0.0357}(1 - P)^{0.269}$ | |
| | $P_d < 0.04$ | $Nu_{PF} = Nu_{SF}\left(0.0307\ \ Re_{D_{SF}}^{0.226}\ +\ 0.583(1 - P)^{0.704}\right)$ | |

## A.3. Pressure drop correlations (channel flow)

Pressure drop correlations (in terms of $f_D$ or $f_F$) are available for the different geometries at different operating conditions. The most relevant ones for this study are presented Table 33:

Table 33. Pressure drop correlations in terms of Darcy friction factor ($f_D$) or Fanning friction factor ($f_F$) for the different compact geometries analysed.

| Receiver | Validity | Correlation | Reference |
|---|---|---|---|
| Plain Rectangular Fin | $2700 < Re_{D_h} < 10100$ | $f_F = 0.059\, Re_{D_h}^{-0.117} \left(\frac{t}{H_c}\right)^{0.118} \left(\frac{p}{H_c}\right)^{-0.253} \left(\frac{L_e}{D_h}\right)^{-0.147}$ | [156],[165] |
| | $Re_{D_h} > 10100$ $0.5 < Pr_{D_h} < 2000$ | $f_D = (1.82\, log10(Re_{D_h}) - 1.64)^{-2}$ | [158],[159] |
| Plain Triangular Fin | $Re_{D_h} > 2300$ $0.5 < Pr_{D_h} < 2000$ | $f_D = (1.82\, log10(Re_{D_h}) - 1.64)^{-2}$ | [158],[159] |
| Wavy Fin | $Re_{D_h} < 1900$ | $f_F = 38.7488\, Re_{D_h}^{-0.3840} \left(\frac{p}{D_h}\right)^{-1.479} \left(\frac{H_c}{D_h}\right)^{-0.3696} \left(\frac{L}{D_h}\right)^{-1.4542} \left(\frac{t}{D_h}\right)^{0.1016} \left(\frac{2A}{D_h}\right)^{1.0903} \left(\frac{L_e}{D_h}\right)^{-0.1549}$ | [160] |
| | $Re_{D_h} > 1900$ | $f_F = 52.2375\, Re_{D_h}^{-0.3524} \left(\frac{p}{D_h}\right)^{-1.6277} \left(\frac{H_c}{D_h}\right)^{-0.3529} \left(\frac{L}{D_h}\right)^{-1.7484} \left(\frac{t}{D_h}\right)^{0.1034} \left(\frac{2A}{D_h}\right)^{1.2294} \left(\frac{L_e}{D_h}\right)^{-0.2371}$ | |
| Offset strip Fin | $Re_{D_h} < 2000$ | $f_F = 5.55\, Re_{D_h}^{-0.67} \left(\frac{L_s}{D_h}\right)^{-0.32} \left(\frac{B_c}{H_c}\right)^{-0.092}$ | [161] |
| | $Re_{D_h} \geq 2000$ | $f_F = 0.83\, Re_{D_h}^{-0.20} \left(\frac{L_s}{D_h} + 0.33\right)^{-0.5} \left(\frac{t}{D_h}\right)^{0.534}$ | |
| Louvred (Triangular) Fin | | $f_F = 0.07667 \left(\frac{L_e}{L_l\, Re_L\, Pr_D}\right)^{0.3211} \left(\frac{L_l}{H_c}\right)^{-2.0217} \left(tan(L_a)\right)^{-2.3501} \left(\frac{L_s}{t}\right)^{-2.5343}$ | [162] |
| Perforated (Rectangular) Fin | The solid fin pressure drop is calculated as was the Plain Rectangular Fin's and its ratio with perforated fins is taken as: $\Delta p_{PF} = \Delta p_{SF}\ \ (0.97 - Re_{D_{SF}}\, 10^{-5})$ | | [163],[164] |

## A.4. Exergy efficiency contour plots

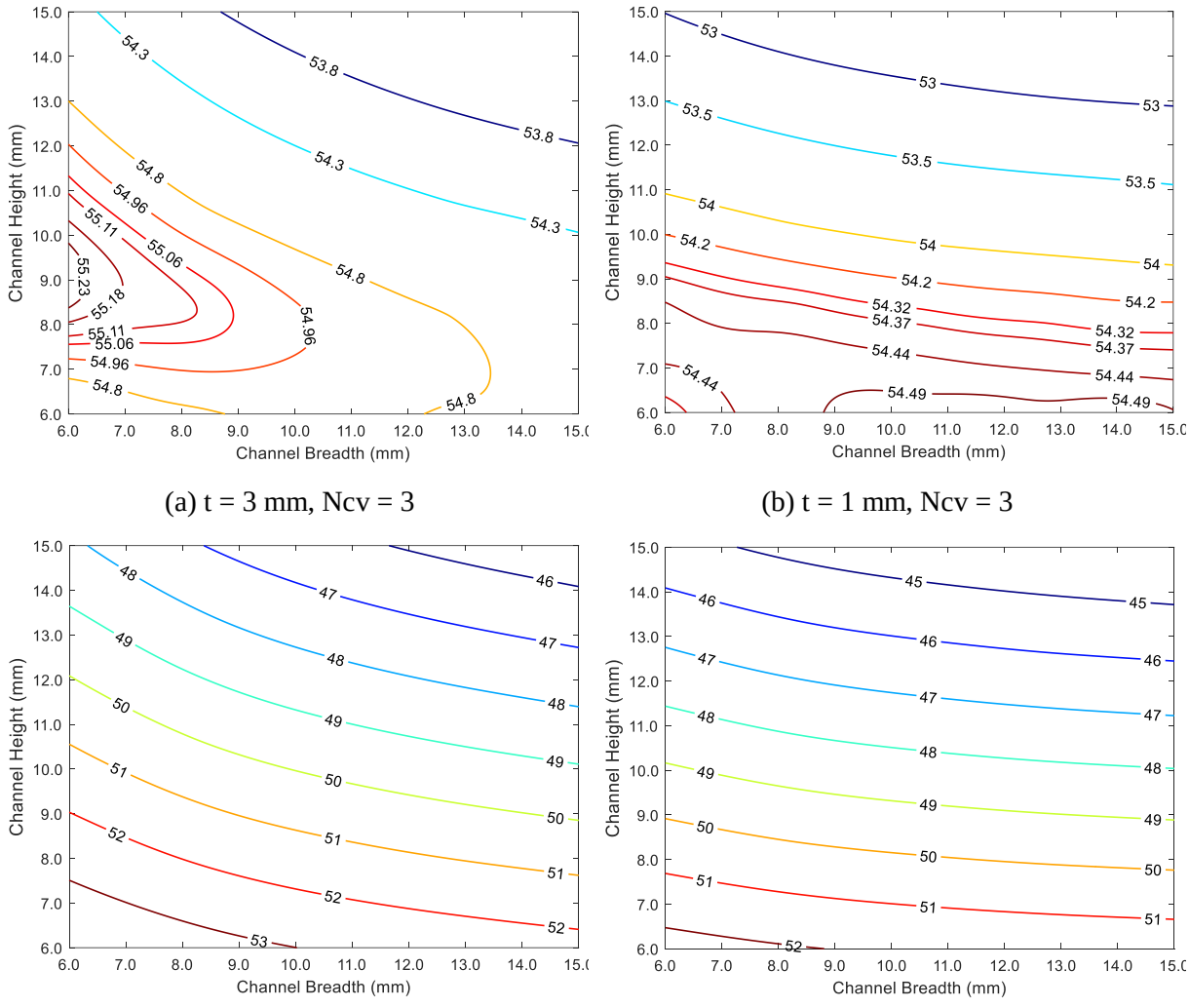


Figure 109. Exergy efficiency (in %) as function of the channel breadth and height for different channel thickness and number of vertical channels for the plain triangular fin geometry. (a) $t$ = 3 mm, $N_{cv}$ = 3; (b) $t$ = 1 mm, $N_{cv}$ = 3; (c) $t$ = 3 mm, $N_{cv}$ = 10; and (d) $t$ = 1 mm, $N_{cv}$ = 10.

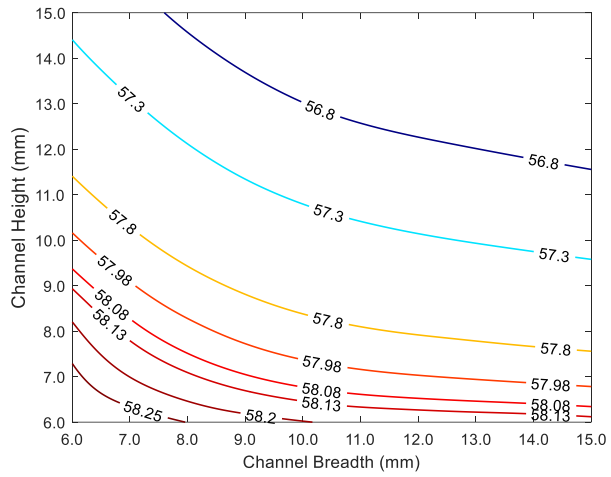


(a) $t$ = 3 mm, $N_{cv}$ = 3

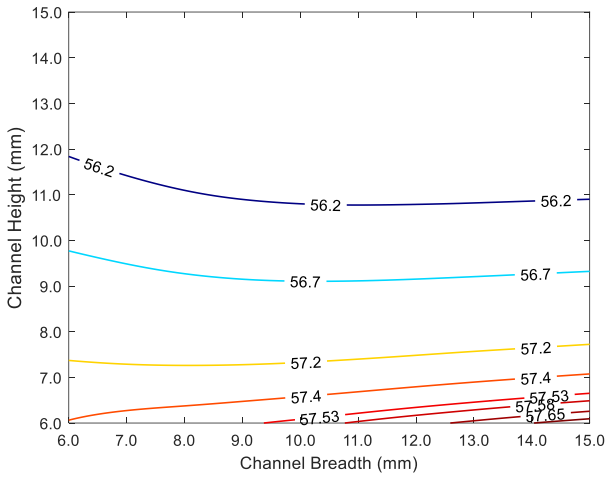


(b) $t$ = 1 mm, $N_{cv}$ = 3

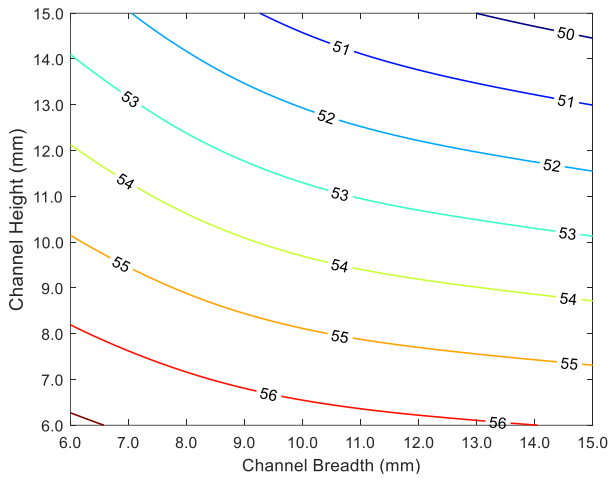


(c) $t$ = 3 mm, $N_{cv}$ = 10

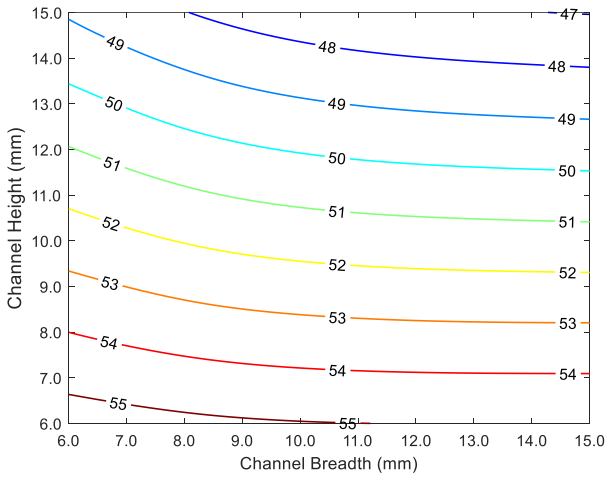


(d) $t$ = 1 mm, $N_{cv}$ = 10

Figure 110. Exergy efficiency (in %) as function of the channel breadth and height for different channel thickness and number of vertical channels for the wavy fin geometry. (a) $t$ = 3 mm, $N_{cv}$ = 3; (b) $t$ = 1 mm, $N_{cv}$ = 3; (c) $t$ = 3 mm, $N_{cv}$ = 10; and (d) $t$ = 1 mm, $N_{cv}$ = 10.

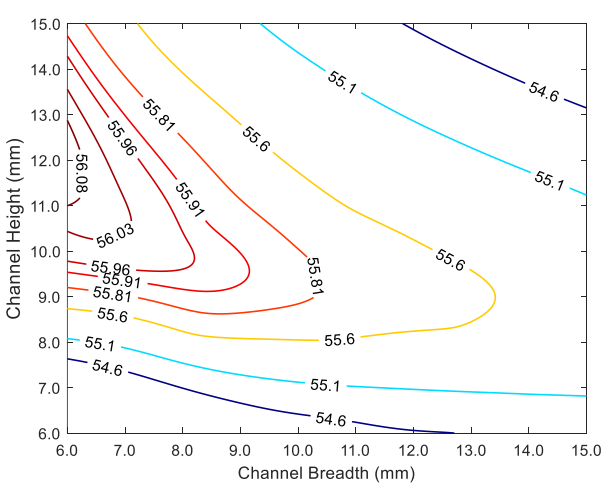


(a) $t$ = 3 mm, $N_{cv}$ = 3

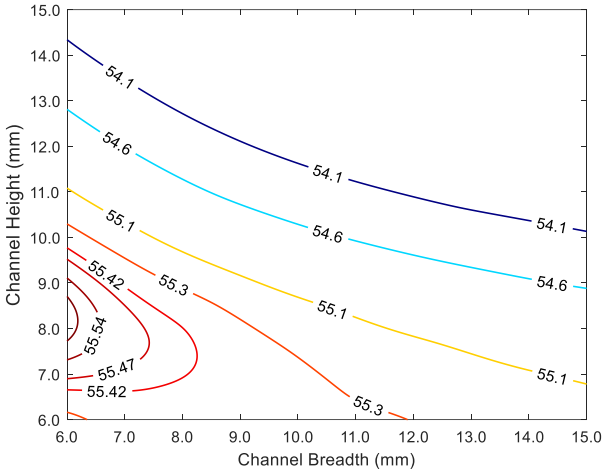


(b) $t$ = 1 mm, $N_{cv}$ = 3

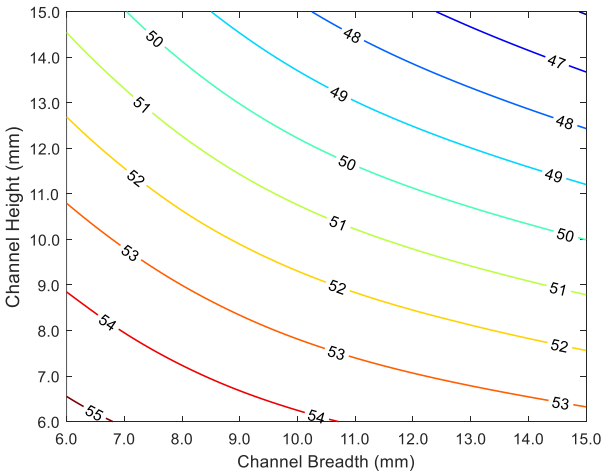


(c) $t$ = 3 mm, $N_{cv}$ = 10

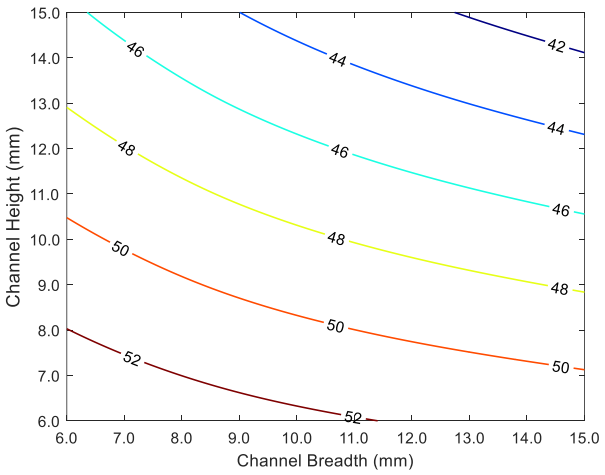


(d) $t$ = 1 mm, $N_{cv}$ = 10

Figure 111. Exergy efficiency (in %) as function of the channel breadth and height for different channel thickness and number of vertical channels for the offset strip fin geometry. (a) $t$ = 3 mm, $N_{cv}$ = 3; (b) $t$ = 1 mm, $N_{cv}$ = 3; (c) $t$ = 3 mm, $N_{cv}$ = 10; and (d) $t$ = 1 mm, $N_{cv}$ = 10.

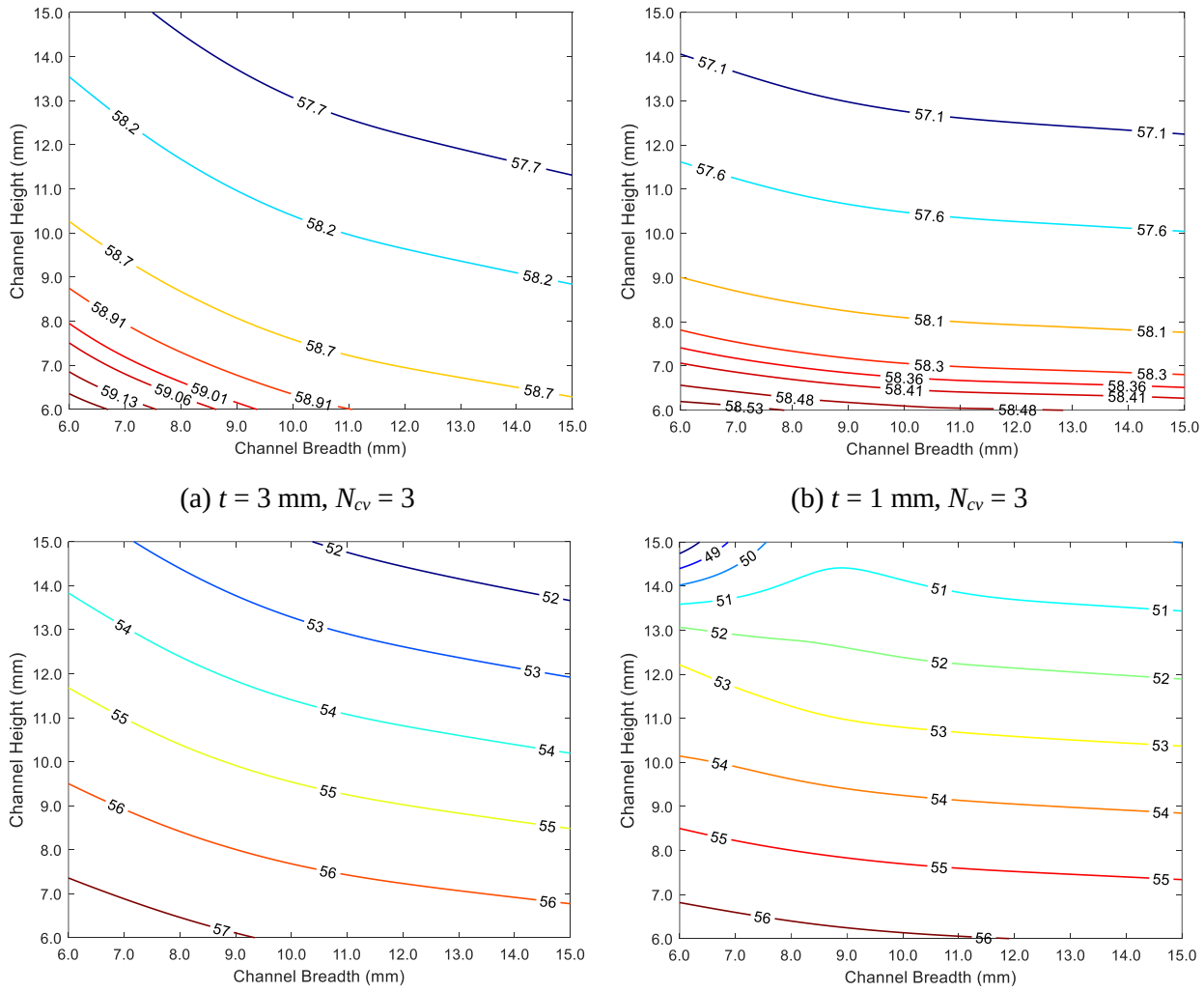


(a) $t$ = 3 mm, $N_{cv}$ = 3

(b) $t$ = 1 mm, $N_{cv}$ = 3

(c) $t$ = 3 mm, $N_{cv}$ = 10

(d) $t$ = 1 mm, $N_{cv}$ = 10

Figure 112. Exergy efficiency (in %) as function of the channel breadth and height for different channel thickness and number of vertical channels for the perforated fin geometry. (a) $t$ = 3 mm, $N_{cv}$ = 3; (b) $t$ = 1 mm, $N_{cv}$ = 3; (c) $t$ = 3 mm, $N_{cv}$ = 10; and (d) $t$ = 1 mm, $N_{cv}$ = 10.

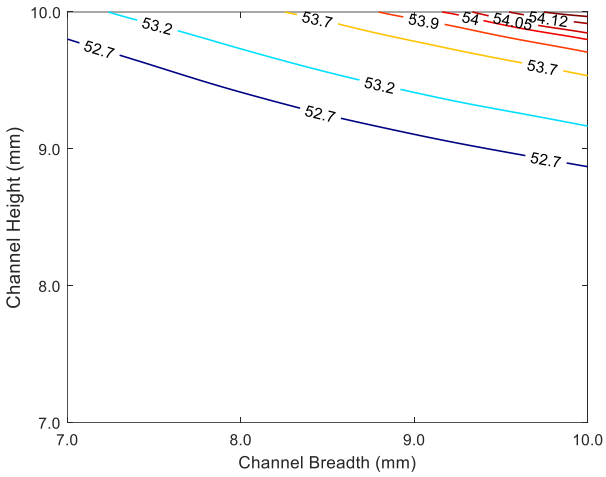


(a) $t$ = 3 mm, $N_{cv}$ = 3

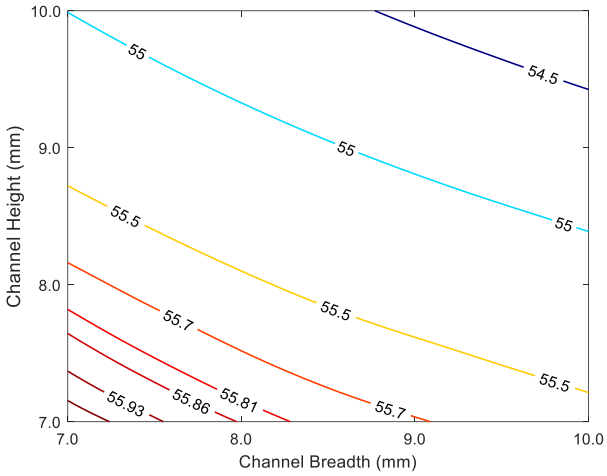


(b) $t$ = 1 mm, $N_{cv}$ = 3

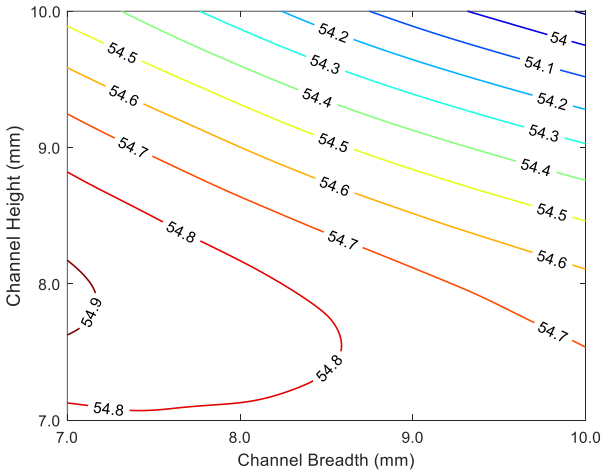


(c) $t$ = 3 mm, $N_{cv}$ = 10

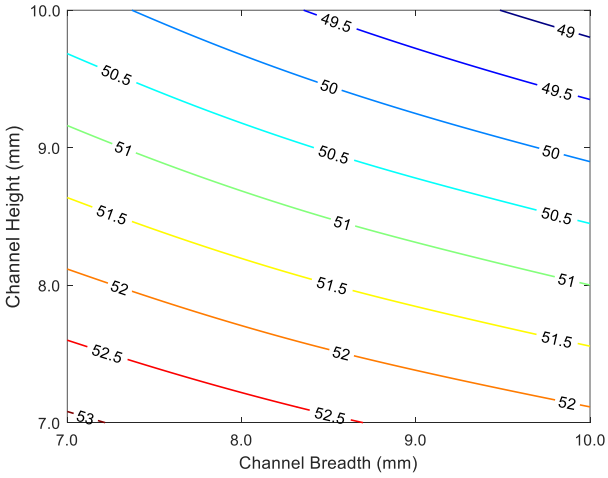


(d) $t$ = 1 mm, $N_{cv}$ = 10

Figure 113. Exergy efficiency (in %) as function of the channel breadth and height for different channel thickness and number of vertical channels for the louvred fin geometry. (a) $t$ = 3 mm, $N_{cv}$ = 3; (b) $t$ = 1 mm, $N_{cv}$ = 3; (c) $t$ = 3 mm, $N_{cv}$ = 10; and (d) $t$ = 1 mm, $N_{cv}$ = 10.

## A.5. Energy efficiency contour plots

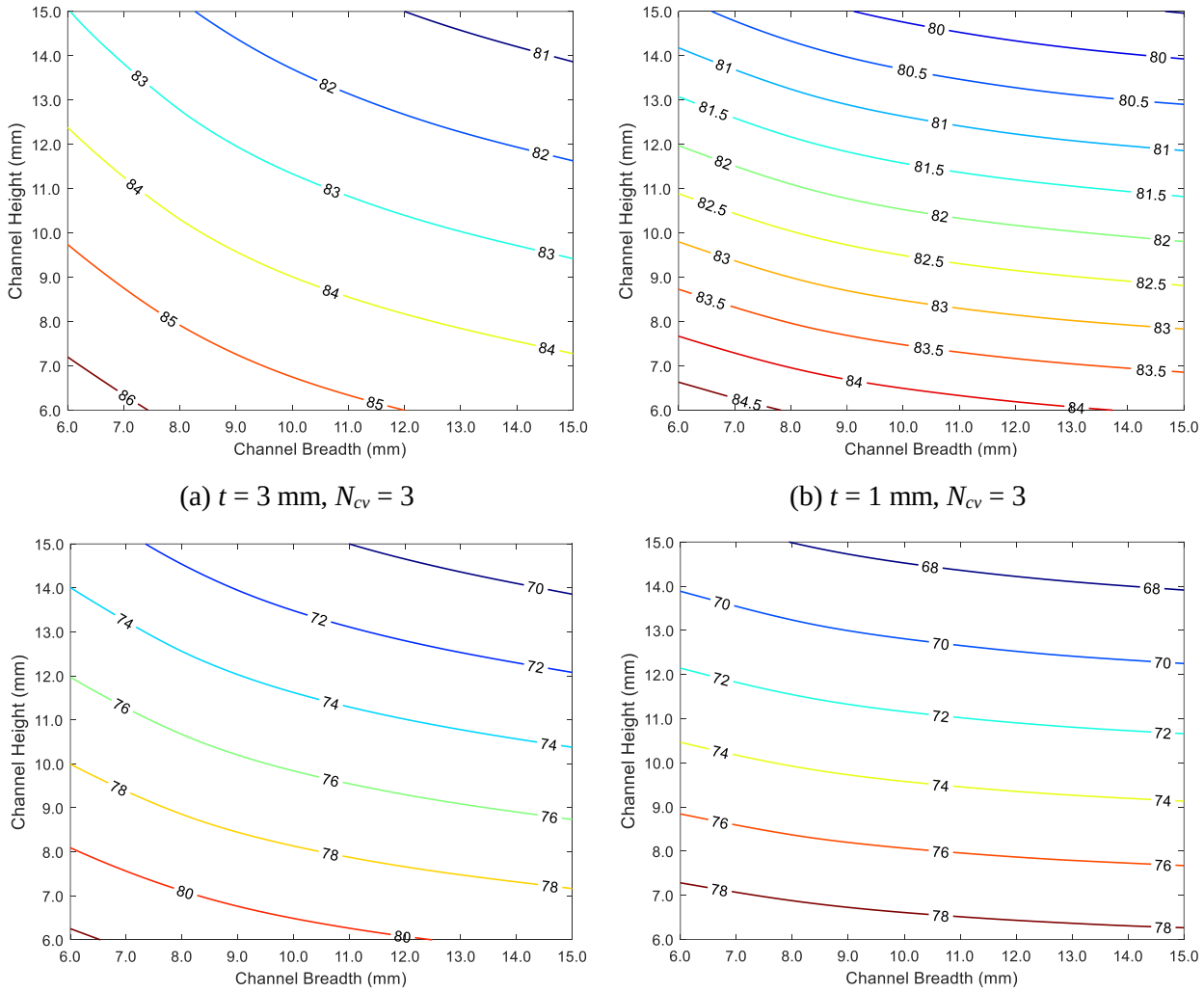


(a) $t$ = 3 mm, $N_{cv}$ = 3

(b) $t$ = 1 mm, $N_{cv}$ = 3

(c) $t$ = 3 mm, $N_{cv}$ = 10

(d) $t$ = 1 mm, $N_{cv}$ = 10

Figure 114. Energy efficiency (in %) as function of the channel breadth and height for different channel thickness and number of vertical channels for the plain triangular fin geometry. (a) $t$ = 3 mm, $N_{cv}$ = 3; (b) $t$ = 1 mm, $N_{cv}$ = 3; (c) $t$ = 3 mm, $N_{cv}$ = 10; and (d) $t$ = 1 mm, $N_{cv}$ = 10.

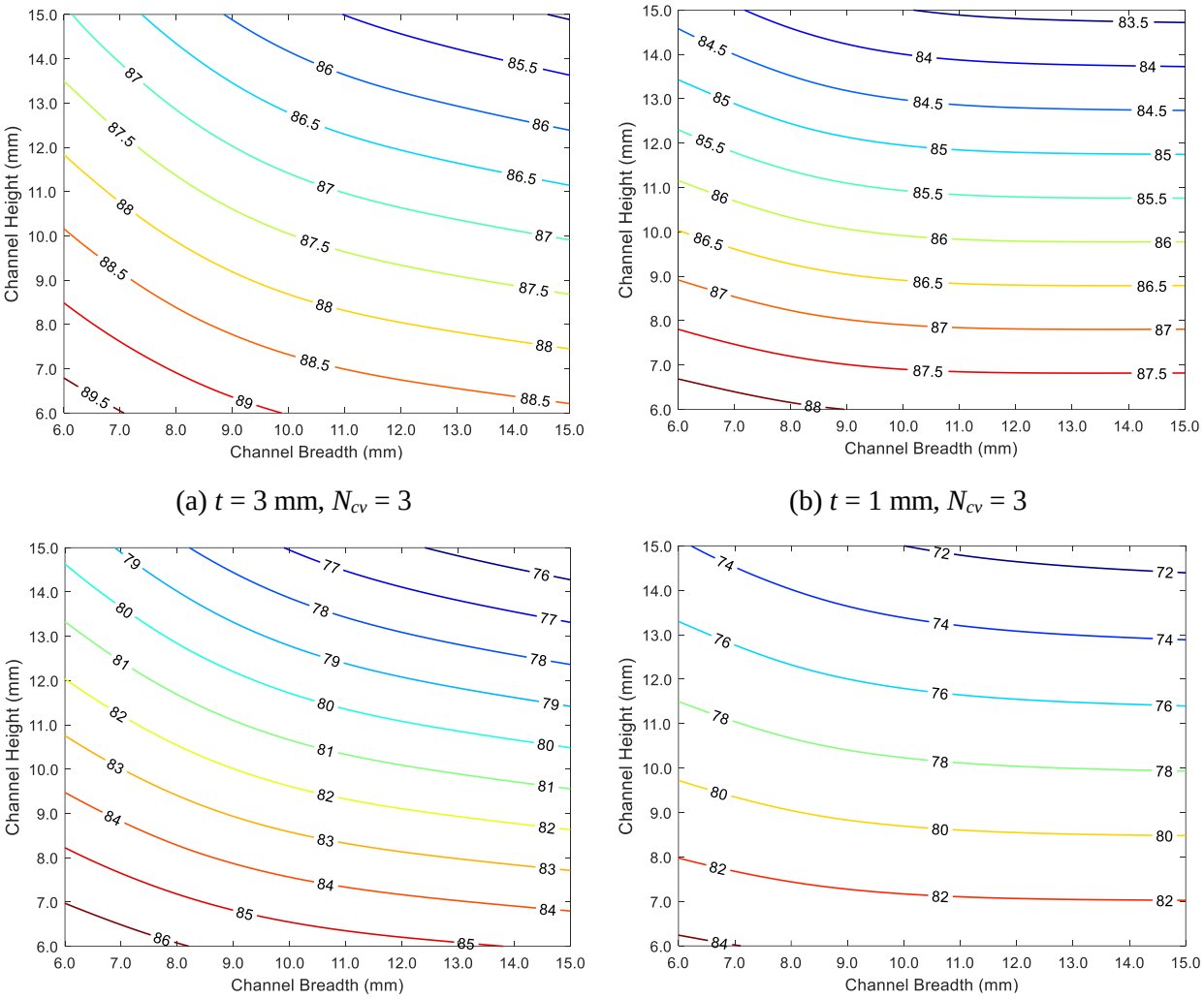


(a) $t$ = 3 mm, $N_{cv}$ = 3

(b) $t$ = 1 mm, $N_{cv}$ = 3

(c) $t$ = 3 mm, $N_{cv}$ = 10

(d) $t$ = 1 mm, $N_{cv}$ = 10

Figure 115. Energy efficiency (in %) as function of the channel breadth and height for different channel thickness and number of vertical channels for the wavy fin geometry. (a) $t$ = 3 mm, $N_{cv}$ = 3; (b) $t$ = 1 mm, $N_{cv}$ = 3; (c) $t$ = 3 mm, $N_{cv}$ = 10; and (d) $t$ = 1 mm, $N_{cv}$ = 10.

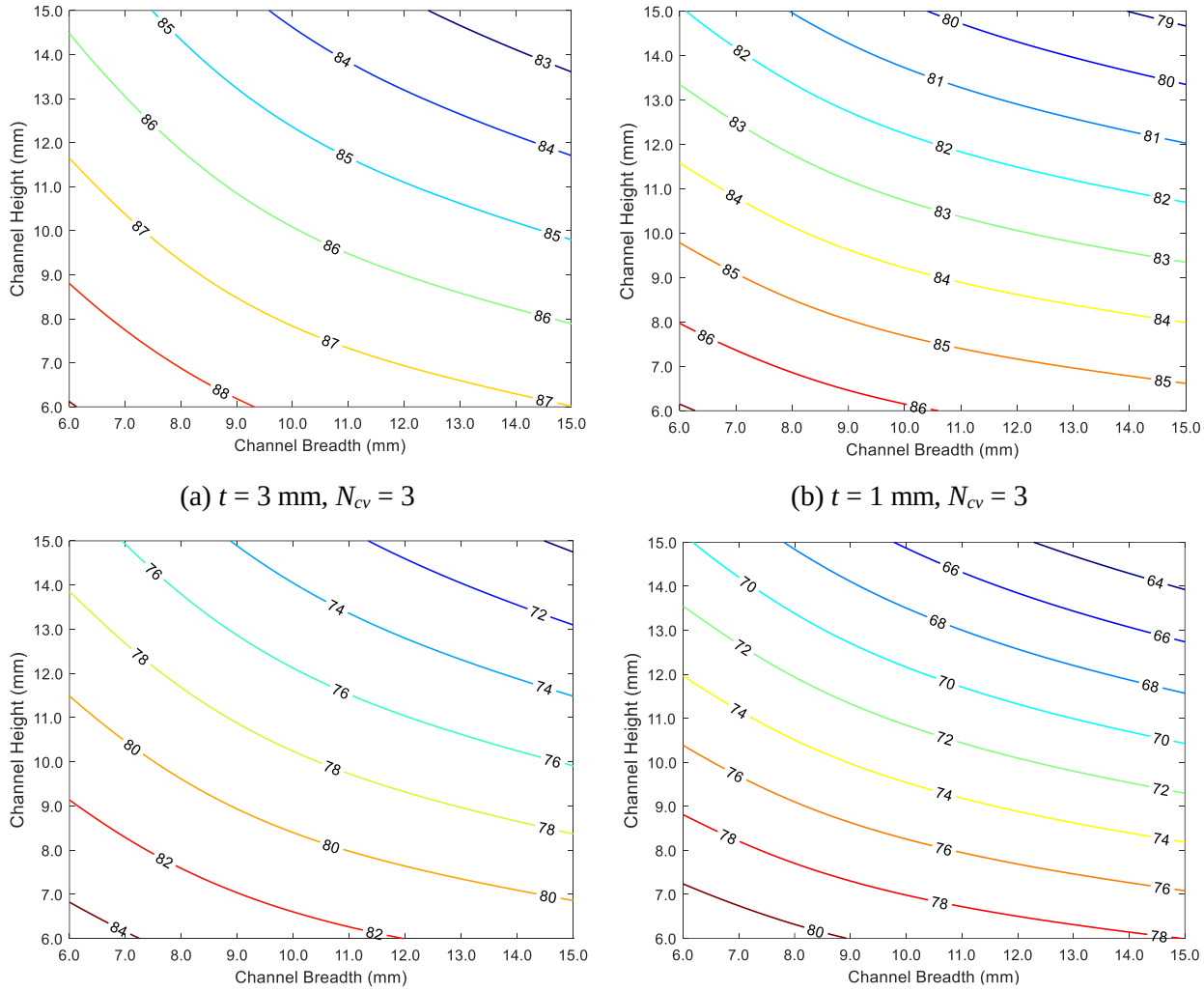


(a) $t$ = 3 mm, $N_{cv}$ = 3

(b) $t$ = 1 mm, $N_{cv}$ = 3

(c) $t$ = 3 mm, $N_{cv}$ = 10

(d) $t$ = 1 mm, $N_{cv}$ = 10

Figure 116. Energy efficiency (in %) as function of the channel breadth and height for different channel thickness and number of vertical channels for the offset strip fin geometry. (a) $t$ = 3 mm, $N_{cv}$ = 3; (b) $t$ = 1 mm, $N_{cv}$ = 3; (c) $t$ = 3 mm, $N_{cv}$ = 10; and (d) $t$ = 1 mm, $N_{cv}$ = 10.

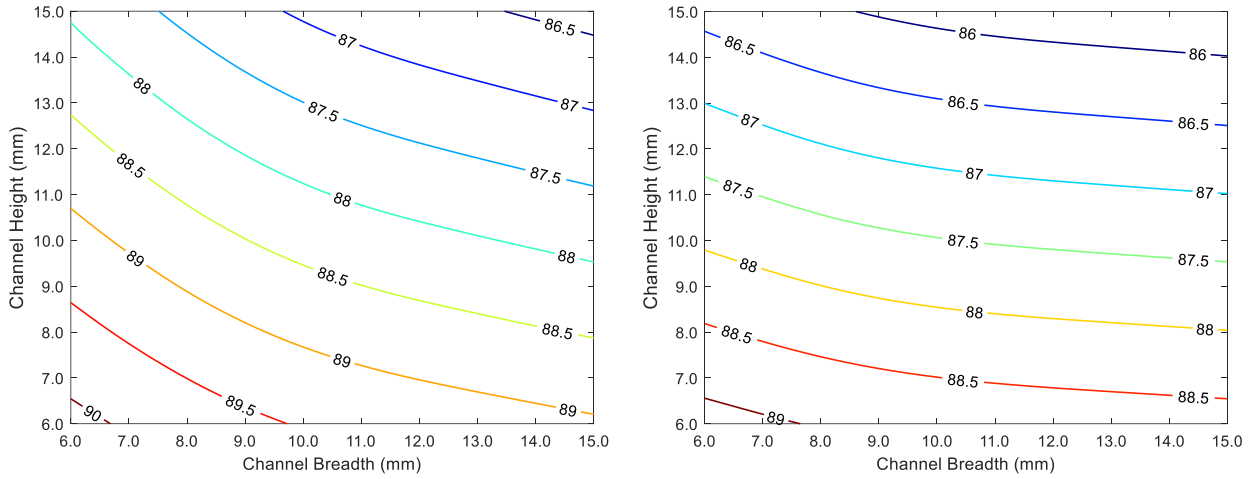


(a) t = 3 mm, Ncv = 3

(b) t = 1 mm, Ncv = 3

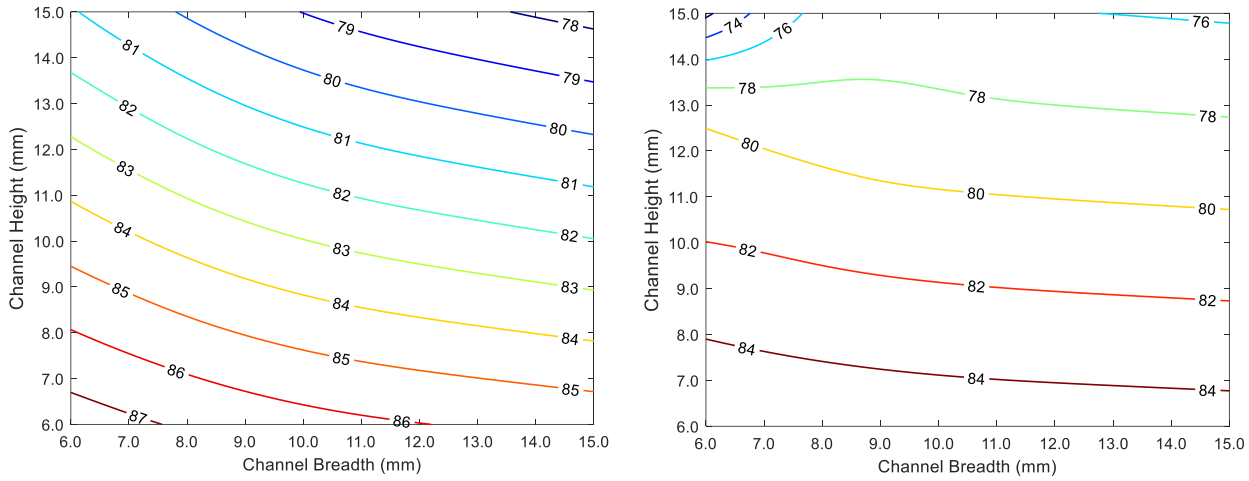


(c) t = 3 mm, Ncv = 10

(d) t = 1 mm, Ncv = 10

Figure 117. Energy efficiency (in %) as function of the channel breadth and height for different channel thickness and number of vertical channels for the perforated fin geometry. (a) $t$ = 3 mm, $N_{cv}$ = 3; (b) $t$ = 1 mm, $N_{cv}$ = 3; (c) $t$ = 3 mm, $N_{cv}$ = 10; and (d) $t$ = 1 mm, $N_{cv}$ = 10.

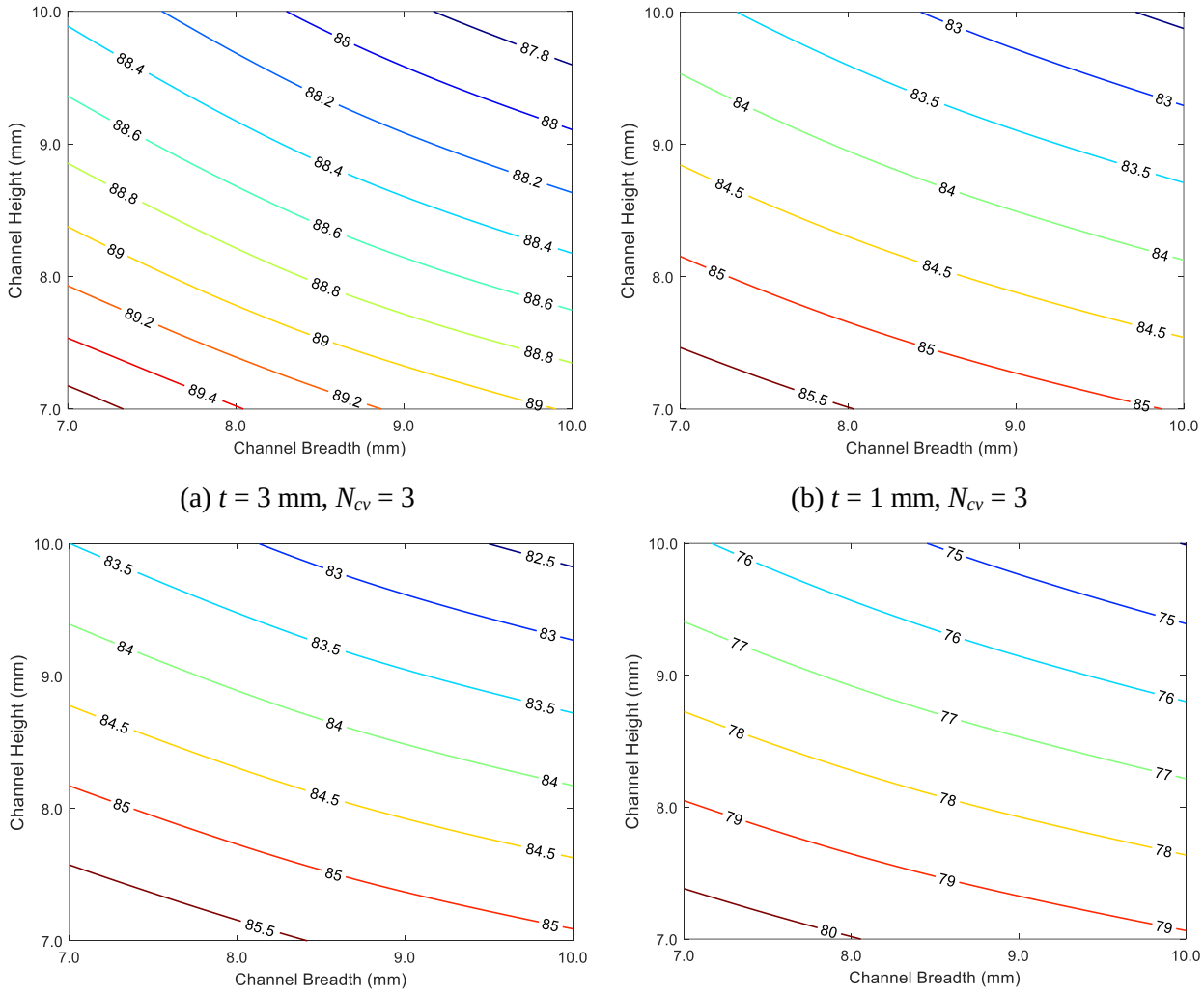


(a) $t$ = 3 mm, $N_{cv}$ = 3

(b) $t$ = 1 mm, $N_{cv}$ = 3

(c) $t$ = 3 mm, $N_{cv}$ = 10

(d) $t$ = 1 mm, $N_{cv}$ = 10

Figure 118. Energy efficiency (in %) as function of the channel breadth and height for different channel thickness and number of vertical channels for the louvred fin geometry. (a) $t$ = 3 mm, $N_{cv}$ = 3; (b) $t$ = 1 mm, $N_{cv}$ = 3; (c) $t$ = 3 mm, $N_{cv}$ = 10; and (d) $t$ = 1 mm, $N_{cv}$ = 10.

## A.6. Key components and instrumentation of testbed

The most relevant instrumentation of the pressurised receiver testbed are presented here with their photos laid over the testbed with indications for clarity.

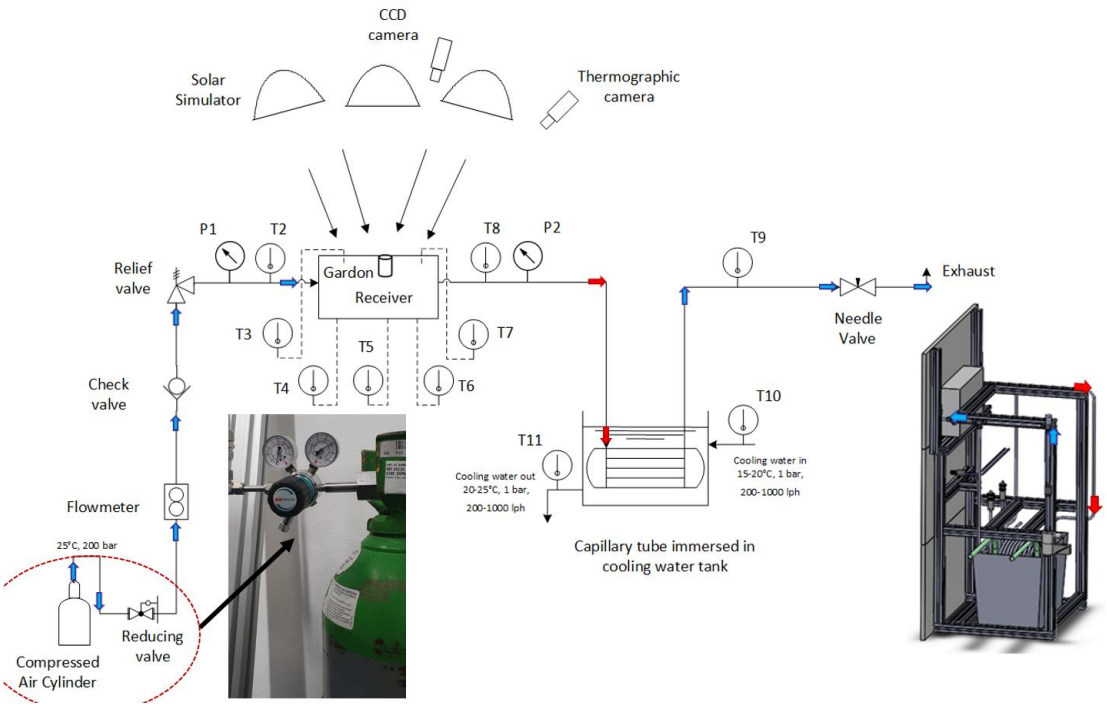


Figure 119. Cylinder and pressure reducing valve

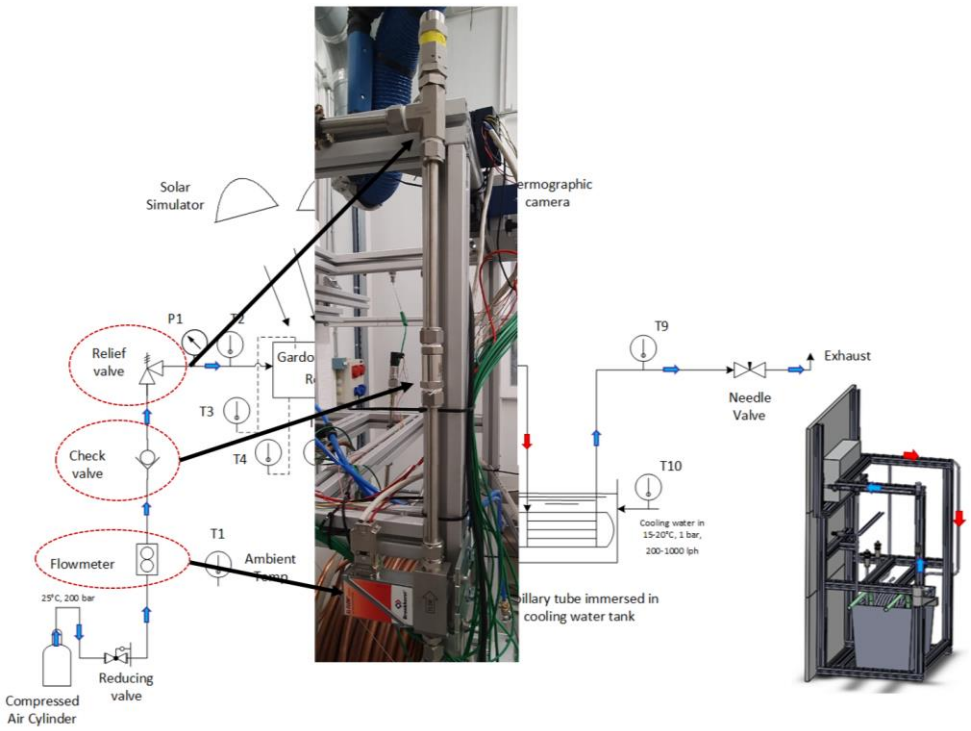


Figure 120. Mass flowmeter, check valve and pressure relief valve

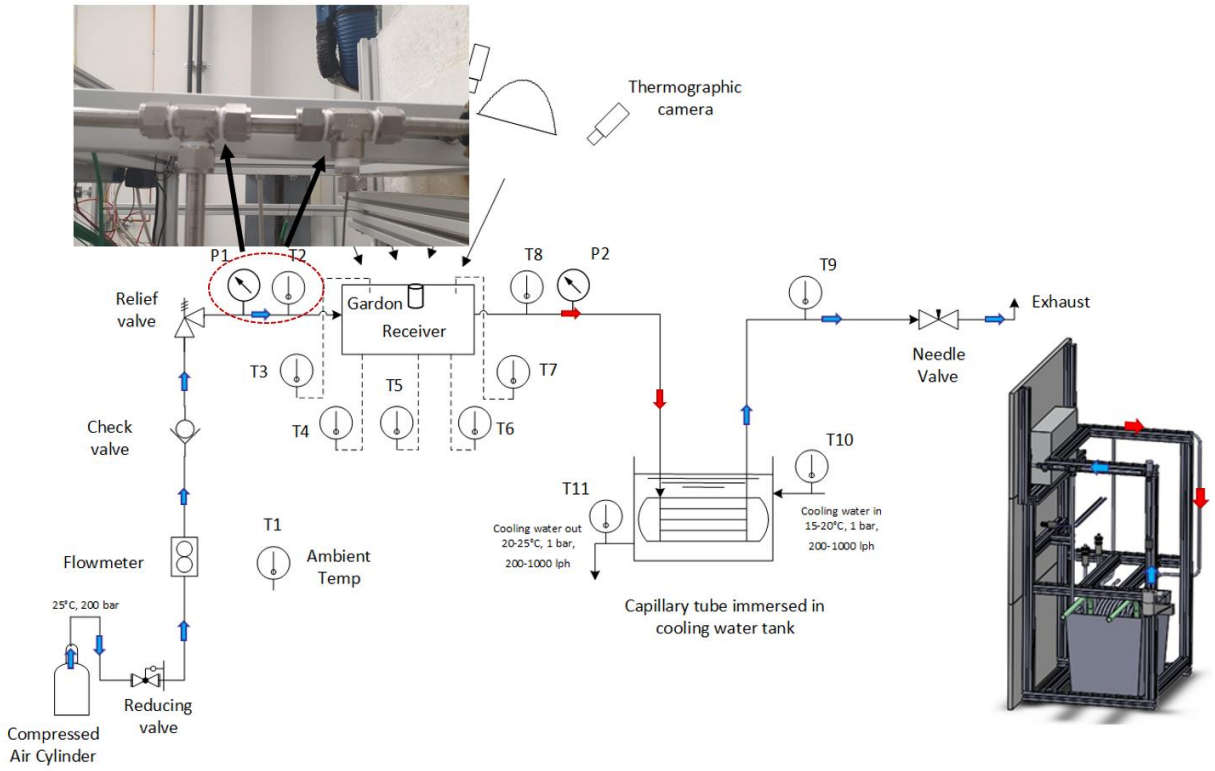


Figure 121. Pressure and temperature fittings

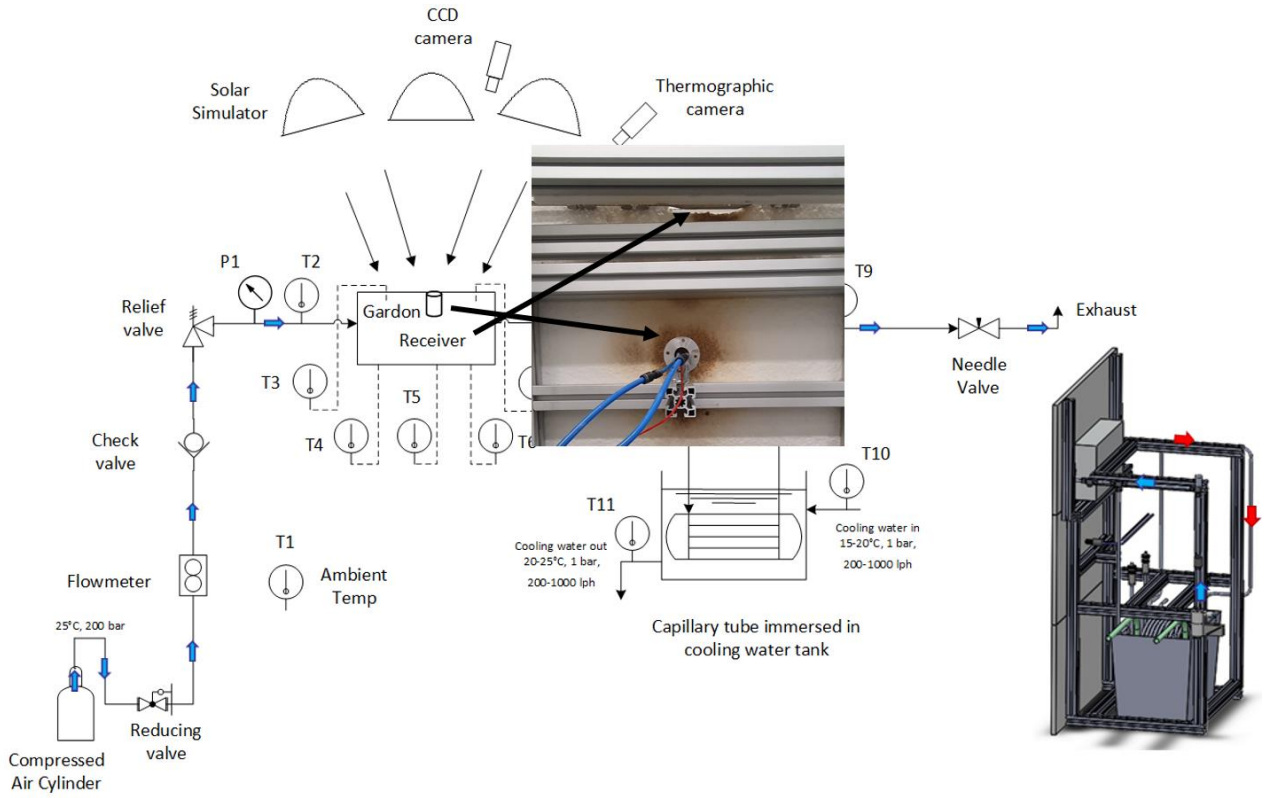


Figure 122. Gardon flux gauge and receiver

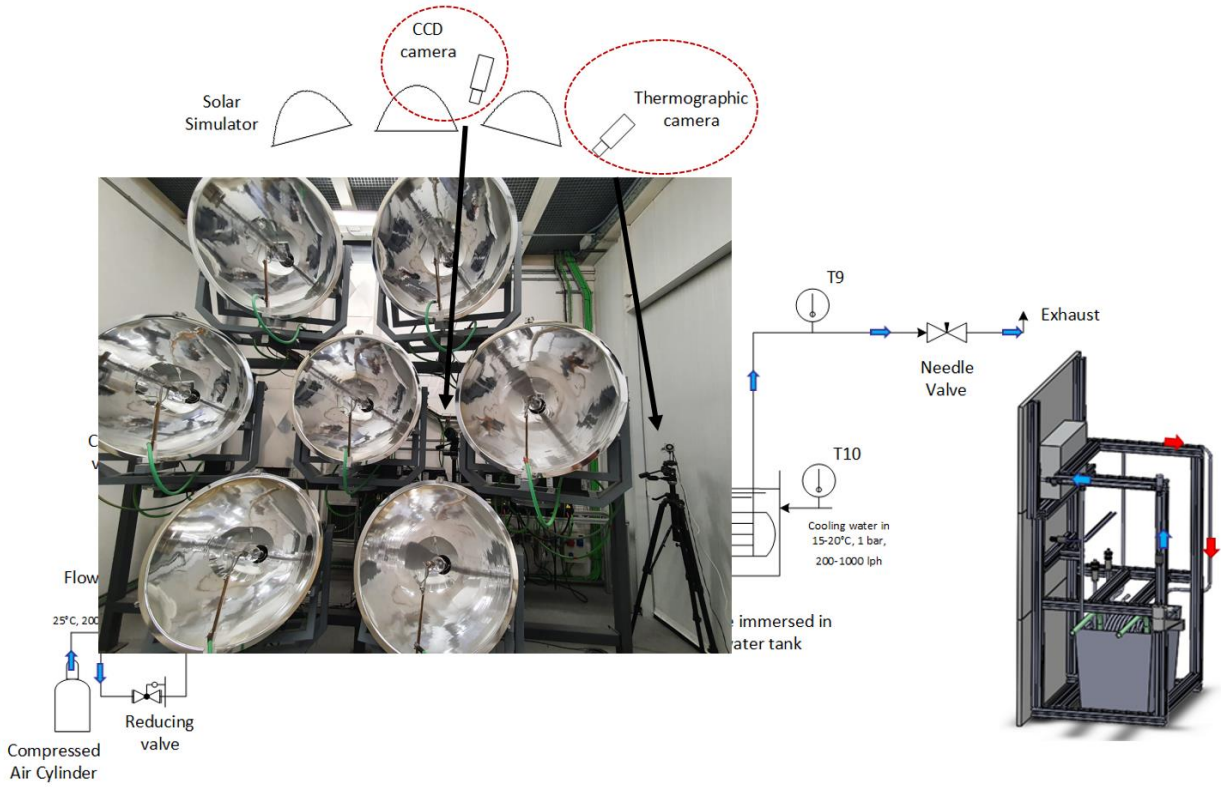


Figure 123. CCD and thermographic camera

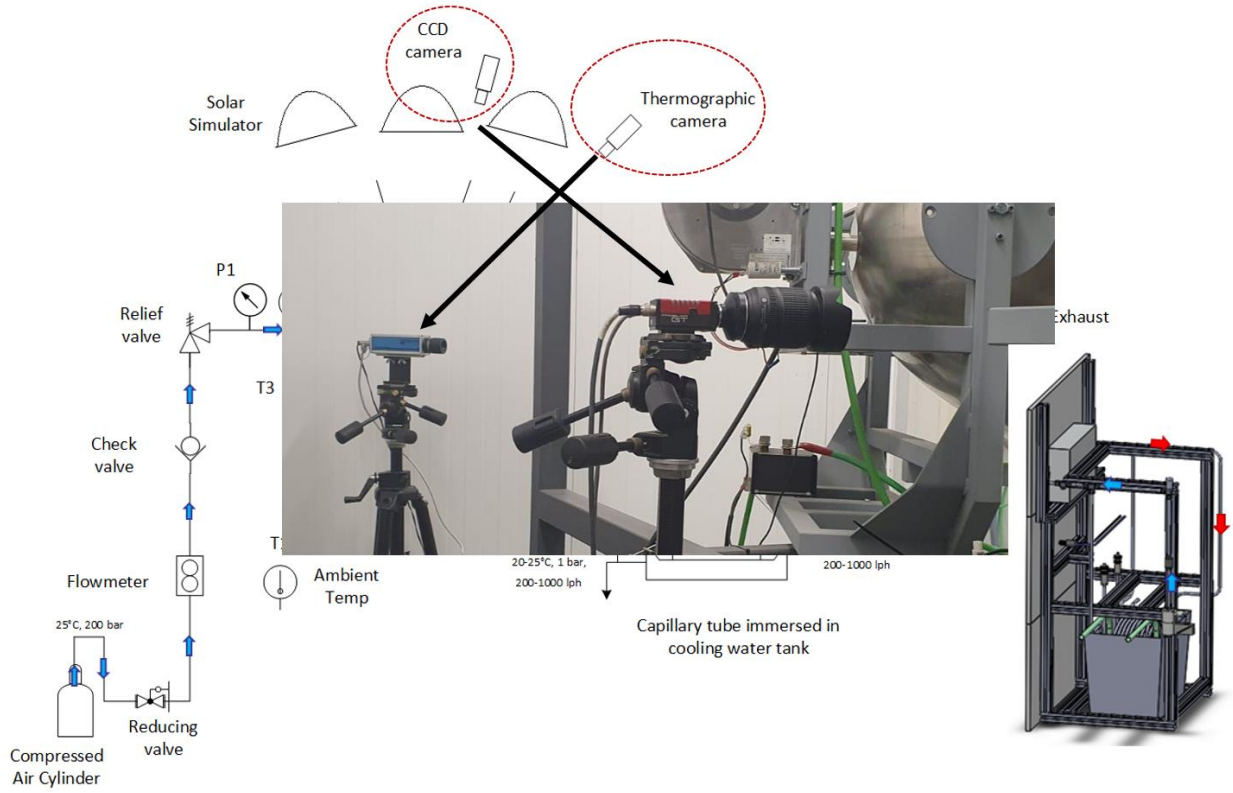


Figure 124. Side view of cameras

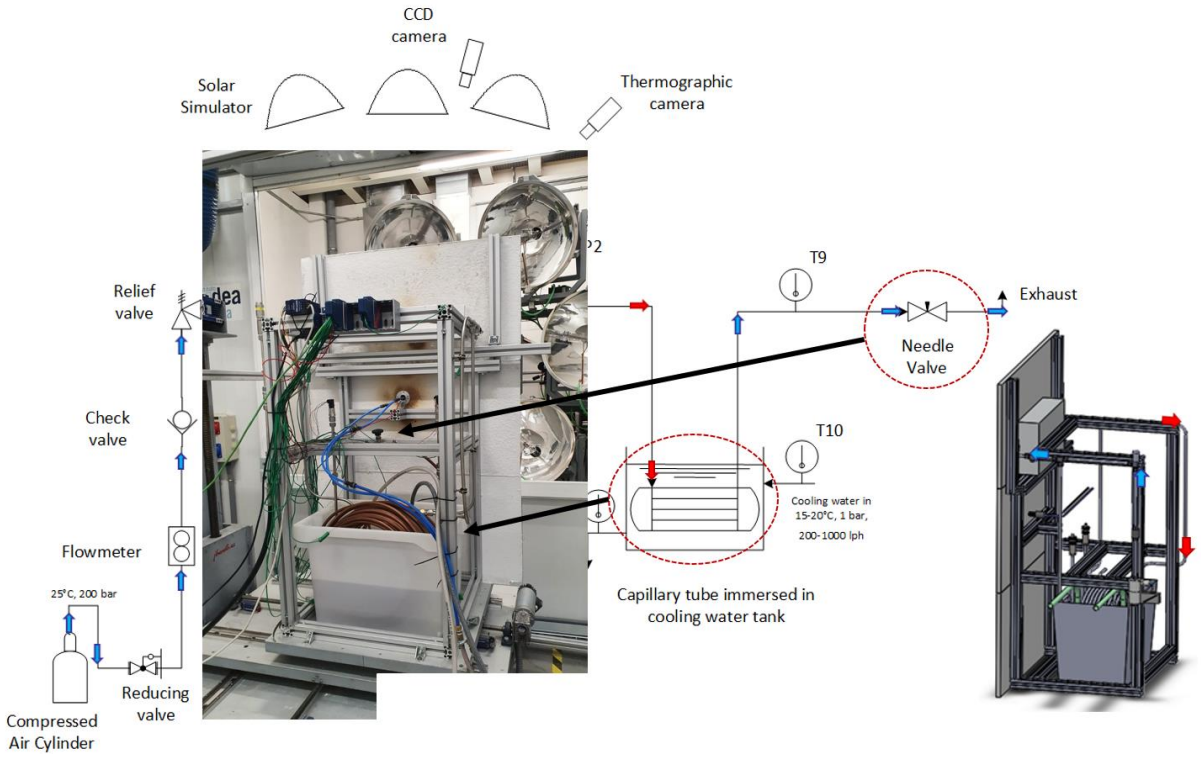


Figure 125. Cooling water tank and exhaust (needle) valve

Figure 126. Spectrophotometer with lamp chamber and measurement chamber open

# A.7. Experiment log

Table 34. Experiment log of entire campaign

| Date | Status of Testbed (Changes to previous) | Experiment Plan | Result/Comment |
|---|---|---|---|
| 14/10/2022 | Air supply from cylinder<br>New receiver in place | SS PR1, 4 bar, 2 g $s^{-1}$, 200-500 kW $m^{-2}$ | Experiment ok |
| 17/10/2022 | Repeat of previous | SS PR1, 4 bar, 2 g $s^{-1}$, 200-500 kW $m^{-2}$ | Experiment ok |
| | Cylinder change | SS PR1, 4 bar, 1.5 g $s^{-1}$, 200-500 kW $m^{-2}$ | Experiment ok |
| 18/10/2022 | Same cylinder | SS PR1, 4 bar, 1 g $s^{-1}$, 200-300 kW $m^{-2}$ | Experiment ok |
| | Cylinder change | SS PR1, 4 bar, 1 g $s^{-1}$, 400-500 kW $m^{-2}$ | After experiment, receiver oxide coating (black) from earlier experiments now gone. Attributed to rapid expansion. Proposed to slow initial rate of heating. |
| | Gardon removed to be used in unrelated other project. New LabVIEW code made with gardon removed, graph of air outlet temp and rate of change indicator | SS PR1, 12 bar, 2 g $s^{-1}$, 200-300 kW $m^{-2}$ | Experiment ok |
| 20/10/2022 | Cylinder change<br>Slow initial heating rate | SS PR1, 12 bar, 2 g $s^{-1}$, 400-500 kW $m^{-2}$ | With slow heating there is no rapid temperature rise and oxide layer loss |
| | | SS PR1, 12 bar, 1 g $s^{-1}$, 200-300 kW $m^{-2}$ | Experiment ok. No change in oxide layer |
| 21/10/2022 | Cylinder change | SS PR1, 12 bar, 1 g $s^{-1}$, 400-500 kW $m^{-2}$ | Experiment ok. No change in oxide layer |
| | | SS PR1, 12 bar, 1.5 g $s^{-1}$, 200-500 kW $m^{-2}$ | Experiment ok. No change in oxide layer |
| 8/11/2022 | New receiver in place (SS PR2) | Cold leak test | |
| 10/11/2022 | | SS PR2, 4 bar, 2 g $s^{-1}$, 200-500 kW $m^{-2}$ | Experiment ok. Light coating at outlet |
| 11/11/2022 | Cylinder change | SS PR2, 4 bar, 1.5 g $s^{-1}$, 200-500 kW $m^{-2}$ | Experiment ok. Light coating at outlet |
| | Cylinder change | SS PR2, 12 bar, 2 g $s^{-1}$, 200-500 kW $m^{-2}$ | Experiment ok. Light coating at outlet |
| 14/11/2022 | Cylinder change | SS PR2, 12 bar, 1.5 g $s^{-1}$, 200-500 kW $m^{-2}$ | Experiment ok. LabVIEW error at 300 kW $m^{-2}$ but data still recorded. Coating darker and more spread out. |
| 15/11/2022 | Cylinder change | SS PR2, 4 bar, 1 g $s^{-1}$, 200-500 kW $m^{-2}$ | Blackening apparent when at 500 kW $m^{-2}$ and experiment stop when back temperature rose above 600 C |
| | No change | SS PR2, 12 bar, 1 g $s^{-1}$, 200-400 kW $m^{-2}$ | No change in oxide layer. |
| 21/11/2022 | New receiver in place (SS PR3) | Cold leak test | Detectable leak in one fitting. Tightening works to an extent but leak persists though small. |
| 22/11/2022 | Cylinder change | SS PR3, 4 bar, 2 g $s^{-1}$, 200-500 kW $m^{-2}$ | Experiment ok. Light oxidation |
| | Cylinder change | SS PR3, 4 bar, 1.5 g $s^{-1}$, 200-500 kW $m^{-2}$ | Experiment ok. Further light oxidation. |
| 23/11/2022 | Cylinder change | SS PR3, 12 bar, 2 g $s^{-1}$, 200-500 kW $m^{-2}$ | Experiment ok. Light oxidation |
| | Cylinder change | SS PR3, 12 bar, 1.5 g $s^{-1}$, 200-500 kW $m^{-2}$ | Experiment ok. Visit to plant extended experiment but no effect. Stayed at |

| | | | |
|---|---|---|---|
| | | | point 3 (400 kW $m^{-2}$) for 50mins. Further oxidation. |
| 24/11/2022 | Cylinder change | SS PR3, 4 bar, 1 g $s^{-1}$, 200-500 kW $m^{-2}$ | Blackening apparent when at 500 kW $m^{-2}$ and experiment stop when back temperature rose above 600 C |
| 25/11/2022 | | SS PR3, 12 bar, 1 g $s^{-1}$, 200-400 kW $m^{-2}$ | Experiment ok |
| 28/11/2022 | New receiver in place (SS PR4) | Cold leak test | |
| 29/11/2022 | Cylinder change | SS PR4, 4 bar, 2 g $s^{-1}$, 200-500 kW $m^{-2}$ | Table y position was reset. 200 and 300 flux levels have to be repeated |
| | Cylinder change | SS PR4, 4 bar, 2 g $s^{-1}$, 200-300 kW $m^{-2}$ | |
| 30/11/2022 | | SS PR4, 4 bar, 1.5 g $s^{-1}$, 200-500 kW $m^{-2}$ | Cylinder at 120 bar. May not be sufficient for entire experiment run. Cylinder change conducted mid-experiment by moving table to standby point away from absorber during cylinder change. |
| 5/12/2022 | Cylinder change | SS PR4, 12 bar, 1.5 g $s^{-1}$, 200-500 kW $m^{-2}$ | Experiment ok. Cylinder changed mid-experiment |
| | Cylinder change | SS PR4, 12 bar, 2 g $s^{-1}$, 200-500 kW $m^{-2}$ | Experiment ok. Cylinder changed mid-experiment. |
| 7/12/2022 | Cylinder change | SS PR4, 4 bar, 1 g $s^{-1}$, 200-400 kW $m^{-2}$ | Experiment ok. |
| 8/12/2022 | Cylinder change | SS PR4, 12 bar, 1 g $s^{-1}$, 200-400 kW $m^{-2}$ | Experiment ok |

## A.8. Leak tests of receivers

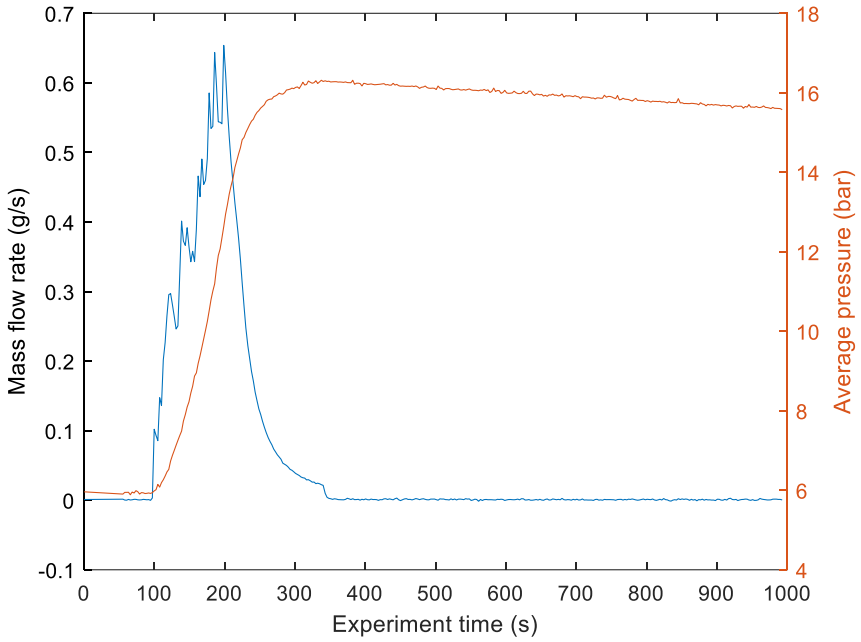


Figure 127. Leak test of PR1

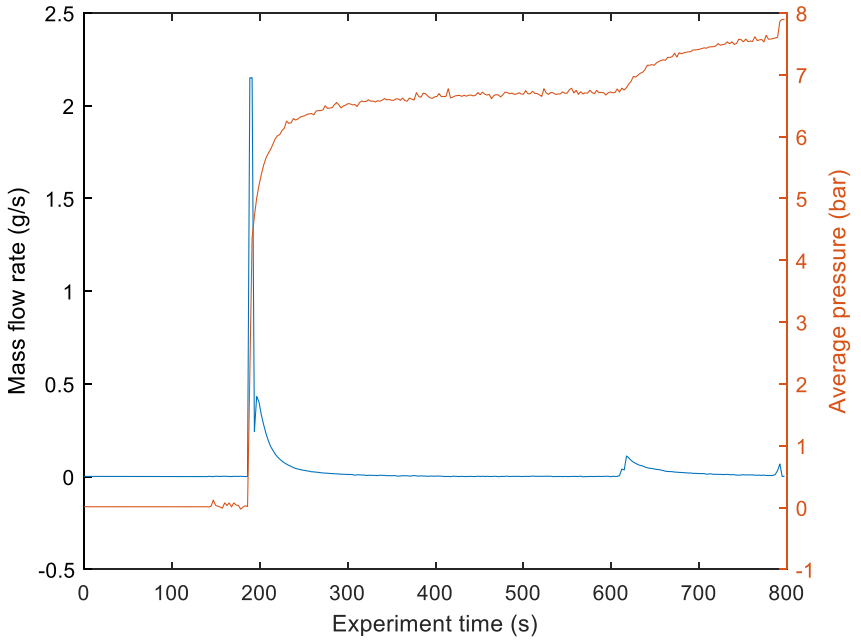


Figure 128. Leak test of PR2

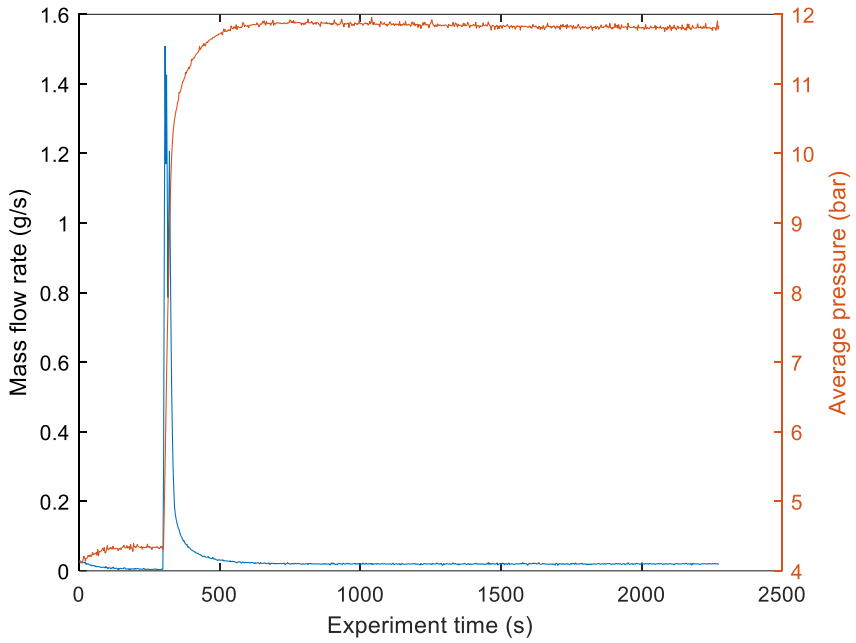


Figure 129. Leak test of PR3

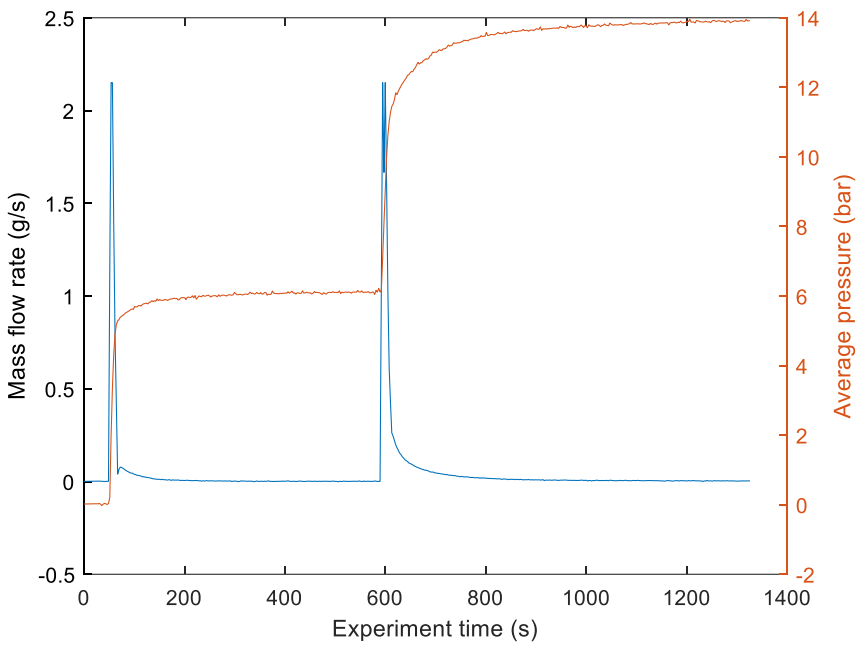


Figure 130. Leak test of PR4

## A.9. Photos of receivers after experiment runs

### Pressurised Receiver 1 (PR1)

After experiment run on 14/10/2022

After experiment run 1 on 17/10/2022

After experiment run 2 on 17/10/2022

After experiment run 1 on 18/10/2022

After experiment run 2 on 18/10/2022

After experiment run 3 on 18/10/2022

After experiment run 1 on 20/10/2022

After experiment run 2 on 20/10/2022

After experiment run 1 on 21/10/2022

After experiment run 2 on 21/10/2022

Figure 131: PR1 receiver after each experiment run

**Pressurised receiver 2 (PR2)**

After experiment run on 10/11/2022

After experiment run on 14/11/2022

After experiment run 1 on 11/11/2022

After experiment run 2 on 11/11/2022

After experiment run 1 on 15/11/2022

After experiment run 2 on 15/11/2022

Figure 132: PR2 receiver after each experiment run

**Pressurised receiver 3 (PR3)**

After experiment run 1 on 22/11/2022

After experiment run 2 on 22/11/2022

After experiment run 1 on 23/11/2022

After experiment run 2 on 23/11/2022

After experiment run on 24/11/2022

After experiment run on 25/11/2022

Figure 133: PR3 receiver after each experiment run

**Pressurised receiver 4 (PR4)**

After experiment run 1 on 29/11/2022

After experiment run 2 on 29/11/2022

After experiment run on 30/11/2022

After experiment run 1 on 5/12/2022

After experiment run 2 on 5/12/2022

After experiment run on 7/12/2022

After experiment run on 8/12/2022

Figure 134: PR4 receiver after each experiment run